

**SELF-ASSEMBLY BASED ON COBALT CHROMIUM LAYER  
DOUBLE HYDROXIDE NANOSHEETS, POLYOXOMETALATES  
ANIONS AND GRAPHENE OXIDE NANOSHEETS FOR  
SUPERCAPACITOR APPLICATION**

**THESIS SUBMITTED TO**



**FOR THE DEGREE OF**

**DOCTOR OF PHILOSOPHY**

**IN**

**PHYSICS**

**BY**

**Mr. SHRIKANT V. SADAVAR**

**M.Sc.**

**UNDER THE SUPERVISION OF**

**Dr. JAYAVANT L. GUNJAKAR**

**M.Sc., Ph.D.**

**RAMANUJAN FELLOW,**

**CENTRE FOR INTERDISCIPLINARY RESEARCH,**

**D. Y. PATIL EDUCATION SOCIETY (DEEMED TO BE UNIVERSITY), KOLHAPUR-  
416 006, MAHARASHTRA, (INDIA)**

**2022**

# DECLARATION

I hereby declare that the thesis entitled **“Self-assembly based on cobalt chromium layer double hydroxide nanosheets, polyoxometalates anions and graphene oxide nanosheets for supercapacitor application”** submitted for the degree of **Doctor of Philosophy (Ph.D.)** in the **Centre for Interdisciplinary Research** faculty of the **D. Y. Patil Education Society (Deemed to be University), Kolhapur** is completed and written by me, has not before made the basis for the award of any degree/diploma/other related heading of this or any other university in india/any other country/examining body to the best of my knowledge. Further, I assert that, I have not dishonored any of the requirements under copyright and piracy/cyber/IPR act amended by UGC from time to time.

**Place: Kolhapur**

**Mr. Shrikant V. Sadavar**

**Date:**

**(Research Student)**

**D. Y. Patil Education Society (Deemed to be  
University), Kolhapur**

***Centre for Interdisciplinary Research***



***Certificate***

This is to certify that the thesis entitled “**Self-assembly based on cobalt chromium layer double hydroxide nanosheets, polyoxometalates anions and graphene oxide nanosheets for supercapacitor application**” which is being submitted herewith for the award of the degree of **Doctor of Philosophy (Ph.D.) in Physics** of **D. Y. Patil Education Society (Deemed to be University), Kolhapur**, is the result of the original research work completed by **Mr. Shrikant Vaiju Sadavar** under my supervision and guidance and to the best of my knowledge and belief the work embodied in this thesis has not formed earlier the basis for the award of any degree or similar title of this or any other university or examining body.

Place: **Kolhapur**

Research Guide

Date:

**Dr. Jayavant L. Gunjekar**  
(Ramanujan Fellow)

Forwarded through,  
**Prof. C. D. Lokhande**  
Head and Research Director,  
Centre for Interdisciplinary Research

# ACKNOWLEDGEMENT

A journey is easier when you travel together. This thesis is the result of work where I have been accompanied and supported by many peoples.

At the completion of my Ph.D. thesis, I would like to express my sincere gratitude towards my guide, **Dr. J. L. Gunjekar** [Ramanujan Fellow, Centre for Interdisciplinary Research (CIR), D. Y. Patil Education Society (Deemed to be University), Kolhapur] for the continuous support during my Ph.D. study and related research, for his motivation, and immense knowledge. I thank him not only for the guidance he rendered in the field of research but also for enlightening the path of my life with a deep love for science. With his support, I could overcome my personal and scientific problems on writing scientific papers including this Ph.D. thesis and this work could not have been completed without his inspiring guidance and constant encouragement during the course of research tenure.

I sincerely acknowledge the whole hearted help, valuable discussions, guidelines and suggestions focused by **Prof. C. D. Lokhande**, Head and Research Director, Centre for Interdisciplinary Research (CIR). He provided a very fruitful discussion and helpful guidance for time management regarding my Ph.D. progress.

I am always grateful to **Dr. U. M. Patil** [DST-Inspire Faculty, Centre for Interdisciplinary Research (CIR), D. Y. Patil Education Society (Deemed to be University), Kolhapur] who was by my side always constantly inspiring, encouraging and guiding me. My association with him for the past few years was a rewarding experience, which will be cherished by me all along.

I would like to express my sincere thanks to Vice-Chancellor **Prof. R. K. Mudgal**, Pro-Vice Chancellor **Dr. Shimpa Sharma** and Registrar **Dr. V. V. Bhosale** for the inspiration and support. I thank **Dr. Meghanad Joshi**, **Dr. Vishwajeet Khot** and **Dr. Shivaji Kashte** who helped me to analyze the results with all their empathy and cooperative mind. I also thank **Dr. R. N. Bulakhe**, **Dr. Saji T. Kochuveedu**, **Dr. V. G. Parale**, and **Dr. Rahul Salunkhe** for providing me very important sample characterization data, during entire research work.

I would like to express sincere thanks to my seniors **Dr. Rahul Pujari, Dr. Pranav Katkar, Dr. Shital Kale and Dr. Supriya Marje** for insightful guidelines, scientific discussions and valuable suggestions on the present work. I am thankful to **Late A. Chavan**, Head, Department of Physics, Y. C. College, Halkarni (Kolhapur) and **Dr. D. R. Patil**, Assistant Professor, School of Materials Science and Engineering, Yeungnam University, Gyeongson, South Korea for their good wishes and support. I am also thankful to non-teaching staff of the CIR Department for their kind co-operation during my research work.

In addition, I acknowledge the funding support from **Chhatrapati Shahu Maharaj Research Training and Human Development Institute (SARTHI), Pune** of the **Government of Maharashtra** State for **Chhatrapati Shahu Maharaj National Research Fellowship (CSMNRF)** sanctioned to me.

I own a word of thanks to all my friends and research colleague from CIR department viz. **Navnath Padalkar, Rohini Shinde, Akash Patil, Vikas Magdum, Yogesh Chitare, Shirin Kulkarni, Sachin Pujari, Satish Jadhav, Shivaji Ubale, Vikas Mane, Dhanaji Malavekar, Suraj Khalate, Priti Bagawade, Vinod Patil, Sambhaji Kumbhar, Ranajit Nikam, Satish Phalake, Sambhaji Khot and Shraddha Bhosale.**

I hereby express my deepest appreciation and regards to my beloved parents (**Aai, Aaba**), brother (**Pundalik**) and all of family members who in spite of their hard times and sufferings, continuously supported and encouraged me to complete my research.

I would like to confess that even though I try my best, it is not possible for me to acknowledge and thank all those known and unknown faces individually for their direct and indirect contribution for the successful completion of this work. I am grateful to all of you for your kind cooperation.

Place- Kolhapur

**-Shrikant**

Date:

## **SUMMARY OF RESEARCH WORK**

### **A) Published (Indian) Patents:**

**1) Title of invention:** A method of producing polyoxovanadate intercalated layered copper hydroxide compound

**(Application No. – 201821018926; Date; 09/03/2019)**

**Inventors:** J. L. Gunjekar, C. D. Lokhande, S. T. Kochuveedu, **S. V. Sadavar**, N. S. Padalkar, V. V. Bhosale

**2) Title of Invention:** A method of preparation of an electrode based on nickel-chromium-layered double hydroxide intercalated with polyoxovanadate for supercapacitor application

**(Application no: 202021001507; Date: 13/01/2020)**

**Inventors:** J. L. Gunjekar, N. S. Padalkar, **S. V. Sadavar**, R. B. Shinde, C. D. Lokhande, V. V. Bhosale

**3) Title of Invention:** A method of preparation of an supercapacitor electrode based on cobalt chromium layered double hydroxide pillared with polyoxovanadate

**(Application no: 202021005460; Date: 07/02/2020)**

**Inventors:** J. L. Gunjekar, **S. V. Sadavar**, N. S. Padalkar, R. B. Shinde, R. N. Bulakhe, C. D. Lokhande, V. V. Bhosale

**4) Title of Invention:** A method of preparation of thin films of zinc chromium layered double hydroxide nanotubes with porous walls

**(Application no: 202021039044; Date: 09/10/2020)**

**Inventors:** J. L. Gunjekar, R. B. Shinde, N. S. Padalkar, **S. V. Sadavar**, A. S. Patil, C. D. Lokhande, V. V. Bhosale

### **B) Papers Published/Submitted at International Journals:**

1) Akash S. Patil, Jayavant L. Gunjekar, Chandrakant D. Lokhande, Umakant M. Patil, **Shrikant V. Sadavar**, Navanath S. Padalkar, Rohini B. Shinde, Mahesh M. Wagh, Jaydeep S. Bagi, Nanocrystalline copper-chromium-layered double hydroxide with tunable interlayer anions for electrochemical capacitor application, Synth. Met., 2020, 264, 116371-116379, <https://doi.org/10.1016/j.synthmet.2020.116371>, (I. F. – 3.26).

- 2) **Shrikant V. Sadavar**, Navnath S. Padalkar, Rohini B. Shinde, Saji T. Kochuveedu, Umakant M. Patil, Akash S. Patil, Ravindra N. Bulakhe, Chandrakant D. Lokhande, Insik In, Rahul R. Salunkhe, Jayavant L. Gunjekar, Mesoporous nanohybrids of 2-D cobalt-chromium layered double hydroxide and polyoxovanadate anions for high performance hybrid asymmetric supercapacitors, *J. Power Sources*, 2022, 524, 231065, <https://doi.org/10.1016/j.jpowsour.2022.231065>, **(I. F. - 9.12)**.
- 3) **Shrikant V. Sadavar**, Navnath S. Padalkar, Rohini B. Shinde, Akash S. Patil, Umakant M. Patil, Vikas V. Magdum, Yogesh M. Chitare, Shirin P. Kulkarni, Ravindra N. Bulakhe, Vinayak G. Parale, and Jayavant L. Gunjekar, Graphene oxide an efficient hybridization matrix for exploring electrochemical activity of 2D cobalt-chromium-layered double hydroxide based nanohybrids, *ACS Appl. Energy Mater.*, 2022, <https://doi.org/10.1021/acsaem.1c03619>, **(I. F. - 6.02)**.
- 4) **Shrikant V. Sadavar**, Navnath S. Padalkar, Rohini B. Shinde, Akash S. Patil, Umakant M. Patil, Vikas V. Magdum, Yogesh M. Chitare, Shirin P. Kulkarni, Ravindra N. Bulakhe, Saji T. Kochuveedu, Jayavant L. Gunjekar, Lattice engineering exfoliation-restacking route for 2D layered double hydroxide hybridized with 0D polyoxotungstate anions: Cathode for hybrid asymmetric supercapacitors, *Energy Storage Mater.* (*Revision submitted*), **(I. F. - 17.78)**.
- 5) Navnath S. Padalkar, **Shrikant V. Sadavar**, Rohini B. Shinde, Akash S. Patil, Umakant M. Patil, Dattatray S. Dhawale, Habib M. Pathan, Shrikrishna D. Sartale, Vinayak G. Parale, Ajayan Vinu, Chandrakant D. Lokhande and Jayavant L. Gunjekar, Mesoporous nanohybrids of 2D Ni-Cr-layered double hydroxide nanosheets pillared with polyoxovanadate anions for high-performance hybrid supercapacitor, *Adv. Mater. Interfaces*, 2021, 2101216, [10.1002/admi.202101216](https://doi.org/10.1002/admi.202101216), **(I. F. - 6.14)**.
- 6) Rohini B. Shinde, Akash S. Patil, **Shrikant V. Sadavar**, Yogesh M. Chitare, Vikas V. Magdum, Navnath S. Padalkar, Umakant M. Patil, Saji T. Kochuveedu, Vinayak G. Parale, Hyung-Ho Park, Chandrakant D. Lokhande, Jayavant L. Gunjekar, Polyoxotungstate intercalated self-assembled nanohybrids of Zn-Cr-LDH for room temperature Cl<sub>2</sub> sensing,

Sens. Actuators B Chem., 2022, 352, 131046,  
<https://doi.org/10.1016/j.snb.2021.131046>, **(I. F. – 7.46)**.

- 7) Rohini B. Shinde, Navnath S. Padalkar, **Shrikant V. Sadavar**, Shital B. Kale, Vikas V. Magdum, Yogesh M. Chitare, Shirin P. Kulkarni, Umakant M. Patil, Vinayak G. Parale, Jayavant L. Gunjekar, 2D-2D Lattice engineering route for intimately coupled nanohybrids of layered double hydroxide and potassium hexaniobate: Chemiresistive SO<sub>2</sub> sensor, *J. Hazard. Mater.*, (*Required Revision*), **(I. F. – 10.58)**.
- 8) Rohini B. Shinde, Navnath S. Padalkar, **Shrikant V. Sadavar**, Akash S. Patil, Shital B. Kale, Vikas V. Magdum, Yogesh M. Chitare, Shirin P. Kulkarni, Umakant M. Patil, Vinayak G. Parale, Jayavant L. Gunjekar, Lattice engineering route for self-assembled nanohybrids of 2D layered double hydroxide with 0D isopolyoxovanadate: Chemiresistive SO<sub>2</sub> sensor, *Mater. Today Chem.*, (*Accepted*), **(I. F. – 8.3)**.
- 9) Navnath S. Padalkar, **Shrikant V. Sadavar**, Rohini B. Shinde, Akash S. Patil, Umakant M. Patil, Dattatray S. Dhawale, Ravindra N. Bulakhe, Hyungsang Kim, Hyunsik Im, Ajayan Vinu, Chandrakant D. Lokhande, Jayavant L. Gunjekar, “Layer-by-Layer nanohybrids of Ni-Cr-LDH intercalated with 0D polyoxotungstate for highly efficient hybrid supercapacitor”, *J. Colloid Interface Sci.*, Elsevier, (*Required Revision*), **(I. F. – 8.12)**.
- 10) Navnath S. Padalkar, **Shrikant V. Sadavar**, Rohini B. Shinde, Akash S. Patil, Umakant M. Patil, Vikas V. Magdum, Yogesh M. Chitare, Shirin P. Kulkarni, Ravindra N. Bulakhe, Vinayak G. Parale, Jayavant L. Gunjekar, “2D-2D nanohybrids of Ni-Cr-layered double hydroxide wrapped with graphene oxide nanosheets: electrode for hybrid asymmetric supercapacitors”, *Electrochim. Acta.*, (*Under Review*), **(I. F. – 6.90)**.

### **C) Papers/Poster Presented at National/International Conferences:**

- 1) **S. V. Sadavar**, N. S. Padalkar, R. B. Shinde, A. S. Patil, C. D. Lokhande, J. L. Gunjekar, Poster presentation “Synthesis of Cobalt Chromium Layer Double Hydroxide (Co-Cr-LDH) in Nitrate Form for Supercapacitor Application”, national workshop on Modern Approaches in Sciences (MAS-2019), 28<sup>th</sup> January, 2019, K. N. Bhise Arts, Commerce and Vinayakarao Patil Science College, Vidyanagar, Bhosare, Kurduwadi, Solapur, India.
- 2) **Shrikant V. Sadavar**, Navnath S. Padalkar, Rohini B. Shinde, Akash S. Patil, Chandrakant D. Lokhande, Jayavant L. Gunjekar, Poster presentation “Synthesis of Exfoliated Cobalt Chromium Layer Double Hydroxide (Co-Cr-LDH) for Supercapacitor Application”, international conference on Physics of Materials and Materials Based Device Fabrication (4<sup>th</sup> ICPM-MDF-2019), 10<sup>th</sup> and 11<sup>th</sup> January, 2019, Shivaji University, Kolhapur, India.
- 3) **S. V. Sadavar**, N. S. Padalkar, R. B. Shinde, A. S. Patil, C. D. Lokhande, J. L. Gunjekar, Poster presentation “Synthesis of Co-Cr-LDH nanosheets for electrochemical capacitor”, national conference on Advanced Materials Synthesis, Characterization and Application (AMSCA-2018), 14<sup>th</sup> and 15<sup>th</sup> December, 2018, Savitribai Phule Pune University, Pune, India.
- 4) **S. V. Sadavar**, N. S. Padalkar, R. B. Shinde, A. S. Patil, C. D. Lokhande, J. L. Gunjekar, Poster presentation “Self-assembly of cobalt chromium layer double hydroxide (Co-Cr-LDH) and polyoxovanadate anion (POV) for supercapacitor application” at Anveshan 2018, 5<sup>th</sup> Dec 2018, D. Y. Patil Education society (Deemed to be University), Kolhapur, India.

# CONTENTS

<b>Chapter No.</b>	<b>Title</b>	<b>Page No.</b>
1	General Introduction and Literature Survey	1-42
2	Theoretical Background of LDH, Synthesis Methods, Exfoliation and Characterization Techniques	43-74
3	Synthesis, Characterization and Electrochemical Performance of Co-Cr-LDH, and rGO Ns	75-96
4	Synthesis, characterization and Electrochemical Performance of Co-Cr-LDH-POV and AHSC Device	97-132
5	Synthesis, Characterization and Electrochemical Performance of Co-Cr-LDH-POW and AHSC Device	133-158
6	Synthesis, Characterization and Electrochemical Performance of Co-Cr-LDH-GO and AHSC Device	159-188
7	Summary and Conclusions	189-194
8	80-Recommendation	195-199

## Abbreviations

- **AHSC** Aqueous hybrid asymmetric supercapacitor
- **CV** Cyclic voltammetry
- **Cs** Specific capacitance
- **Csp** Specific capacity
- **ED** Energy density
- **EDS** Energy dispersive spectroscopy
- **EIS** Electrochemical impedance spectroscopy
- **FTIR** Fourier transform infrared spectroscopy
- **FESEM** Field emission scanning electron microscopy
- **GCD** Galvanostatic charge discharge
- **GO** Graphene oxide
- **HRTEM** High resolution transmission electron microscopy
- **HSC** Hybrid supercapacitor device
- **LDH** Layer double hydroxide
- **Ns** Nanosheets
- **PD** Power density
- **PXRD** Powder X-ray diffraction
- **rGO** Reduced graphene oxide
- **SC** Supercapacitor
- **SS** Stainless steel
- **XPS** X-ray photoelectron spectroscopy



# **CHAPTER-1**

## **GENERAL INTRODUCTION AND LITERATURE SURVEY**

# CHAPTER-1

## General Introduction and Literature Survey

Sr. No.	Title		Page No.
1.1	Introduction: Electrochemical energy storage		1
	1.1.1	Background and development of electrochemical energy storage devices	1
	1.1.2	Working principle of capacitor	5
1.2	Supercapacitor		6
	1.2.1	Working principle of supercapacitor	6
	1.2.2	Classification of supercapacitors	8
	1.2.3	Electric double layer capacitors (EDLCs)	9
	1.2.4	Pseudocapacitors	9
		1.2.4.1 Intrinsic or surface redox pseudocapacitors	10
		1.2.4.2 Intercalation pseudocapacitors	11
		1.2.4.3 Extrinsic pseudocapacitors	11
	1.2.5	Hybrid supercapacitors	11
1.3	Materials for supercapacitor		12
	1.3.1	Carbon derivatives	13
	1.3.2	Metal oxides	13
	1.3.3	Conducting polymers	14
	1.3.4	Metal sulfides	14
	1.3.5	Layer double hydroxides	14
1.4	Literature survey		15
	1.4.1	Literature survey of LDH based electrochemical energy storage	15
	1.4.2	Literature survey of 2D inorganic nanosheets (INs)	23
1.5	Thesis: Orientation and purpose		33
1.6	References		36

---

## 1.1 Introduction: Electrochemical energy storage

### 1.1.1 Background and development of electrochemical energy storage devices:

Worldwide consistently increased globalization and living standard of humankind require more and more energy. Presently electrical energy from hydropower plants and fossil fuels are satisfying this need. Nowadays electrical energy is an indissoluble part of a human being. Presently, society consumes  $606.7 \times 10^{18}$  J of energy per day and requires  $776.5 \times 10^{18}$  J of energy in the near future. [1] Current hydropower projects are not satisfying the need for energy according to the requirement. Fossil fuels are the most favorites and prove their advantages as fuel in the automobile sector. The burning of fossil fuels for power generation is the largest single source responsible for nearly 25 % of the global greenhouse gas emissions. [2] Moreover, their rapid consumption and limited resources restrict their long-term perspective uses. Therefore many global efforts are put forward to explore green renewable sources for their efficient utilization. [3]

Renewable energy sources mainly consist of solar power, wind power, hydro power, tidal, geothermal, and biomass. Though renewable energy sources are non-polluted and abundant green energy sources, the utilization of these renewable energy sources is limited by their non-continuous nature. For instance, solar energy is one of the most promising renewable energy source. However, its weather fluctuating nature restricts its practical uses. Also, solar energy is not continuous and homogeneous on each part of the earth's surface. On the other hand, wind power is also not readily available continuously, as its availability and intensity are dependent on natural instances. Hence, energy storage systems are much needed to utilize renewable energy sources effectively and realistically.

Thus, various energy storage technologies can be systematized and categorized into four general types according to their charge storage principle, such as chemical, mechanical, electrical, and electrochemical. [4] The classification of the energy storage systems is shown in figure 1.1.

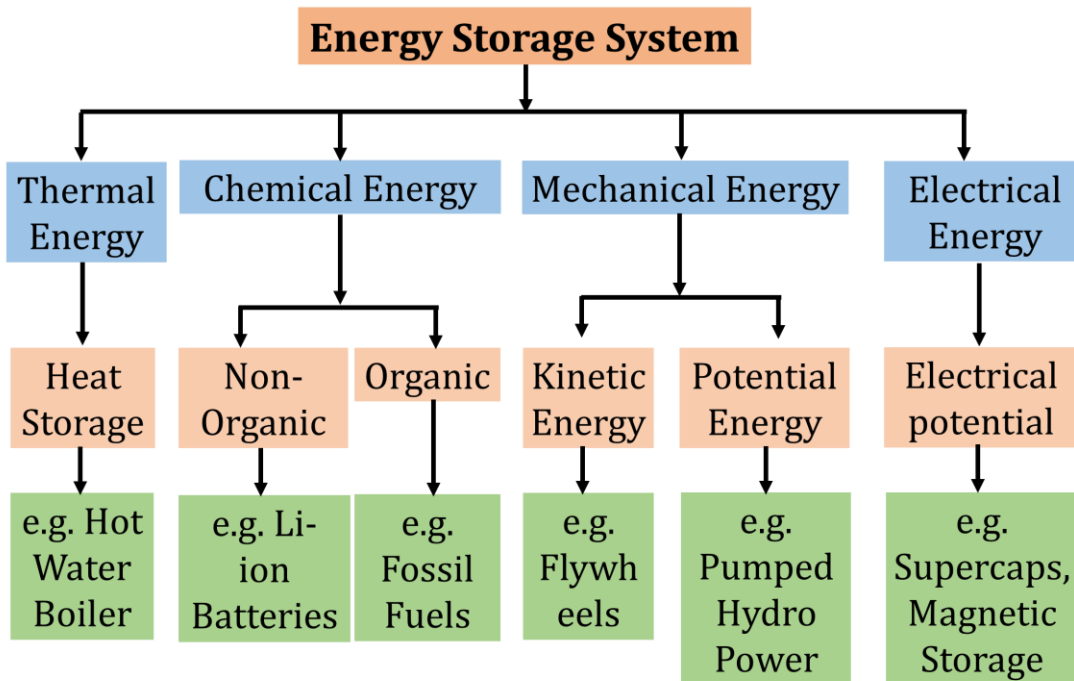


**Figure 1.1:** Classification of the energy storage systems. [5]

This situation encourages researchers to investigate reliable energy storage technologies useful for electric vehicles (EVs), hybrid electric vehicles (HEVs), portable electronic devices etc. Hence, supercapacitors (SCs) have attracted more attention due to the unique characteristic of a much higher energy density (ED) and power density (PD) in comparison with conventional capacitors and batteries. [6]

Batteries store energy by the net chemical reaction between the electrode and an electrolyte. Commonly, batteries can be divided mainly into two types such as primary and secondary batteries. Primary batteries, primary cells, or disposable batteries are needed to discard after full usage. It means that while charging, irreversible redox reaction occurs at electrodes of primary batteries, so there is no more chemical reaction possible after one time charging-discharging due to permanent change in the chemical structure of the electrodes. Zinc chloride, lithium-manganese, and alkaline batteries are examples of commercially available primary batteries. Secondary batteries are rechargeable batteries. These can be charged-discharged multiple times by reversing the current flow. In the secondary batteries, the original composition of electrodes can be restored by reversible electrochemical reactions. Generally, primary batteries have higher ED as compare to secondary batteries. Examples of secondary rechargeable batteries are lead-

acid, nickel-cadmium, nickel-metal hydride and lithium-ion batteries. The operating voltage of lithium-ion batteries is high due to the use of organic electrolytes. Moreover, specialty batteries are constructed for specific purposes such as military and medical persistence. Lithium-iodine, nickel-hydrogen, manganese-silver chlorides are examples of specialty batteries. [7] The major advantage of rechargeable batteries is that they can be reused several times. It is also recyclable. Alkaline batteries hold a charge for a long time (five to seven years) even don't charge while not in use. However, the main disadvantages of nickel-metal hybrid (NiMH) batteries are must be recharged even they are not in use. Also, lower ED, poorer charge retention, safety issues, lack of standards, and high initial costs are the disadvantages of batteries.

Another type of electrical energy storage device is a capacitor made up of dielectric material sandwiched between two metal plates. This device can be charged by applying external electric potential that causes the accumulation of charges on the metal plates with the polarization of dielectric material. This phenomenon is responsible for the electrical charge storage on both conductive metal plates. Mechanism of polarization of dielectric material is shown in figure 1.2.

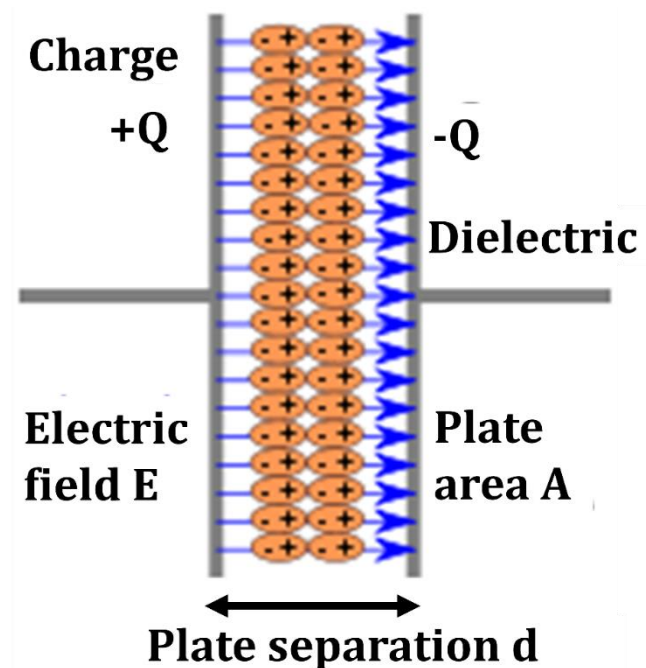


**Figure 1.2:** Mechanism of polarization of dielectric material.

As shown in figure 1.2, when potential is applied across the capacitor, instantaneous current flows and, one plate gets positively charged, and the other gets negatively charged. These charges get remained on the metallic plate even after removal of applied field. [8] In electronic circuits, capacitor plays numerous roles like backup circuits for microcomputers, smoothing power supplies, resisting the DC flow in a circuit etc. Other roles of the capacitor are to deliver leading current in AC circuits, act as an open switch in DC circuit, as a filter in DC circuit, as decoupling the two electronics circuits (decoupling capacitor), as a separation of AC and DC signal and removes the ripples from pulsating DC supply voltage to convert it into pure AC voltage after rectification (coupling capacitor). Thus initially, parallel plate capacitors are not useful to store high-energy applications. [9]

Advanced applications (hybrid vehicles, maglev trains, power-braking recuperation, truck lifts, and track switching) required energy storage devices with high energy and high power. Thus from the last decades, many efforts have been put forward to develop energy storage devices with the capability of high energy and power.

The SCs are attractive energy storage devices that can deliver high energy and power. SC can able to store high PD ( $>10 \text{ kW kg}^{-1}$ ) and high ED ( $\sim 10 \text{ Wh kg}^{-1}$ ) as compared with batteries (PD  $\sim 10$  to  $800 \text{ W kg}^{-1}$  & ED  $\sim 10$  to  $100 \text{ Wh kg}^{-1}$ ). Therefore, SCs are useful in applications where high energy is required in a very short time. Also, SCs demonstrate excellent stability over thousands of charge-discharge cycling. [10] The comparative Ragone plot of different energy storage devices is shown in figure 1.3.

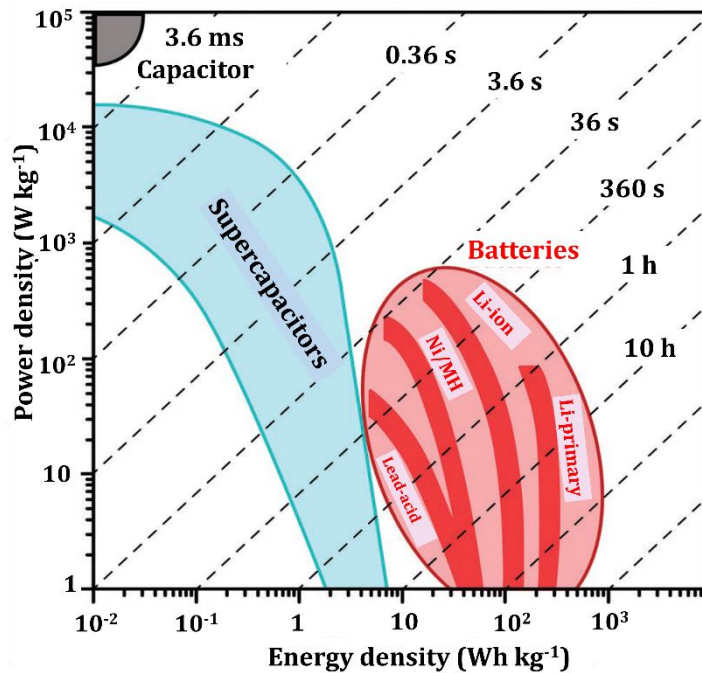


**Figure 1.3:** Comparative Ragone plot of different energy storage devices with average discharge time. [11-17]

### 1.1.2 Working principle of capacitor:

The capacitor comprises two metal plates and a dielectric. When we apply DC voltage across the metal plates, one metal plate get positively charged, and another negatively charged. An electric field is generated across the capacitor. At a certain stage, the capacitor holds the maximum charge during the charging process. After removing the DC voltage from the capacitor, both plates hold the charges for a certain time, and the capacitor acts as an electrical energy source. When the load is applied across the metal plates, the capacitor gets discharged due to the current flow in the external load. The working principle of the capacitor is shown in figure 1.4.

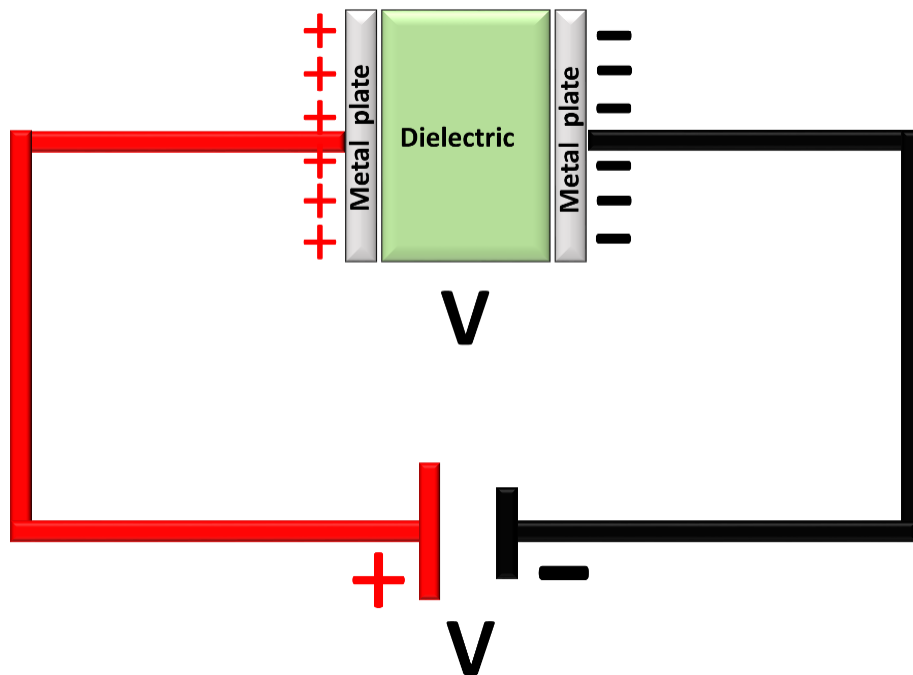


**Figure 1.4:** Working principle of the capacitor. [18]

The basic formula for calculation of charge stored in a capacitor is,

$$\text{Charge (Q)} = \text{capacitance (C)} \times \text{voltage (V)} \quad 1.1$$

The Farad is a unit of capacitance. Using equation 1.1, we can calculate the capacitance, but that is not convenient or true because capacitance depends on the dimensions of the metal plates and dielectric medium. [19]

The capacitance of capacitor is calculated by the following equation,

$$C_s = \epsilon A / d \quad 1.2$$

Where C is capacitance,  $\epsilon$  is the permittivity of dielectric, A is the surface area of each plate, and d is the distance between two metal plates. So, the capacitance is depends on the surface area and distance between two metal plates also depends on the permittivity of dielectric medium.

## 1.2 Supercapacitor:

### 1.2.1 Working principle of supercapacitor:

The SC has a similar working principle like the capacitor. Commonly SC comprises three parts, electrodes coated with electroactive materials, electrolyte (organic/aqueous), and current collector. When SC electrodes are dipped in the electrolyte, charges get accumulated at an electrode-electrolyte interface forming

an electrochemical double layer. The schematic presentation of the SC working principle and related parameters is shown in figure 1.5. [20-21]

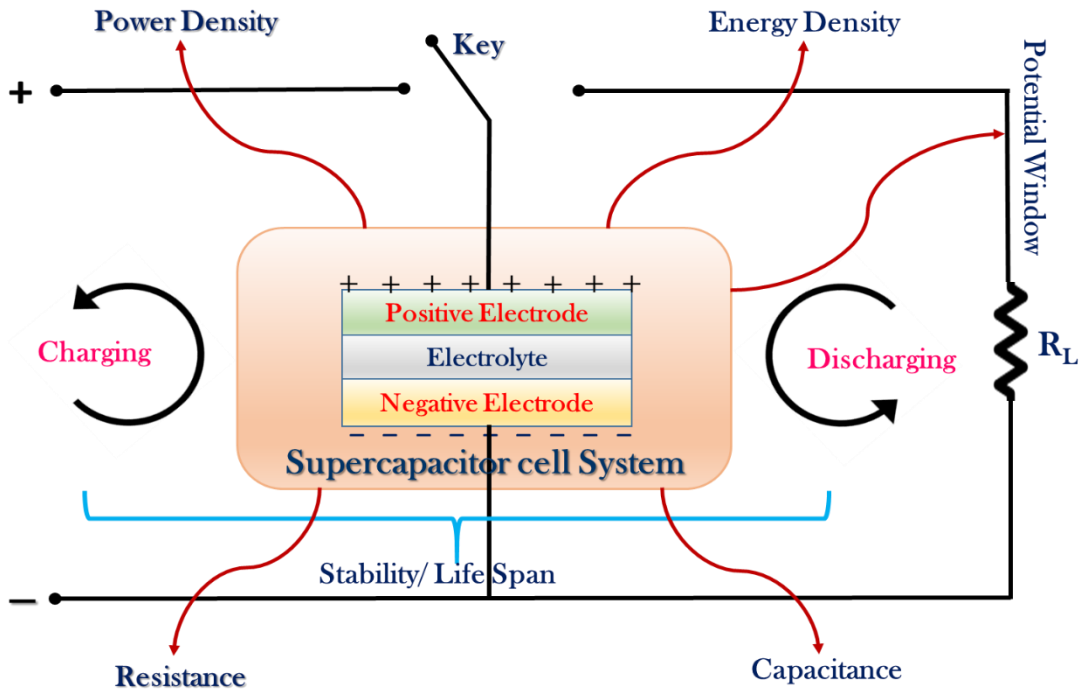


**Figure 1.5:** Schematic presentation of SC working procedure and related parameters. [22]

The charge storage mechanism of the SC is schematically represented in figure 1.6.

The Cs of the SC is calculated by using the following equation.

$$C_s = \frac{I \Delta t}{m \Delta V} \quad 1.3$$

The ED of the SC is calculated as follows,

$$ED = \frac{C_s V^2}{2} \quad 1.4$$

Where,  $C_s$  and  $V$  are the specific capacitance and operational potential window of SC, respectively.

The PD of the SC is calculated as follows,

$$PD = \frac{ED}{\Delta t} \quad 1.5$$

Where, ED - energy density ( $\text{Wh Kg}^{-1}$ ), PD - power density ( $\text{W Kg}^{-1}$ ) and  $\Delta t$  - discharging time (s), respectively.

The charge storage mechanism of conventional SC is represented in figure 1.6.

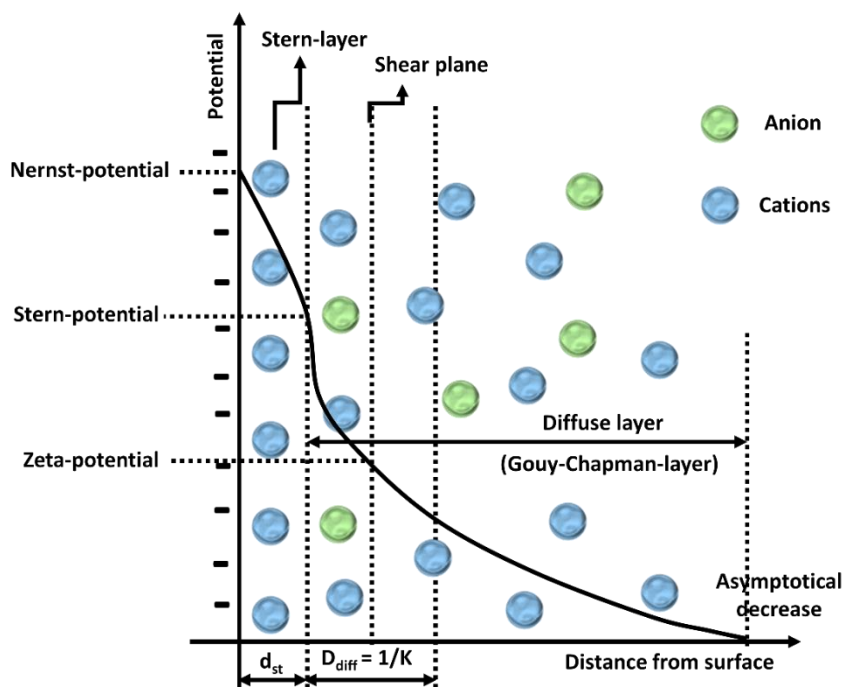


**Figure 1.6:** Charge storage mechanism in the conventional SC. [23]

### 1.2.2 Classification of supercapacitors:

On the basis of charge storage mechanism, SCs are divided into electrochemical double-layer capacitors (EDLCs), pseudocapacitors and hybrid capacitors. Figure 1.7, represents the different types and subtypes of SCs. The faradic, non-faradic and composite of these two processes are the three charge storage mechanisms involved in charge storage process in SC. In EDLC-type, charges are stored by non-faradic processes via the formation of Helmholtz double-layer (electrostatically). On the other hand, in pseudocapacitors-type, charges are stored by reversible faradic processes. [24-26] In the case of pseudocapacitors charge storage mechanism involves an exchange of electrons. Generally, pseudocapacitive materials must have several oxidation states so that redox reaction can occur, thus materials like transition metal oxides, hydroxides, phosphides, sulphides, conducting polymers, phosphates, layer double hydroxide, etc. are applicable as an electrodes. [27-28]

On the other hand, both faradaic and non-faradaic mechanisms are involved in hybrid supercapacitors (HSCs). The carbon-based materials with metal oxides or conducting polymers, or both are used to construct HSCs. [29-31] In an SCs, electrode materials play a crucial role in enhancement of electrochemical performance.

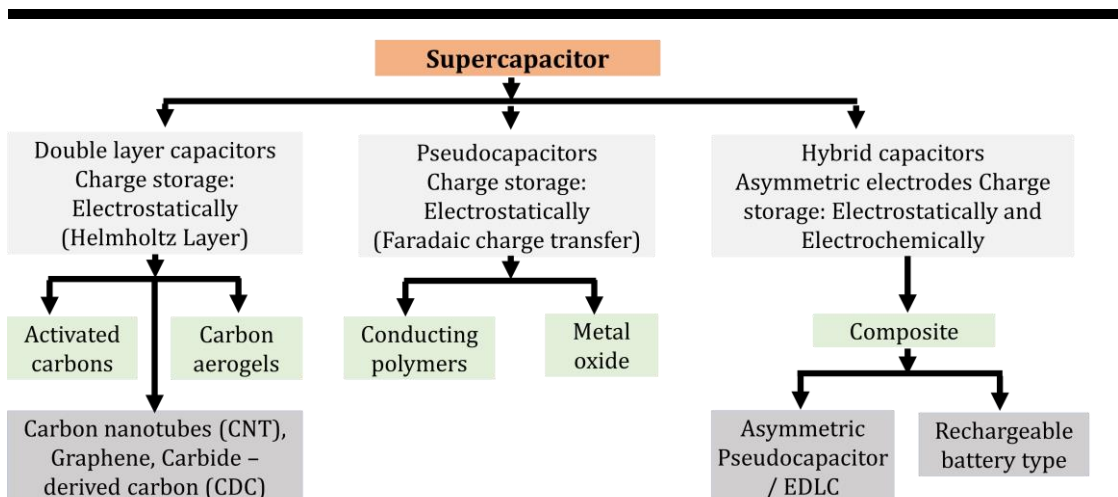


**Figure 1.7:** Classification of SCs.

**1.2.3 Electric double-layer capacitors (EDLCs):**

In the case of EDLCs charge storage mechanism is similar to the conventional capacitors that utilizes the electrode-electrolyte interface for charge storage instead of dielectric layer in the conventional capacitors. EDLCs consists of three main components non-redoxable high surface area electrodes, separator and electrolyte. As EDLCs electrodes are non redoxable, there is no charge transfer occurs between electrode and electrolyte. Thus, the electrolyte concentration always remains constant after multiple charging-discharging processes. [15] The charge storage process in EDLC is non-faradaic so the EDLC electrodes offer high reversibility and stability. Consequently, EDLC electrodes show stable performance up to  $1 \times 10^6$  charging-discharging cycles. [15, 32] Also, charge storage in EDLCs occurs at the electrode-electrolyte interface, therefore electrode conductivity crucially affects the EDLC performance. High surface area and high conductivity electrode materials offer quicker charge-discharge rates and higher cycle life in EDLCs with higher PD. [16] Accordingly, different derivatives of carbon materials such as carbon nanotubes, carbon aerogels, activated carbon and graphene are potential materials for EDLC. The decomposition potential of electrolytes plays a crucial role in determining the operating voltage range of EDLC; thus, ED of EDLCs depends on the use of aqueous or non-aqueous electrolytes.

**1.2.4 Pseudocapacitors:**

In the case of pseudocapacitors, fast and reversible redox surface reactions are occurred due to the movement of charges between electrode and electrolyte,

and charges can be stored through reversible faradaic reactions. The charge storage mechanism in pseudocapacitors is shown schematically in figure 1.8.

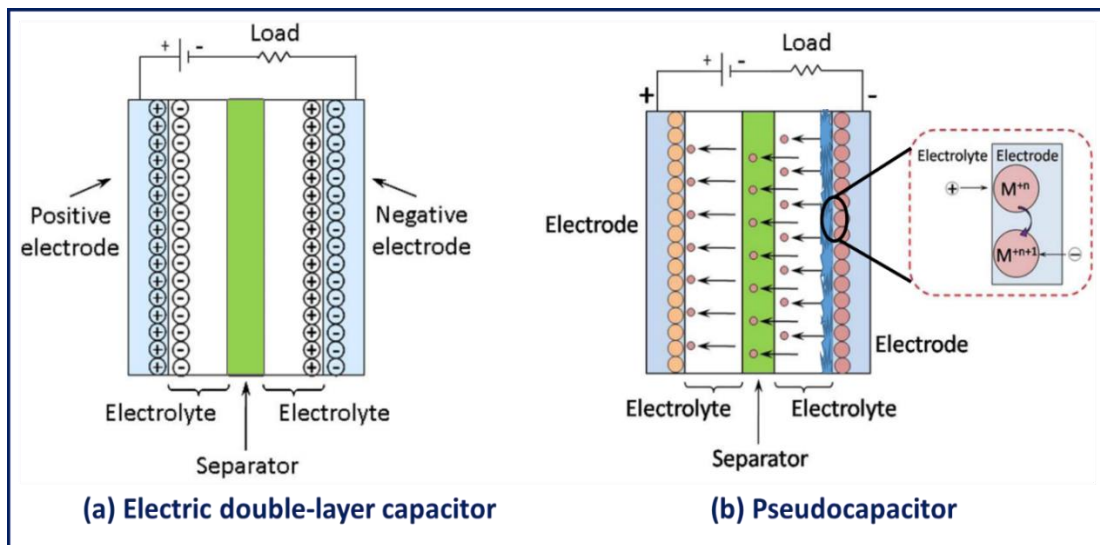


**Figure 1.8:** Charge storage mechanism of (a) EDLC and (b) pseudocapacitor. [17]

The pseudocapacitors can show high capacitance with high EDs compared to EDLCs due to the involvement of reversible faradaic processes during charge storage. Since the reversible faradaic reactions primarily occur at the electrode surface, thus the performance of pseudocapacitors depends on the particle size, surface area and conductivity of active material.

On the basis of charge storage mechanisms, pseudocapacitor is further divided into three categories such as a) intrinsic pseudocapacitor (on or near material surface faradaic reactions), b) intercalation-type pseudocapacitor (charge stored in tunnels or layers of materials), and c) extrinsic pseudocapacitor (faradaic reaction at the surface of nano-sized battery like materials).

#### 1.2.4.1 Intrinsic or surface redox pseudocapacitors:

At many instances,  $\text{RuO}_2$  demonstrated linear or approximately linear charge-discharge curves without significant voltage plateau, and quasi-rectangular cyclic voltammetry (CV) curves with almost overlapped redox peaks can be regarded as intrinsic pseudocapacitive materials. [33] These intrinsic pseudocapacitive materials exhibit the characteristics of capacitive charge storage, irrespective of their crystalline structure, surface morphology or particle size. [34] The transition metal oxides like  $\text{RuO}_2$ ,  $\text{MnO}_2$ , and  $\text{IrO}_2$  display intrinsic pseudocapacitive nature. Due to charge storage via surface redox reaction makes

---

them high-performance electrodes compared to EDLCs electrodes. Though these materials demonstrated promising electrochemical performance, their stability under prolonged cycling, cost and scarcity are the issues to be overcome.

#### **1.2.4.2 Intercalation pseudocapacitors:**

In intercalation pseudocapacitor materials, charges are stored due to intercalation of electrolyte ions Faradaically without disturbing phase of the material. This type of charge storage mechanism is found by Augustyn et. al in  $\text{Nb}_2\text{O}_5$  material, and it is known as "intercalation pseudocapacitors." [35] Electrode material does not change phase; this is the fascinating property of intercalation pseudocapacitor. [36] The charge storage process in intercalation pseudocapacitor not only utilizes surface but also the bulk of electrode material for the electrochemical reaction. Thus, materials like layered metal oxides and double hydroxides can be regarded as a potential electrode materials for intercalation pseudocapacitors.

#### **1.2.4.3 Extrinsic pseudocapacitors:**

In their bulk form, the typical battery materials show redox peaks in CV curves and voltage plateau in galvanostatic charge discharge (GCD) curves, indicating battery-type behavior. However, some battery-type materials in nano-size form show almost linear GCD curve and improved high rate behavior with suppression of phase change can be regarded as extrinsic pseudocapacitor materials. [36, 35] When such battery materials with reduced dimensions from bulk to nano-sized, its surface dominant ion storage mechanism increase due to decreased ion diffusion lengths, and typical battery type materials behave like pseudocapacitive in nature. Examples of extrinsic pseudocapacitive materials are nano-sized cobalt oxide,  $\text{V}_2\text{O}_5$ ,  $\text{CeO}_2$ ,  $\text{LiCoO}_2$ . [37-38]

#### **1.2.5. Hybrid supercapacitors (HSCs):**

As intrinsic as well as extrinsic pseudocapacitor materials are explored for the SC. The variety of materials are amply exploited for pseudocapacitors. However, SC cell comprising only intrinsic or extrinsic suffers limited PD, ED, and cycling performance. This issue can be overcome by developing a HSC comprising of one battery type and other capacitive type electrode material in a single SC cell. This type of design can improve the operating potential window and thus ED of the

---

---

SC. As both battery type and EDLCs-type electrode materials are used in HSCs, these types of SCs can deliver high rate, improved Cs with high ED and PD. [39-42] These types of HSC cell assemblies may minimize the gap between the batteries and SCs. [43]

### **1.3. Materials for supercapacitor:**

The SC consists of four main components: an electrode, electrolyte, current collector, and separator. The selection of active material with desired properties can significantly enhance electrochemical performance.

#### ***The required features of SCs electrode materials***

The electrode used in SCs should have high surface area, long-term stability and high cyclability.

*High surface area:* The electrodes in SCs should possess ultra-high surface area, this can be achieved by making the material of the electrode in the nanocrystalline form with enhanced porosity. The high surface area allows the number of active sites available to store charge (pseudocapacitance).

*Long-term stability:* In SCs, the charge-discharge mechanism involves the transfer of electric charge between the phases but without any permanent phase transformation. Accordingly, the material for SCs should be stable through redox cycling.

*High cyclability:* The electrode material for SCs should have high cyclability. Unlike charge-discharge processes in batteries, which often have faradaic reactions and electrode phase transformation. By contrast, energy storage by a SCs occurs by only reversible redox reactions and no chemical changes are involved. Accordingly, SCs have almost unlimited recyclability, typically between  $10^5$  and  $10^6$  times as compare to capacitor.

#### ***Characteristics of electrolyte***

*High conductivity:* The electrolyte must possess high conductivity for delivering optimum power.

*Viscosity:* The electrolyte for SCs should have minimum viscosity solvent (of solution) to enable high ionic mobility and transportation.

*Solubility:* The electrolyte for SCs should have maximum salt solubility to enable high conductivity.

---

*Ion pairing:* The electrolyte for SCs should have minimum ion-pairing to reduce its resistance. [44, 45]

### **1.3.1 Carbon derivatives:**

The various carbon materials are used as electrode materials for the EDLCs. Activated carbon (AC), [46] carbon nanotubes (CNTs) [47] and graphene oxide (GO) [48] have been used as electrode material in EDLCs. The Cs of EDLCs is proportional to the surface area of active material. Thus, carbon aerogels received much attention due to their high surface area and low electrochemical series resistance as compared to AC. Aerogel can link with the current collector chemically. Due to the continued linking of the carbon network, there is no requirement of any additional binder for linkage. Moreover, CNTs with good mechanical strength, tubular network, low mass and resistivity received much attention as SC electrodes. However, its low surface area ( $<500 \text{ m}^2 \text{ g}^{-1}$ ) and high cost of synthesis limit its application in practical EDLCs. In the aqueous electrolyte, CNTs possess SC in the range of 4-180 F  $\text{g}^{-1}$ . [49]

The graphene with honey comb like crystal lattice formed by two-dimensional (2D) planar sheet with densely packed  $\text{sp}^2$  carbon bonded atoms also received high attention for SCs electrodes. It is derived from graphite's exfoliation with thickness up to one atom size. Due to the outstanding properties such as electrical, mechanical, best young's modulus value, large spring constant, and excellent carrier mobility, graphene is regarded as a promising material for SCs. Moreover, it shows excellent surface area properties. Recently GO nanosheets (Ns) were synthesized by chemical exfoliation of graphite crystals, which gives a large colloidal yield. Due to various functional groups attached to the GO, GO Ns demonstrated excellent processibility and can be used to develop hybrid electrode materials with tailorable electronic properties with high stability [50-51]

### **1.3.2 Metal oxides:**

Because of high Cs and superior oxidation-reduction characteristics, transition metal oxides are regarded as interesting pseudocapacitive electrodes. [52] The transition metal oxides like  $\text{RuO}_2$ ,  $\text{IrO}_2$ ,  $\text{NiO}$ ,  $\text{MnO}_2$ ,  $\text{Co}_2\text{O}_3$ , etc. are studied widely as electrodes materials for pseudocapacitors. The charge storage mechanism in metal oxides involves faradaic reactions. Though  $\text{RuO}_2$

---

demonstrated excellent SC performance, its high cost limits its use at large-scale applications. [53] Consequently, significant efforts are put forward to investigate other transition metal oxides like  $\text{Co}_3\text{O}_4$ ,  $\text{NiO}$ ,  $\text{MnO}_2$ ,  $\text{TiO}_2$ ,  $\text{Fe}_2\text{O}_3$ , etc. as electrode materials for SCs. Recently  $\text{MnO}_2$  demonstrated intrinsic pseudocapacitive properties with square shape CV and linear charge-discharge behavior, thus regarded as a highly promising material for SCs. [54-56]

### 1.3.3 Conducting polymers:

The conducting polymer shows many advantages as electrode material for SCs that include easy synthesis process, relatively cheap, flexibility, and good conductivity. Lots of efforts are taken to improve the electrochemical performance of conducting polymers. By the use of different dopants and levels of doping, the conductivity of conducting polymers can be modified in a wide range from  $10^{-10}$  to  $10^4 \text{ Scm}^{-1}$ . Thus, conducting polymers can be readily used as pseudocapacitive electrode materials due to their controllable electrical conductivity (from an insulator to metal) and redox states. [57] Among the various conducting polymers, polythiophene, polyaniline and polypyrrole are commonly used as electrode material for SC application.

### 1.3.4 Metal sulfides:

Metal sulfides (MSs) have emerged as a promising electrode aspirant for SCs. The MSs has interesting physicochemical properties like good mechanical, thermal and electrical properties that make them a potential candidate for the SCs. [58] Therefore, lots of efforts are taken to develop MSs electrodes to improve their ED, PD with high stability. [59-61] Many reports are available on MSs as electrode material for SCs that include manganese sulfide ( $\text{MnS}$ ) [62], molybdenum sulfide [63], cobalt sulfide ( $\text{CoS}_2$ ) [64], etc.

### 1.3.5 Layer double hydroxides:

Layered double hydroxide (LDH) materials is a special class of the layered inorganic solid represented by the general formula  $[\text{M}^{2+}_{1-x} \text{M}^{3+}_x(\text{OH})_2]^{x+}[\text{A}^{n-}_{x/n}]^{x-} \cdot m\text{H}_2\text{O}$ . In this formula, appropriate divalent, trivalent metal ions and charge compensating negative ions are represented by  $\text{M}^{2+}$ ,  $\text{M}^{3+}$ , and  $\text{A}^{n-}$ , respectively. [65] The LDHs comprise basic structural units of brucite like layers,  $\text{M}^{2+}(\text{OH})_2$ , in which  $\text{M}^{2+}(\text{OH})_6$  octahedras are bonded to each other by sharing their edges to form

infinite solid planes extending along the crystallographic a and b directions. The hydroxide sheet in LDH crystals acquires a permanent positive charge on the layers due to partial substitution of  $M^{2+}$  with  $M^{3+}$ . Therefore, the charge-balancing anionic species are intercalated in the interlayer space to satisfy the charge neutralization condition. LDHs have attracted high attention as a highly efficient SC electrode due to their tunable chemical composition and special layered structure, as shown in figure 1.9. [66, 67]

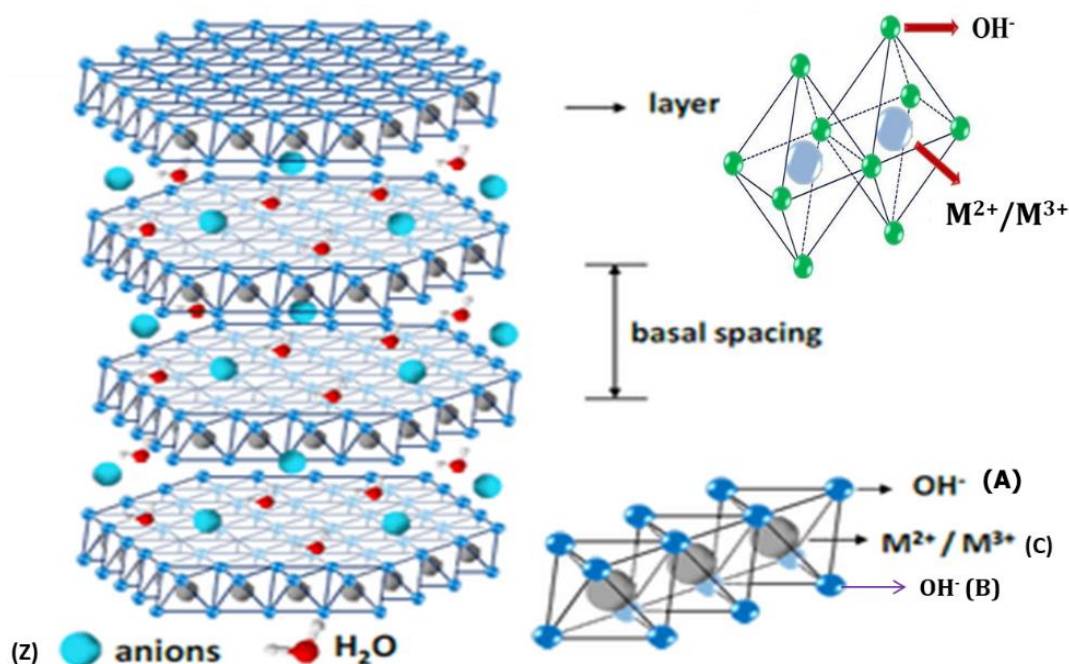


**Figure 1.9:** Structure of LDH.

One of the major advantages of LDHs as an SC material is their accessible hydrated interlayer space between the positively charged brucite layers that can facilitate the accumulation of large amounts of charges. In general, such gallery space is blocked by the charge-balancing anions, thereby LDH materials suffering from limited intergallery space and functionality. Thus, tuning LDH gallery space by pillaring, intercalation, and interstratification is highly important.

#### 1.4 Literature survey:

##### 1.4.1 Literature survey of LDH based electrochemical energy storage:

Among various layered electrode materials, LDHs have been extensively studied for high-performance SC electrodes. LDHs exhibits properties like multiple

---

redox states, high anion exchange ability, intercalation capability and tunable chemical composition, which are highly advantageous for SC application [68]

The Ni-Co-LDH graphene composite was synthesized using the reflux method and used for the SC application. The Ni-Co-LDH with 15 mg graphene composite showed a Cs of 1265 F g<sup>-1</sup> with 92.9 % capacitance retention. [69] The solvothermally prepared Ni-Co-LDH exhibited Cs and capacitance retention of 3168.3 F g<sup>-1</sup> at 1 A g<sup>-1</sup> and 90.5 % after 3000 cycles, respectively. [70] The values of Cs, ED, PD, and capacitance retention of solvothermally synthesized Ni-Co-LDH/CFC were 2762.7 F g<sup>-1</sup> at 1 A g<sup>-1</sup>, 59.2 Wh kg<sup>-1</sup>, 34 kW kg<sup>-1</sup>, 82 % after 5000 cycles, respectively. [71]

The Ni-Fe-LDH-Uns@rGO was synthesized using the in situ reflux method and used for the SC study. [72] The synthesized material demonstrated Cs of 2715 F g<sup>-1</sup> at 3 A g<sup>-1</sup> with ED of 82.3 Wh kg<sup>-1</sup> at PD of 661 W kg<sup>-1</sup>. The Mn-Co-LDH@Ni(OH)<sub>2</sub> was synthesized by the hydrothermal method, which showed high Cs of 2320 F g<sup>-1</sup> at 3 A g<sup>-1</sup> with ED of 47.9 Wh kg<sup>-1</sup>, PD of 5020.5 W kg<sup>-1</sup>, and capacitance retention of 90.9 %. [73] The Ni<sup>3+</sup> doped Co-Ni-LDH was synthesized by pulsed laser ablation method and showed Cs and capacitance retention of 2275 F g<sup>-1</sup> at 1 A g<sup>-1</sup> and ~100 % after 1800 cycles, respectively. [74] The rGO/Ni<sub>0.83</sub>-Co<sub>0.17</sub>-Al-LDH was synthesized by hydrothermal process and used for the SC study. [75] The rGO/Ni<sub>0.83</sub>-Co<sub>0.17</sub>-Al-LDH electrode showed the Cs of 1902 F g<sup>-1</sup> at 1 A g<sup>-1</sup> with 75 % capacitance retention.

The Co-Al-LDH-NF/LDH@MnO<sub>2</sub> binder-free SC electrode was synthesized by hydrothermal method [76], which displayed high Cs (1837.8 F g<sup>-1</sup> at 1 A g<sup>-1</sup>), ED (34.2 Wh kg<sup>-1</sup>), PD (9 kW kg<sup>-1</sup>), and capacitance retention (91.8 % after 5000 cycles). The Co-Mn-LDH/CF was synthesized by in situ growth process. The Co-Mn-LDH/CF showed high Cs of 1089 F g<sup>-1</sup> at 2.1 A g<sup>-1</sup>, ED (126.1 Wh kg<sup>-1</sup>), PD (65.6 W kg<sup>-1</sup>), and capacitance retention (82.5 %). [77] The Co-Al-LDH-NS/GO was synthesized by the solution dispersion method. [78] The prepared electrode showed a Cs of 1031 F g<sup>-1</sup> at 1 A g<sup>-1</sup>.

Hydrothermally synthesized Nifoam@Cu-Al-LDH/g-C<sub>3</sub>N<sub>4</sub> displayed Cs of 831.871 F g<sup>-1</sup> at 0.4 A g<sup>-1</sup> and capacitance retention of 92.71 % after 5000 cycles. [79] Liquid phase hetero assemble approach was used to synthesize Ti<sub>3</sub>C<sub>2</sub>/Ni-Co-

---

---

Al-LDH and obtained material applied for the all-solid-state flexible asymmetric SC. [80] The developed asymmetric SC device demonstrated the Cs of  $748.2 \text{ F g}^{-1}$  at  $1 \text{ A g}^{-1}$  and ED of  $45.8 \text{ Wh kg}^{-1}$ . The 3D porous structure of Co-Al-LDHs/GHAs hybrid aerogel was synthesized by the hydrothermal method. [81] Due to the 3D porous structure of Co-Al-LDHs/GHAs aerogel, SC performance was enhanced with the value of Cs of  $640 \text{ F g}^{-1}$  at  $1 \text{ A g}^{-1}$  and capacitance retention of 97 % after 10000 cycles. The thermal chemical vapor deposition method was used to synthesize the 3D core-shell Ni-Co-LDH@CNT and APDC SC electrodes. [82] The Ni-Co-LDH@CNT and APDC supercapacitor electrodes showed Cs of  $487 \text{ F g}^{-1}$  at  $1 \text{ A g}^{-1}$ , ED of  $89.7 \text{ Wh kg}^{-1}$  at PD of  $87 \text{ W kg}^{-1}$ . The carbon-Co-Al-LDH based SC electrodes were prepared by homogeneous precipitation method. [83] They showed a Cs of  $70 \text{ F g}^{-1}$  at  $50 \text{ mA g}^{-1}$ .

For the study of high-performance SCs, a hierarchical NiO/Ni-Mn-LDH nanosheet array on Ni foam electrode was synthesized by hydrothermal method. [84] The enhanced electrochemical activity was ascribed to the synergistic properties of hierarchical NiO/LDH Ns composites. The NiO/Ni-Mn-LDH/AC ACS exhibited outstanding electrochemical activity with Cs of  $66.4 \text{ F g}^{-1}$  at  $1 \text{ A g}^{-1}$ , ED of  $27.8 \text{ Wh kg}^{-1}$  at PD of  $401.3 \text{ W kg}^{-1}$  with excellent electrochemical stability of 85 % over 5000 cycles. The electrochemical activity was enhanced due to hierarchical nanoarchitecture and porous structure of Co-based porous LDH arrays derived via alkali etching from  $\text{Co(OH)}_2$ @Co-Al-LDH nanoarrays. [85] Ni-Co-LDH@rGO electrode showed Cs of  $2640 \text{ F g}^{-1}$  at  $1 \text{ A g}^{-1}$  due to the surface-engineered rGO nanoshells which provide large surface area, high porosity, enhanced redox sites, and easy transport of ions. [86] The obtained Ni-Co-LDH@rGO exhibit an ED of  $35 \text{ Wh kg}^{-1}$  and PD of  $750 \text{ W kg}^{-1}$ .

The monolayered Ni-Ti-LDH with tunable architecture was synthesized through bottom up approach with highly exposed conductive  $\text{Ni}^{3+}$  species and used for SC application. [87] Monolayered Ni-Ti-LDH demonstrated the Cs of  $2310 \text{ F g}^{-1}$  and capacitance retention of 82 %. The Co-Mn-LDH nanowalls supported on carbon fibers (CF) were synthesized by scalable one-step synthetic route. [88] The synthesized electrode showed high Cs ( $1079 \text{ F g}^{-1}$  at  $2.1 \text{ A g}^{-1}$ ), ED ( $126.1 \text{ Wh kg}^{-1}$ ), PD ( $65.6 \text{ W kg}^{-1}$ ), and capacitance retention (82.5 %). For the study of high

---

---

performance SCs, unique MOF-derived hierarchical nanotubes@Ni-Co-LDH/CoS<sub>2</sub> nanocage was synthesized by hydrothermal method. [89] The enhanced electrochemical activity was ascribed to the presence of CoS<sub>2</sub> nanoparticles in the nanocage. The MnO<sub>2</sub>@Ni-Co-LDH/CoS<sub>2</sub> electrode exhibited outstanding electrochemical activity with Cs of 1547 F g<sup>-1</sup> at 1 A g<sup>-1</sup>, ED of 50 Wh kg<sup>-1</sup> at PD of 9658 W kg<sup>-1</sup> with excellent electrochemical stability of 82.3 % over 2000 cycles. The 17 % Co doped rGO/Ni<sub>0.83</sub>-Co<sub>0.17</sub>-Al-LDH exhibited an enhanced electrochemical activity due to high surface area and sandwich structure. [90] The rGO/Ni<sub>0.83</sub>-Co<sub>0.17</sub>-Al-LDH electrode exhibit Cs of 1902 F g<sup>-1</sup> at 1 A g<sup>-1</sup> and deliver 75 % capacitance retention. The unique structure with Cu nanowires network crossed through Ni-Co-LDHs Ns was synthesized by three-step electrochemical procedure. [91] Due to porous structure with improved specific surface areas, conductivity, and mechanical strength of Ni-Co-LDH showed enhanced SC performance with improved Cs (2170 F g<sup>-1</sup> at 1 A g<sup>-1</sup>) and capacitance retention (80.46 % after 2000 cycles).

The Ni-Co-LDH/GNR was prepared by co-precipitation process. [92] The obtained Ni-Co-LDH/GNR exhibited a high Cs of 1765 F g<sup>-1</sup> at 5 A g<sup>-1</sup> and capacitance retention of 83 % over 2000 cycles. The 3D core-shell structured Ni-Co-LDH@carbon nanotube and activated polyaniline-derived carbon electrodes were synthesized and used for the supercapacitive study. [93] Due to its unique core-shell structure it demonstrated the Cs of 487 F g<sup>-1</sup> at 1 A g<sup>-1</sup>, ED of 89.7 Wh kg<sup>-1</sup> at PD of 456.8 W kg<sup>-1</sup>. The Co-Al-LDH-carbon nanotube composites were synthesized by electrostatic assembly route. [94] The synthesized electrode exhibited Cs of 884 F g<sup>-1</sup> at 1 A g<sup>-1</sup> and capacitance retention of 75 % after 2000 cycles. For the study of high performance SCs, Ni-Co-LDH directly grown on Ni-foam was synthesized by hydrothermal method. [95] The synthesized electrode exhibited outstanding electrochemical activity with Cs of 1445 F g<sup>-1</sup> at 1 A g<sup>-1</sup>, and capacitance retention of 90 % over 5000 cycles. The enhanced electrochemical activity was ascribed to unique spatial structure, excellent electrochemical activity, and good electrical conductivity of Ni-Co-LDH.

The Co-Mn-LDH/CF electrode was prepared by in situ growth and used as an SC electrode in LiOH electrolyte. [96] The Co-Mn-LDH/CF electrode showed an

---

---

ED of  $126 \text{ Wh kg}^{-1}$  at PD of  $65.6 \text{ W kg}^{-1}$ . The Cs was found to be  $1079 \text{ F g}^{-1}$  at  $2.1 \text{ A g}^{-1}$  with capacitance retention of 82.5%. Heterostructures of Ni-Co-Al-LDH assembled on  $\text{V}_4\text{C}_3$  MXene were synthesized by hydrothermal method and used for the SC electrode. [97] Due to interconnected porous network microstructures, Ni-Co-Al-LDH/ $\text{V}_4\text{C}_3\text{Tx}$  electrode demonstrated Cs of  $627 \text{ F g}^{-1}$  at  $1 \text{ A g}^{-1}$ , ED of  $71.7 \text{ Wh kg}^{-1}$  at PD of  $20000 \text{ W kg}^{-1}$ , and capacitance retention of 98 % after 10000 cycles. The Ns like morphology of the Zn-Co-LDH electrode was prepared by a successive ionic layer deposition method. [98] The prepared electrode was used in the hybrid device which exhibited a high specific capacity (Csp) of  $270 \text{ mA h g}^{-1}$  at  $1 \text{ A g}^{-1}$ , and capacitance retention of 97 % after 1000 cycles. For the study of high performance SCs, Ni-Co-LDH Ns modified Ni-P nanorod arrays were successfully grown on NF by the direct phosphorization of NF and subsequent electrodeposition. [99] The Ni-P@Ni-Co-LDH exhibited enhanced electrochemical activity with Cs of  $3470.5 \text{ F g}^{-1}$  at  $1.3 \text{ A g}^{-1}$  and capacitance retention of 96 % after 10000 cycles. The enhancement in electrochemical activity was ascribed to optimized core-shell structure of Ni-P@Ni-Co-LDH.

The Co-Ni-LDH/graphene electrode was prepared by co-precipitation method and used as a SC electrode in 2 M KOH. [100] The Cs of the prepared electrode was found to be  $2360 \text{ F g}^{-1}$  at  $0.5 \text{ A g}^{-1}$  with capacitance retention of ~86 %. The 17 % Co doped Ni-Co-Al-LDH was synthesized via in situ growth route and used for SC application. [101] Monolayered rGO/ $\text{Ni}_{0.83}\text{-Co}_{0.17}\text{-Al-LDH}$  demonstrated the Cs of  $1902 \text{ F g}^{-1}$  at  $1 \text{ A g}^{-1}$  and capacitance retention of 75 % after 1500 cycles. Ni-Al-LDH nanoflakes were grown on well-activated graphene Ns by in situ growth route and used for the SC. [102] The a-GNS/Ni-Al-LDH showed enhanced electrochemical performance due to the single atomic layered structure. The synthesized material demonstrated the Cs of  $1730.2 \text{ F g}^{-1}$  at  $0.1 \text{ A g}^{-1}$  and capacitance retention of 99.2 % after 5000 cycles. The rGO modified Ni-Mn-LDH nanoflake arrays were synthesized by facile dip-coating method. [103] The synthesized electrode exhibited a high Cs of  $\sim 1696 \text{ F g}^{-1}$  at  $1 \text{ A g}^{-1}$ , ED of  $22.5 \text{ Wh kg}^{-1}$  at PD of  $700 \text{ W kg}^{-1}$ , and capacitance retention of 91 % after 1000 cycles. Such composite electrode provided rapid charge transport pathway which leads to improved electrochemical reaction kinetics. The Ni-Mn-LDH/PC-1 composite

---

---

material was prepared by hydrothermal method and used as an electrode in 6 M KOH electrolyte for the study of SC. [104] Ni-Mn-LDH/PC-1 composite electrode showed the improved Cs ( $1634 \text{ F g}^{-1}$  at  $1 \text{ A g}^{-1}$ ), ED ( $18.60 \text{ Wh kg}^{-1}$ ), and PD ( $225.03 \text{ W kg}^{-1}$ ) with capacitance retention of 86 % after 3000 cycles.

For the study of high performance SCs, 3D binary Ni-Co hydroxide-graphene-NF (NCH11/G/NF) was synthesized via chemical vapour deposition. [105] The NCH11/G/NF electrode exhibited outstanding electrochemical activity with Cs of  $1410 \text{ F g}^{-1}$  at  $2 \text{ A g}^{-1}$ , ED of  $33.75 \text{ Wh kg}^{-1}$  at PD of  $750 \text{ W kg}^{-1}$  with excellent capacitance retention of 94.2 % after 2500 cycles. The enhanced electrochemical activity was ascribed to the formation of 3D structure which can improve the electron transport ability and increase the contact of the active sites with electrolyte. A sandwich-type 3D LDH Ns array/graphene composite was synthesized by layer-by-layer deposition technique and used for the supercapacitive study. [106] Due to high surface area and mesoporous characteristic, the as synthesized composite material enhanced electrochemical activity with the Cs of  $1329 \text{ F g}^{-1}$  at  $3.57 \text{ A g}^{-1}$ , and capacitance retention of 91 % after 500 cycles. The MOF derived Co-Co-LDH hollow nanocages/graphene composite prepared by reflux method and used as electrode in 1 M KOH electrolyte for SC application. [107] The Co-Co-LDH/graphene composite electrode showed the Cs of  $1205 \text{ F g}^{-1}$ , ED of  $49.5 \text{ Wh kg}^{-1}$  at PD of  $7000 \text{ W kg}^{-1}$  with capacitance retention of  $\sim 86$  %. For the study of high performance SCs, 3D Ni-Fe-LDH/graphene aerogel SC electrode material was prepared by simple hydrothermal method. [108] The prepared electrode showed enhanced electrochemical activity with Cs of  $1196 \text{ F g}^{-1}$  at  $1 \text{ A g}^{-1}$ , ED of  $17.6 \text{ Wh kg}^{-1}$  at PD of  $650 \text{ W kg}^{-1}$  and capacitance retention of 80 % after 2000 cycles.

Microstructural modification of Ni-Al-LDH electrodes by adding graphene Ns prepared by hydrothermal method. [109] The prepared Ni-Al/G-50 electrode exhibited a high Cs of  $1147 \text{ F g}^{-1}$  and capacitance retention of 83.3 % after 2000 cycles. Layered assembly of graphene oxide and Co-Al-LDH Ns was synthesized by in situ growth route and used for the supercapacitive study. [110] The electrochemical performance of Co-Al-LDH-NS enhanced due to the single atomic

---

layered structure. The Co-Al-LDH-NS/GO composite electrode demonstrated the Cs of 1031 F g<sup>-1</sup> at 1 A g<sup>-1</sup> and ED of 7.7 Wh kg<sup>-1</sup> at PD of 4.8 W kg<sup>-1</sup>.

Hydrothermally synthesized graphene/Ni-Al-LDH composite material displayed the Cs of 915 F g<sup>-1</sup>, ED of 27.6 Wh kg<sup>-1</sup>, and PD of 500 W kg<sup>-1</sup> with 95 % capacitance retention after 1500 cycles. [111] A hybrid aerogel of Co-Al-LDH/graphene with 3D porous structure as a novel electrode material was prepared by hydrothermal method and used as electrode in 6 M KOH electrolyte for SC study. [112] Synthesized electrode showed the Cs of 640 F g<sup>-1</sup> at 1 A g<sup>-1</sup> with excellent stability (97 %) over 10000 cycles.

For the study of high performance SCs, rationally designed ultrathin Ni-Al-LDH and graphene heterostructure was synthesized by hydrothermal method. [113] Ni-Al-LDH/rGO/AC exhibited electrochemical activity with Cs of 629.8 F g<sup>-1</sup> at 1 A g<sup>-1</sup>, an ED of 56.8 Wh kg<sup>-1</sup> at PD of 359 W kg<sup>-1</sup> with excellent electrochemical retention of 80.63 % after 5000 cycles. The enhanced electrochemical activity was ascribed to more stable structure, more active site, and faster ion diffusion. [114] The Fe-Ni<sub>3</sub>-C (Graphene) electrode exhibited Cs of 607 F g<sup>-1</sup>, ED of 16.9 Wh kg<sup>-1</sup> at PD of 10483.5 W kg<sup>-1</sup>, and deliver 99 % capacitance retention after 1000 cycles. The results showed that electrochemical activity was enhanced by the coexistence of metal NPs and nanostructured carbon. A Ni-Mn-LDH Ns@graphene foam hierarchical structure was synthesized by hydrothermal method and used for the supercapacitive study. [115] Due to increased surface area and interfacial strength, enhanced electrochemical activity with Cs of 420 F g<sup>-1</sup> at 1 A g<sup>-1</sup>, ED of 34.83 Wh kg<sup>-1</sup>, PD of 1.01 kW kg<sup>-1</sup> and capacitance retention of 94.9 % after 1000 cycles.

Graphene/Ni-Al-LDH electrode exhibited Cs 213.57 F g<sup>-1</sup> and deliver 100 % capacitance retention after 1000 cycles. [116] The results showed that electrochemical activity was enhanced by the presence of Ni-Al-LDH nanocomposites which prevents the restacking of graphene and decreases the charge-transfer resistance. 3D-architected Ni-Co-Mn-LDH/rGO composite prepared by solution method and used as an electrode in 2 M KOH electrolyte for SC study. [117] The prepared electrode exhibited the Cs of 206 F g<sup>-1</sup> at 5 A g<sup>-1</sup>, with ED of 92.8 Wh kg<sup>-1</sup> at PD of 0.46 kW kg<sup>-1</sup>.

---

LDH with vertically aligned graphene material was synthesized by a hydrothermal method. [118] Assembly of Ni-Mn-LDH-NF and vertically grown graphene showed the Cs of  $160 \text{ F g}^{-1}$ , ED of  $56.8 \text{ Wh kg}^{-1}$ , PD of  $260 \text{ W kg}^{-1}$  with 87 % capacitance retention after 10000 cycles. For the supercapacitive study, solid state SC based on Ni-Co-Al-LDH nanopetals was synthesized by hydrothermal method. [119] The synthesized electrode exhibited electrochemical activity with Cs of  $141.6 \text{ F g}^{-1}$  at  $0.4 \text{ A g}^{-1}$ , an ED of  $57.1 \text{ Wh kg}^{-1}$  at PD of  $339.46 \text{ W kg}^{-1}$  with excellent electrochemical retention of 93.6 % over after 4500 cycles. The enhanced electrochemical activity was ascribed to 3D rGO and mesoporous carbon. rGO/hierarchical core-shell Ag nanowire@Ni-Al-LDH film electrode was synthesized by hydrothermal method and used for the supercapacitive study. [120] The electrochemical activity was enhanced with the value of Cs  $127.2 \text{ F g}^{-1}$  at  $1 \text{ A g}^{-1}$ , ED of  $35.75 \text{ mW cm}^{-3}$ , PD of  $1.01 \text{ W cm}^{-3}$ , and capacitance retention of 83.2 % after 10000 cycles due to the hierarchical core-shell structure of composite and rGO as a source of electrical conductivity.

High performance asymmetric SC based on Co-Al-LDH/GF and activated carbon from expanded graphite was prepared by hydrothermal method and tested SC performance in 6 M KOH electrolyte. [121] The Cs for the prepared electrode was found to be  $104.4 \text{ F g}^{-1}$  at  $0.5 \text{ A g}^{-1}$  with ED of  $28 \text{ Wh kg}^{-1}$  at PD of  $1420 \text{ kW kg}^{-1}$  and capacitance retention of  $\sim 100$  after 500 cycles. Mesoporous graphene-LDH was prepared by co-precipitation method for flexible SCs. [122] The electrode displayed Cs of  $99.5 \text{ F g}^{-1}$  at  $1 \text{ A g}^{-1}$  and ED of  $22.6 \text{ Wh kg}^{-1}$ , PD of  $0.09 \text{ kW kg}^{-1}$  with capacitance retention of 94 % after 5000 cycles. The electrochemical activity of Ni-Mn-LDH/rGO-4//rGO was enhanced by incorporation of rGO. [123] Ni-Mn-LDH/rGO-4//rGO exhibited Cs of  $82.5 \text{ F g}^{-1}$  at  $0.5 \text{ A g}^{-1}$ , ED of  $29.4 \text{ Wh kg}^{-1}$  at PD of  $400 \text{ W kg}^{-1}$  and delivered 90.5 % capacitance retention after 5000 cycles. For the study of high performance SCs, Co-LDH nanocages/graphene composite electrode was synthesized by hydrolysis technique. [124] The synthesized material exhibited high electrochemical activity with Cs of  $76.4 \text{ F cm}^{-3}$  with excellent electrochemical stability of  $\sim 90.4$  % after 1000 cycles. The enhanced electrochemical activity was ascribed to the effective combination and porous architecture of Co-LDH nanocages/graphene composites.

---

---

### 1.4.2 Literature survey of 2D inorganic nanosheets (INs):

Various layered inorganic materials, including LDHs, attracted attention for their potential use in SC. However, these layered materials are commonly synthesized by solution-based synthesis of chemical growth and contain charge balancing ions at their interlayer space. [125] Thus, control of size in these materials is difficult. Also, LDHs commonly possess smaller charge balancing ions in inter layer space, so the interlayer space is densely packed, and LDHs suffer from limited functional activities. [126] For the application in SCs, the 2D INs have sufficient electronic conductivity, electrochemical stability, high electrochemically active surface area, and wide working potential window. [127]

Presently, lots of research work has been done to prepare 2D INs and much progress on developing different synthesis routes of 2D INs. There are various bulk inorganic materials that can be explored for the synthesis of 2D INs via exfoliation of respective highly crystalline bulk material e. g. layered transition metal oxides, molybdenum oxide, dichalcogenides, boron nitride, metal hydroxide, double hydroxides, metal selenide, metal carbide, metal sulfide, etc. [128] Recently, the 2D INs are used as building block for hybridization. The 2D INs have ability to form extra bonding with guest chemical species. This type of coordinative bonding plays crucial role to explore highly competent hybrid materials with a sturdy interfacial electronic coupling. [129] The 2D nanostructure displays high surface area with interlayer spacing which is appropriate for diffusion of ion. This type of morphology is beneficial for intercalation pseudocapacitances. Moreover, 2D INs are used as active component, as additive, as substrate, etc. [130]

Due to these properties, INs based electrodes revealed better structural and chemical stability when used in electrochemical study. [131] The table 1.4.2 represent the INs based hybrids for SC application.

The silver (Ag) nanoparticle loaded  $\text{MnO}_2$  NSs were prepared by the exfoliation-reassembling method and used for the supercapacitive study. [132] An electrode demonstrated a Cs of  $272 \text{ F g}^{-1}$  at  $10 \text{ mV s}^{-1}$  due to increased conductivity. The Alkali metal manganates were synthesized by exfoliation-reassembling route. It showed Cs of  $160 \text{ F g}^{-1}$  and capacitance retention of 99 % over 1000 cycles. [133] The highly electrochemical active 2D nanostructure leads to improved Cs. The PEI-

---

---

layered MnO<sub>2</sub> was synthesized by exfoliation-reassembling route and used for the supercapacitive study. [134] The low charge density of polyelectrolyte is beneficial for optimized specific capacitance. The PEI-layered MnO<sub>2</sub> demonstrate that the Cs of PEI-layered MnO<sub>2</sub> is 100 F g<sup>-1</sup>. The Ni-Co-Mo oxide NSs was synthesized by hydrothermal method. [135] The Ni-Co-Mo oxide NSs showed the Cs of 1366 F g<sup>-1</sup> at 2 A g<sup>-1</sup>, ED of 46.2 Wh kg<sup>-1</sup> at PD of 713 W kg<sup>-1</sup> with capacitance retention of 89.75 % over 5000 cycles. The Co-Al-LDH/GO composite material was prepared via hydrothermal method. [136] The Co-Al-LDH/GO composite delivered Cs of 581.6 F g<sup>-1</sup>. The Cs of LDHs was improved due to the facile electron movement in between nanoplates and graphene Ns. The 3D RGO/Ni-Al-LDH-NSs was synthesized by hydrothermal method. [137] An electrode showed Cs of 2712.7 F g<sup>-1</sup> at 1 A g<sup>-1</sup> and capacitance retention of 98.9 % after 5000 cycles. The improved electrochemical performance of an prepared electrode was ascribed to conducting carbon framework and mesoporous network in between LDH/carbon composite. The CoSe NSs were synthesized by hydrothermal method and tested SC performance. The Csp for the prepared electrode was found to be 70.6 mAh g<sup>-1</sup> at 1 A g<sup>-1</sup> with ED of 18.6 Wh kg<sup>-1</sup> at PD of 750 W kg<sup>-1</sup> and capacitance retention of 95.4 % after 20000 cycles. [138] The MnO<sub>2</sub> NSs/PEI films were prepared via LBL method, which displayed Cs of 288 F g<sup>-1</sup> at 1.25 A g<sup>-1</sup> and 90.5 % capacitance retention after 1000 cycles. [139] The obtained electrochemical performance of prepared electrode due to the special microstructure of electrode. The Ni(OH)<sub>2</sub> NS/graphene composite synthesized by LBL restacking route. The electrode demonstrated Cs of 660.8 F cm<sup>-3</sup> and capacitance retention of 98.2 % after 2000 cycles. [140] The observed supercapacitive performance attributed to the unique LBL structure of Ni(OH)<sub>2</sub> and graphene Ns. The prepared Co-Al-LDH NS/GO material via LBL method and used for supercapacitive study. The Cs of prepared electrode found to be 1204 F g<sup>-1</sup> at 5 mV s<sup>-1</sup> and 99 % capacitance retention After 2000 cycles. [141] The enhanced electrochemical performance due to the face to face contact of Co-Al-LDH and GO Ns, which provides efficient mobility for electron. The joint-welded CNT foam @Ni(OH)<sub>2</sub> NSs nanosheet-based core-shell 3D structure synthesized by CBD method. [142] The material demonstrated Cs of 1272 F g<sup>-1</sup> at 2 A g<sup>-1</sup>, ED of 17.50 Wh kg<sup>-1</sup>, PD of 0.76 kW kg<sup>-1</sup> with excellent stability of

---

---

83.7 % after 3000 cycles. The enhanced electrochemical performance is credited to 3D core shell design of prepared material.

The porous 3D C@ZnNiCo-CHs core shell heterostructure was synthesized by simple CBD method and tested for SC study. [143] It carried maximum Cs of 166 F g<sup>-1</sup> at 1 A g<sup>-1</sup>, ED of 70.9 W h kg<sup>-1</sup> at PD of 966 W kg<sup>-1</sup> and capacitance retention of 91 % over 20000 cycles. The supercapacitive activity was enhanced due to 3D core shell heterostructure. The layered  $\alpha$ -Co(OH)<sub>2</sub> Ns prepared by exfoliation route. The prepared electrode demonstrate Cs of 952 F g<sup>-1</sup> at 5 mA cm<sup>-2</sup>. [144] The high electrochemical performance was attributed to the high surface area by sheet like nanostructure morphology which also provides many active sites which are favorable for electrochemical reactions. The Co-Al-LDH Ns material prepared by an exfoliation route. It delivered Cs of 833 F g<sup>-1</sup> and 95 % of capacitance retention over 2000 cycles. [145] The improved electrochemical performance was obtained due to partially isomorphous substitution of Co<sup>2+</sup> by Al<sup>3+</sup>. The Zn-Co-LDHs were prepared by co-precipitation method. The prepared electrode exhibited Cs of 170 F g<sup>-1</sup> with capacitance retention of 50 %. [146] The multicomponent design of Fe<sub>3</sub>O<sub>4</sub>-Fe Ns @GO material was synthesized by an electrochemical method. [147] The obtained electrode demonstrated Cs of 442 F g<sup>-1</sup> at 3 A g<sup>-1</sup> and capacitance retention of 98.9 % over 25000 cycles. The enhancement in electrochemical performance was attributed to accessible redox sites. The MnO<sub>2</sub> Ns was synthesized by electrophoretic deposition method. [148] The MnO<sub>2</sub> Ns thin film electrode showed Cs of 1200 F g<sup>-1</sup> at 3 mV s<sup>-1</sup>, ED of 200 W h kg<sup>-1</sup> at PD of 2 kW kg<sup>-1</sup>. The heterogeneous microstructure and lots of pores were attributed to the electrochemical performance.

The Cobalt oxyhydroxide NWs/MnO<sub>2</sub> Ns films were synthesized by electrostatic self-assembly route and tested for SC study. The prepared electrode carried maximum Cs of 507 F g<sup>-1</sup> at 1 A g<sup>-1</sup> and capacitance retention of 98 % after 5000 cycles. [149] The CoOOH/NW is main factor to exhibit admirable electrochemical performance because it provides high surface area due to dispersion of MONS. The VS<sub>2</sub> Ns were synthesized by exfoliation with ammonia-assisted strategy. [150] The VS<sub>2</sub> electrode showed Cs of 4760  $\mu$ F cm<sup>-2</sup> and capacitance retention of 90 % after 1000 cycles. The metallic nature exfoliative nature

---

of VS<sub>2</sub> provided high performance SC electrode. The cobalt-nickel-sulfide Ns (CoNi<sub>2</sub>S<sub>4</sub>) was synthesized by microwave-anion-exchange route and tested for SC study. The CoNi<sub>2</sub>S<sub>4</sub> delivered a maximum C<sub>sp</sub> of 247 mAh g<sup>-1</sup> at 8 A g<sup>-1</sup>, ED of 67.7 Wh kg<sup>-1</sup> at PD of 0.8 kW kg<sup>-1</sup> and capacitance retention of 82 % after 10000 cycles. [151] The CoNi<sub>2</sub>S<sub>4</sub> electrode showed better charge storage performance due to extra electrons and holes from Ni<sup>3+</sup> and Co<sup>2+</sup> sites, respectively.

## General introduction and literature survey

**Table 1.4.1:** Comparative literature survey of electrochemical capacitive performance of LDH based materials for electrochemical energy storage.

Sr. No.	Material /Nanohybrid	Method	Cs (F g <sup>-1</sup> )	ED (Wh kg <sup>-1</sup> )	PD (W kg <sup>-1</sup> )	Stability (%)	Cycles	Ref.
1	Ni-Co-LDH-1 5mg graphene	Reflux	1265	-	-	92.9	-	69
2	Ni-Co-LDHs	Solvothermal	3168.3, 1 A g <sup>-1</sup>	-	-	90.5	3000	70
3	Ni-Co-LDH/CFC	Solvothermal	2762.7, 1 A g <sup>-1</sup>	59.2	34 k	82	5000	71
4	Ni-Fe-LDH-Uns@rGO	In situ reflux	2715, 3 A g <sup>-1</sup>	82.3	6.61	-	-	72
5	Mn-Co-LDH@Ni(OH) <sub>2</sub>	Hydrothermal	2320, 3 A g <sup>-1</sup>	47.9	5020.5	90.9	-	73
6	Co-Ni-LDHs Ni <sup>3+</sup> ion doped	Pulse laser ablation	2275, 1 A g <sup>-1</sup>	-	-	80	1800	74
7	rGO/Ni <sub>0.83</sub> -Co <sub>0.17</sub> -Al-LDH	Hydrothermal	1902, 1 A g <sup>-1</sup>	-	-	75	-	75
8	Co-Al-LDH-NF/LDH@MnO <sub>2</sub>	Hydrothermal	1837.8, 1 A g <sup>-1</sup>	34.2	9 k	91.8	5000	76
9	Co-Mn-LDH/CF	In situ growth	1089, 2.1 A g <sup>-1</sup>	126.1	65.6	82.5	-	77
10	Co-Al-LDH-NS/GO	Exfoliation	1031, 1 A g <sup>-1</sup>	-	-	-	-	78
11	Nifoam@Cu-Al-LDH/g-C <sub>3</sub> N <sub>4</sub>	Hydrothermal	831.871, 0.4 A g <sup>-1</sup>	-	-	92.71	5000	79
12	Ti <sub>3</sub> C <sub>2</sub> /Ni-Co-Al-LDH	Liquid phase approach	748.2, 1 A g <sup>-1</sup>	45.8	-	-	-	80

General introduction and literature survey

Sr. No.	Material /Nanohybrid	Method	Cs (F g <sup>-1</sup> )	ED (Wh kg <sup>-1</sup> )	PD (W kg <sup>-1</sup> )	Stability (%)	Cycles	Ref.
13	Co-Al-LDHs/GHAs	Hydrothermal	640, 1 A g <sup>-1</sup>	-	-	97	10000	81
14	Ni-Co-LDH@CNT/Nickel foam(NF) APDC/NF	TCVD	487, 1 A g <sup>-1</sup>	89.7	87	-	-	82
15	Co-Al-LDH RCo-Au	Homogeneous precipitation	70, 50 mA g <sup>-1</sup>	-	-	-	-	83
16	NiO/Ni-Mn-LDH/AC ACS	Hydrothermal	66.4, 1 A g <sup>-1</sup>	27.8	401.3	-	-	84
17	Co(OH) <sub>2</sub> @Co-Al- LDH	Hydrothermal	1734, 5 mA cm <sup>-2</sup>	-	-	85	5000	85
18	Ni-Co-LDH@rGO	Hydrothermal	2640, 2.1 A g <sup>-1</sup>	35	750	-	-	86
19	Monolayer Ni-Ti-LDH	Bottom-up approach	2310	-	-	82	-	87
20	Co-Mn-LDH/CF	scalable one-step synthetic route	1079, 2.1 A g <sup>-1</sup>	126.1	65.6 k	82.5	-	88
21	MnO <sub>2</sub> @Ni-Co-LDH/CoS <sub>2</sub>	Hydrothrmal	1547, 1 A g <sup>-1</sup>	50	9658	82.3	2000	89
22	rGO/Ni <sub>0.83</sub> -Co <sub>0.17</sub> -Al-LDH	in situ growth route	1902, 1 A g <sup>-1</sup>	-	-	75	-	90
23	Ni-Co-LDH	Electrochemical	2170,1 A g <sup>-1</sup>	-	-	80.46	2000	91
24	Ni-Co-LDH/GNR	Co-precipitation	1765, 5 A g <sup>-1</sup>			83	2000	92
25	Ni-Co-LDH@CNT/NF//APDC/NF	TCVD	487, 1 A g <sup>-1</sup>	89.7	456.8	-	-	93
26	Co-Al-LDHs-CNTs	Hydrothermal	884, 1 A g <sup>-1</sup>	-	-	88	2000	94
27	Ni-Co-LDH-NF	Hydrothermal	1445,1 A g <sup>-1</sup>	-	-	90	3000	95
28	Co-Mn-LDH/CF	In situ growth	1079, 2.1 A g <sup>-1</sup>	126	65.6	82.5	-	96
29	Ni-Co-Al-LDH/V <sub>4</sub> C <sub>3</sub> Tx	Hydrothermal	627 C g <sup>-1</sup> , 1 A g <sup>-1</sup>	71.7	20000	98	10000	97

General introduction and literature survey

Sr. No.	Material /Nanohybrid	Method	Cs (F g <sup>-1</sup> )	ED (Wh kg <sup>-1</sup> )	PD (W kg <sup>-1</sup> )	Stability (%)	Cycles	Ref.
30	Zn-Co-LDH	successive ionic layer deposition	270 mA h g <sup>-1</sup> , 1 A g <sup>-1</sup>	-	-	97	1000	98
31	Ni-P@Ni-Co-LDH	Electrodeposition	3470.5, 1.3 A g <sup>-1</sup>	-	-	96	10000	99
32	CO-Ni-LDH/graphene	Co-precipitation	2360, 0.5 A g <sup>-1</sup>	-	-	~86	-	100
33	rGO/Ni <sub>0.83</sub> -Co <sub>0.17</sub> -Al-LDH	In situ growth	1902, 1 A g <sup>-1</sup>	-	-	75	1500	101
34	a-GNS/Ni-Al-LDH	In situ growth	1730.2, 0.1 A g <sup>-1</sup>	-	-	99.2	5000	102
35	rGO@Ni-Mn-LDH@NF	In situ growth	1696, 1 A g <sup>-1</sup>	22.5	700	91	1000	103
36	Ni-Mn-LDH/PC-1	Hydrothermal	1634, 1 A g <sup>-1</sup>	18.60	225.03	84.58	3000	104
37	NCH11/G/NF	CVD	1410, 2 A g <sup>-1</sup>	33.75	750	94.2	2500	105
38	Ni-Al-LDH-Ns array/graphene composite	LBL deposition	1329, 3.57 A g <sup>-1</sup>	-	-	91	500	106
39	Co-Co-LDH/graphene	Reflux	1205	49.5	7000	60.3	-	107
40	Ni-Fe-LDH/GHA	Hydrothermal	1196, 1 A g <sup>-1</sup>	17.6	650	80	2000	108
41	Ni-Al/G-50	Hydrothermal	1147, 5 mV s <sup>-1</sup>	-	-	83.3	2000	109
42	Co-Al-LDH-NS/GO	In situ growth	1031, 1 A g <sup>-1</sup>	7.7	4.8	-	-	110
43	Graphene/Ni-Al-LDH	Hydrothermal	915	27.6	500	95	1500	111
44	Co-Al-LDH/GHAs	Hydrothermal	640, 1 A g <sup>-1</sup>	-	-	97	10000	112
45	Ni-Al-LDH/rGO//AC	Hydrothermal	629.8, 1 A g <sup>-1</sup>	58.6	359	80.63	5000	113
46	Fe-Ni <sub>3</sub> -C (Graphene)	Thermal decomposition	607, 10 mV s <sup>-1</sup>	16.9	10483.5	99	1000	114
47	Ni-Mn-LDH@graphene//AC	Hydrothermal	420, 1 A g <sup>-1</sup>	34.83	1.01	94.9	1000	115

General introduction and literature survey

Sr. No.	Material /Nanohybrid	Method	Cs (F g <sup>-1</sup> )	ED (Wh kg <sup>-1</sup> )	PD (W kg <sup>-1</sup> )	Stability (%)	Cycles	Ref.
48	Graphene/Ni-Al-LDH	Hydrothermal	213.57, 1 A g <sup>-1</sup>	-	-	100	1000	116
49	Ni-Co-Mn-LDH//AC	Solution method	206, 5 A g <sup>-1</sup>	92.8	0.46	-		117
50	Ni-Mn-LDH-NF@VG	Hydrothermal	160, 2 mV s <sup>-1</sup>	56.8	260	87	10000	118
51	Ni-Co-Al-LDH/3D RGO	Hydrothermal	141.6, 0.4 A g <sup>-1</sup>	57.1	339.46	93.6	4500	119
52	GAL//GAL AFSC	Hydrothermal	127.2, 1 A g <sup>-1</sup>	35.75 mW h cm <sup>-3</sup>	1.01 W cm <sup>-3</sup>	83.2	10000	120
53	Co-Al-LDH/GF//AEG	Hydrothermal	101.4, 0.5 A g <sup>-1</sup>	28	1420	~100	5000	121
54	rGO/Co-Al-LDH//rGO	Co-precipitation	99.5, 1 A g <sup>-1</sup>	22.6	0.09 k	94	5000	122
55	Ni-Mn-LDH/rGO-4//rGO	Solvothermal	82.5, 0.5 A g <sup>-1</sup>	29.4	400	90.5	5000	123
56	Co-LDH/G2	Hydrolysis	76.4 F cm <sup>-3</sup>	-	-	90.4	10000	124

## General introduction and literature survey

**Table 1.4.2:** Comparative literature survey of electrochemical capacitive performance of 2D INs based electrodes for electrochemical energy storage.

Sr. No.	Material /Nanohybrid	Method	Cs (F g <sup>-1</sup> )	ED (Wh kg <sup>-1</sup> )	PD (W kg <sup>-1</sup> )	Stability (%)	Cycles	Ref. No.
1	Ag-MnO <sub>2</sub> NSs	Electrostatic reassembly	272, 10 mV s <sup>-1</sup>	-	-	-	-	132
2	Alkali metal manganates	Electrostatic reassembly	160	-	-	99	1000	133
3	PEI-layered MnO <sub>2</sub>	Electrostatic reassembly	100	-	-	-	-	134
4	Ni-Co-Mo oxide NSs	Hydrothermal	1366, 2 A g <sup>-1</sup>	46.2	713	89.75	5000	135
5	Co-Al-LDH/GO	Hydrothermal	581.6, 2 A g <sup>-1</sup>	-	-	-	-	136
6	3D RGO/Ni-Al-LDH-NSs	Hydrothermal route	2712.7, 1 A g <sup>-1</sup>	-	-	98.9	5000	137
7	CoSe NSs	Hydrothermal	70.6 mAh g <sup>-1</sup> , 1 A g <sup>-1</sup>	18.6	750	95.4	20000	138
8	MnO <sub>2</sub> NSs/PEI films	LBL	288, 1.25 A g <sup>-1</sup>	-	-	90.5	1000	139
9	Ni(OH) <sub>2</sub> NS/ graphene	LBL restacking	660.8, F cm <sup>-3</sup>	-	-	98.2	2000	140
10	Co-Al-LDH NS/GO	LBL	1204, 5 mV s <sup>-1</sup>	-	-	99	2000	141
11	CNT@Ni(OH) <sub>2</sub> NSs	CBD	1272, 2 A g <sup>-1</sup>	17.50	0.76 k	83.7	3000	142
12	C@ZnNiCo-CHs	CBD	166, 1 A g <sup>-1</sup>	70.9	966	91	20000	143

General introduction and literature survey

Sr. No.	Materials	Methods	Cs (F g <sup>-1</sup> )	ED (Wh kg <sup>-1</sup> )	PD (W kg <sup>-1</sup> )	Stability (%)	Cycles	Ref. No.
13	Co(OH) <sub>2</sub> NSs	Exfoliation	952, 5 mA cm <sup>-2</sup>	-	-	-	-	144
14	Co-Al-LDH NSs	Exfoliation	833	-	-	95	2000	145
15	Zn-Co-LDHs	Co-precipitation	170	-	-	50	-	146
16	Fe <sub>3</sub> O <sub>4</sub> -Fe NSs@GO	Electrochemical	442, 3 A g <sup>-1</sup>	-	-	98.9	25000	147
17	MnO <sub>2</sub> NSs	Electrophoretic	1200, 3 mV s <sup>-1</sup>	200	2 k	-	-	148
18	Cobalt oxyhydroxide NWs/MnO <sub>2</sub> NSs films	Electrostatic self-assembly	507	-	-	98	5000	149
19	VS <sub>2</sub> NSs	Ammonia-assisted	4760 μF cm <sup>-2</sup>	-	-	90	1000	150
20	CoNi <sub>2</sub> S <sub>4</sub> NSs	Microwave-anion-exchange	247 mAh g <sup>-1</sup> , 8 A g <sup>-1</sup>	67.7	0.8 k	82	10000	151

---

## 1.5 Thesis: Orientation and purpose

The SCs with its high ED ( $> 10 \text{ kW kg}^{-1}$ ) and superior cycle life with moderate PD ( $\sim 10 \text{ Whkg}^{-1}$ ) are potential energy-storage devices due to their applications in heavy duty power tools, hybrid-electric vehicles, and portable electronic devices such as mobile phones, laptops, wearable devices, rollup displays, electronic papers etc. Therefore, researchers worldwide concentrated on improving the electrochemical performance of SCs by means of enhanced ED, PD, long cycle life and preparation of cost-effective electrodes

Generally SCs are working based on their charge-storage mechanism such as ion adsorption (EDLC) or reversible surface oxidation-reduction reactions (pseudocapacitors) at the interface of electrode and electrolyte. Therefore, carbon materials, conducting polymers, nanocrystalline transition metal oxides and hydroxides are potential materials for SCs. Precise control of size, shape, porosity and electrical properties are considered the keys to enhancing the desired SC performance. Currently, commercial SC electrode materials based on EDLC uses various carbon allotropes as active electrode materials. These carbon-based electrodes exhibit prolonged cycling life and high PD. However, they cannot provide high ED, thus not applicable in heavy-duty applications like electric vehicles, cranes, forklifts, turbines, etc. On the other side, pseudocapacitive materials (transition metal oxides, hydroxides, chalcogenides, etc.) can demonstrate high Cs and ED via interfacial reversible faradaic reactions. However, these electrode materials have drawbacks, such as low stability and conductivity.

Recently reported Co-based LDH electrodes demonstrated excellent electrode performance. However, the performance of these Co-based LDH materials is highly limited due to the limited gallery space, compact layered structure, low surface area, and low conductivity. Also, Co-based LDH mainly comprises trivalent Al in LDH lattice. However, Al is not electrochemically active and has amphoteric properties, further limiting their performance. Recently reported Co-Cr-LDH is regarded as a potential candidate for SC electrode. To further enhance electrode performance of Co-Cr-LDH, widening the gallery space by pillaring Co-Cr-LDH with polyoxometalate (POM) anions and hybridizing it with highly conducting GO Ns will be the best choices. Therefore, nanohybrids based on

---

---

Co-Cr-LDH hybridized with POM anions (polyoxotungstate (POW), and polyoxovanadate (POV) anions) and Co-Cr-LDH hybridized with highly conducting GO Ns are chosen for the investigation.

In this work, Co-Cr-LDH is synthesized by the conventional co-precipitation method. The mesoporous Co-Cr-LDH-based nanohybrids are synthesized by self-assembly process. The Co-Cr-LDH hybridized with POV anions (Co-Cr-LDH-POV nanohybrids) are prepared by self-assembly process between exfoliated Co-Cr-LDH Ns and POV anions. The Co-Cr-LDH hybridized with POW anions (Co-Cr-LDH-POW nanohybrids) are prepared by self-assembly process between exfoliated Co-Cr-LDH Ns and POW anions. The Co-Cr-LDH hybridized with GO nanosheets (Co-Cr-LDH-GO nanohybrids) are prepared by self-assembly process between exfoliated Co-Cr-LDH Ns and GO Ns. The physicochemical properties of Co-Cr-LDH, Co-Cr-LDH-POV, Co-Cr-LDH-POW and Co-Cr-LDH-GO nanohybrids are studied using various physicochemical characterization techniques.

The crystal structure and phase identification of nanohybrids are carried using the X-ray diffraction (XRD) technique. Surface topographic features and special elemental distribution of nanohybrids are studied by field emission scanning electron microscopy (FESEM, Jeol JSM-6700F) which is equipped with energy-dispersive spectroscopy (EDS). The presence of functional groups and nature of chemical bonding in nanohybrids are studied using Fourier-transform infrared (FT-IR) (Bruker ALPHA II) and Raman (532 nm laser excitation wavelength by 2.5 mW power and a 50× objective.) spectroscopic techniques. The surface area, pore structure and distribution of the nanohybrids are estimated from the N<sub>2</sub> adsorption-desorption isotherms at a temperature of 77 K using a gas sorption analyzer (BELSORP mini II, Japan). The quantitative analysis of chemical composition and oxidation states of nanohybrids are probed using X-ray photoelectron spectroscopy (XPS).

The electrochemical performance of nanohybrids is tested using cyclic voltammetry (CV), galvanostatic charge-discharge (GCD) and electrochemical impedance spectroscopy (EIS) techniques, which is recorded with a ZIVE MP1 multichannel electrochemical workstation. A conventional three-electrode cell system is used to test the electrochemical performance. A Pt mesh is served as

---

counter and Hg/HgO is served as reference electrodes. The working electrodes of nano hybrids are prepared by the doctor-blade method. The 2M KOH aqueous solution is used as an electrolyte.

The HSC devices are fabricated using Co-Cr-LDH-POV or Co-Cr-LDH-POW, or Co-Cr-LDH-GO as a positive electrode and rGO as a negative electrode. Moreover, the electrochemical performance of HSC devices is studied in terms of Cs, ED, PD, and capacitance retention. Finally, conclusions are made on the basis of the electrochemical performance of fabricated HSC devices.

---

**1.6 References:**

1. DOE-EIA international energy outlook 2017 (Sept. 2017) report No: DOE/EIA-0484(2017).
2. K. S. Kumar, N. Choudhary, Y. Jung, J. Thomas, , ACS Energy Lett., 2018, 3, 482–495.
3. T. M. Gür, Energy Environ. Sci., 2018, 11, 2696-2767.
4. T. M. Gür, Science, 2016, 54, 1-64.
5. T. M. Gür, Chem. Rev., 2013, 113, 6179–6206.
6. S. Lou, Y. Zhao, J. Wang, G. Yin, C. Du, X. Sun, Small, 2019, 52, 1904740-1904783.
7. P. Simon, Y. Gogotsi, Nat, Mater., 2008, 7, 845–854.
8. A. Nishino, J. Power Sources, 1996, 60, 137-147.
9. M. Jayalakshmi, K. Balasubramanian, Int. J. Electrochem. Sci., 2008, 3, 1196-1217.
10. S. Liu, S. Lee, U. Patil, I. Shackery, S. Kang, K. Zhang, J. Park, K. Chung, S. Jun, J. Mater. Chem. A, 2017, 5, 1043-1049.
11. T. Mathis, N. Kurra, X. Wang, D. Pinto, P. Simon, Y. Gogotsi, Adv. Energy Mater., 2019, 9, 1902007(1-13).
12. H. Becker, U. S. Patent, 2800616, 1957.
13. R. Rightmire, U. S. Patent, 3288641, 1966.
14. G. Wang, H. Wang, B. Zhong, L. Zhang, J. Zhang, LLC, 2016, 479-492.
15. H. Shao, PhD Thesis, University College Cork, 2018.
16. M. Jayalakshmi, K. Balasubramanian, Int. J. Electrochem. Sci., 2008, 3, 1196–1217.
17. M. Vangari, T. Pryor, L. Jiang, J. Energy Eng., 2013, 139, 72-79.
18. <https://byjus.com/questions/principle-of-capacitor/#:~:text=A%20capacitor%20works%20on%20the,having%20equal%20and%20opposite%20charges>.
19. <https://www.eleccircuit.com/what-is-capacitor-principle-working-types/>
20. C. Zhou, Y. Zhang, Y. Li, J. Liu, Nano Lett., 2013, 13, 2078-2085.
21. W. Lu, R. Hartman, L. Qu, L. Dai, J. Phys. Chem. Lett., 2011, 2, 655-660.
22. H. Shao, PhD thesis, University college cork, 2018.
23. A. Filby, 2010, ISBN-13: 978-3838113708.
24. T. Chen, L. Dai, Mater. Today, 2013, 16, 272-280.
25. W. Wang S. Wu, Surf. Sci., 2017, 396, 1360-1367.
26. X. Li, Y. Zhao, Y. Bai, X. Zhao, R. Wang, Y. Huang, Q. Liang, Z. Huang, Electrochim. Acta, 2017, 230, 445-453.
27. M. Mastragostino, C. Arbizzani, F. Soavi, Solid State Ion., 2002, 148, 493-498.
28. S. Gowda, A. Reddy, X. Zhan, P. Ajayan, Nano Lett., 2011, 11, 3329-3333.
29. Y. Li, X. Wang, Q. Yang, M. S. Javed, Q. Liu, W. Xu, C. Hu, D. Wei, Electrochim. Acta, 2017, 234, 63-70.
30. M. G. Hosseini, E. Shahryari, J. Colloid Interf. Sci., 2017, 496, 371-381.

- 
31. M. Gopalakrishnan, G. Srikesh, A. Mohan, V. Arivazhagan, *Appl. Surf. Sci.*, 2017, 403, 578-583.
  32. B. K. Kim, S. Sy, A. Yu, J. Zhang, in: L. John Wiley & Sons (Ed.) *Handbook of Clean Energy Systems*, John Wiley & Sons, Ltd.2015, pp. 1-25.
  33. N. Chodankar, H. Pham, A. Nanjundan, J. Fernando, K. Jayaramulu, D. Golberg, Y. Han, D. Dubal, *Small*, 2020, 16, 1-35.
  34. J. Liu, J. Wang, C. Xu, H. Jiang, C. Li, L. Zhang, J. Lin, Z. X. Shen, *Adv. Sci. (Weinh.)*, 2018, 5, 1700322.
  35. V. Augustyn, P. Simon, B. Dunn, *Energy Environ. Sci.*, 2014, 7, 1597-1614.
  36. P. Simon, Y. Gogotsi, B. Dunn, *Science*, 2014, 343, 1210-1211.
  37. J.-P. Brog, A. Crochet, J. S. doux, M. J. D. Clift, B. Baichette, S. Maharajan, H. Barosova, P. Brodard, M. Spodaryk, A. Züttel, B. R.-Rutishauser, N. H. Kwon, K. M. Fromm, J. *Nanobiotechnol.*, 2017, 15, 58.
  38. H. Li, M. Yu, F. Wang, P. Liu, Y. Liang, J. Xiao, C. Wang, Y. Tong, G. Yang, *Nat. Commun.*, 2013, 4, 1-7.
  39. A. Muzaffara, M. B. Ahamed, K. Deshmukh, J. Thirumalai, *Renew. Sustain. Energy Rev.*, 2019, 101, 123-145.
  40. D. Dubal, R. Holze, P. Romero, *Sci. Rep.*, 2014, 4, 7349 (1-10).
  41. T. Lin, C. Dai, K. Hung, *Sci. Rep.*, 2014, 4, 7274 (1-10).
  42. R. S. Kate, S. A. Khalate, R. J. Deokate, *J. Alloys Compd.*, 2018, 734, 89-111.
  43. D. Cericol, R. Kotz, *Electrochim. Acta*, 2012, 72, 1-17.
  44. K. D. Verma, P. Sinha, S. Banerjee, K. K. Kar, In: Kar K. (eds) *handbook of nanocomposite supercapacitor materials I*. springer series in materials science, Springer, 2020, 300.
  45. J. Come, V. Augustyn, J. W. Kim, P. Rozier, P.-L. Taberna, P. Gogotsi, J. W. Long, B. Dunn, P. Simon, *J. Electrochem. Soc.*, 2014, 161, A718-A725.
  46. C.-S. Yang, Y. S. Jang, H. K. Jeong, *Curr. Appl. Phys.*, 2014, 14, 1616-1620.
  47. C. Portet, P. L. Taberna, P. Simon, E. Flahaut, *J. Power Sources*, 2005, 139, 371-378.
  48. K. S. Novoselov, A. K. Geim, S. V. Morozov, D. Jiang, Y. Zhang, S. V. Dubonos, I. V. Grigorieva, A. A. Firsov, *Science*, 2004, 306, 666-669.
  49. V. Ruiza, C. Blanco, R. Santamari'a, J. M. R.-Ferna'ndez, M. M.-Escandell, A. S.-Escribanob, F. R.-Reinoso, *Carbon*, 2009, 47, 195-200.
  50. Y. B. Tana, J.-M. Lee, *J. Mater. Chem. A*, 2013, 1, 14814-14843.
  51. S. Willam, Jr. Hummers, R. E. Offeman, *J. Am. Chem. Soc.*, 1958, 80, 1339.
  52. M. A. A. M. Abdah, N. H. N. Azman, S. Kulandaivalu, Y. Sulaiman, *Mater. Des.*, 2019, 186, 108199.
  53. Y. Wang, J. Guo, T. Wang, J. Shao, D. Wang, Y.-W. Yang, *Nanomaterials*, 2015, 5, 1667-1689.
  54. R. S. Kate, S. A. Khalate, R. J. Deokate, *J. Alloys Compd.*, 2018, 734, 89-111.
  55. S. M. Sun, P. Y. Wang, Q. Wu, S. Wang, S. M. Fang, *Mater. Lett.*, 2014, 137, 206-209.
-

- 
56. Q. Wang, Z. S. Li, Y. G. Huang, Q. Y. Li, X. Y. Wang, *J. Mater. Chem.*, 2010, 20, 3883–3889.
  57. B. H. Patil, A. D. Jagadale, C. D. Lokhande, *Synth. Met.*, 2012, 162, 1400-1405.
  58. S. R. Sivakkumar, D.-W. Kim, *J. Electrochem. Soc.*, 2007, 154, A134-A139.
  59. E. Meyer, A. Bede, N. Zingwe, R. Taziwa, *Materials*, 2019, 12, 1980.
  60. P. K. Sharma, A. Arora, S. K. Tripathi, *J. Energy Storage*, 2019, 21, 801-825.
  61. X. Rui, H. Tan, Q. Yan, *Nanoscale*, 2014, 6, 9889-9924.
  62. Y. Tang, T. Chena, S. Yu, *Chem. Commun.*, 2015, 51, 9018-9021.
  63. S. Chen, H. Chen, C. Li, M. Fan, C. Lv, G. Tian, K. Shu, *J. Mater. Sci.*, 2017, 52, 6687–6696.
  64. D. Zhang, H. Liu, J. Zhang, X. Wang, R. Zhang, J. Zhou, J. Zhong, B. Yuan, *Int. J. Electrochem. Sci.*, 2016, 11, 6791 – 6798.
  65. R. Ma, Z. Liu, L. Li, N. Iyi, T. Sasaki, *J. Mater. Chem.*, 2006, 16, 3809-3813.
  66. J.-H. Choy, *J. Phys. Chem. Solids*, 2004, 65, 373–383.
  67. R. Patel, J. T. Park, M. Patel, J. K. Dash, E. B. Gowd, R. Karpoomath, A. Mishra, J. Kwak, J. H. Kim, *J. Mater. Chem. A*, 2018, 6, 12–29.
  68. H. Liang, J. Lin, H. Jia, S. Chen, J. Qi, J. Cao, T. Lin, W. Fei, J. Feng, *J. Mater. Chem. A*, 2018, 6, 15040-15046.
  69. X. Bai, Q. Liu, Z. Lu, J. Liu, R. Chen, R. Li, D. Song, X. Jing, P. Liu, J. Wang, *ACS Sustainable Chem. Eng.*, 2017, 5, 9923–9934.
  70. T. Dong, X. Zhang, M. Li, P. Wang, P. Yang, *Inorg. Chem. Front.*, 2018, 5, 3033-3041.
  71. T. Wang, S. Zhang, X. Yan, M. Lyu, L. Wang, J. Bell, H. Wang, *ACS Appl. Mater. Interfaces*, 2017, 9, 15510–15524.
  72. Y. Jiang, Y. Song, Y. Li, W. Tian., Z. Pan, P. Yang, Y. Li, Q. Gu, L. Hu, *ACS Appl. Mater. Interfaces*, 2017, 9, 37645–37654.
  73. S. Liu, S. C. Lee, U. Patil, I. Shackery, S. Kang, K. Zhang, J. H. Park, K. Y. Chung, S. C. Jun, *J. Mater. Chem. A*, 2017, 5, 1043-1049.
  74. H. M. Sun, Y. X. Ye, Z. F. Tian, S. L. Wu, J. Liu, C. H. Liang, *RSC Adv.*, 2017, 7, 49010–49014.
  75. J. Xu, S. Gai, F. He, N. Niu, P. Gao, Y. Chen, P. Yang, *Dalton Trans.*, 2014, 43, 11667-11675.
  76. X. Hao, Y. Zhang, Z. Diao, H. Chen, A. Zhang, Z. Wang, *RSC Adv.*, 2014, 4, 63901-63908.
  77. J. Zhao, J. Chen, S. Xu, M. Shao, D. Yan, M. Wei, D. G. Evans, X. Duana, *J. Mater. Chem. A*, 2013, 1, 8836-8843.
  78. L. Wang, D. Wang, X. Y. Dong, Z. J. Zhang, X. F. Pei, X. J. Chen, B. Chen, J. Jin, *Chem. Commun.*, 2011, 47, 3556-3558.
  79. S. P. Adhikari, G. P. Awasthi, K-S. Kim, C. H. Park, C. S. Kim, *Dalton Trans.*, 2018, 47, 4455-4466.
  80. R. Zhao, M. Wang, D. Zhao, H. Li, C. Wang, L. Yin, *ACS Energy Lett.*, 2018, 3, 132–140.
  81. A. Zhang, C. Wang, Q. Xu, H. Liu, Y. Wang, Y. Xi, *RSC Adv.*, 2015, 5, 26017-26026.
  82. X. Li, J. Shen, W. Sun, X. Hong, R. Wang, X. Zhao, X. Yan, *J. Mater. Chem. A*, 2015, 3, 13244-13253.
-

- 
83. A. M.-Polaczyk, C. V.-Guter, E. Frackowiak, *Energy Fuels*, 2010, 24, 3346–3351.
  84. P-F. Liu, J-J. Zhou, G-C. Li, M-K. Wu, K. Tao, F-Y. Yi, W-N Zhao, L. Han, *Dalton Trans.*, 2017, 46, 7388-7391.
  85. N. Abushrenta, X. Wu, J. Wang, J. Liu, X. Sun, *Sci. Rep.*, 2015, 5, 13082.
  86. S. K. Kiran, S. Shukla, A. Struck, S. Saxena, *ACS Appl. Mater. Interfaces*, 2019, 11, 20232–20240.
  87. Y. Zhao, Q. Wang, T. Bian, H. Yu, H. Fan, C. Zhou, L.-Z. Wu, C.-H. Tung, D. O'Hare, T. Zhang, *Nanoscale*, 2015, 7, 7168-7173.
  88. J. Zhao, J. Chen, S. Xu, M. Shao, D. Yan, M. Wei, D. G. Evans, X. Duan, *J. Mater. Chem. A*, 2013, 1, 8836-8843.
  89. X. Wang, F. Huang, F. Rong, P. He, R. Que, S. P. Jiang, *J. Mater. Chem. A*, 2019, 7, 12018-12028.
  90. J. Xu, S. Gai, F. He, N. Niu, P. Gao, Y. Chen, P. Yang, *Dalton Trans.*, 2014, 43, 11667.
  91. Y. Liu, X. Teng, Y. Mi, Z. Chen, *J. Mater. Chem. A*, 2017, 5, 24407-24415.
  92. H. Jin, D. Yuan, S. Zhu, X. Zhu, *J. Zhu, Dalton Trans.*, 2018, 47, 8706-8715.
  93. X. Li, J. Shen, W. Sun, X. Hong, R. Wang, X. Zhao, X. Yan, *J. Mater. Chem. A*, 2015, 3, 13244-13253.
  94. L. Yu, N. Shi, Q. Liu, J. Wang, B. Yang, B. Wang, H. Yan, Y. Sun, X. Jing, *Phys. Chem. Chem. Phys.*, 2014, 16, 17936.
  95. C. Xing, F. Musharavati, H. Li, E. Zalezhad, O. K. S. Hui, S. Bae, B. -Y. Choe, *RSC Adv.*, 2017, 7, 38945-38950.
  96. J. Zhao, J. Chen, S. Xu, M. Shao, D. Yan, M. Wei, D. G. Evans, X. Duan, *J. Mater. Chem. A*, 2013, 1, 8836-8843.
  97. X. Wang, H. Li, H. Li, S. Lin, J. Bai, J. Dai, C. Liang, X. Zhu, Y. Sun, S. Dou, *J. Mater. Chem. A*, 2019, 7, 2291-2300.
  98. A. A. Lobinsky, V. P. Tolstoy, *RSC Adv.*, 2018, 8, 29607-29612.
  99. J. Xing, J. Du, X. Zhang, Y. Shao, T. Zhang, C. Xu, *Dalton Trans.*, 2017, 46, 10064-10072.
  100. Y. Cheng, H. Zhang, C. V. Varanasi, J. Liu, *Energy Environ. Sci.*, 2013, 6, 3314-3321.
  101. J. Xu, S. Gai, F. He, N. Niu, P. Gao, Y. Chen, P. Yang, *Dalton Trans.*, 2014, 43, 11667-11675.
  102. N. Yuliana, L. Ruiyi, L. Zaijun, F. Yinjun, L. Junkang, *Electrochim. Acta*, 2013, 94, 360–366.
  103. L. Sun, Y. Zhang, Y. Zhang, H. Si, W. Qin, Y. Zhang, *Chem. Commun.*, 2018, 54, 10172-10175.
  104. M. Yu, R. Liu, J. Liu, S. Li, Y. Ma, *Small*, 2017, 13, 1702616-1702624.
  105. Y. Bai, W. Wang, R. Wang, J. Sun, L. Gao, *J. Mater. Chem. A*, 2015, 3, 12530-12538.
  106. J. Xu, S. Gai, F. He, N. Niu, P. Gao, Y. Chen, P. Yang, *J. Mater. Chem. A*, 2014, 2, 1022-1031.
  107. X. Bai, J. Liu, Q. Liu, R. Chen, X. Jing, B. Li, J. Wang, *Chem. Eur. J.*, 2017, 23, 14839-14847.
  108. X. Gao, H. Lv, Z. Li, Q. Xu, H. Liu, Y. Wang, Y. Xia, *RSC Adv.*, 2016, 6, 107278-107285.
  109. Y. Kim, S. Kim, *Bull. Korean Chem. Soc.*, 2015, 36, 665-671.
  110. L. Wang, D. Wang, X. Y. Dong, Z. J. Zhang, X. F. Pei, X. J. Chen, B. Chen, J. Jin, *Chem. Commun.*, 2011, 47, 3556-3558.
-

- 
111. Y. Wimalasiri, R. Fan, X. S. Zhao, L. Zou, *Electrochim. Acta*, 2014, 134, 127-135.
112. A. Zhang, C. Wang, Q. Xu, H. Liu, Y. Wang, Y. Xia, *RSC Adv.*, 2015, 5, 26017-26026.
113. Q. Du, L. Su, L. Hou, G. Sun, M. Feng, X. Yin, Z. Ma, G. Shao, W. Gao, *J. Alloys Compd.*, 2018, 740, 5, 1051-1059.
114. G. Abellán, E. Coronado, C. M.-Gastaldo, A. Ribera, T. F. Otero, *Part. Part. Syst. Charact.*, 2013, 30, 853-863.
115. W. Lia, Y. Lib, Q. Meng, Y. Xu, B. Yang, T. Li, *Mater. Res. Bull.*, 129, 2020, 110889-110897.
116. Z. Wang, X. Zhang, J. Wang, L. Zou, Z. Liu, Z. Hao, *J. Colloid Interface Sci.*, 2013, 396, 251-257.
117. M. Li, J. P. Cheng, F. Liu, X. B. Zhang, *Electrochim. Acta.*, 2016, 206, 108-115.
118. W. Guo, C. Yu, S. Li, J. Yang, Z. Liu, C. Zhao, H. Huang, M. Zhang, X. Han, Y. Niu, J. Qiu, *Small*, 2017, 1701288-1701297.
119. X. Bai, Q. Liu, J. Liu, Z. Gao, H. Zhang, R. Chen, Z. Li, R. Li, P. Liu, J. Wang, *Chem. Eng. J.*, 2017, 328, 873-883.
120. L. Li, K. S. Hui, K. N. Hui, T. Zhang, J. Fu, Y.-R. Choa, *Chem. Eng. J.*, 2018, 348, 338-349.
121. T. M. Masikhwa, M. J. Madito, D. Y. Momodu, J. K. Dangbegnon, O. Guellati, A. Harat, M. Guerioune, F. Barzegar, N. Manyala, *RSC Adv.*, 2016, 6, 46723-46732.
122. R. Zhang, H. An, Z. Li, M. Shao, J. Han, M. Wei, *Chem. Eng. J.*, 2016, 289, 85-92.
123. L. Huang, B. Liu, H. Hou, L. Wu, X. Zhu, J. Hu, J. Yang, *J. Alloys Compd.*, 2018, 730, 71-80.
124. X. Chu, T. Deng, W. Zhang, D. Wang, X. Liu, C. Zhang, T. Qin, L. Zhang, B. Zhang, C. Chen, W. Zheng, *J. Energy Chem.*, 2017, 000, 1-6.
125. Q. Wang, D. O'Hare, *Chem. Rev.*, 2012, 112, 4124-4155.
126. V. P. Tolstoy, A. A. Lobinsky, M. V. Kaneva, *J. Mol. Liq.*, 2019, 282, 32-38.
127. T. Nakato, J. Kawamata, S. Takagi, Springer nature, Japan-127, 2017.
128. P. Xiong, Y. Wu, Y. Liu, R. Ma, T. Sasaki, X. Wang, J. Zhu, *Energy Environ. Sci.*, 2020, 13, 4834-4853.
129. S. M. Oh, S. J. Hwang, *J. Korean Ceram. Soc.*, 2020, 57, 119-134.
130. X. Jin, T. H. Gu, K. G. Lee, M. J. Kim, M. S. Islam, S. J. Hwang, *Coord. Chem. Rev.*, 2020, 415, 213280-213307.
131. Y. Guo, T. Park, J. W. Yi, J. Henzie, J. Kim, Z. Wang, B. Jiang, Y. Bando, Y. Sugahara, J. Tang, Y. Yamauchi, *Adv. Mater.*, 2019, 31, 1807134.
132. G. Zhang, L. Zheng, M. Zhang, S. Guo, Z.-H. Liu, Z. Yang, Z. Wang, *Energy Fuels*, 2012, 26, 618-623.
133. M.-S. Song, K. M. Lee, Y. R. Lee, I. Y. Kim, T. W. Kim, J. L. Gunjakar, S.-J. Hwang, *J. Phys. Chem. C*, 2010, 114, 22134-22140.
-

- 
134. K. M. Lee, M. S. Song, I. Y. Kim, T. W. Kim, S.-J. Hwang, *Mater. Chem. Phys.*, 2011, 127, 271-277.
  135. Y. She, B. Tang, D. Li, X. Tang, J. Qiu, Z. Shang, W. Hu, *Coatings*, 2018, 8, 340-341.
  136. S. Huang, G. N. Zhu, C. Zhang, W. W. Tjiu, Y. Y. Xia, T. Liu, *ACS Appl. Mater. Interfaces*, 2012, 4, 2242-2249.
  137. Y. Lin, L. Ruiyi, L. Zaijun, L. Junkang, F. Yinjun, W. Guangli, G. Zhiguo, *Energy Fuels*, 2010, 24, 3346-3351.
  138. Y. Zhu, Z. Huang, Z. Hu, L. Xi, X. Ji, Y. Liu, *Electrochim. Acta*, 2018, 269, 30-37.
  139. X. Zhang, W. Yang, D. G. Evans, *J. Power Sources*, 2008, 184, 695-700.
  140. J. Xie, X. Sun, N. Zhang, K. Xu, M. Zhou, Y. Xie, *Nano Energy*, 2013, 2, 65-74.
  141. X. Dong, L. Wang, D. Wang, C. Li, J. Jin, *Langmuir*, 2012, 28, 293-298.
  142. S. Anwer, A. B. Ari, G. Bharath, P. Cao, S. P. Patole, S. Luo, H. T. Masood, J. Cantwell, K. Liao, Q. Li, L. Zheng, *Adv. Mater. Interfaces*, 2019, 6, 1-10.
  143. Q. Zhang, Z. Liu, B. Zhao, Y. Cheng, L. Zhang, H. Wu, M. S. Wang, S. Dai, K. Zhang, D. Ding, Y. Wu, M. Liu, *Energy Storage Mater.*, 2019, 16, 632-645.
  144. Z. Gao, W. Yang, Y. Yan, J. Wang, J. Ma, X. Zhang, B. Xing, L. Liu, *Eur. J. Inorg. Chem.*, 2013, 4832-4838.
  145. Y. Wang, W. Yang, C. Chen, D. G. Evans, *J. Power Sources*, 2008, 184, 682-690.
  146. M. A. Woo, M. S. Song, T. W. Kim, I. Y. Kim, J. Y. Ju, Y. S. Lee, S. J. Kim, J. H. Choy, S. J. Hwang, *J. Mater. Chem.*, 2011, 21, 4286-4292.
  147. J. Guan, Y. Chen, L. Cao, Y. Liu, P. Lian, Y. Gao, X. Shi, *J. Power Sources*, 2020, 469, 228307-228319.
  148. M. Yano, S. Suzuki, M. Miyayama, M. Ohgaki, *Solid State Ion.*, 2013, 233, 32-37.
  149. H. Zheng, F. Tang, M. Lim, A. Mukherji, X. Yan, L. Wang, G. Q. Lu, *J. Power Sources*, 2010, 195, 680-683.
  150. J. Feng, X. Sun, C. Wu, L. Peng, C. Lin, S. Hu, J. Yang, Y. Xie, *J. Am. Chem. Soc.*, 2011, 133, 17832-17838.
  151. S. Rafai, C. Qiao, M. Naveed, Z. Wang, W. Younas, S. Khalid, C. Cao, *Chem. Eng. J.*, 2019, 362, 576-587.





# **CHAPTER-2**

**THEORETICAL BACKGROUND  
OF LDH, SYNTHESIS  
METHODS, EXFOLIATION  
AND CHARACTERIZATION  
TECHNIQUES**

# CHAPTER-2

## Theoretical Background of LDH, Synthesis Methods, Exfoliation and Characterization Techniques

Sr. No.	Title	Page No.
2.1	Introduction	43
2.2	Synthesis method of LDH	43
	2.2.1 Co-precipitation method	44
2.3	Synthesis of 2D Ns	45
	2.3.1 Introduction	45
	2.3.2 Synthesis methods of 2D INs	45
	2.3.3 Nanosheets-based nanostructures	50
2.4	Material characterization techniques	51
	2.4.1 X-Ray diffraction (XRD)	52
	2.4.2 Fourier transform infrared spectroscopy (FTIR)	53
	2.4.3 Raman spectroscopy	55
	2.4.4 X-ray photoelectron spectroscopy (XPS)	57
	2.4.5 Energy dispersive X-ray spectroscopy (EDS)	59
	2.4.6 Scanning electron microscopy (SEM) and transmission electron microscopy (TEM)	60
	2.4.7 N <sub>2</sub> adsorption and desorption (Brunaur-Emmett-Teller, BET)	64
	2.4.8 Particle size and zeta potential analyzer	65
2.5	Electrochemical techniques	66
	2.5.1 Introduction	66
	2.5.2 Cyclic voltammetry (CV)	67
	2.5.3 Galvanostatic charge-discharge (GCD)	69
	2.5.4 Electrochemical impedance spectroscopy (EIS)	70
2.6	References	71

## 2.1 Introduction:

LDHs are lamellar hydroxalcalite-like compounds or anionic clays. The structure of LDHs is composed of metal cations which are octahedrally coordinated by hydroxyl groups. During the formation of structure, sharing edges of octahedra form an infinitely large layers where hydroxyl groups cover both surfaces of layer. The typical feature in LDH is that metal cations must be a combination of divalent and trivalent cations. [1] LDH monolayers are therefore positively charged, and the charge density is proportional to the trivalent to divalent metal ratio  $x = M^{3+}/(M^{2+} \cdot M^{3+})$ . [2, 3] The ionic radii are in the range of 0.65 - 0.80 Å for divalent cations and 0.62 - 0.69 Å for trivalent cations (with the exception of Al: 0.50 Å). [2]

*Interlayer anions:* In LDHs, the interlayer space contains water molecules, charge balancing anions and sometimes charged or other neutral moieties. One major characteristic of LDHs is weak bonding between these interlayer ions and the host LDH monolayers. Diverse anionic species can therefore be found between the LDH layers during the crystallization. According to the charge-to-size ratio and orientation of interlayer species, the basal spacing (gallery height) can be significantly changed. The chart of various interlayer anions in LDH is shown in figure 2.1.

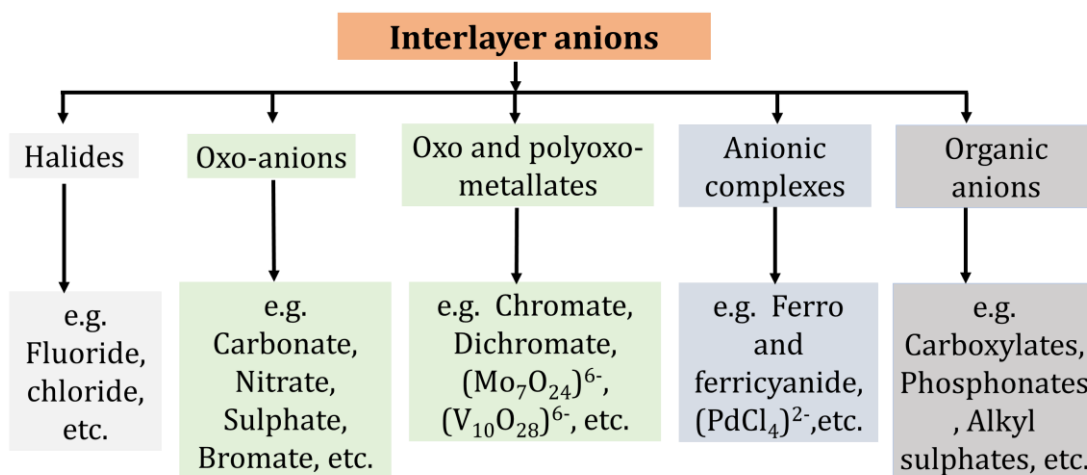


**Figure 2.1:** Types of interlayer anions in LDH. [4]

## 2.2 Synthesis method of LDH:

According to the literature study, the LDHs possess versatile physico-chemical properties, thus being applicable in different fields such as catalysis, electrocatalysis, photocatalysis, fire retardants and energy storage. [5] Most of the

researchers describe various synthesis methods for LDH and the effect of the synthesis method on the formation of LDH structure. Various synthesis methods such as electrodeposition, sol-gel, hydrothermal, urea hydrolysis, and co-precipitation have been reported for the synthesis of LDHs. [6-11] Among the various synthesis methods, the conventional co-precipitation method is strongly recommended by many researchers for the synthesis of LDHs due to its simplicity and better control over chemical composition. The highly pure and good crystallinity of LDHs can be obtained by co-precipitation method.

This chapter deals with three major parts: the first part deals with the theoretical background of LDHs, the second part is the discussion about synthesis of 2D Ns and LDH Ns, and the third part briefly elaborates characterization techniques practical to probe the properties of LDHs and LDH-based nanohybrids (structural, morphological and electrochemical).

Various synthesis methods for LDHs includes the co-precipitation, hydrothermal method, ion-exchange, rehydration using structural memory effect, intercalation method involving dissolution and re-co-precipitation procedures, secondary intercalation (pre-pillaring method), salt-oxide(or hydroxide) method, non-equilibrium aging, sol-gel, electrosynthesis, in situ oxidation of  $M^{II}$ , and “chimie douce” methods, etc [12]

### **2.2.1 Co-precipitation method:**

The conventional co-precipitation method is widely used for the synthesis of LDHs materials. An aqueous precursor solution containing  $M^{2+}$  and  $M^{3+}$  (species) with anions are used to synthesize LDHs. One of the interesting feature of the co-precipitation method is that, the various anionic species can be intercalated between two consecutive LDHs Ns. This can be achieved by the selection of metal salt of desired anions and avoiding the interference of other anions. This synthetic route is often the method of choice for the preparation of organic anion-containing LDHs, which are difficult to obtain by other methods. Generally, two approaches, are involved in co-precipitation such as precipitation at low and high supersaturation. [13, 14]

## **2.3 Synthesis of 2D Ns:**

### **2.3.1 Introduction:**

Currently, various nanostructure materials are being used as electrode materials in energy storage devices; however, the upcoming energy storage devices require more promising and reliable electrode materials. [15] The 2D materials possess several advantages like well-defined anisotropic surface structure, ultrathin thickness, short ion-diffusion paths, tailorable electronic structure and controllable chemical compositions. [16] Analogous to graphene Ns, 2D inorganic Ns possess high anisotropy, with thickness at the nanometer level and lateral size in the micrometer range. [17] The motion of charge carriers in 2D materials is much sophisticated along the in-plane direction than the out-of-plane due to the remarkable structural anisotropy of Ns.

The extremely high surface area of Ns due to their ultrathin thickness makes them highly useful for different applications such as adsorbents, catalysts, electrodes, etc. [18] Also, exfoliated 2D Ns can be used for the synthesis of other nanostructures like 1D nanotubes via rolling and 0D hollow spheres via coating. Moreover, INs can be used as basic building blocks to design nanosheet-based hybrid materials. [19]

### **2.3.2 Synthesis methods of 2D INs:**

The synthesis approach of 2D INs has a strong impact on their physicochemical properties and their functionalities. The synthesis methods of 2D INs are divided into two approaches: top-down and bottom-up approaches. [19] The 2D INs can be synthesized by a top-down approach from their pristine material via the exfoliation technique. The formation of 2D INs using the bottom-up approach is primarily based on precisely controlled growth of materials in 2D via chemical reactions of respective precursors. This section describes various approaches for the synthesis of 2D Ns. Various approaches for the synthesis of 2D Ns are shown in figure 2.2.

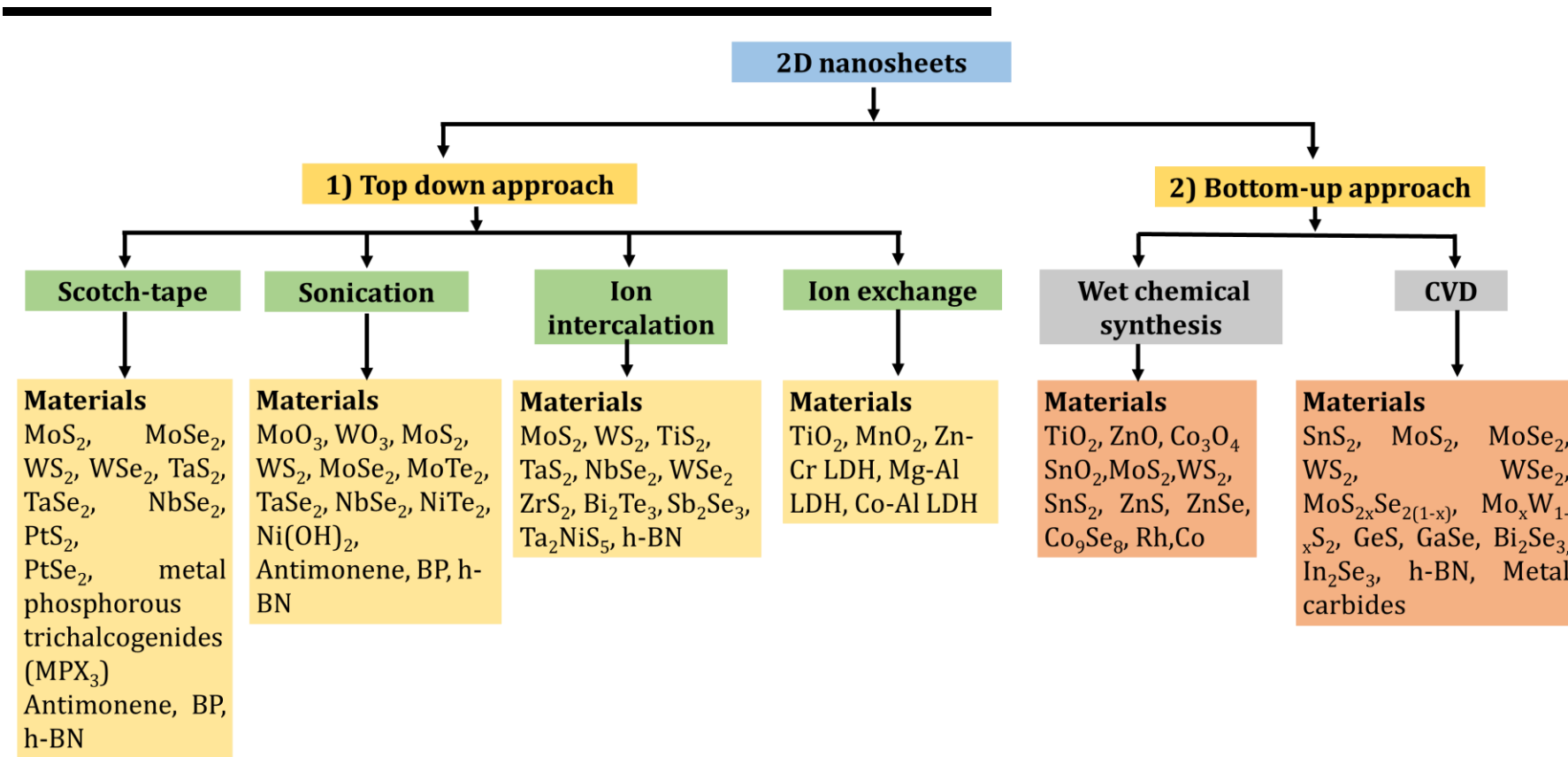
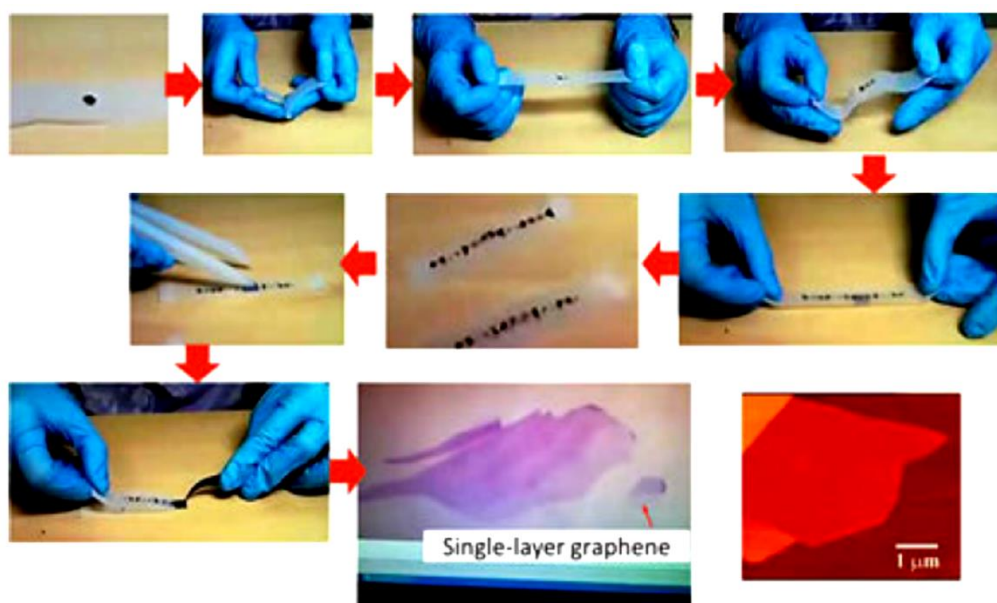


Figure 2.2: Various approaches for the synthesis of 2D Ns. [20]

**1) Top down approach:**

Production of ultrathin Ns by the top-down approach can be possible through a physical or chemical process. The top-down approach mainly relies on eliminating Van der Waals forces between the stacked layers of bulk pristine layered materials followed by the exfoliation process. The highly crystalline bulk pristine layered material can be synthesized by conventional solid-state reaction at elevated temperatures. The top-down approach is advantageous due to its high production yields with low cost, and hence it is useful in various applications. The top-down chemical strategy essentially relies on an ion-exchange chemical reaction that is assisted by heat or ultrasonication. [19-21]

**Scotch tape method:**



**Figure 2.3:** The procedure to produce 2D INs by scotch-tape method. [22]

The scotch-tape method is shown in figure 2.3. This is one of the simplest methods to produce monolayer 2D INs in which extrinsic force is applied via scotch tape. In this method, single layers from bulk layered compounds can be peeled off against the Van der Waals forces. [23] The obtained Ns by this method are of very high quality and pure because in this process, there is no involvement of any chemicals, surfactants, or any chemical reactions.

***Advantages and disadvantages of scotch tape method***

Sr. No.	Advantages	Disadvantages
1	It is simple method to produce monolayer 2D inorganic Ns.	It is not scalable and limited solely to laboratory research.
2	There is no involvement of any chemicals, surfactant or any chemical reactions.	The product yield is very low.
3	The obtained nanosheets are of very high quality and pure.	

***Ultrasonic exfoliation process:***

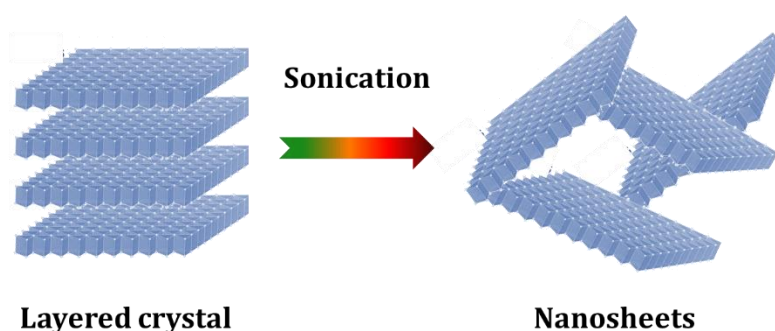


**Figure 2.4:** Schematic representation of the ultrasonic exfoliation process.

The schematic representation of the ultrasonic exfoliation process is shown in figure 2.4. An ultrasonic exfoliation process is highly efficient for the production of single or few-layer INs. Comparatively, this method has a higher production yield than mechanical exfoliation. In this method, highly crystalline particles of layered materials are dispersed in a suitable solvent, and the exfoliation occurs via the application of ultrasonication. Thus, solvent plays a crucial role in this method, the exfoliation yield depends on the type of solvents. [24]

***Advantages and disadvantages of ultrasonic exfoliation process [25]***

Sr. No.	Advantages	Disadvantages
1	Ultrathin and several hundreds of nanometer lateral size Ns can be obtained.	It is hard to get high-purity single layer 2D materials.
2	Layered materials can be extraordinarily exfoliate and disperse in solution.	
3	This method allow to prepare suspension with less defective, large nanosheets without decomposition of used solvents.	

***Ion-exchange exfoliation process:***

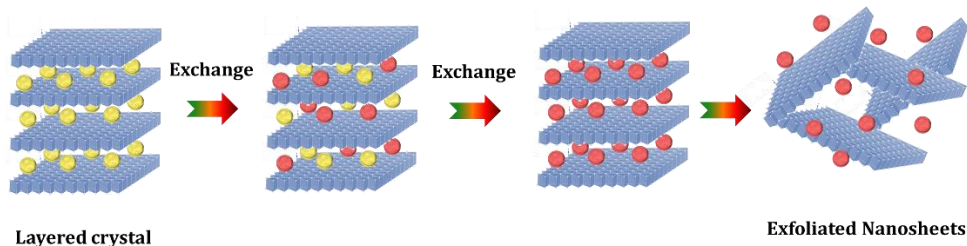


**Figure 2.5:** Schematic representation of the ion-exchange exfoliation process. [26]

The schematic representation of ion-exchange exfoliation process is shown in figure 2.5. This method belongs to the liquid exfoliation technique. Generally, layered materials contain charge balancing ions in the layers. Due to these ions, layered materials balance layered surface charge and maintain layered structure. In this method, the interlayer forces between the layered materials are weakened by the intercalation of bulky organic anions, and subsequent shaking or ultrasonication leads to the exfoliation of layered crystals. Therefore, the ion-exchange exfoliation process is applicable for obtaining Ns of various layered inorganic materials. Also, this method produces monolayer Ns with high production yields.

***Advantages and disadvantages of ion-exchange exfoliation process***

Sr. No.	Advantages	Disadvantages
1	This method is inexpensive.	Sedimentation can occur if choice of solvent is inappropriate.
2	Easy to implement and to scale.	

***2) Bottom-up approaches:***

In the bottom-up approaches, numerous chemical methods like wet chemical method, atomic or molecular condensation, CVD etc. are used to synthesize INs. CVD and wet-chemical synthesis are most frequently used bottom-up approaches to produce 2D INs. The INs prepared by these methods are frequently used in the biological or chemical sector and possess advantages of large-scale production and cost-effectiveness. Though bottom-up approaches are reported to synthesize many types of INs, the INs prepared by this approach possess few layers of INs. Also, these INs contains a surfactant in most cases which restrict the growth of INs in 3D. [20, 21]

### 2.3.3. Nanosheets-based nanostructures:

As 2D Ns, possess unique properties, these materials can be regarded as basic building blocks to synthesize various nanostructures and nanohybrids. The schematic of synthesis processes and typical Ns-based hybrid structures is shown in figure 2.6. Nanostructure materials showing certain properties at nanoscale dimensions, particularly unique 2D anisotropic shape and ultrathin thickness, make them macromolecular building blocks for designing and developing higher-order structures. On the basis of their shape, nanostructure materials can be classified into 0D ((Nanospheres, nanodots)), 1D (nanotubes, NWs, nanorod), 2D (nanoplates, Ns) and 3D (pyramidal, hexagonal, flower-like) nanomaterials. Ns with highly anisotropic 2D shape enables easier and accelerated charge transport through it than the other shaped nanostructures. [27]

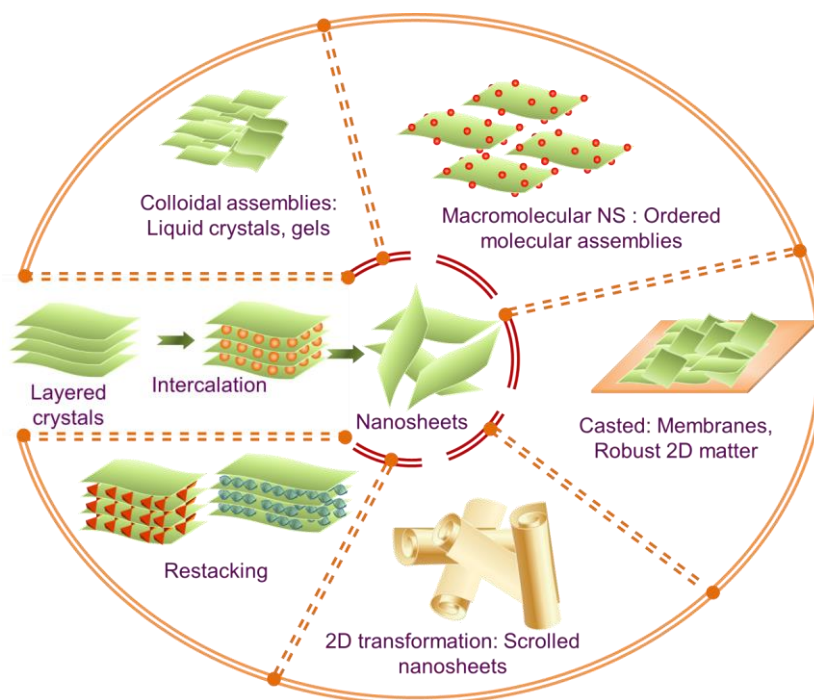


**Figure 2.6:** Synthesis processes and typical Ns-based hybrid structures. [28]

The exfoliated INs with expanded surface area and maximum surface exposure of the component ions are promising building blocks for hybrid materials. Furthermore, as all the component ions reside on the surface of Ns, the nanohybrids based on Ns display strong electronic coupling between the hybridized components. Moreover, Ns-based hybrids exhibit expanded surface area, highly mesoporous morphology, tunable pore structure, and flexible chemical composition. Consequently, various strategies are developed for the synthesis of

Ns-based hybrids. Such strategies mainly include exfoliation-restacking of INs with oppositely charged species, anchoring or growth of other nanostructures on INs, and layer-by-layer deposition of INs with oppositely charged molecular species. Thus, the various organic, inorganic, polymeric, and biological guest nanostructure species are useful for the hybridization with INs. [29, 30] INs-based hybrids display unique physicochemical properties and find applications in various fields. Therefore, INs-based hybrids are applicable in catalysis, sensors, electrochemistry, photoluminescent materials, high-T<sub>c</sub> superconductors, ferroelectric/ferromagnetic, and biomolecule/drug reservoirs. [31]

It is easily possible to tune the desired properties of INs-based hybrids by simply changing the type of hybridized component and constituent INs chemical composition. Thus electrodes prepared by the INs-based hybrids demonstrated excellent performance when used in SCs, batteries, and fuel cells. [32] The Ns derived from the redoxable layered inorganic solids like layered transition metal chalcogenides (LMC), layered metal oxides (LMO), and LDHs are useful candidates for electrochemical energy storage devices. [33]

#### **2.4 Material characterization techniques:**

The physical and chemical properties of materials are most crucial aspects for their usage in corresponding application. To achieve excellent performance of materials for the desired application, it is essential to study the physico-chemical properties of materials by using various characterization techniques such as XRD, FTIR, RAMAN, FESEM, EDS, XPS, TEM, BET, and zeta potential.

### 2.4.1 X-ray diffraction (XRD):

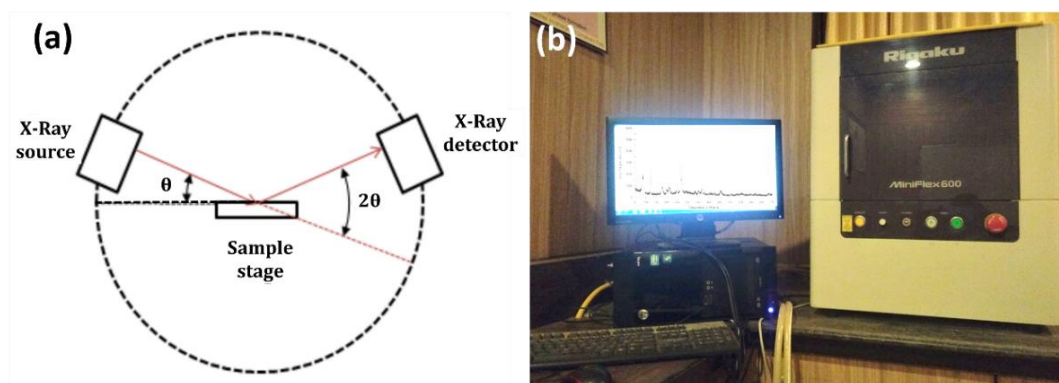


**Figure 2.7:** (a) Schematic of X-ray diffractometer and (b) photograph of XRD instrument (Rigaku Miniflex 600).

The schematic diagram of X-Ray diffractometer and photograph of XRD instrument is shown in figure 2.7.

#### **Working principle**

XRD is a well-known technique to study the crystal structure, phase, lattice parameters, grain size and crystallite orientations of the materials. [34, 35] XRD technique is based on the phenomenon of X-ray reflection from the crystallographic planes and is governed by Bragg's equation;

$$2d \sin\theta = n\lambda \quad (2.1)$$

Where,  $d$ ,  $\lambda$ ,  $n$  and  $\theta$  are the basal spacing, wavelength of X-ray, order of diffraction and diffraction angle, respectively. Crystallite size of the sample can be estimated from Scherrer's equation (equation 2.2) using the FWHM of the most significant diffraction peak.

$$D = \frac{K\lambda}{\beta \cos\theta} \quad (2.2)$$

Where  $D$ ,  $\lambda$ ,  $\beta$ ,  $\theta$ , and  $K$  are crystallite (grain) size, the wavelength of X-ray, FWHM of diffraction peak in radians, Bragg's angle, and shape factor, respectively. The value of  $K$  lies between 0.89 to 1.39, but for most cases, it is taken as  $\sim 1$ . [36] From these calculations, we can get precise information about the atomic arrangements of an unknown sample.

**Advantages and disadvantages of XRD [37]**

Sr. No.	Advantages	Disadvantages
1	The most convenient and least expensive.	X-rays do not interact very strongly with lighter elements.
2	Widely used method to determine crystal structure.	The intensity is $10^8$ times less than that of electron diffraction.
3	The best method for phase analysis.	
4	X-ray are not absorbed very much by air, so the sample not be in an evacuated chamber.	

In the present research work and dissertation, the XRD technique is used to probe the crystal structure of pristine Co-Cr-LDH and Co-Cr-LDH-based nanohybrids. By using XRD analysis, the crystal dimensions of Co-Cr-LDH and Co-Cr-LDH-based nanohybrids are estimated. Thus, the gallery space of Co-Cr-LDH-based nanohybrids upon the hybridization is determined using the c-axis parameter. Moreover, the crystal size along with the c-axis parameter is estimated using Scherrer's equation. Consequently, the number of monolayers in layered crystals can be judged by the crystal size analysis.

**2.4.2 Fourier transform infrared spectroscopy (FTIR):**

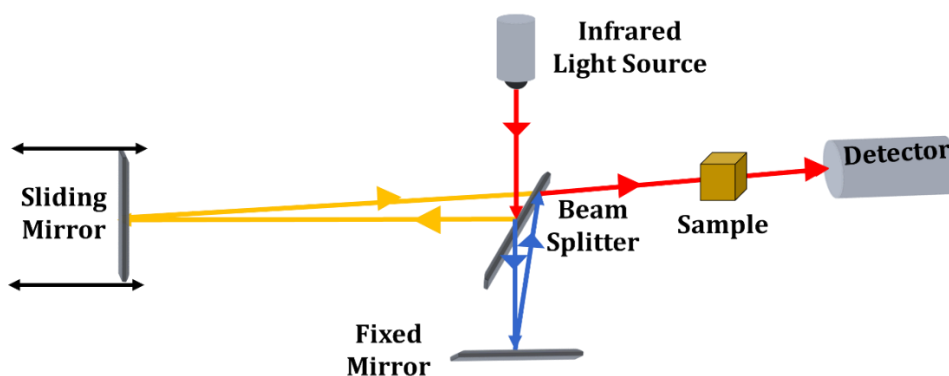


**Figure 2.8:** Ray diagram of FTIR spectrometer. [38]

**Working principle**

FTIR spectroscopy is used to investigate the presence of functional groups and chemical bonding nature in the materials. In an electromagnetic field, the difference between two energy levels ( $E_1$  and  $E_2$ ) of material is equal to Planck's constant ( $h$ ) times incident radiation frequency ( $\nu$ ) and it is written as,

$$\Delta E = h\nu \tag{2.3}$$

## Theoretical background of LDH, synthesis methods, exfoliation and characterization techniques

Here,  $\Delta E$  is negative when radiation is emitted and positive when energy is absorbed by the molecule. The resulting signal at the detector presents as a spectrum demonstrating a molecular impression of the sample. An organic/inorganic compound can vibrate in six ways: symmetrical and anti-symmetrical stretching, wagging, scissoring, rocking, and twisting. [39] After the satisfaction of equation 2.3, we can get the vibration spectrum of intensity versus frequency. Also, different spectra are raised by molecules or atoms depending on the energy levels involved in the transition. Therefore, the energy contribution can be represented by the following equation

$$E_{\text{tot}} = E_{\text{elect}} + E_{\text{rot}} + E_{\text{vib}} + E_{\text{trans}} \quad (2.4)$$

Where  $E_{\text{tot}}$ ,  $E_{\text{elect}}$ ,  $E_{\text{rot}}$ ,  $E_{\text{vib}}$ , and  $E_{\text{trans}}$  are the total, electronic, rotational, vibrational, and translation energy, respectively. [40] The ray diagram of the FTIR spectrometer is displayed in figure 2.8.

### Uses of FTIR analysis

- Identification of unknown materials (e.g., films, powders, solids, liquids).
- Identification of contamination in a material
- Identification of additives after extraction from a polymer matrix.
- Identification of oxidation, decomposition, or uncured monomers in failure analysis investigations. [41]

### Advantages and disadvantages of FTIR [42]

Sr. No.	Advantages	Disadvantages
1	Simpler mechanical design.	Can not detect atoms or monoatomic ions-single atomic entities contain no chemical bonds.
2	Elimination of stray light and emission contributions.	Can not detect molecules comprised of two identical atoms symmetric-such as $N_2$ or $O_2$ .
3	Majority of molecules in the universe absorb mid-infrared light, making it a highly useful tool.	Aqueous solutions are difficult to analyze - water is a strong IR absorber.
4	Sensitive, fast and easy.	Complex mixtures - samples give rise to complex spectra.
5	Relatively inexpensive and provides rich information.	

In the present research work and dissertation, the FTIR technique is used to probe the nature of chemical bonding in pristine Co-Cr-LDH and Co-Cr-LDH-

based nanohybrids. By using FTIR analysis, the intercalated anions in pristine Co-Cr-LDH and Co-Cr-LDH-based nanohybrids are judged and validated by the characteristic IR features. Moreover, the intactness of host Co-Cr-LDH Ns is supported by the IR features related to the host Co-Cr-LDH lattice.

### 2.4.3 Raman spectroscopy:

#### *Working principle*

Raman spectroscopy is used to identify the functional groups present in the material. When monochromatic light is incident on a sample, it absorbs some light, and a maximum part of light is transmitted. However, a minute portion of the light is scattered by the sample in all directions.

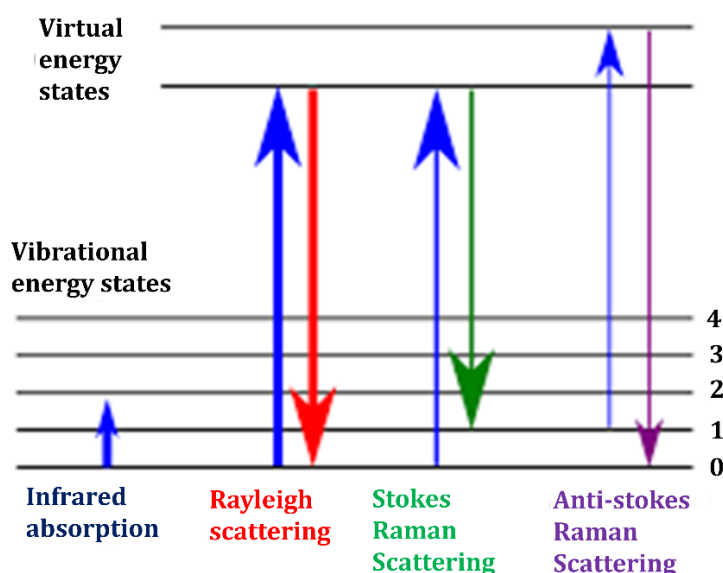


**Figure 2.9:** Energy level diagram of Raman spectroscopy. [43]

Rayleigh scattering is observed when the scattering occurred at the right angles to the incident beam in which 99% of the scattered light has a same frequency as that of the incident light. Raman scattering is possible with scattered light (1%) of different frequencies other than the incident frequency.

The various vibrational levels of electrons are stated by specific energy differences (figure 2.9). When electron in the material is interacted with the incident monochromatic light, the electron makes a transition to a virtual state of energy by absorbing energy and again comes to the original energy level by losing energy. Rayleigh scattering is observed when the energy lost is equal to the energy of the incident photon and the electron comes to its initial level with the loss of one photon. However, sometimes electrons losing energy from the virtual state can fall

## Theoretical background of LDH, synthesis methods, exfoliation and characterization techniques

back to a different vibrational level. In this instant, the energy lost by the electron is different than the energy absorbed from the incident photon. As a result, the emitted photon has a different frequency than the incident photon. This gives the Raman scattering. Depending on the final vibrational level of the electron, Raman scattering is classified into stokes lines and anti-stokes lines. When the frequency of the scattered photon is less than that of the incident photon, stokes lines are observed on the Raman spectrum. This happens when an electron absorbs energy. Conversely, anti-stokes lines are observed when the emitted photon's frequency is greater than that of the incident photon. Hence energy is released by the electron. [44] The Raman shift  $\Delta$  is positive for stokes and negative for anti-stokes lines. [45-47]

### *Uses of Raman analysis*

- Identification of the rotational levels of the molecules.
- Determination of molecular concentration in the sample.
- Identification of the functional groups present in the material

### *Advantages and disadvantages of Raman spectroscopy* [48]

Sr. No.	Advantages	Disadvantages
1	Less sensitive to temperature changes.	Prone to interference from other molecules.
2	Minimally sensitive to water.	Unstable laser wavelength and intensity.
3	Suitable on any surface since it measures scattered light, including opaque substrates.	Long collection time.
4	High specificity.	Susceptible to noise interference (low signal to noise ratio), fluorescence and turbidity.

#### 2.4.4 X-ray photoelectron spectroscopy (XPS):

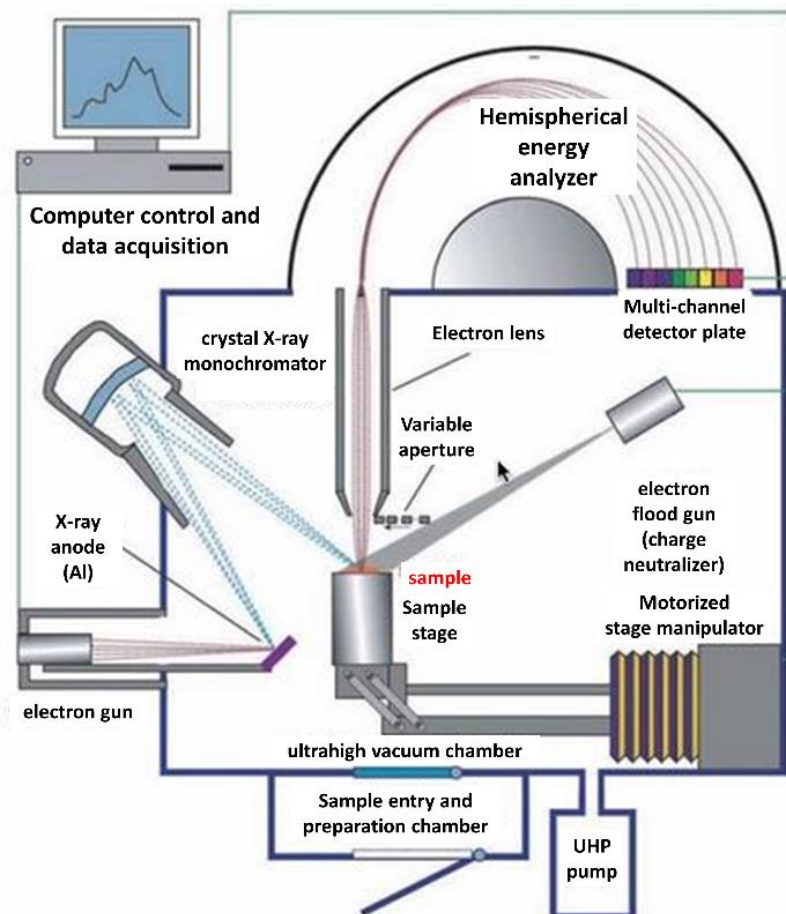


**Figure 2.10:** Schematic diagram of the components of an XPS Instrument. [49]

#### *Working principle*

The XPS technique identifies the surface chemical composition and oxidation states of elements present in the material. The schematic diagram of the components of an XPS instrument is shown in figure 2.10. XPS technique is based on the principle of the photoelectric effect. [50] When the X-ray beam is incident on the surface of material, electrons are emitted from the material. The kinetic energies of emitted photoelectrons associated to the binding energy of each electron, are used for elemental identification. The kinetic energy of ejected electrons can be calculated by the relation, [51]

$$KE = hv - BE - \phi s \quad (2.5)$$

Where,  $hv$  is photon energy,  $BE$  is the binding energy of atomic orbital, and  $\phi s$  is the work function.

## Theoretical background of LDH, synthesis methods, exfoliation and characterization techniques

Each element produces a set of characteristic peaks. A typical XPS spectrum is a plot of the number of electrons detected versus specific binding energy. These peaks correspond to the electron configuration within the atoms. The number of detected electrons in each peak is directly related to the amount of element within the sampling volume. The peaks at particular energies represents presence of respective element.

### *Use of XPS analysis*

- XPS can be used to determine quantitative analysis of elements in sample.
- XPS can be used to determine oxidation states of surface elements and their identification
- With the angle resolved, XPS electronic configuration and electronic band structure can be possible to probe.
- XPS can be used to probe uniformity of elemental composition across the top surface (or line profiling or mapping)
- XPS can be used to probe uniformity of elemental composition as a function of ion beam etching (or depth profiling)
- XPS can be used to probe empirical formula of pure materials

### *Advantages and disadvantages of X-ray photoelectron spectroscopy [52]*

Sr. No.	Advantages	Disadvantages
1	Non destructive technique.	Very expensive technique.
2	Surface sensitive (10-100 Å).	High vacuum is required.
3	Qualitative measurements are obtained .	Slow processing.
4	Provides information about chemical bonding.	Large area analysis is required.
5	Elemental mapping.	Data collection is slow (5 to 10 min.) and poor lateral resolution.

### 2.4.5 Energy-dispersive X-ray spectroscopy (EDS):

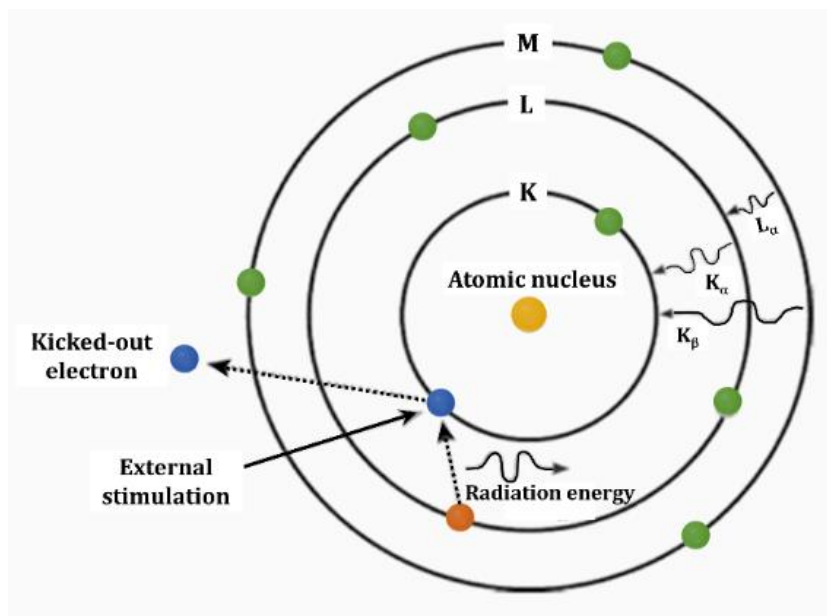


**Figure 2.11:** Mechanism of X-ray emission in EDS.

#### ***Working principle***

EDS is used to determine the composition of elements present in the material. The mechanism of X-ray emission in EDS is shown in figure 2.11. The highly energetic X-rays leads to eject core electrons. These ejected electrons leaves behind holes and that holes can be filled by higher energy electrons and it will release energy. The energy released during this process is unique to each element and used to identify which elements are present with what proportion. Elemental composition of the material is analyzed through spectrum from number of counts against the energy of X-rays. [53]

#### ***Use of EDS analysis***

- Identification of composition of elements present in the material.

**Advantages and disadvantages of EDS [54]**

Sr. No.	Advantages	Disadvantages
1	High speed of data collection in most cases.	Is destructive analysis in many cases.
2	High detector efficiency.	Poor energy resolution of the peaks.
3	Able to scan areas (raster scanning) and single spots.	Low peak-to-background ratio.
4	Elemental spectra are linked to image maps generated by SEM and TEM.	Limit on the input signal rate because of pulse processing requirements.
5	Map a large spatial range from $\sim 1 \text{ mm}^2$ to $\mu\text{m}^2$ .	Surface sensitive complicates bulk analysis.
6	A most widely used method in electron microscopes because of ease of interfacing to existing data. microscopes and of a higher speed of detection.	Quantitative analysis of heterogeneous materials often provides inaccurate

**2.4.6 Scanning electron microscopy (SEM) and transmission electron microscopy (TEM):**

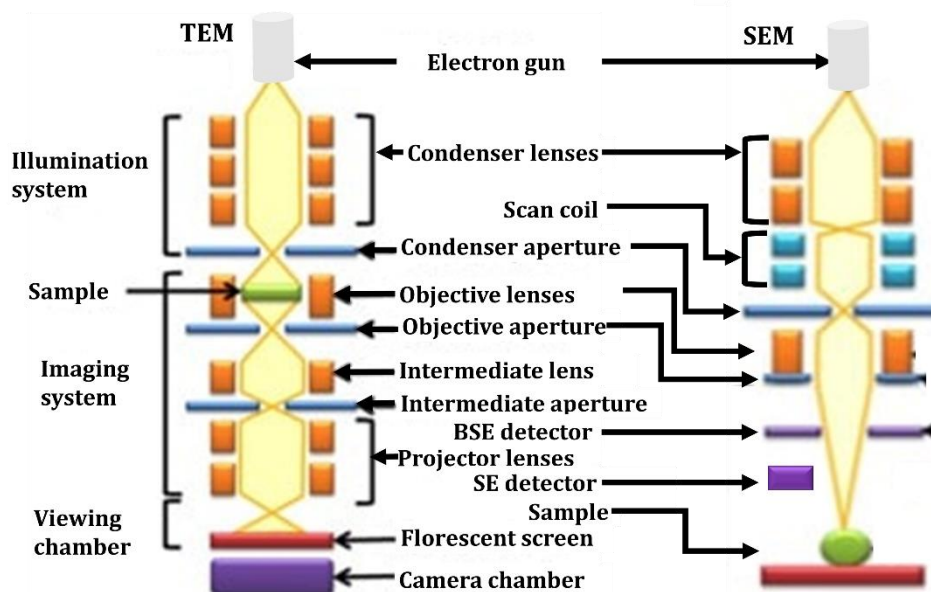


Figure 2.12: The optics of a TEM and SEM. [55]

**Scanning electron microscopy (SEM)**

**Working principle**

Figure 2.12 shows the optics of TEM and SEM. SEM is a kind of electron microscope that uses a fine beam of focused electrons to scan a sample's surface. The microscope records information about the interaction of electrons with the sample and creates magnified image. [56]

The accumulation of electrons into a fine beam is possible through a condenser lens. The beam focuses onto the sample with the help of an objective lens. Deflection coils help to move the beam in a rectangular X and Y track, creating a raster scan across the surface of the specimen. The topography and elemental composition are obtained from the SEM image of the material. In addition, the 3D black-and-white images of the thin or thick samples are possible to capture by SEM.

***Field emission scanning electron microscopy (FESEM)***

In FESEM, a very fine beam can be obtained from the electron gun, which has a high and stable current. A thermionic emission source is used in the SEM, whereas a field emission source is used in FESEM. The difficulties of evaporation of cathode material, thermal drift during operation, and relatively low brightness in SEM are overcome in FESEM by placing a filament in a large electrical potential gradient.

***Transmission electron microscopy (TEM)***

***Working principle***

TEM uses a broad high-energy beam of electrons to generate an image of a sample's interior structure. A beam of electrons transmitted through a sample is used to obtain information about the sample's composition, crystal structure, and morphology. TEM can obtain atomic-level information with high magnification and resolution compared to any other electron microscopy technique. TEM is also used to inspect molecular and cellular structures.

An electron source sends a beam of electrons through an ultrathin sample. When the electrons penetrate the sample, they pass through the lenses below. This data is used to create images directly on a fluorescent screen or onto a computer screen using a charge-coupled device (CCD) camera. [56]

TEM is an analytical tool for the visualization and analysis of specimens (micro to nano space). The detailed microstructural examination is possible through high resolution and high magnification. TEM enables the investigation of crystal structures, specimen orientations, and chemical compositions through diffraction patterns. Metals, alloys, ceramic, glasses, polymers, semiconductors, composites, etc. and nanostructures: graphene sheet, nanotubes, nanowires,

## Theoretical background of LDH, synthesis methods, exfoliation and characterization techniques

quantum dots, nanoparticles, etc., materials can be analyzed through TEM. TEM is also applicable for analyzing biological samples such as bacteria, viruses, fungi, etc.

### *Difference between the SEM and TEM*

Parameter	Scanning Electron Microscopes (SEM)	Transmission Electron Microscopes (TEM)
Electron stream	Fine, focused beam	Broad beam
Image taken	Topographical/surface	Internal structure
Resolution	Lower resolution	Higher resolution
Magnification	Up to 2,000,000 times	Up to 50,000,000 times
Image dimension	3-D	2-D
Sample thickness	Thin and thick samples okay	Ultrathin samples only
Penetrates sample	No	Yes
Sample restriction	Less restrictive	More restrictive
Sample preparation	Less preparation required	More preparation required
Cost	Less expensive	More expensive
Speed	Faster	Slower
Operation	Easy to use	More complicated; requires training

### *Use of SEM analysis*

- SEM can obtain the topography, surface characteristics, specimen composition, etc.

### *Use of TEM analysis*

- TEM can obtain the crystal structures, specimen orientations, and chemical compositions.

## Theoretical background of LDH, synthesis methods, exfoliation and characterization techniques

### ***Advantages and disadvantages of SEM*** [57]

Sr. No.	Advantages	Disadvantages
1	It gives detailed 3D and topographical imaging and the versatile information garnered from different detectors.	SEMs are expensive and large.
2	SEM works very fast.	Special training is required to operate an SEM.
3	Modern SEMs allow for the generation of data in digital form.	The preparation of samples can result in artifacts.
4	Most SEM samples require minimal preparation actions.	SEMs are limited to solid samples.
5		SEMs carry a small risk of radiation exposure associated with the electron that scatter from beneath the sample surface.

### ***Advantages and disadvantages of TEM*** [57]

Sr. No.	Advantages	Disadvantages
1	TEMs offer very powerful magnification and resolution.	TEMs are large and very expensive.
2	TEMs have a wide range of applications and can be utilized in a variety of different scientific, educational and industrial fields.	Laborious sample preparation.
3	TEMs provide information of element and compound structure.	Operation and analysis requires special training.
4	Images are high quality and detailed.	Samples are limited to those that are electron transparent.
5		TEMs require special housing and maintenance.
6		Images are black and white.

2.4.7 N<sub>2</sub> adsorption and desorption (Brunaur-Emmett-Teller, BET):

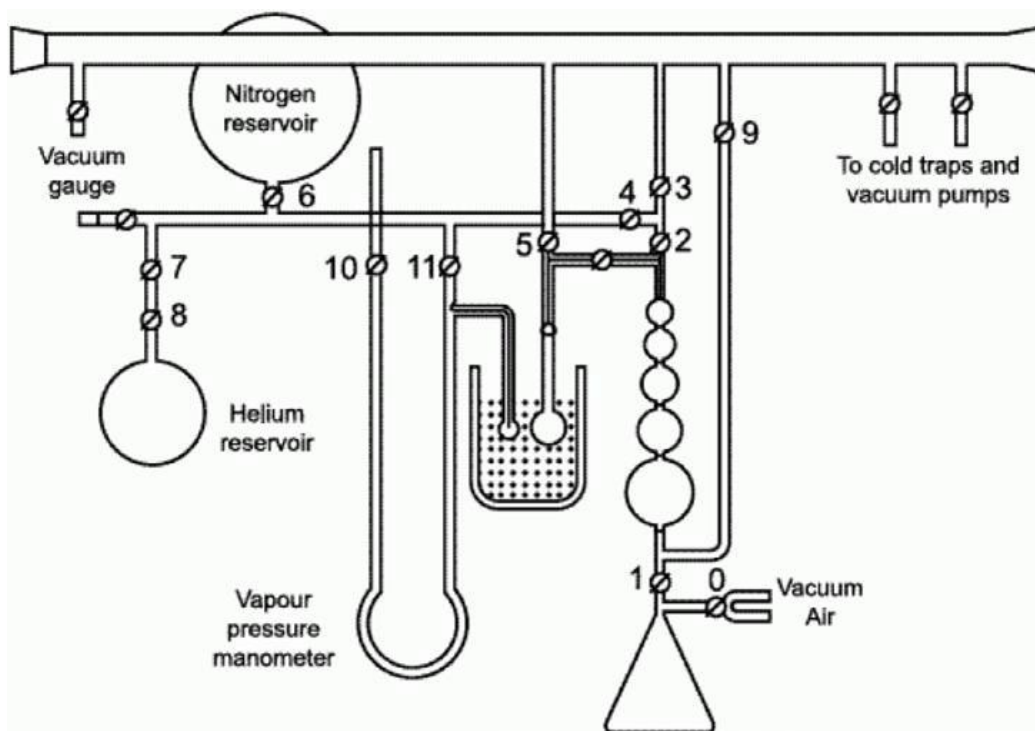


Figure 2.13: Schematic of the dynamic flow method apparatus. [58]

**Working principle**

Specific surface area and porosity of prepared material are determined using BET analysis. In this method, the surface area is determined by the adsorption of a gas on the solid surface and the amount of adsorbed gas calculated with the corresponding monomolecular layer on the surface. Gas adsorbed on the surface, pores of the specimen, and the amount of gas condensed or adsorbed at a constant temperature on the solid surface depend on gas pressure. Adsorbed and condensed gas provides the pore structure information of solids. For the BET measurement, generally, noncorrosive gases are used. [59] The schematic of the dynamic flow method apparatus is shown in figure 2.13.

BET theory is the extension of Langmuir's theory. It is for the monolayer molecular to multilayer adsorption with the hypothesis as a) physically gas molecules adsorbed on a solid, b) no interaction between each adsorption layer, and c) the Langmuir theory can be applied to each layer. The specific surface area ( $S_{BET}$ ) and total surface area ( $S_{total}$ ) are represented by the following expressions,

$$S = \frac{V_m N a}{m 22400} \quad (2.6)$$

$$S_t = \frac{N_s v_m}{V} \quad (2.7)$$

## Theoretical background of LDH, synthesis methods, exfoliation and characterization techniques

$$S_{BET} = \frac{S_{total}}{a} \quad (2.8)$$

Where, S is the specific surface area ( $\text{m}^2 \text{g}^{-1}$ ), N is Avogadro's number,  $a$  is an effective cross sectional area of one adsorbate molecule ( $\text{m}^2$ ), m is mass of the test powder (g). [60]

### Use of BET analysis

- Determination of specific surface area, pore size distribution and pore structure of the materials.

### Advantages and disadvantages of $N_2$ adsorption and desorption [61]

Sr. No.	Advantages	Disadvantages
1	Detects smaller pores than Hg porosimetry (can obtain data from porous materials with pore diameters between 0.3 nm and 300 nm).	Fine pore structure are difficult to degas.
2		Overestimates large pore diameters.

### 2.4.8 Particle size and zeta potential analyzer:

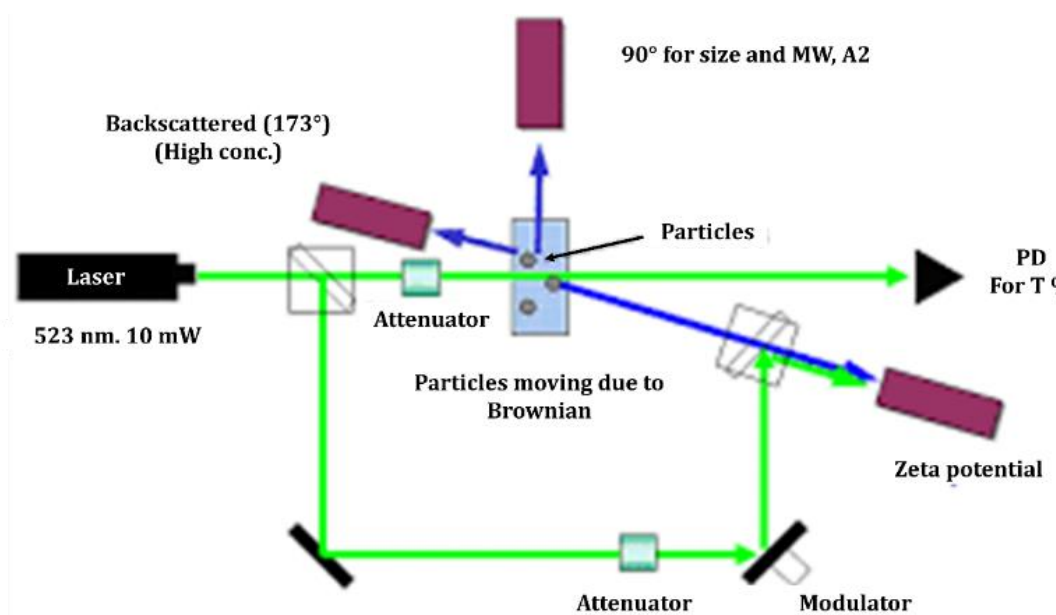


**Figure 2.14:** Particle size and zeta potential analyzer. [62]

The properties like zeta potential and hydrodynamic particle size of the colloidal/nanoparticulate/macromolecular system can be probed using the zeta potential equipped with particle size analyzer. The zeta potential with particle size analyzer is shown in figure 2.14. It is used to determine particles zeta potential, particle size distribution and molecular weight of large polymeric substances

dispersed in water. The significance of zeta potential is that its value can be related to the stability of colloidal dispersions. The zeta potential provides information about the degree of repulsion between the adjacent and similarly charged particles present in a dispersion. The solution or dispersion will resist the aggregation of molecules and particles that are small enough. When the potential is low, attraction exceeds repulsion, and the dispersion will break and flocculate. [63]

***Use of particle size and zeta potential analyzer***

- Used for the charge stability and quantification of the magnitude of the electric charge of disperse system.

***Advantages and disadvantages of particle size analyser [64]***

Sr. No.	Advantages	Disadvantages
1	Simple	Slow
2	Inexpensive	Measures very few particles
3	Can see shape	Very tedious

**2.5 Electrochemical techniques:**

**2.5.1 Introduction:**

SC has three main components, an electrode, suitable electrolyte, and separator. For the calculations of Cs, ED and PD of SC following formulae are used.

$$(Cs) = \frac{I \Delta t}{m \Delta V} \tag{2.9}$$

$$(ED) = \frac{Cs \Delta V^2}{7.2} \tag{2.10}$$

$$(PD) = \frac{ED \ 3600}{\Delta t} \tag{2.11}$$

Where Cs is specific capacitance, I is applied current density,  $\Delta t$  is discharge time, m is mass of active material, and  $\Delta V$  is the potential window. [65]

The maximum values of Cs, ED and PD of SC can be achieved by tuning the properties of active electrode material and suitable electrolyte. Various electrochemical measurement techniques are useful to probe the electrochemical properties of the electrode materials. Different electrochemical measurement techniques are shown in figure 2.15. [64]

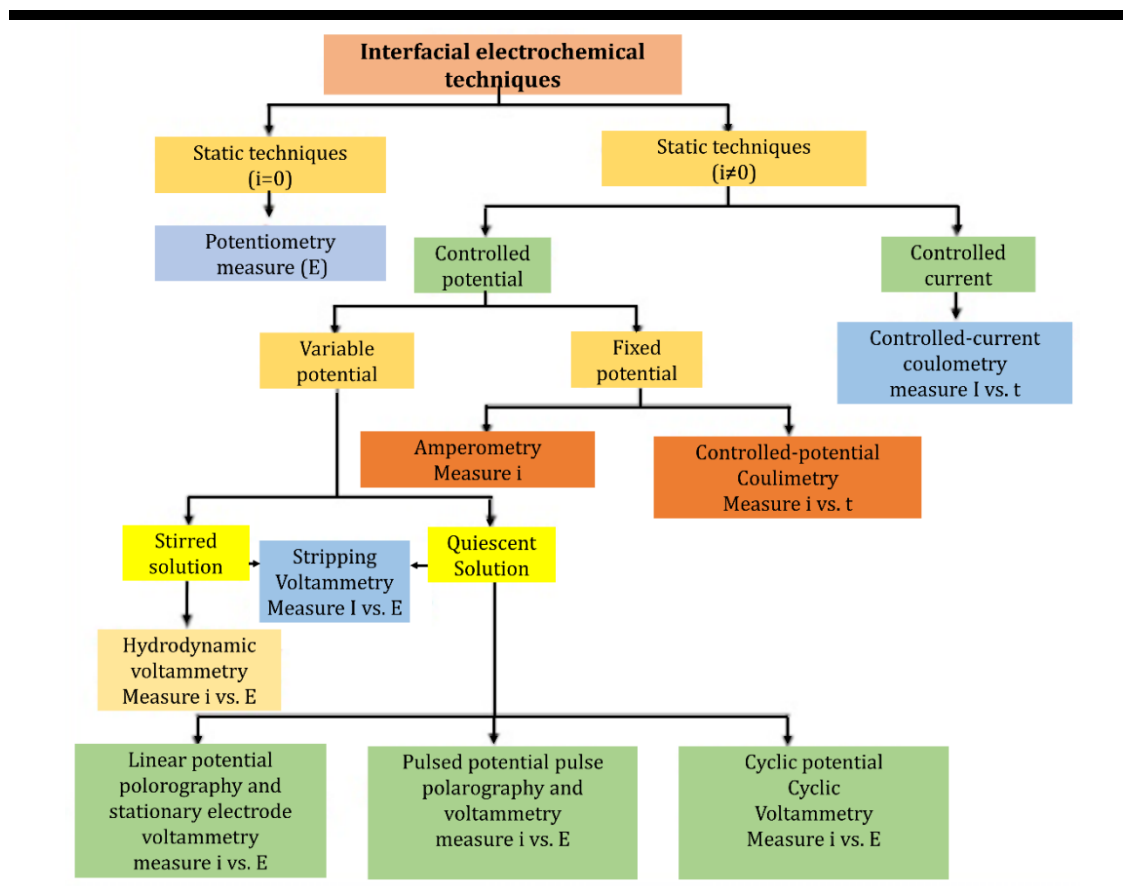
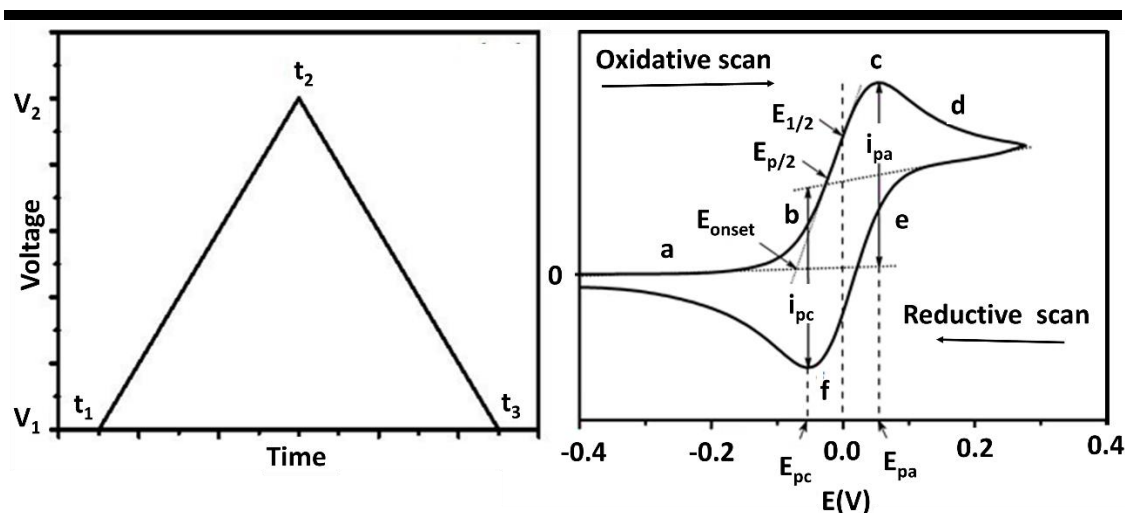


Figure 2.15: Interfacial electrochemical measurement techniques. [66]

### 2.5.2 Cyclic voltammetry (CV):

CV technique is used to measure the electrode activity in the electrolyte solution. It is a useful method for quickly determining information about the redox processes and the kinetics of electron-transfer reactions. In the CV experiments, the current is generated after the electron transition between the electrodes and the redox species. In the three-electrode electrochemical cell, the potential is applied with respect to the reference electrode, and the current at working electrode is measured. [67]



**Figure 2.16:** (left) Ramping applied voltage with time and (right) a typical cyclic voltammogram for a reversible single electrode transfer reaction. [67]

In CV technique, the constantly varying potential is applied to the working electrode within the fixed potential window. After reaching the potential limit, potential is ramped in the opposite direction to return the initial potential. This variation of potential is schematically presented in figure 2.16 (left). A typical CV curve of reversible reaction for the single electrode is shown in figure 2.16 (right). In this figure,  $I_{pa}$  and  $I_{pc}$  are the anodic and cathodic peak currents, and  $E_{pa}$  and  $E_{pc}$  are anodic and cathodic peak voltages of resulted voltammogram, respectively. The current response decreases linearly as the analyte is depleted and the diffuse double layer raises. In reverse scan, the reduced analyte will re-oxidized, which delivers reverse polarity current, called anodic current. Thus, selecting initial and final potential in the CV measurement is very important. [68] For the reversible electrochemical reactions, the process for reduction is a mirror image of the oxidation, only with an opposite scan direction. It is represented as a cathodic peak ( $i_{pc}$ ) at the cathodic peak potential ( $E_{pc}$ ). The anodic and cathodic peak currents should be of equal magnitude but in opposite direction, provided that the process is reversible.

### 2.5.3 Galvanostatic charge-discharge (GCD):

The electrochemical performance of SC can be tested by the GCD technique. In the GCD technique, the potential is measured as a function of time by applying a constant current to the working electrode. The schematic of the GCD curve is represented in figure 2.17. When a constant current is applied to the working electrode, due to internal resistance, potential quickly develops and grows progressively due to the exhaustion of reactant concentration at the electrode surface. Moreover, potential instataniously drops during discharging due to internal resistance. Therefore, a constant current is used for achieving the desired voltage during charging and discharging.

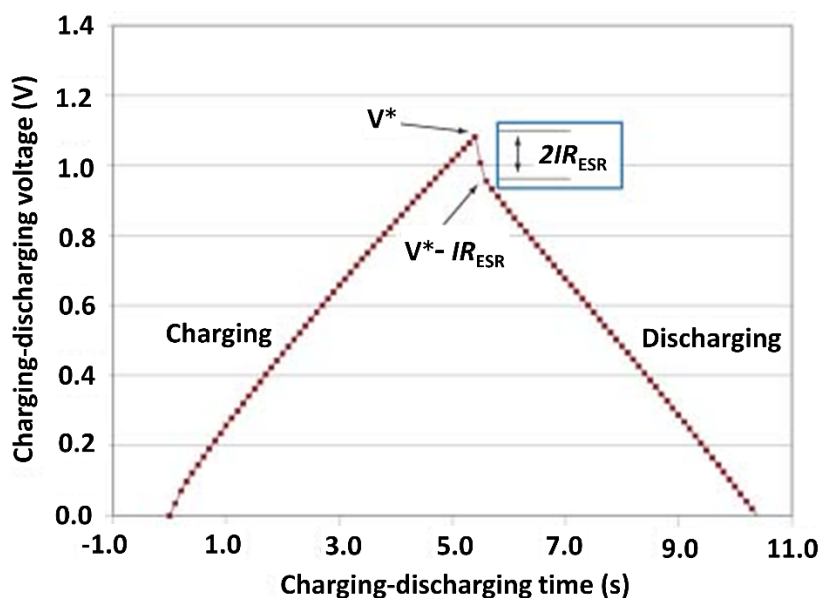


**Figure 2.17:** Plot of GCD curve. [69]

From the behavior of the GCD curve, confirmation of the charge storage mechanism is possible. Non-linear GCD behavior is indicative of the pseudocapacitive charge storage mechanism, while linear GCD behavior is indicative of the EDLCs mechanism. [67] ED and PD of SC can be possible using the analysis of the GCD curve. [70]

2.5.4 Electrochemical impedance spectroscopy (EIS):

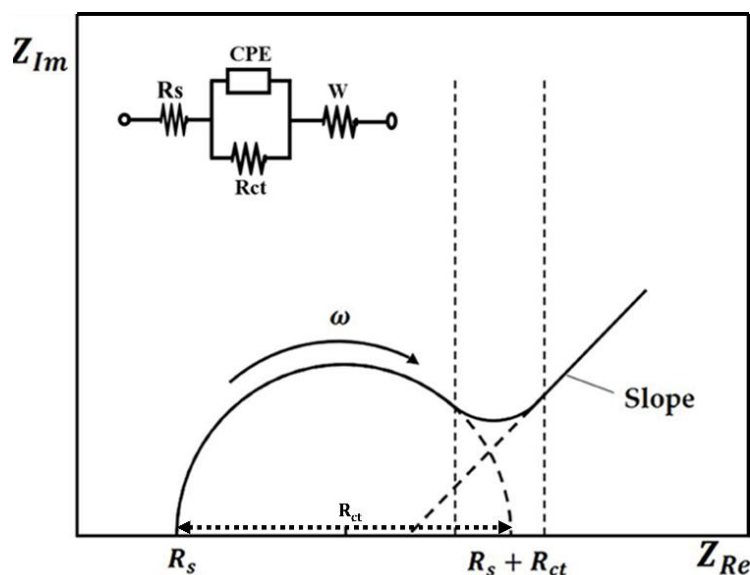


**Figure 2.18:** Nyquist plot with an electrical equivalent circuit. [71]

Impedance is nothing but the AC resistance of the cell, which consists of imaginary and real parts. The electrochemical cell contains capacitive, resistive, and inductive properties. The information about capacitive/inductive properties can be gained by analyzing the imaginary part, while the analysis of the real part can gain resistive properties information.

As the capacitor acts as an open circuit for DC and the inductor acts as a straight conductor wire for DC, however, both appear as imaginary resistors in an AC circuit. Figure 2.18 represents a typical Nyquist plot obtained through EIS technique. The real and imaginary parts of EIS are denoted by  $Z_{Re}$  and  $Z_{Im}$ , respectively. The intercept of the Nyquist plot to the X-axis (i.e. real part) in the lower frequency region represents the solution resistance ( $R_s$ ), while the intercept in the higher frequency region represents the sum of a solution resistance ( $R_s$ ) and charge transfer resistance ( $R_{ct}$ ). Hence, the diameter of the semicircle is nothing but  $R_{ct}$ . All these characterization techniques are used to find out operating potential window, Cs, ED, PD, Coulombic efficiency and stability retention of SC.

## Theoretical background of LDH, synthesis methods, exfoliation and characterization techniques

### 2.6 References:

1. G. G. C. Arizaga, C. S. Jiménez, A. Viruete, J. A.-Quijada, In Tech, Janeza Terdine, 9, 51000, Rijeka, Croatia.
2. V. Rives, Layered double hydroxides: Present and future, Nova Science Publishers, Inc., New York, 2001.
3. J. L. Gunjekar, A. I. Inamdar, B. Hou, S. N. Cha, S. M. Pawar, A. Talha A. A., H. S. Chavan, J. Kim, S. Cho, S. Lee, Y. Jo, H. Kim, H. Im, *Nanoscale*, 2018, 10, 8953-8961.
4. R. Allmann, *Acta Cryst. B*24, 972, 1968.
5. J. Feng, Y. He, Y. Liu, Y. Du, D. Li, *Chem. Soc. Rev.*, 2015, 44, 5291-5319.
6. H. S. Panda, R. Srivastava, D. Bahadur, *Bull. Mater. Sci.*, 2011, 34, 1599-1604.
7. L. Zhang, J. Zhu, X. Jiang, D. G. Evans, F. Li, *J. Phys. Chem. Solids*, 2006, 67, 1678-1686.
8. T. Lopez, P. Bosch, E. Ramos, R. Gomez, O. Novaro, D. Acosta, F. Figueras, *Langmuir*, 1996, 12, 189-192.
9. M. Jitianu, D. C. Gunness, D. E. Aboagye, M. Zaharescu, A. Jitianu, *Mater. Res. Bull.*, 2013, 48, 1864-1873.
10. M. Ogawa, H. Kaiho, *Langmuir*, 2002, 18, 4240-4242.
11. P. P. Huang, C. Y. Cao, F. Wei, Y. B. Sun, W. G. Song, *RCS Adv.*, 2015, 5, 10412-10417.
12. J. He, M. Wei, B. Li, Y. Kang, D. G. Evans, X. Duan, 119. Springer, Berlin, Heidelberg.
13. F. Cavani, F. Trifirb, A. Vaccari, *Catal. Today*, 1991, 11, 173-301.
14. M. Lok, 2009, WILEY-VCH Verlag GmbH & Co. KGaA, Weinheim, ISBN: 978-3-527-32040-0.
15. E. Pomerantseva, Y. Gogotsi, *Nat. Energy.*, 2017, 2, 17089-17094.
16. C. Tan, X. Cao, X.-J. Wu, Q. He, J. Yang, X. Zhang, J. Chen, W. Zhao, S. Han, G.-H. Nam, M. Sindoro, H. Zhang, *Chem. Rev.*, 2017, 117, 6225-6331.
17. E. R. Hitzky, P. Aranda, M. Dardera, G. Rytwo, *J. Mater. Chem.*, 2010, 20, 9306-9321.
18. X. Jin, S.-J. Shin, J. Kim, N.-S. Lee, H. Kim, S.-J. Hwang, *J. Mater. Chem. A*, 2018, 6, 15237-15244.
19. B. J. Wang, G. Li, L. Li, Open access peer-reviewed chapter, 2016, 10.5772/63918.
20. S. M. Oh, S. B. Patil, X. Jin, S.-J. Hwang, *Chem. Eur. J.*, 2018, 24, 4757-4773.
21. C. Murugana, V. Sharma, R. K. Murugan, G. Malaimegud, A. Sundaramurthy, *J. Control. Release*, 2019, 10, 1-20.
22. Z. G. Shen, *J. Mater. Chem. A.*, 2015, 3, 11700-11715.
23. J. N. Coleman, *Science*, 2013, 334, 72-75.
24. K. Fukuda, J. Sato, T. Saida, W. Sugimoto, Y. Ebina, T. Shibata, M. Osada, T. Sasaki, *Inorg. Chem.*, 2013, 52, 2280-2282.
25. J. T. Han, J. I. Jang, H. Kim, J. Y. Hwang, H. K. Yoo, J. S. Woo, S. Choi, H. Y. Kim, H. J. Jeong, S. Y. Jeong, K.-J. Baeg, K. Cho, G.-W. Lee, *Sci. Rep.*, 2014, 4, 5133.
26. S. Xiong, X. Chen, Y. Liu, T. Fan, Q. Wang, H. Zhang, T. Chen, *J. Innov. Opt. Health Sci.*, 2020, 13, 2030008.
27. M. Xu, T. Liang, M. Shi, H. Chen, *Chem. Rev.*, 2013, 113, 3766-3798.

## Theoretical background of LDH, synthesis methods, exfoliation and characterization techniques

28. S. P. Kulkarni, A. S. Patil, V. V. Patil, U. M. Patil, J. L. Gunjekar, In: Ezema F. I., Lokhande C. D., Jose R. (eds) Chemically deposited nanocrystalline metal oxide thin films, Springer, Cham., ISBN: 978-3-030-68462-4, 2021.
29. J. Zhu, W. Sun, D. Yang, Y. Zhang, H. H. Hoon, H. Zhang, Q. Yan, *Small*, 2015, 11, 4123-4129.
30. M. A. Bizeto, A. L. Shiguihara, V. R. Constantino, *J. Mater. Chem.*, 2009, 19, 2512-2525.
31. E. R. Hitzky, P. Aranda, M. Dardera, G. Rytwo, *J. Mater. Chem.* 2010, 20, 9306-9321.
32. S. J. Kim, I. Y. Kim, S. B. Patil, S. M. Oh, N. S. Lee, S. J. Hwang, *Chem. Eur. J.*, 2014, 20, 5132-5140.
33. B. R. Ma, T. Sasaki, *Adv. Mater.*, 2010, 22, 5082-5104.
34. G. Hodes, Marcel Dekker Inc., New York, 2001, pp. 64.
35. B. Cullity, S. Stock, 3<sup>rd</sup> Ed<sup>n</sup>., Prentice Hall, New York, 2001.
36. B. D. Cullity, 2<sup>nd</sup> Edn., Addison- Wesley, London, 1978.
37. R. Vilar, Woodhead Publishing, 2016.
38. R. Nyquist, R. Kagel, Academic Press INC, New York, 2-6, 1971.
39. D. Titus, E. J. J. Samuel, S. M. Roopan, *Micro and Nano Technologies*, 2019, 303-319.
40. S. Spiegelberg, *UHMWPE Biomaterials Handbook*, Second Edition, 2009, 355-368.
41. [https://en.wikipedia.org/wiki/Fourier-transform\\_infrared\\_spectroscopy](https://en.wikipedia.org/wiki/Fourier-transform_infrared_spectroscopy)
42. B. C. Smith, Second Edn., CRC Press, Taylor & Francis Group, 6000 Broken Sound Parkway NW, Suite 300, Boca Raton, FL 33487-2742, 2011.
43. [https://www.google.com/url?sa=i&url=https%3A%2F%2Fen.wikipedia.org%2Fwiki%2Faman\\_spectroscopy&psig=A0vVaw39B2rgP01\\_bkzoU63tyu5z&ust=1618951622879000&source=images&cd=vfe&ved=2ahUKEwjgmLL0lovwAhUWsksfHWWeAGoQr4kDegUIARC1AQ](https://www.google.com/url?sa=i&url=https%3A%2F%2Fen.wikipedia.org%2Fwiki%2Faman_spectroscopy&psig=A0vVaw39B2rgP01_bkzoU63tyu5z&ust=1618951622879000&source=images&cd=vfe&ved=2ahUKEwjgmLL0lovwAhUWsksfHWWeAGoQr4kDegUIARC1AQ)
44. R. A. Nyquist, R. O. Kagel, Academic press, inc., 111 Fifth Avenue, New York, 10003, 1971.
45. G. S. Bumbrah, R. M. Sharm, *Egypt. J. Forensic Sci.*, 2016, 6, 209-215.
46. R. S. Das, Y. K. Agrawal, *Vib. Spectrosc.*, 2011, 57, 163-176.
47. R. R. Jones, D. C. Hooper, L. Zhang, D. Wolverson, V. K. Valev, *Nanoscale Res. Lett.*, 2019, 14, 231-265.
48. N. B. Colthup, L. H. Daly, S. E. Wiberley, 3rd ed., Academic Press, 542, 1990.
49. [https://serc.carleton.edu/msu\\_nanotech/methods/xps.html](https://serc.carleton.edu/msu_nanotech/methods/xps.html)
50. C. Battistoni, G. Mattocono, E. Paparazzo, *Surf. Interface Anal.*, 1985, 7, 117-121.
51. S. Kerber, T. Barr, G. Mann, W. Brantley, E. Papazoglou, J. Mitchell, *J. Mater. Eng. Perform.*, 1998, 7, 329-333.
52. <https://www.slideshare.net/faheemmaqsood/xray-photoelecctron-spectroscopy-xps>
53. [https://en.wikipedia.org/wiki/Energy-dispersive\\_X-ray\\_spectroscopy](https://en.wikipedia.org/wiki/Energy-dispersive_X-ray_spectroscopy)
54. <https://www.globalsino.com/EM/page4661.html>
55. T. D. Allen, 1<sup>st</sup> Edn., Kindle Edn., ISSN Book 88, 2008.
56. A.M.Paredes, *Encyclopedia of food microbiology* (second edition), 2014, 711-720.
57. <https://www.slideshare.net/damarisb/sem-n-tem>

## Theoretical background of LDH, synthesis methods, exfoliation and characterization techniques

- 
58. J. B. Condon, Elsevier Science; 1st edition, 296, 2006.
  59. <https://www.iitk.ac.in/che/pdf/resources/BET-TPX-Chemi-reading-material.pdf>
  60. Y. I. Nikitin, G. A. Petasyuk, J. Superhard Mater., 2008, 30, 58–70.
  61. L. Bayne, R. V. Ulijn, P. J. Halling, Chem. Soc Rev., 2013, 42 9000-10.
  62. R. Shah, D. Eldridge, E. Palombo, I. Harding, J. Phys. Sci., 2014, 25, 59–75.
  63. <https://www.iitk.ac.in/dordoldn/dynamic-light-scattering-particle-size-and-zeta-potential-analyzer>
  64. K. Dhamoon, H. Popli, G. Aggarwal, M. Gupta, Int. J. Drug Deliv., 2018, 10, 01-11.
  65. G. S. R. Raju, E. Pavitra, G. Nagaraju, N. R. Chodankar, S. K. Vishwanath, J. Y. Park, Y. S. Huh, Y.-K. Han, J. Mater. Chem. A, 2019, 7, 26893-26904.
  66. <https://www.slideshare.net/SihamAbdallaha/electrochemical-method-of-analysis-31352857>
  67. S. Dai, Y. Xi, C. Hu, X. Yue, L. Cheng, G. Wang, J. Power Sources, 2015, 274, 477-482.
  68. G. Luongo, F. Giubileo, L. Genovese, L. Iemmo, N. Martucciello, A. D. Bartolomeo, Nanomaterials, 2017, 7, 158.
  69. S. Dai, Y. Xi, C. Hu, X. Yue, L. Cheng, G. Wang, J. Power Sources, 2015, 274, 477-482.
  70. T. S. Mathis, N. Kurra, X. Wang, D. Pinto, P. Simon, Y. Gogotsi, Adv. Energy Mater. 2019, 9, 1902007-1902020.
  71. K. Fushimi, L. Neelakantan, G. Eggeler, A. W. Hassel, Phys. Status Solidi A, 2018, 215, 1800011-1800017.



# CHAPTER-3

**SYNTHESIS,  
CHARACTERIZATION AND  
ELECTROCHEMICAL  
PERFORMANCE OF Co-Cr-LDH,  
AND rGO Ns**

# CHAPTER-3

## Synthesis, Characterization and Electrochemical Performance of Co-Cr-LDH, and rGO Ns

Sr. No.	Title	Page No.
3.1	Introduction	75
3.2	Synthesis and characterization of Co-Cr-LDH, GO and rGO Ns	76
	3.2.1 Experimental details	76
	3.2.2 Chemicals	76
	3.2.3 Synthesis of Co-Cr-LDH	76
	3.2.4 Synthesis of GO Ns	77
	3.2.5 Synthesis of rGO Ns	77
3.3	Characterizations of Co-Cr-LDH, GO and rGO Ns	77
	3.3.1 XRD analysis of Co-Cr-LDH	78
	3.3.2 FTIR analysis of Co-Cr-LDH	79
	3.3.3 Raman analysis of Co-Cr-LDH	80
	3.3.4 FESEM analysis of Co-Cr-LDH	81
	3.3.5 EDS analysis of Co-Cr-LDH	81
	3.3.6 XPS analysis of Co-Cr-LDH	82
	3.3.7 N <sub>2</sub> adsorption-desorption (BET analysis) of Co-Cr-LDH	83
	3.3.8 XRD analysis of (Go and rGO)	84
3.4	Conclusions	84
3.5	Experimental set-up and electrode preparation	85
3.6	Electrochemical performance of Co-Cr-LDH	86
3.7	Results and discussion	86
	3.7.1 Cyclic voltammetry (CV) study	86
	3.7.2 Galvanostatic charge-discharge (GCD) study	88
	3.7.3 Electrochemical impedance spectroscopy (EIS) study	89
3.8	Electrochemical performance of rGO	90
	3.8.1 Cyclic voltammetry (CV) study	90
	3.8.2 Galvanostatic charge-discharge (GCD) study	91
	3.8.3 Electrochemical impedance (EIS) study	92
3.9	Conclusions	93
3.10	References	94

### **3.1 Introduction:**

Currently, CO<sub>2</sub> emissions are consistently increasing and causes global warming. Due to the consumption of fossil fuels, enormous CO<sub>2</sub> is emitted, which is the main environmental threat and is mainly responsible for the greenhouse effect. [1] Thus, clean, efficient, and sustainable renewable energy sources with energy transformation and storage technologies are needed to avoid environmental deterioration. [2] Renewable energy sources demand support of energy storage devices due to their intermittency response. SCs are attracting comprehensive research attention due to their high energy output, power capability, eco-friendly nature, and low fabrication cost. [3] Still, the SC has moderate ED values, which could not match the current necessity of electrical appliances, which is the prime need for modern life and economic development. [4] Therefore, researchers have made numerous efforts to enhance the ED of SCs. [5] Due to the attractive structural, redox-active, mechanical, and electronic properties, the transition metal oxides, carbides, nitrides, sulfides, hydroxides, etc. are received significant attention as active electrode materials for SCs. [6] The RuO<sub>2</sub> has been widely investigated for the SC study owing to its Cs (1500 F g<sup>-1</sup>), but its high cost and toxicity restricted its commercial use. [3]

Therefore many reports are available on the preparation of transition metal oxides (TMOs), conducting polymers, [7] and LDHs [8] as promising active materials for SC application. Furthermore, the LDH materials are explored for many advanced applications such as photocatalysis, carbon dioxide capture, flame retardant, drug carrier, polymer additive, etc. [9-12] On this backdrop, Co-Cr-LDH material was synthesized by co-precipitation method.

The present chapter deals with the synthesis of Co-Cr-LDH and rGO Ns. The preparative parameters like concentration of precursors, pH of solutions, aging time, reaction temperature, etc., were optimized to achieve highly crystalline Co-Cr-LDH. The prepared materials were characterized by various physic-chemical characterization techniques: XRD, FTIR, Raman, FESEM, EDS, XPS, and BET. The SC performance of Co-Cr-LDH and rGO Ns was tested by CV, GCD, and EIS techniques.

### 3.2 Synthesis and characterization of Co-Cr-LDH, GO and rGO Ns:

#### 3.2.1 Experimental details:

#### 3.2.2 Chemicals:

Cobalt nitrate ( $\text{Co}(\text{NO}_3)_2 \cdot 6\text{H}_2\text{O}$ ), chromium nitrate ( $\text{Cr}(\text{NO}_3)_3 \cdot 9\text{H}_2\text{O}$ ), sodium hydroxide ( $\text{NaOH}$ ), sodium nitrate ( $\text{NaNO}_3$ ), activated carbon, nitric acid ( $\text{HNO}_3$ ) polyvinylidene fluoride (PVDF) and N-methylpyrrolidone (NMP) were purchased from Sigma Aldrich chemical co. and utilized as it is. Stainless steel (SS) (304 grade) substrates were served as a current collector for the fabrication of SC electrodes.

#### 3.2.3 Synthesis of Co-Cr-LDH:

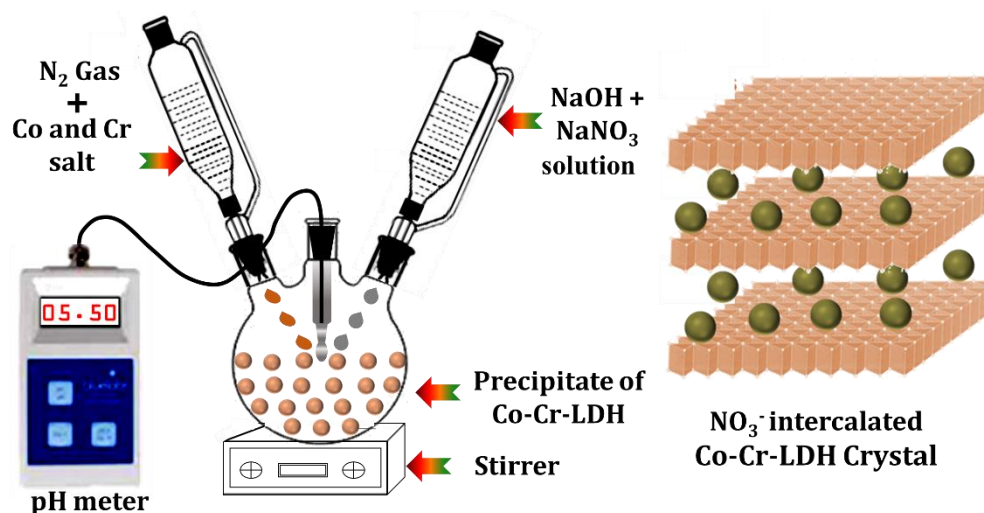


**Figure 3.1:** Schematic of co-precipitation method for the synthesis of Co-Cr-LDH.

The pristine Co-Cr-LDH was synthesized in the nitrate form using a conventional co-precipitation method (figure 3.1) at room temperature by Reichle process. [13] The aqueous solution A was made by mixing cobalt nitrate (0.06 M) and chromium nitrate (0.03 M) solutions with a molar ratio of 2:1. Similarly, the aqueous solution B was made by mixing sodium hydroxide (1 M) and sodium nitrate (1 M) aqueous solutions with a molar ratio of 1:1. Solutions A and B were dropwisely added together with an addition rate of 1 ml/min. The pH of the resultant slurry was adjusted at  $5.5 \pm 0.1$  by precise addition of solution B. This synthesis process was carried out under a  $\text{CO}_2$ -free  $\text{N}_2$  atmosphere with decarbonated water at room temperature to avoid  $\text{CO}_2$  contamination in the LDH. The resulting slurry was kept 24 h for aging at room temperature ( $28^\circ$ ), followed by washing at 6000 rpm (centrifuge), and repeatedly washed with decarbonated

## Synthesis, characterization and electrochemical performance of Co-Cr-LDH and rGO Ns

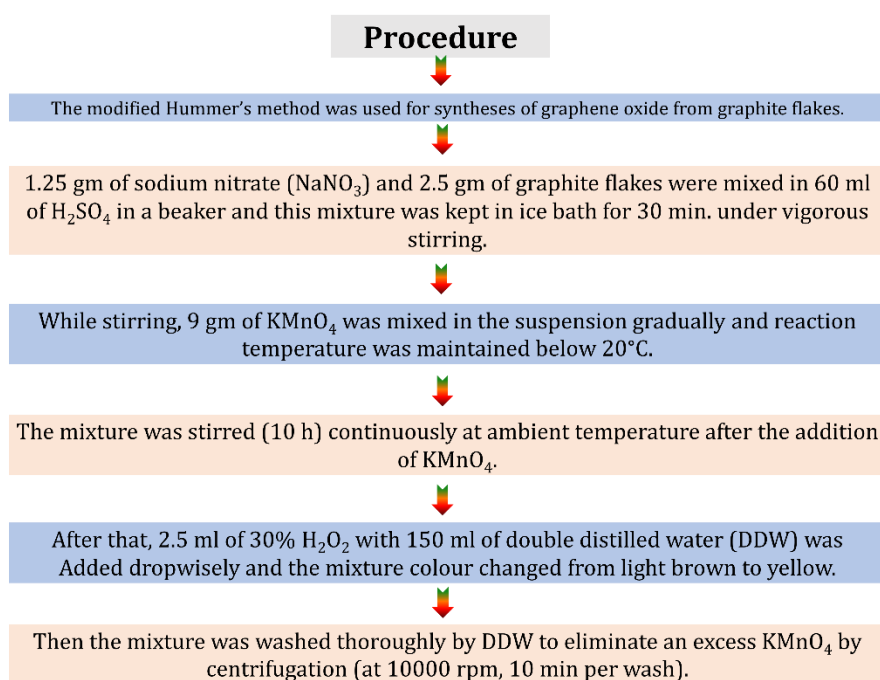
water. To ensure the solid form of Co-Cr-LDH sample, the resulting brown precipitate was freeze-dried at 10 °C for 30 h.

### 3.2.4 Synthesis of GO Ns:

**Chemicals:** Graphite flakes, NaNO<sub>3</sub>, sulfuric acid (H<sub>2</sub>SO<sub>4</sub>), potassium permanganate (KMnO<sub>4</sub>), hydrogen peroxide (H<sub>2</sub>O<sub>2</sub>) and potassium hydroxide (KOH) were purchased from Sigma-Aldrich. All the chemicals were of AR grade and used without further purification. [14]

### 3.2.5 Synthesis of rGO Ns:

The GO was synthesized by the modified Hummers methods, as described in the following flowchart. [15]



The rGO was synthesized by reducing the GO through the hydrothermal method. The well-dispersed 50 ml homogeneous suspension of GO (2 mg ml<sup>-1</sup>) was heated in a hydrothermal autoclave at 160 °C for 12h. Then the obtained rGO was freeze-dried for 48 h to eliminate water content and avoid aggregation of rGO.

### 3.3 Characterizations of Co-Cr-LDH, GO and rGO Ns:

The phase of the Co-Cr-LDH was studied by PXRD analysis using Rigaku miniflex-600 with Cu Kα<sub>1</sub> (λ= 0.15406 nm) radiation, operated at 30 kV, with scan-rate of 1° min<sup>-1</sup>. FTIR and Micro-Raman spectroscopic studies were executed to analyze the chemical bonding nature of the present LDH material. FTIR spectra was recorded on Bruker ALPHA II and Micro-Rama spectra was recorded on

## Synthesis, characterization and electrochemical performance of Co-Cr-LDH and rGO Ns

SENTERRA II Compact Raman microscope, using 532 nm wavelength with 2.5 mW power and a 50× objective. The morphology and stacking structure of Co-Cr-LDH was examined with FESEM (JEOL JSM-6700F) and HRTEM (JEOL JEM 2100F, 200 kV). Elemental composition of pristine Co-Cr-LDH was examined with EDS elemental mapping analysis. The surface area, pore structure and size distribution of pristine Co-Cr-LDH were investigated by N<sub>2</sub> adsorption-desorption isotherms at a temperature of -196.15 °C using gas sorption analyzer (BELSORP mini II, Japan). Before the above analysis, pristine Co-Cr-LDH was degassed at 140 °C in a vacuum below 10<sup>-3</sup> Torr for 8 h.

### 3.3.1 XRD analysis of Co-Cr-LDH:

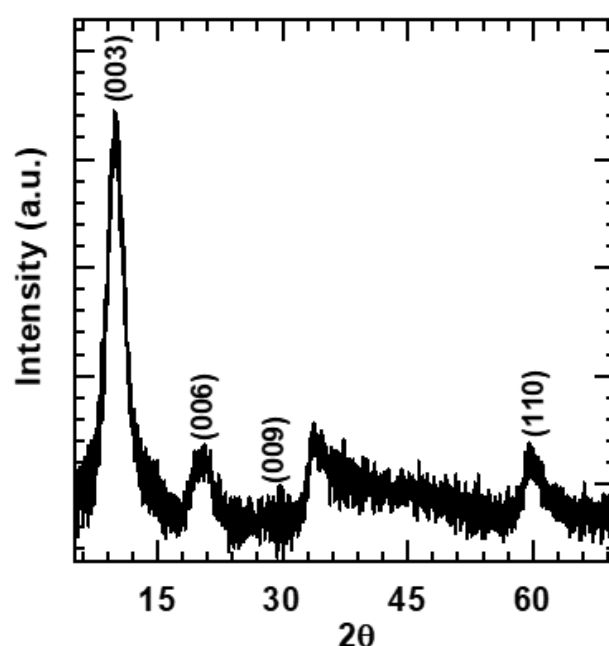


**Figure 3.2:** XRD pattern of Co-Cr-LDH.

Figure 3.2, the Co-Cr-LDH shows (001), (002), (003) and (110) Bragg reflections. These Bragg reflections are characteristics of the hexagonal crystal structure with R3m rhombohedral symmetry. The calculated lattice parameters  $a = b = 0.308$  nm and  $c = 0.88$  nm of the Co-Cr-LDH sample are well-matched to the NO<sub>3</sub><sup>-</sup> intercalated Co-Cr-LDH (JCPDS card: 38-0487). The interlayer spacing of 0.88 nm is higher than the reported interlayer spacing due to CO<sub>3</sub><sup>2-</sup> intercalated LDH ( $d_{003} = 0.75$  nm). [16-17] The crystallite size according to Scherrer's formula with FWHM for (003) plane is ~12 nm. Judging from the basal spacing of Co-Cr-LDH, the gallery height between the two consecutive Co-Cr(OH)<sub>2</sub> Ns is estimated as 0.48 nm. The Co-Cr-LDH sample showed an in-plane (110) peak and a broad hump at  $2\theta = \sim 60.2^\circ$  and  $2\theta = \sim 32^\circ$

to  $44^\circ$ , respectively, that are attributed to the development of in-plane hexagonal turbostatic crystal structure. [18] These results provide strong evidence of effective synthesis of Co-Cr-LDH with  $\text{NO}_3^-$  interlayer anions.

### 3.3.2 FTIR analysis of Co-Cr-LDH:

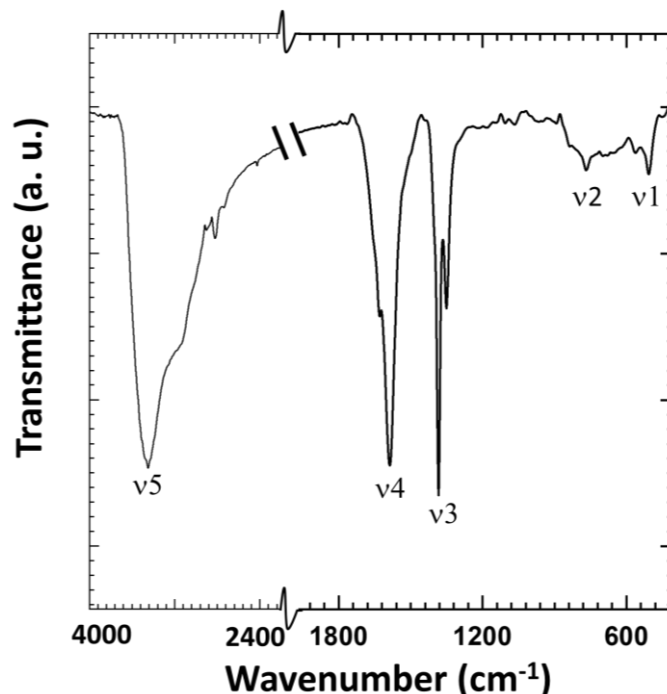


**Figure 3.3:** FTIR spectrum of Co-Cr-LDH.

Figure 3.3 shows the FTIR spectrum of the Co-Cr-LDH in the range of 400 to 4000  $\text{cm}^{-1}$ . The FTIR spectrum of Co-Cr-LDH displays strong and sharp absorption bands at  $\nu_1$  (514  $\text{cm}^{-1}$ ),  $\nu_2$  (770  $\text{cm}^{-1}$ ),  $\nu_3$  (1380  $\text{cm}^{-1}$ ),  $\nu_4$  (1600  $\text{cm}^{-1}$ ) and  $\nu_5$  (3465  $\text{cm}^{-1}$ ). The absorption bands at  $\nu_1$  (514  $\text{cm}^{-1}$ ) and  $\nu_2$  (770  $\text{cm}^{-1}$ ) are attributed to the metal-oxygen and metal-oxygen-hydrogen bending vibrations in the brucite-like Co-Cr-LDH phase, respectively. [19-20] The strong and sharp absorption band at  $\nu_3$  (1380  $\text{cm}^{-1}$ ) is attributed to the anti-symmetric stretching mode of intrasheet nitrate anions. [21-22] The broad absorption band at  $\nu_5$  (3546  $\text{cm}^{-1}$ ) and sharp band  $\nu_4$  (1610  $\text{cm}^{-1}$ ) are attributed to the stretching vibration of the H-bound O-H groups in Co-Cr-LDH and bending vibration of intergallery  $\text{H}_2\text{O}$ , respectively. [19] The presence of these bands confirmed the formation of Co-Cr-LDH with  $\text{NO}_3^-$  as interlayer anions and free water molecules.

### 3.3.3 Raman analysis of Co-Cr-LDH:

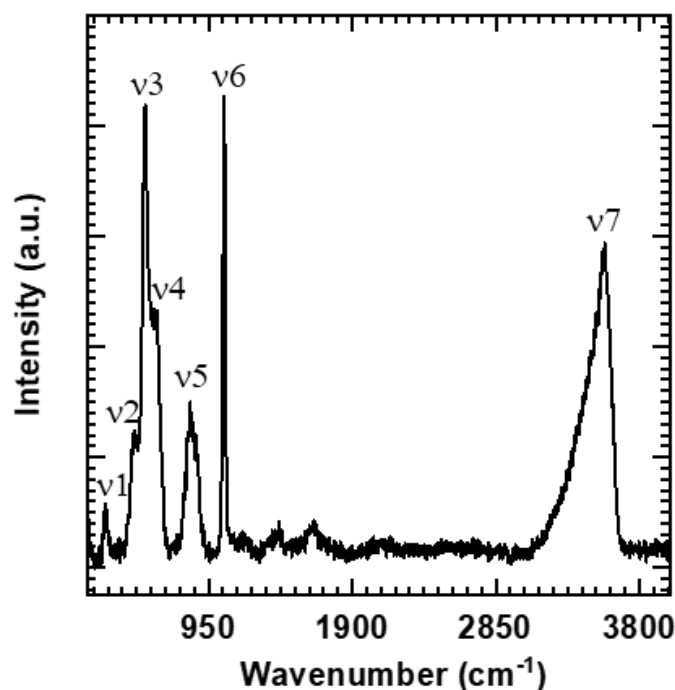


**Figure 3.4:** Micro-Raman spectrum of Co-Cr-LDH.

Figure 3.4 shows the Micro-Raman spectrum of Co-Cr-LDH. The Co-Cr-LDH display  $\nu_1$  to  $\nu_7$  Raman peaks attributed to the characteristic Raman shift from the Co-Cr-LDH, intercalated nitrate anions and water molecules. The peaks at  $\nu_1$  (265  $\text{cm}^{-1}$ ),  $\nu_2$  (455  $\text{cm}^{-1}$ ),  $\nu_3$  (530  $\text{cm}^{-1}$ ),  $\nu_4$  (600  $\text{cm}^{-1}$ ),  $\nu_5$  (840  $\text{cm}^{-1}$ ), and  $\nu_6$  (1055  $\text{cm}^{-1}$ ) are allocated to the lattice (metal-oxygen) translational vibrations ( $E_g$  mode), O-Co-O bending ( $A_{1g}$  mode), Co-O stretching ( $A_{2u}$  mode), Co-O rotational ( $E_g$  mode), symmetric/anti-symmetric Cr-OH stretching and symmetric stretching of  $\text{NO}_3^-$  modes, respectively. [23-30] The internal O-H stretching modes from the lattice OH and the intrasheet water molecules is displayed by the broad signature peak around  $\nu_7$  (3575  $\text{cm}^{-1}$ ). The  $\text{NO}_3^-$  intercalated Co-Cr-LDH phase with the incorporation of  $\text{H}_2\text{O}$  molecules is confirmed by the obtained Raman features.

### 3.3.4 FESEM analysis of Co-Cr-LDH:

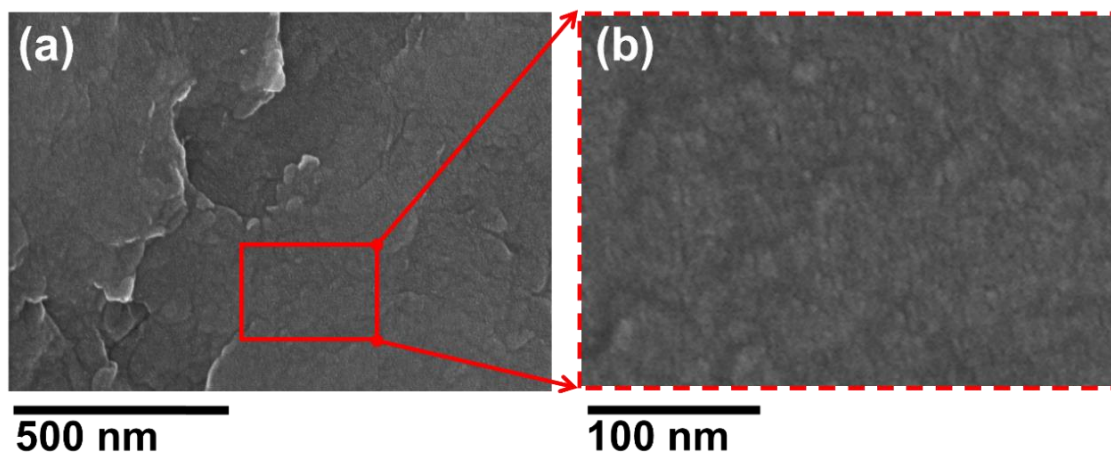


**Figure 3.5:** FESEM images (a) and (b) of Co-Cr-LDH.

The FESEM is used to probe the surface morphology of the Co-Cr-LDH. The FESEM micrographs of Co-Cr-LDH at 50 and 100 K magnifications are shown in figure 3.5. As displayed in figure 3.5, the Co-Cr-LDH displays compact-plate-shaped particles composed of densely stacked Co-Cr-(OH)<sub>2</sub> monolayers. The Co-Cr-LDH shows plate-like morphology due to the slow nucleation process during co-precipitation. A careful topographical examination of micrographs reveals the crystal size variation from ~230 to 450 nm. Such a coarse particle topography is commonly observed for co-precipitated hydroxide materials. [31]

### 3.3.5 EDS analysis of Co-Cr-LDH:

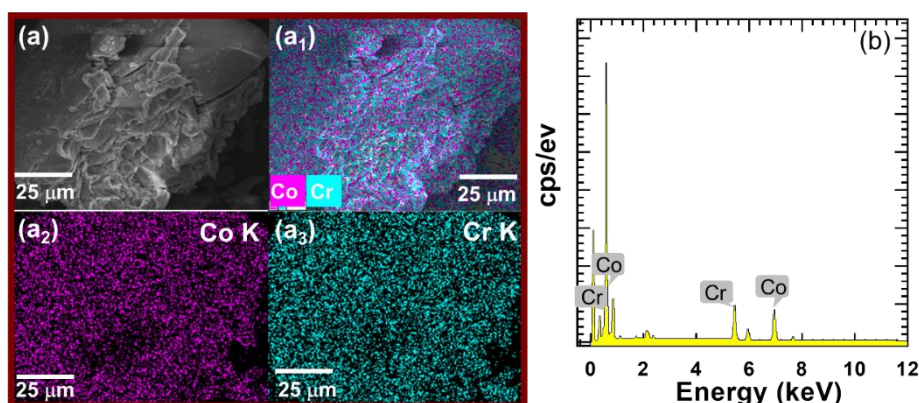


**Figure 3.6:** EDS-elemental mapping of Co-Cr-LDH, (a) FESEM image, (a<sub>1</sub>) mapped FESEM image, (a<sub>2</sub>) Co K elemental map and (a<sub>3</sub>) Cr K elemental map. (b) EDS spectrum of Co-Cr-LDH.

The spatial distributions of constituent elements in the Co-Cr-LDH at the nanometer scale are examined through an EDS elemental mapping analysis and EDS spectra. Figure 3.6 shows the EDS-elemental mapping images and EDS spectrum of Co-Cr-LDH. All of the constituent metal elements i.e. Co, Cr and O are

## Synthesis, characterization and electrochemical performance of Co-Cr-LDH and rGO Ns

uniformly spread within the entire part of the elemental mapping area of Co-Cr-LDH material which demonstrates the homogeneous distribution of the constituent element in Co-Cr-LDH without any phase separation. The EDS spectrum showed the Co:Cr ratio of ~2:1 in Co-Cr-LDH. From the EDS and elemental mapping analyses, the chemical composition of Co-Cr-LDH is estimated as  $\text{Co}_{0.65}\text{Cr}_{0.35}(\text{OH})_2 \cdot 0.35(\text{NO})_3 \cdot y\text{H}_2\text{O}$ .

### 3.3.6 XPS analysis of Co-Cr-LDH:

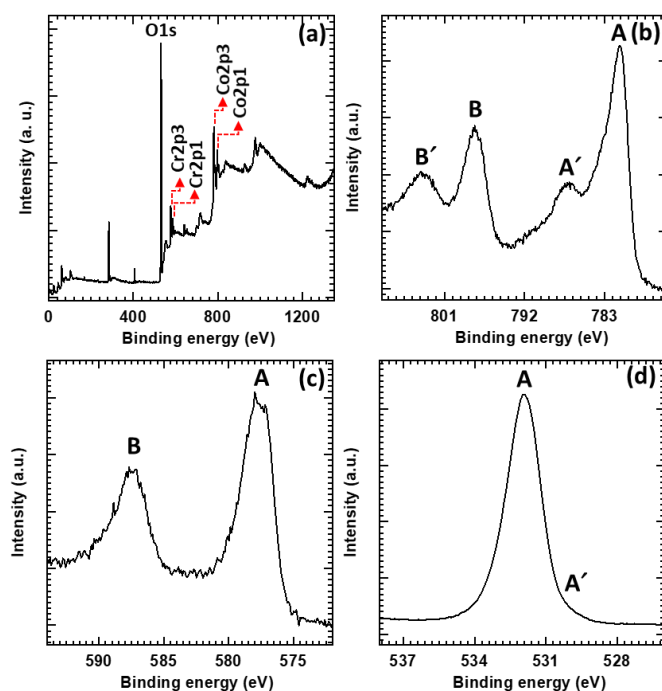


**Figure 3.7:** (a) Survey, (b) Co 2p, (c) Cr 2p and (d) O 1s XPS spectra of the Co-Cr-LDH.

The chemical composition of pristine Co-Cr-LDH is studied using XPS measurements, as shown in figure 3.7 (a). The survey XPS spectrum shows spectral features at binding energies of the element Co, Cr, and O in Co-Cr-LDH. As shown in figure 3.7 (b), Co-Cr-LDH exhibited two spectral features, A (781.2 eV) and B (797.4 eV), with their satellite peaks at A' (786.8 eV) and B' (803.2 eV), both of which are attributed to spin-orbit splitting into Co 2p<sub>3/2</sub> and Co 2p<sub>1/2</sub>, respectively. [20, 32] The binding energy difference (16.2 eV) of peaks A and B can be regarded as an indicator for Co<sup>+2</sup> in Co-Cr-LDH. As shown in figure 3.7 (c), the high-resolution Cr 2p spectrum shows A (577.6 eV) and B (587.3 eV) peaks, that arised due to spin orbit splitting of Cr 2p<sub>3/2</sub> and Cr 2p<sub>1/2</sub> components. [33-34] The binding energy of broad peak A is associated with the Cr<sup>3+</sup> attached with the intergallery ligands like OH<sup>-</sup> and H<sub>2</sub>O. [35-36] The O 1s XPS spectrum of Co-Cr-LDH is plotted in figure 3.7

(d). Interestingly, O 1s spectrum of Co-Cr-LDH demonstrates the broad peak A (531.9 eV) with a shoulder at A' (530.1 eV), indicating the presence of oxygen from metal hydroxide, surface hydroxyl group and bound water. The present XPS features clearly indicated that Co and Cr in Co<sup>+2</sup> and Cr<sup>+3</sup> oxidation states are present in Co-Cr-LDH.

### 3.3.7 N<sub>2</sub> adsorption-desorption (BET analysis) of Co-Cr-LDH:

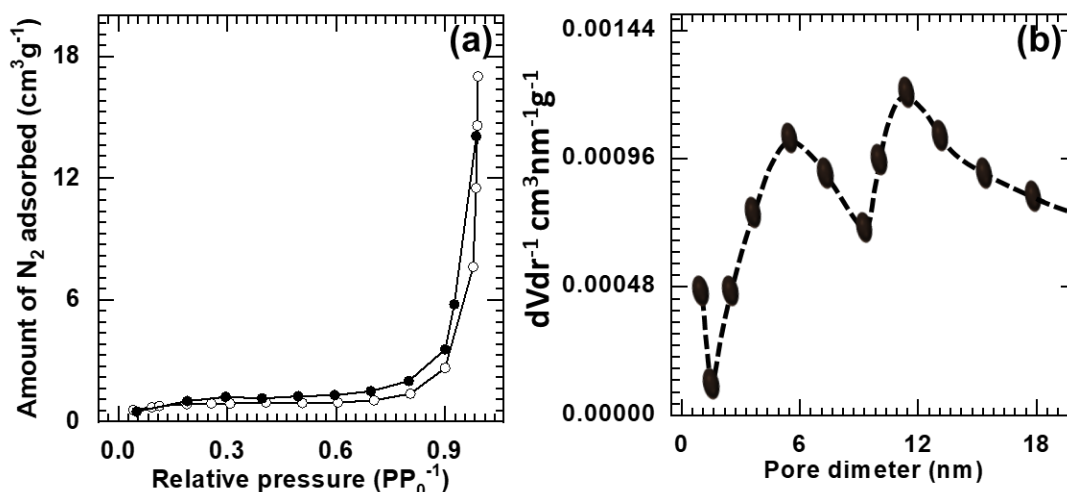


**Figure 3.8:** (a) N<sub>2</sub> adsorption-desorption isotherm and (b) Pore-size distribution curve for Co-Cr-LDH. In (a) the open symbols represent the adsorption and closed symbols represent desorption data.

The N<sub>2</sub> adsorption-desorption isotherm measurements were carried out to study the pore structure and specific surface area of the Co-Cr-LDH. As illustrated in figure 3.8 (a), Co-Cr-LDH exhibits mild and high N<sub>2</sub> adsorption in the low-pressure ( $PP_0^{-1} < 0.4$ ) and high-pressure region ( $PP_0^{-1} > 0.45$ ), respectively with BDDT shape. The presence of the type III isotherm is a characteristic of a nonporous material with low adsorption energy. [37-38] The surface area of Co-Cr-LDH is estimated from BET equation. The Co-Cr-LDH demonstrated the surface area of 5 m<sup>2</sup> g<sup>-1</sup>. The distribution of pore size is estimated by BJH method for the desorption branch, as shown in figure 3.8 (b). The Co-Cr-LDH shows an average pore diameter of ~31.23 nm that originates from random staking of sheets like LDH crystallite.

### 3.3.8 XRD analysis of GO and rGO:

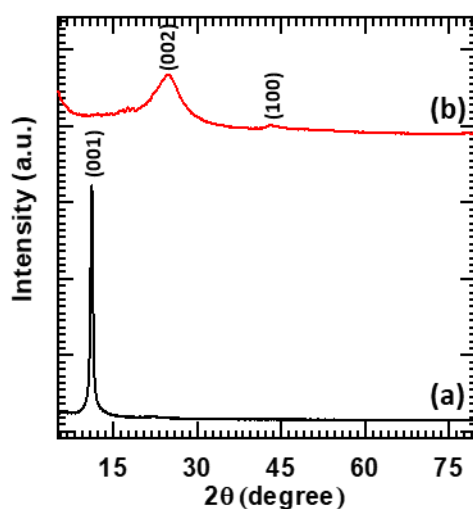


**Figure 3.9:** XRD patterns of (a) GO and (b) rGO.

The XRD patterns of GO and rGO are shown in figure 3.9. The highly intense peak (figure 3.9 (a)) at  $2\theta = 11^\circ$  corresponding to the (002) plane validates the formation of GO. GO sample shows a d-spacing of  $\sim 0.80$  nm calculated from the (002) plane position. This d-spacing is attributed to the intercalation of the oxygen-containing functional groups into the layers. [39] The XRD pattern of rGO is shown in figure 3.9 (b). The broad peak at  $24.4^\circ$  and  $42.9^\circ$  observed in the XRD pattern corresponds to (002) and (100) planes of rGO. The rGO displays a d-spacing of  $\sim 0.36$  nm calculated from the (002) plane position. Thus, reduced d-spacing confirms compact stacking of GO Ns due to the removal of oxygen-containing groups and indicates the formation of multilayered rGO Ns. [40]

### 3.4 Conclusions:

In conclusion, nitrate intercalated Co-Cr-LDH phase was synthesized by the simple co-precipitation method. The obtained sample was characterized for structural and surface morphological study by powder XRD and FESEM. Structural study of Co-Cr-LDH revealed the layered arrangement of Co-Cr-(OH)<sub>2</sub> Ns stacked together with nitrate anions and water molecule. Surface morphological study demonstrated compact morphology of Co-Cr-LDH with average particle size of  $\sim 230$  nm to 500 nm. Moreover, the obtained sample was characterized by FTIR, Raman, FESEM, EDS, XPS, and BET analysis techniques to study chemical bonding, surface topographical features, elemental distribution, chemical states and surface area with a pore-size distribution, respectively. The FTIR and Raman study

## Synthesis, characterization and electrochemical performance of Co-Cr-LDH and rGO Ns

confirmed the presence of nitrate anion. Also, present results indicate the successful formation of a GO by hummers method and rGO by hydrothermal reduction method. Moreover, rGO shows an intense high peak at  $2\theta = 24.4^\circ$  with a reduction of d-spacing compared to GO. These results clearly demonstrate the removal of oxygen-containing groups and the formation of multilayered rGO.

### 3.5 Experimental set-up and electrode preparation:

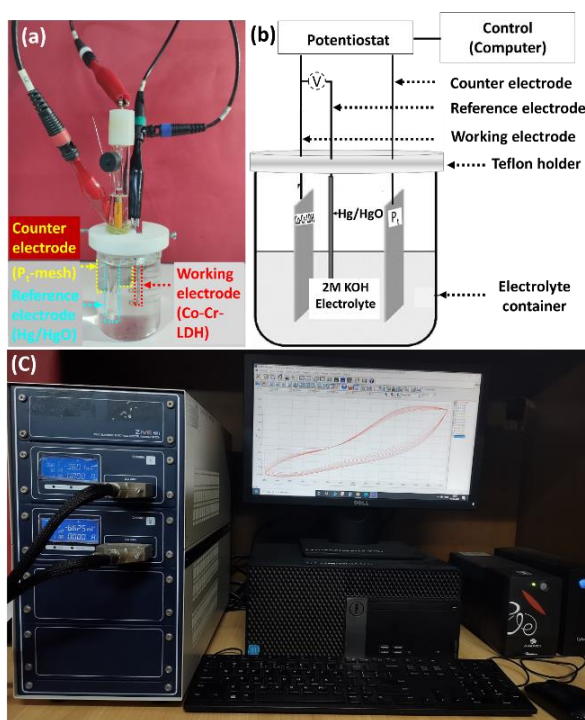


**Figure 3.10:** (a) Photograph of the three-electrode experimental set-up. (b) Schematic of three-electrode cell with electrochemical workstation. (c) Photograph of an electrochemical workstation.

Figure 3.10 shows photograph of the three-electrode experimental set-up, schematic of a three-electrode cell attached to an electrochemical workstation and a photograph of an electrochemical workstation. The electrode performance of the Co-Cr-LDH and rGO electrodes are examined with CV, GCD, EIS analysis. The data were collected with a conventional three-electrode cell using a ZIVE MP1 multichannel electrochemical workstation.

**Electrode preparation:** The Co-Cr-LDH electrode was prepared by mixing the active material (Co-Cr-LDH), acetylene black and poly(vinylidene difluoride) (PVDF) with a mass ratio of 80:15:5 in n-methyl-2-pyrrolidone (NMP) until it becomes a homogeneous slurry with proper viscosity. The resultant paste was then homogeneously coated on a cleaned SS substrate of  $1 \text{ cm}^2$  area and vacuum dried at  $80^\circ \text{C}$  for 12 h. [41]

## Synthesis, characterization and electrochemical performance of Co-Cr-LDH and rGO Ns

For the conventional three-electrode electrochemical cell, the Co-Cr-LDH deposited on SS substrate, Hg/HgO, and a platinum mesh were used as a working, reference and counter electrodes, respectively. An aqueous solution of 2 M KOH was used as an electrolyte. The CV data were obtained in 0.05 to +0.6 V vs Hg/HgO potential window with sweep rate of 4 to 100 mV s<sup>-1</sup>. The GCD data were obtained at 1–5 A g<sup>-1</sup>. EIS measurements were carried out in the frequency range of 0.01–10<sup>5</sup> Hz. The C<sub>sp</sub> and C<sub>s</sub> are calculated by using the following equation.

$$C_{sp} = \frac{I\Delta t}{m} \quad (3.1)$$

$$C_s = \frac{I}{m} \frac{\Delta t}{\Delta V} \quad (3.2)$$

Where, C<sub>sp</sub> is the specific capacity (C g<sup>-1</sup>), C<sub>s</sub> is specific capacitance (F g<sup>-1</sup>), I is current density (mA cm<sup>-2</sup>), m is mass of active material (mg) and ΔV is potential window (V).

### 3.6 Electrochemical performance of Co-Cr-LDH:

### 3.7 Results and discussion:

#### 3.7.1 Cyclic voltammetry (CV) study:

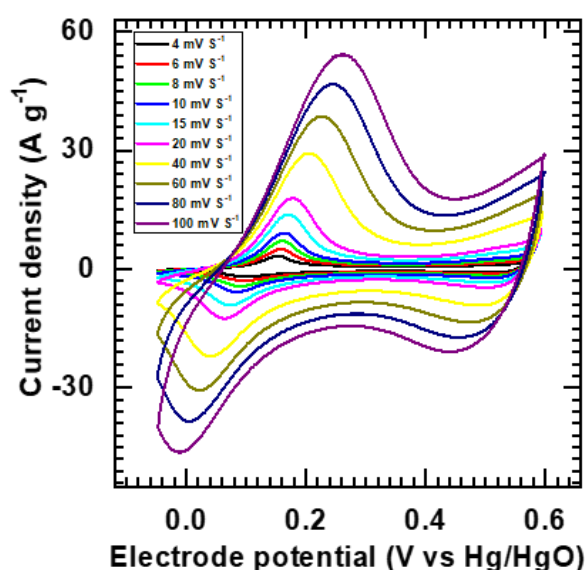


**Figure 3.11:** The CV curves of Co-Cr-LDH at various scan rates (4-100 mV s<sup>-1</sup>). Figure 3.11 presents the CV curves of Co-Cr-LDH at various scan rates (4 mV s<sup>-1</sup> to 100 mV s<sup>-1</sup>) in a 2 M KOH electrolyte. The Co-Cr-LDH electrode showed pairs of apparent redox peaks at 0.015 V, suggesting the electrochemical charge storage mechanism such as capacitive and diffusion-controlled types. The redox peaks are discernible at 0.015 V for the reference Co-Cr-LDH that are assigned to the quasi

reversible oxidation-reduction reactions between  $\text{Co}(\text{OH})_2$  and  $\text{CoOOH}$  transformation, which is represented in following reaction:



As presented in figure 3.11, the redox peak current and area under CV curves increase with scan rates. The shifting of a cathodic peak with scan rate towards more positive potential indicates both capacitive and diffusion-controlled type charge storage mechanisms in Co-Cr-LDH. The contribution of each can be resolved by the electrochemical kinetics study via following relation,

$$Q_t = Q_s + cv^{-\frac{1}{2}} \quad (3.4)$$

In this equation,  $Q_t$ ,  $Q_s$ ,  $c$ , and  $v$  are the total voltammetric charge, surface capacitive charge, constant, and scan rate, respectively. The surface capacitive charge ( $Q_s$ ) can be resolved by  $Q_t$  vs  $(v)^{-1/2}$  (figure 3.12) plot and deducing  $v$  to infinity by assuming semi-infinite linear diffusion, within a reasonable range of sweep rates.

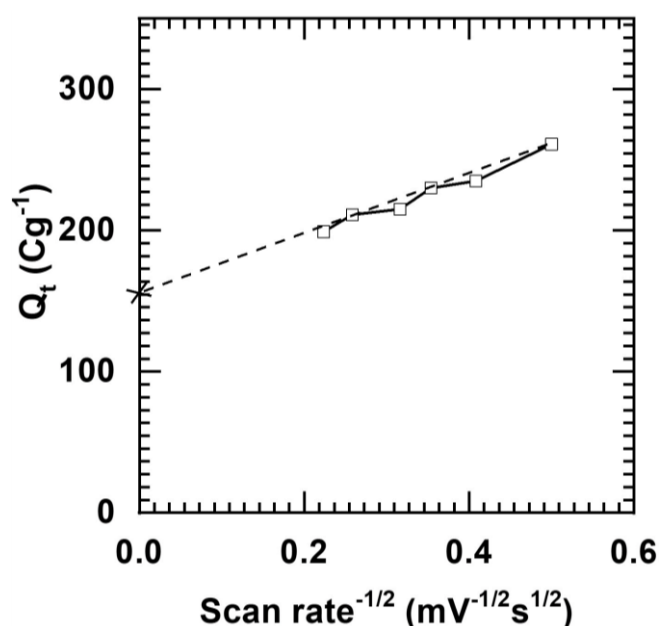


**Figure 3.12:** Plot of total charge ( $Q_t$ ) vs the reciprocal of the square root of the scan rate ( $v^{-1/2}$ ).

The high scan rates above  $20 \text{ mV s}^{-1}$  are ignored in the fitting to avoid the polarization effect. [42] Figure 3.13 shows the fractions of capacitive and diffusion-controlled contributions of Co-Cr-LDH represented by solid-filled and pattern-filled columns, respectively. The Co-Cr-LDH electrode shows that capacitive charge ( $Q_s$ ) is prominent at a high scan rate, whereas the diffusion-controlled ( $Q_d$ ) charge is prominent at a low scan rate. The Co-Cr-LDH shows the capacitive contributions

## Synthesis, characterization and electrochemical performance of Co-Cr-LDH and rGO Ns

of 58 % and 76 % at a scan rate of  $4 \text{ mV s}^{-1}$  and  $20 \text{ mV s}^{-1}$ , respectively. The Co-Cr-LDH has a high percentage of surface atoms and high efficient active sites on the surface layer; thus, Co-Cr-LDH shows the more capacitive dominant reaction at a high scan rate. [43]

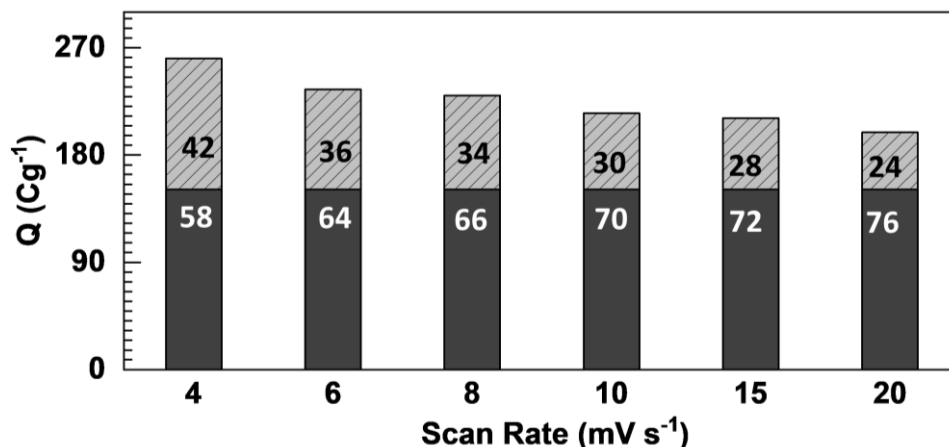


**Figure 3.13:** The fraction of the capacitive contribution of Co-Cr-LDH (solid) and diffusion-controlled contribution of Co-Cr-LDH (pattern) (values in bar assigned for the respective percentage contributions).

### 3.7.2 Galvanostatic charge-discharge (GCD) study:

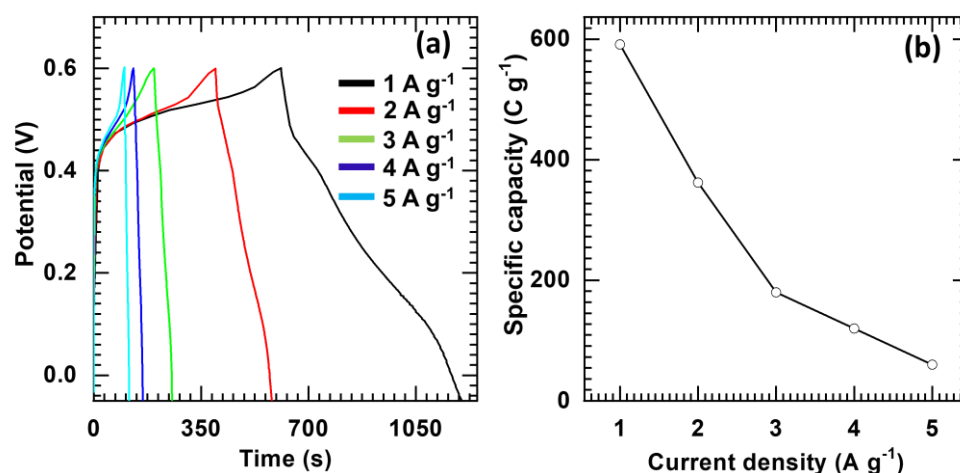


**Figure 3.14:** (a) GCD plot of the Co-Cr-LDH at various current densities ( $1 - 5 \text{ A g}^{-1}$ ). (b) The variation of  $C_{sp}$  of Co-Cr-LDH electrode with current density ( $1 - 5 \text{ A g}^{-1}$ ).

The electrode performance of Co-Cr-LDH was evaluated by GCD measurements. Figure 3.14 (a) represents GCD curves of the Co-Cr-LDH, measured at various current densities ( $1-5 \text{ A g}^{-1}$ ). The Co-Cr-LDH electrode exhibits characteristic nonlinear GCD curves with some curvature due to reversible Faradaic reactions. To probe the charge transfer kinetics, GCD performance of Co-Cr-LDH was tested at various current densities from  $1-5 \text{ A g}^{-1}$ , as shown in figure

3.14 (b). The Co-Cr-LDH displays a Csp of 591 C g<sup>-1</sup> at 1 A g<sup>-1</sup> that decrease to 60 C g<sup>-1</sup> at 5 A g<sup>-1</sup>. The decrease of Csp of Co-Cr-LDH at high current density indicates the slow charge transfer kinetics of the electrode. Thus efforts are escalated to improve the electrode performance of Co-Cr-LDH by making various nanohybrids in this study.

### 3.7.3 Electrochemical impedance spectroscopy (EIS) study:

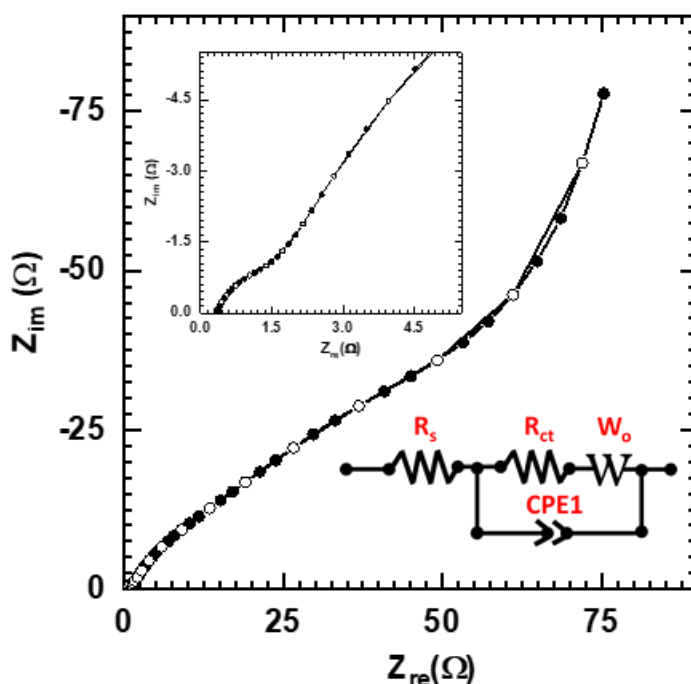


**Figure 3.15:** Nyquist plot of Co-Cr-LDH electrode with the best fitted equivalent circuit, inset (high frequency region EIS spectrum).

The charge carriage rate of Co-Cr-LDH is further studied with EIS analysis, and the corresponding Nyquist plot is presented in figure 3.15. The Co-Cr-LDH electrode commonly exhibits a semicircle and straight line in the high-frequency and low-frequency region, respectively. The starting point of the Nyquist plot represents series resistance ( $R_s$ ) and diameter of extrapolated semicircle represents charge transfer resistance ( $R_{ct}$ ). The Co-Cr-LDH showed a small semicircle radius in the Nyquist plot, which clearly indicates rapid and easy charge transfer kinetics. Thus, the size of the semicircle in Co-Cr-LDH is directly correlated with the electrical conductivity of the Co-Cr-LDH electrode. From the curve simulation and fitting analysis, the Co-Cr-LDH electrode shows  $R_s$  and  $R_{ct}$  values such as 0.36  $\Omega$  and 95  $\Omega$ , respectively. Co-Cr-LDH displays a stiff slope of the straight line in the low-frequency region. The observed stiff slope due to electrolyte ion diffusion of Co-Cr-LDH electrode confirms its lower resistance (Warburg

impedance). The noteworthy electrode performance of Co-Cr-LDH is attributed to its unique layered structure, a high percentage of electroactive surface atoms, and plenty of electroactive sites.

### 3.8 Electrochemical performance of rGO:

#### 3.8.1 Cyclic voltammetry (CV) study:

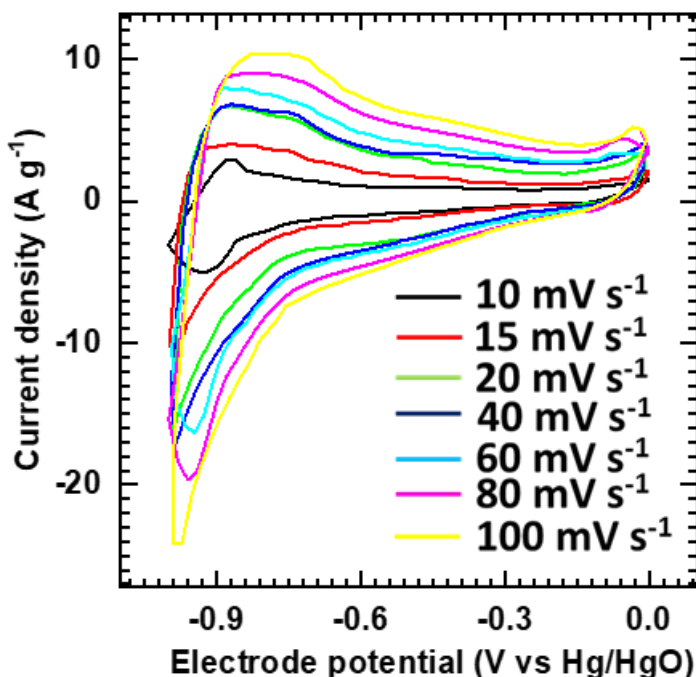


**Figure 3.16:** The CV curves of rGO at various scan rates (10–100 mV s<sup>-1</sup>).

The CV plot of rGO electrode at various scan rates (10–100 mV s<sup>-1</sup>) in the potential range of 0 to -1 V vs Hg/HgO in 2 M KOH electrolyte are represented in figure 3.16. The quasi-rectangular shape of CV plot confirms charge storage like EDLC-type in the rGO electrode. Also, large and symmetric current responses in anodic and cathodic directions are observed, representing the EDLC-type nature of the rGO electrode. Furthermore, the area enclosed in the CV plot increases with increasing sweep rate. This shows that voltammetric current is proportional to the scan rate of CV.

3.8.2 Galvanostatic charge–discharge (GCD) study:

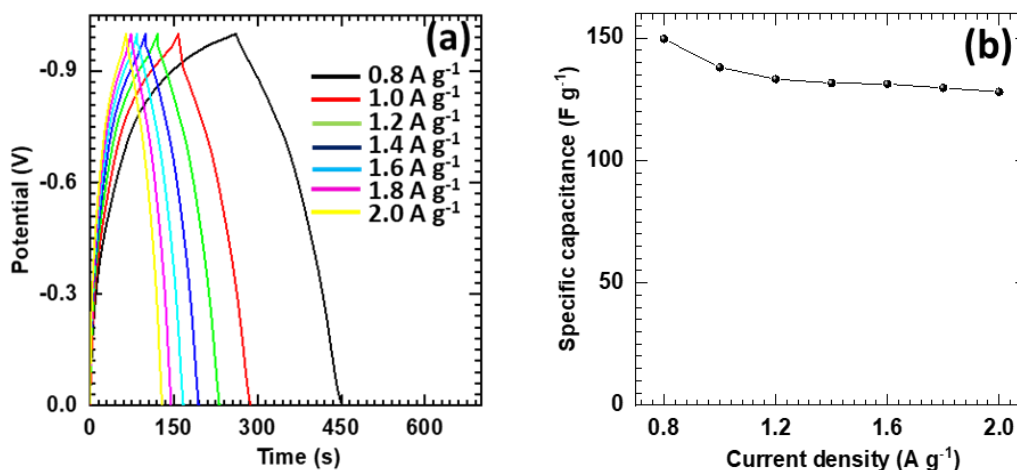


**Figure 3.17:** (a) The GCD curves and (b) Cs of the rGO at various current densities (0.8 – 2 A g<sup>-1</sup>).

The GCD study of rGO electrode is carried out in the potential window of 0 to -1 V vs Hg/HgO and shown in figure 3.17 (a). The nearly linear charge-discharge curves are obtained for the rGO electrode, which shows its EDLC-type nature. The Cs of the rGO electrode calculated by GCD analysis is plotted in figure 3.17 (b) with respective current densities (0.8-2 A g<sup>-1</sup>). As plotted in figure 3.17 (b), the rGO electrode exhibits a Cs of 149 F g<sup>-1</sup> at 0.8 A g<sup>-1</sup> that decreased to 128 F g<sup>-1</sup> at 2 A g<sup>-1</sup>. [44, 45] The rGO electrode maintains good electrode performance at high current densities indicating its high rate capability.

3.8.3 Electrochemical impedance spectroscopy (EIS) study:

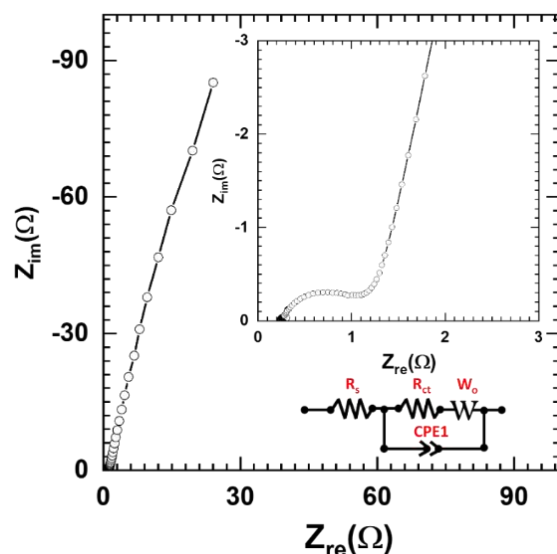


**Figure 3.18:** Nyquist plot of rGO electrode with the best fitted equivalent circuit, inset (high frequency region EIS spectrum).

The Nyquist plot of the rGO electrode is shown in figure 3.18. The fitted equivalent circuit in inset with components of solution resistance ( $R_s$ ), charge transfer resistance ( $R_{ct}$ ), constant phase element (CPE1) and Warburg resistance ( $W_o$ ). The solution resistance ( $R_s$ ) of rGO is  $0.22 \Omega$ , and charge transfer resistance ( $R_{ct}$ ) is  $1.27 \Omega$ . The small  $R_s$  and  $R_{ct}$  values indicate excellent electrical conductivity of the rGO electrode.

### **3.9 Conclusions:**

In conclusion, the electrochemical performance of Co-Cr-LDH was tested by a three-electrode system in a 2 M KOH aqueous electrolyte. The Co-Cr-LDH electrode exhibited a redox-type charge storage mechanism with a  $C_{sp}$  of  $591 \text{ C g}^{-1}$  at  $1 \text{ A g}^{-1}$ . The Co-Cr-LDH showed 58 % and 76 % capacitive contribution at scan rates of  $4 \text{ mV s}^{-1}$  and  $20 \text{ mV s}^{-1}$ , respectively. The good supercapacitive activity of the Co-Cr-LDH electrode is owing to the typical layered structure of Co-Cr-LDH and in which electrochemically active Co and Cr have a significant impact on the supercapacitive activity of Co-Cr-LDH. Moreover, the rGO electrode displays charge storage mechanism like EDLC-type with a  $C_s$  of  $149 \text{ F g}^{-1}$  at  $0.8 \text{ A g}^{-1}$ .

## Synthesis, characterization and electrochemical performance of Co-Cr-LDH and rGO Ns

### 3.10 References:

1. M. F. Demirbas, K. Bozbas, M. Balat, *Energy Explor. Exploit.*, 2004, 22, 355–366.
2. G. Wang, L. Zhang, J. Zhang, *Chem. Soc. Rev.*, 2012, 41, 797-828.
3. G. S. Gund, D. P. Dubal, S. B. Jambure, S. S. Shinde, C. D. Lokhande, *J. Mater. Chem. A*, 2013, 1, 4793-4803.
4. A. Bello, M. Fabiane, D. Y. Momodu, S. Khamlich, J. K. Dangbegnon, N. Manyala, *J. Solid State Chem.*, 2014, 18, 2359–2365.
5. A. Bello, K. Makgopa, D. Fabiane, K. D.-Ahrin, I. Ozoemena, N. Manyal, *J. Mater. Sci.*, 2013, 48, 6707–6712.
6. A. Tyagi, K. M. Tripathia, R. K. Gupta, *J. Mater. Chem. A*, 2015, 3, 22507-22541.
7. J. L. Gunjakar, A. I. Inamdar, B. Hou, S. N. Cha, S. M. Pawar, A. A. Abu Talha., H. S. Chavan, J. Kim, S. Cho, S. Lee, Y. Jo, H. Kim, H. Im, *Nanoscale*, 2018, 10, 8953-8961.
8. T.-H. Gu, J. L. Gunjakar, I. Y. Kim, S. B. Patil, J. M. Lee, X. Jin, N.-S. Lee, S.-J. Hwang, *Small*, 2015, 11, 3921-3931.
9. J. L. Gunjakar, T. W. Kim, H. N. Kim, I. Y. Kim, S. -J. Hwang, *J. Am. Chem. Soc.*, 2011, 133, 14998–15007.
10. J. L. Gunjakar, T. W. Kim, I. Y. Kim, J. M. Lee, S.-J. Hwang, *Sci. Rep.*, 2013, 3, 2080.
11. J. L. Gunjakar, I. Y. Kim, J. M. Lee, N.-S. Lee, S.-J. Hwang, *Energy Environ. Sci.* 2013, 6, 1008–1017.
12. J. L. Gunjakar, I. Y. Kim, S. J. Hwang, *Eur. J. Inorg. Chem.*, 2015, 1198-1202.
13. W. Reichle, *Solid State Ion.*, 1986, 22, 135-141.
14. B. Paulchamy, G. Arthi, B. D. Lignesh, *J Nanomed. Nanotechnol.*, 2015, 6, 1000253-1000256.
15. W. S. Hummers, R. E. Offema, *Preparation of Graphitic Oxide*, *J. Am. Chem. Soc.* 208 (1957) 1937.
16. L. Tian, Y. Zhao, S. He, M. Wei, X. Duan, *Chem. Eng. J.*, 2012, 184, 261-267.
17. Z. Liu, R. Ma, Y. Ebina, N. Iyi, K. Takada, T. Sasaki, *Langmuir*, 2007, 23, 861-867.
18. R. Ma, Z. Liu, L. Li, N. Iyi, T. Sasaki, *J. Mater. Chem.*, 2006, 16, 3809–3813.
19. S. K. Kiran, M. Padmini, H. T. Das, P. Elumalai, *J. Solid State Electrochem.*, 2017, 21, 927-938.
20. R. A. Nyquist, R. O. Kagel, *Academic Press*, New York, 1971.
21. M. Aureliano, C. A. Ohlin, M. O. Vieira, M. P. M. Marques, W. H. Casey, L. Carvalho, *Dalton Trans.*, 2016, 45, 7391-7399.
22. R. L. Frost, K. L. Erickson, M. L. Weier, O. Carmody, *Spectrochim. Acta. A Mol. Biomol. Spectrosc.*, 2005, 61, 829-834.
23. S. K. Kiran, M. Padmini, H. T. Das, P. Elumalai, *J. Solid State Electrochem.*, 2017, 21, 927-938.
24. J. L. Gunjakar, B. Hou, A. I. Inamdar, S. M. Pawar, A. T. A. Ahmed, H. S. Chavan, J. Kim, S. Cho, S. Lee, Y. Jo, S.-J. Hwang, T. G. Kim, S. N. Cha, H. Kim, H. Im, *Small*, 2018, 14, 1703481.
25. J. Yang, H. Liu, W. N. Martens, R. L. Frost, *J. Phys. Chem. C*, 2010, 114, 111-119.
26. S. R. Shieh, T. S. Duffy, *Phy. Rev. B* 2002, 66, 134301.
27. J. A. Koza, C. M. Hull, Y. C. Liu, J. A. Switzer, *Chem. Mater.*, 2013, 25, 1922-1926.

## Synthesis, characterization and electrochemical performance of Co-Cr-LDH and rGO Ns

---

28. I. M. B. Nielsen, M. D. Allendorf, *J. Phys. Chem. A*, 2006, 110, 4093-4099.
29. J. Yang, W. N. Martens, R. L. Frost, *J. Raman Spectrosc.*, 2011, 42, 1142-1146.
30. A. S. O. Gomes, N. Yaghini, A. Martinelli, E. Ahlberg, *J. Raman Spectrosc.*, 2017, 48, 1256-1263.
31. M. Ma, C. Zhang, G. Huang, B. Xing, Y. Duan, X. Wang, Z. Yang, C. Zhang, *J. Nanomater.*, 2015, 16, 269.
32. J. Yang, H. Liu, W. N. Martens, R. L. Frost, *J. Phys. Chem. C*, 2010, 114, 111-119.
33. M. C. Biesinger, C. Brown, J. R. Mycroft, R. D. Davidson, N. S. McIntyre, *Surf. Interface Anal.*, 2004, 36, 1550-1563.
34. J. Yang, A. G. Baker, H. Liu, W. N. Martens, R. L. Frost, *J. Mater. Sci.*, 2010, 45, 6574-6585.
35. S. Wu, X. Yang, J. Hu, H. Ma, Z. Lin, C. Hu, *Cryst. Eng. Comm.*, 2015, 17, 1625-1630.
36. G. Silversmit, D. Depla, H. Poelman, G. B. Marin, R. D. Gryse, *J. Electron Spectrosc.*, 2004, 135, 167-175.
37. J. L. Gunjaker, I. Y. Kim, J. M. Lee, Y. K. Jo, S. J. Hwang, *J. Phys. Chem. C*, 2014, 118, 3847-3863.
38. J. T. Kloprogge, D. Wharton, L. Hickey, R. L. Frost, *Am. Mineral.*, 2002, 87, 623-629.
39. X. Jiao, Y. Qiu, L. Zhang, X. Zhang, *RSC Adv.*, 2017, 7, 52337.
40. P. Xu, K. Ye, D. Cao, J. Huang, T. Liu, K. Cheng, J. Yin, G. Wang, *J. Power Sources*, 2014, 268, 204-211.
41. P. Y. Chuang, C. C. Hu, *Mater. Chem. Phys.*, 2005, 92, 138-145.
42. S. D. Perera, X. Ding, A. Bhargava, R. Hovden, A. Nelson, L. F. Kourkoutis, R. D. Robinson, *Chem. Mater.*, 2015, 27, 7861-7873.
43. X. Li, D. Du, Y. Zhang, W. Xing, Q. Xue, Z. Yana, *J. Mater. Chem. A*, 2017, 5, 15460-15485.
44. W. S. Hummers, R. E. Offeman, *J. Am. Chem. Soc.*, 1958, 80, 1339.
45. S. S. Patil, D. P. Dubal, V. G. Deonikar, M. S. Tamboli, J. D. Ambekar, P. Gomez-Romero, S. S. Kolekar, B. B. Kale, D. R. Patil, *ACS Appl. Mater. Interfaces*, 2016, 8, 31602-31610.



# CHAPTER-4

**SYNTHESIS,  
CHARACTERIZATION AND  
ELECTROCHEMICAL  
PERFORMANCE OF Co-Cr-LDH-  
POV AND AHSC DEVICE**

# CHAPTER-4

## Synthesis, Characterization and Electrochemical Performance of Co-Cr-LDH-POV and AHSC device

Sr. No.	Title	Page No.
4.1	Introduction	97
4.2	Synthesis and characterization of Co-Cr-LDH-POV	98
4.3	Experimental details	98
	4.3.1 Chemicals	98
	4.3.2 Synthesis of Co-Cr-LDH-POV	98
4.4	Characterizations of Co-Cr-LDH-POV	100
	4.4.1 Zeta potential measurement	100
	4.4.2 XRD analysis	100
	4.4.3 FTIR analysis	102
	4.4.4 Raman analysis	103
	4.4.5 FESEM analysis	105
	4.4.6 EDS analysis	106
	4.4.7 XPS analysis	107
	4.4.8 TEM analysis	109
	4.4.9 N <sub>2</sub> adsorption-desorption (BET) analysis	111
4.5	Conclusions	113
4.6	Electrochemical performance of Co-Cr-LDH-POV	114
4.7	Results and discussion	114
	4.7.1 Cyclic voltammetry (CV) study	114
	4.7.2 Galvanostatic charge-discharge (GCD) study	116
	4.7.3 Electrochemical Impedance spectroscopy (EIS) study	118
4.8	Fabrication and supercapacitive performance of aqueous hybrid supercapacitor (AHSC) device: CCV-2  rGO	119
4.9	Result and Discussion	120
	4.9.1 Cyclic voltammetry (CV) study	120
	4.9.2 Galvanostatic charge-discharge (GCD) study	121
	4.9.3 The capacitance retention, EIS, and demonstration of CCV-2  rGO AHSC device	126
4.10	Conclusions	128
4.11	References	129

#### **4.1 Introduction:**

As SCs are worthy energy storage devices with characteristics of fast charging-discharging ability (a few seconds; thereby high PD ( $> 10 \text{ kW kg}^{-1}$ )), moderate ED ( $\sim 10 \text{ Wh kg}^{-1}$ ), and excellent cycle life. [1-3] Consequently, SCs are readily applicable whenever pulse power is required in hybrid electric automotive to assist batteries and portable electronic devices. From a fundamental point of view, the phenomenon of electric double layer formation offers a basis for EDLCs and oxidation-reduction reactions at interface offers a basis for pseudocapacitors (PCs). [4] Thus, high surface area carbon structures can help EDLCs. In contrast, transition metal oxides, hydroxides, and conductive polymers are the appropriate materials for PCs. [1-3] However, SCs can only deliver moderate ED, valuable where pulse power is required. The issue of limited ED can be overcome by utilizing a HSC device comprising battery- and capacitive-type electrode materials in a single electrochemical cell. In this regard, GO, or rGO, is the best choice as capacitive-type electrode materials due to their excellent conductivity, electrochemical stability, expanded surface area, and 2D Ns morphology. [5, 6]

LDHs demonstrated enormous potential as a battery-type electrode in HSC with the capability to store a large amount of charge storing ions in the interlayer space and tunable electronic properties. [7-13] In particular, Ni, Co and Al-based LDH phases receive prime attention as battery-type HSC electrodes because of their promising electrochemical performance ( $800\text{-}2000 \text{ F g}^{-1}$ ). [11, 13] In this context, Co-Cr-LDH displays superior electrode activity with a hybrid-type charge storage mechanism (EDLC and redox-type) due to its unique layered structure, anions intercalation capability, hydrated gallery space, and redox-active elemental composition. Thus, Co-Cr-LDH is regarded as a highly potential battery-type electrode (positive electrode) material for HSC. However, the electrode performance of Co-Cr-LDH is highly limited due to the compact layered structure, low surface area, low conductivity, and restricted gallery space. [14-18] A strategy to enable accessible intergallery space comprises expanding intergallery space via intercalation of bulky anions or various anionic guest nanostructures, such as polymeric, inorganic, organic, and bio-molecules. [9, 19-22] Many attempts were made to expand the intergallery spacing of LDHs via in situ anion exchange processes, which is limited by the kinetically-unfavorable sluggish diffusion

process of anionic guest species within constrained interlayer space of host LDH. [19, 23]

On the other hand, exfoliation of Co-Cr-LDHs crystal leading to positively charged Co-Cr-LDH monolayer Ns and pH-controlled hydrolysis of vanadium salt solution results in polyoxovanadium (POV) anions with well-defined molecular dimension (~1 nm). The electrostatic self-assembly between POV anions and positively charged Co-Cr-LDHs Ns can lead to Co-Cr-LDH-POV nanohybrids (CCV nanohybrids) with expanded interlayer space, mesoporous structure with enhanced surface area, and well-arranged pore structure owing to the development of intercalative structure. [24-28] Also, intercalated POV anions with well-defined reversible redox states can act as an effective reversible electron transfer mediator, which is advantageous for the electrochemical activity of resultant nanohybrids. [24]

The present chapter deals with the synthesis and characterizations of CCV nanohybrids by self-assembly of positively charged Co-Cr-LDH Ns and POV anions. Furthermore, the evolution of electrode activity of CCV nanohybrids is explored to achieve the optimum electrochemical activity. Finally, the HSC is fabricated using the best optimized CCV nanohybrid as a cathode (positive electrode) and rGO as an anode.

## **4.2 Synthesis and characterization of Co-Cr-LDH-POV:**

### **4.3 Experimental details:**

#### **4.3.1 Chemicals:**

Co(NO<sub>3</sub>)<sub>2</sub>·6H<sub>2</sub>O, Cr(NO<sub>3</sub>)<sub>3</sub>·9H<sub>2</sub>O, NaOH, NaNO<sub>3</sub>, Na<sub>3</sub>VO<sub>4</sub>, Graphite flakes, NMP, PVDF, PVA and KOH were purchased from Sigma-Aldrich. SS substrates (304 grade) were served as a current collector to prepare the Co-Cr-LDH and CCV nanohybrid electrodes.

#### **4.3.2 Synthesis of Co-Cr-LDH-POV:**

The pristine Co-Cr-LDH in the nitrate form was synthesized using a conventional co-precipitation method according to Reichle protocol. [1] The monolayers of Co-Cr-LDH was achieved by the dispersion of pristine Co-Cr-LDH powder in formamide. [2] The self-assembled CCV nanohybrids were prepared via rate-controlled simultaneous addition of POV solution and exfoliated Co-Cr-LDH monolayers colloidal suspension. The subsequent flocculation products of CCV

---

## Synthesis, characterization and electrochemical performance of Co-Cr-LDH-POV and AHSC device

nanohybrids were immediately collected by centrifugation, cleaned with formamide and absolute ethanol. Finally, to ensure solid CCV nanohybrid product freeze-drying process was adopted. All the processes were done with decarbonated water and under inert ( $N_2$ ) atmosphere to avoid contamination of Co-Cr-LDH and CCV nanohybrids from  $CO_3^{2-}$  anions. The schematic for the synthesis of exfoliated Co-Cr-LDH Ns and CCV nanohybrids is displayed in figure 4.1.

The ability of the exfoliation–restacking process to control the chemical composition of CCV nanohybrids was investigated by preparing the nanohybrid materials with three representative Co–Cr–LDH/POV molar ratios of 0.66, 0.5, and 0.2, and the obtained CCV nanohybrids are denoted as CCV–1, CCV–2, and CCV–3, respectively. The POV/Co–Cr–LDH molar ratios of 0.66, 0.5, and 0.2 correspond to 2–, 4–, and 6–fold excesses of POV required to balance the LDH monolayer charge, respectively, which were obtained by the lower–nuclearity  $[V_2O_7]^{4-}$  POV anions.

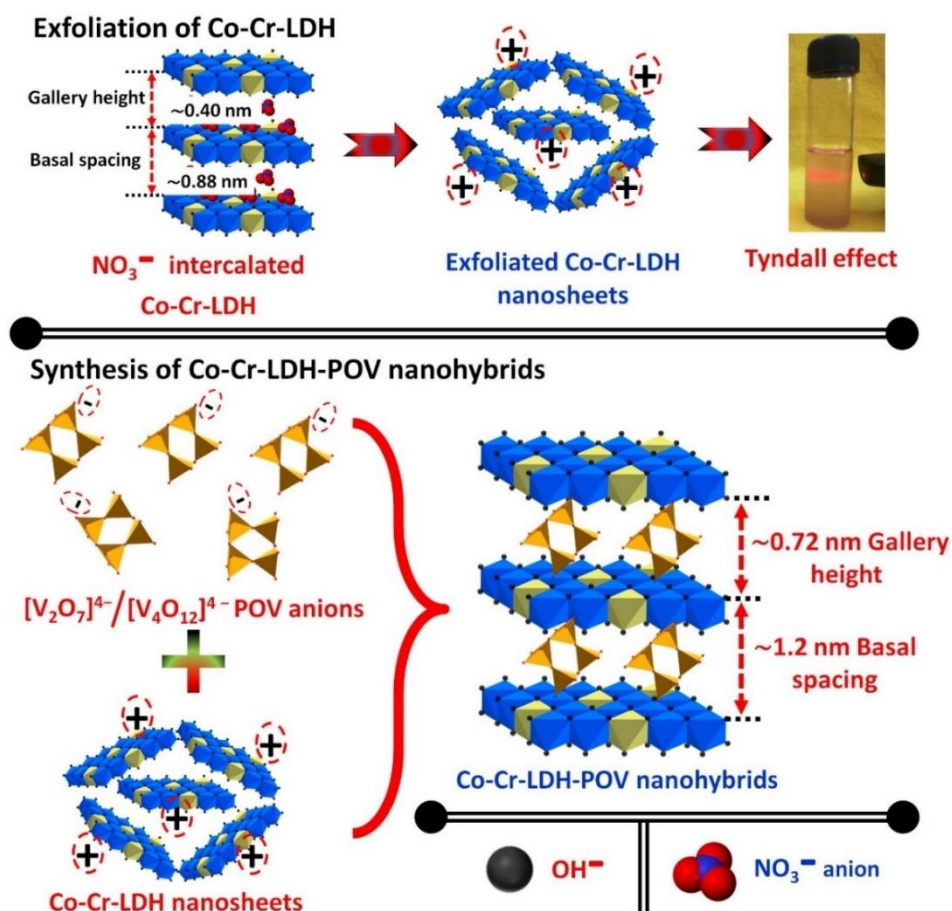


**Figure 4.1:** Schematic model of Co-Cr-LDH and Co-Cr-LDH-POV nanohybrids.

#### 4.4 Characterizations of Co-Cr-LDH-POV:

The pristine Co-Cr-LDH and the self-assembled CCV nanohybrids were characterized by various physicochemical characterization techniques as described in Chapter-3, section 3.3.

##### 4.4.1 Zeta potential measurement:

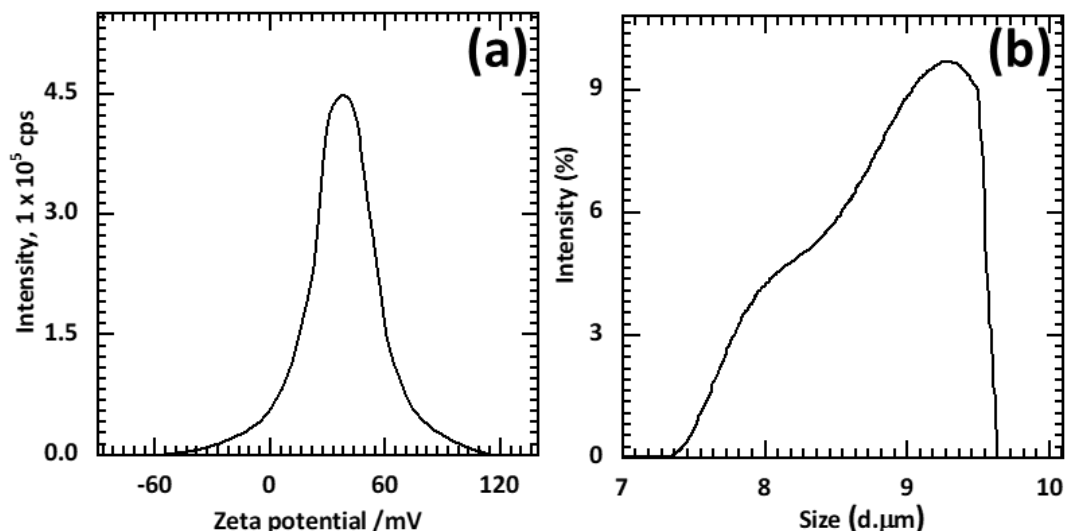


**Figure 4.2:** (a) Zeta potential curve and (b) particle size distribution of the colloidal suspension of exfoliated Co-Cr-LDH Ns.

The quality of Co-Cr-LDH Ns colloidal and the type of surface electrostatic charge on Co-Cr-LDH Ns is probed with Zeta potential and particle-size measurement. As shown in figure 4.2 (a) Co-Cr-LDH Ns exhibits a zeta-potential of +38.56 mV, indicating positively charged Co-Cr-LDH Ns with excellent stability. As shown in figure 4.2 (b), Co-Cr-LDH Ns show a particle-size distribution range of ~7 to 9.8 μm with a polydispersity index (PDI) of 0.39, indicating homogeneously dispersed Co-Cr-LDH Ns in formamide. [29]

##### 4.4.2 XRD analysis:

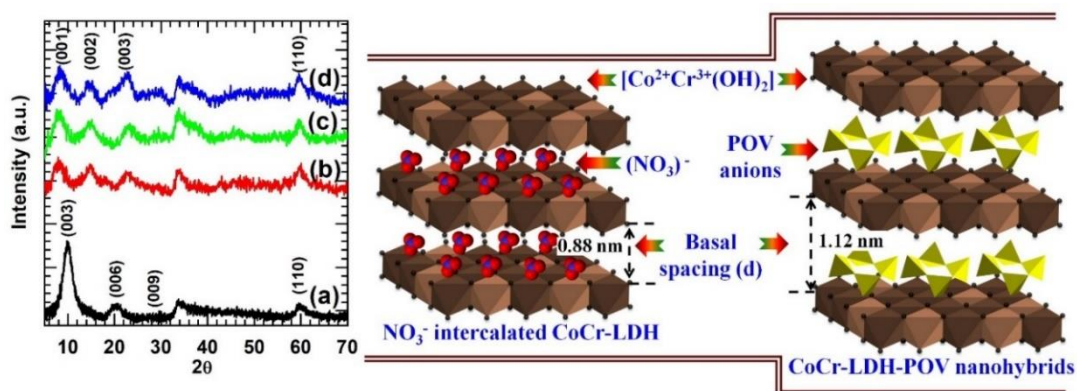


**Figure 4.3:** (Left) PXRD patterns of (a) Co-Cr-LDH, (b) CCV-1, (c) CCV-2 and (d)

## Synthesis, characterization and electrochemical performance of Co-Cr-LDH-POV and AHSC device

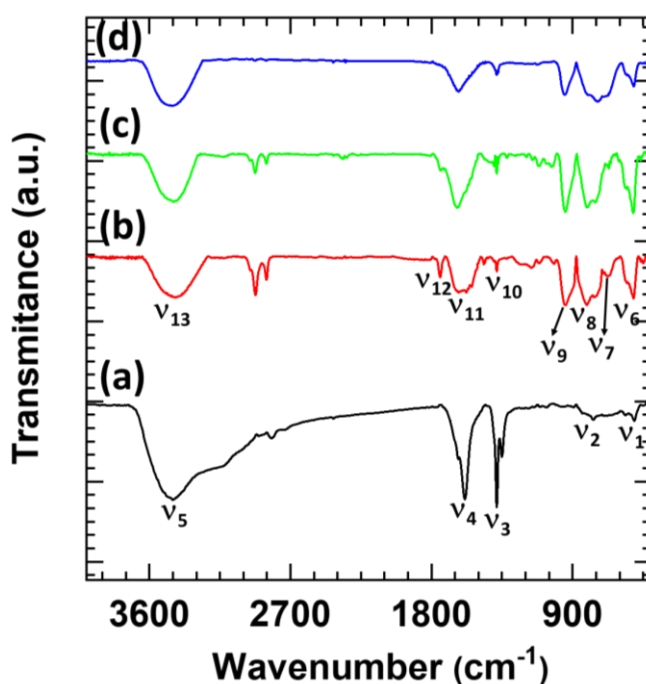
CCV-3 nanohybrids, (Right) structural schematic model of Co-Cr-LDH and Co-Cr-LDH-POV nanohybrids.

The PXRD patterns of the as-prepared CCV nanohybrids are plotted in figure 4.3 (left), compared with the pristine Co-Cr-LDH. The pristine Co-Cr-LDH shows well-developed (003), (006), (009) and (110) Bragg reflections discernible for hexagonal LDH phase possessing R-3m rhombohedral symmetry, which is well-matched with JCPDS card no (38-0487). [30] The lattice dimensions of Co-Cr-LDH are  $a = b = 0.31$  nm and  $c = 0.88$  nm estimated using least-squares fitting analysis. [31, 32] All of the CCV nanohybrids exhibit equally spaced (001), (002) and (003) Bragg reflections with peak positions lower than that of pristine Co-Cr-LDH. This underscores the formation of a c-axis-vertically-ordered intercalation compound with significant expansion of basal spacing. The interplanar spacing corresponding to these (00*l*) reflections is directly related to the c-axis parameter. Regardless of the LDH/POV ratio, all of the CCV self-assembled nanohybrids demonstrated expanded c-axis parameters of 1 to 1.2 nm. Judging from the LDH monolayer thickness (0.48 nm), the c-axis parameters of 1 to 1.2 nm correspond to the enlarged gallery height of 0.52 to 0.72 nm (gallery height = c-axis parameter-LDH monolayer thickness), respectively. This result indicates that the present exfoliation-restacking route offers high flexibility concerning the chemical composition of the hybrid materials.

From all the prepared nanohybrids, CCV-1 and CCV-2 nanohybrids prepared at 2- and 4-fold excesses of POV required to balance the Co-Cr-LDH monolayer charge display the most significant basal spacing of 1.12 and 1.1 nm, respectively. On the other hand, CCV-3 nanohybrid prepared at 6-fold excesses of POV shows the basal spacing of 1 nm. The observed expanded basal spacing of ~1.1 nm in CCV-1 and CCV-2 nanohybrids underscores the stabilization of more condensed high-nuclearity cyclic metavanadate  $[V_4O_{12}]^{4-}$  anions in Co-Cr-LDH interlayer space upon hybridization. Whereas, slightly less expansion in basal spacing (~1 nm) observed for CCV-3 nanohybrid indicates stabilization of low-nuclearity dimeric  $[V_2O_7]^{4-}$  anions in Co-Cr-LDH interlayer space. [23, 33] The crystallite thickness of CCV nanohybrids, by the Scherrer's formula for the (00*l*) plane, is ~10 nm. Referring to the basal spacing of the CCV nanohybrids (1.1 nm), the estimated crystallite thickness corresponds to the ~8-10 monolayers of Co-Cr-LDH restacked

with the POV anions. Furthermore, prepared CCV nanohybrids and reference Co-Cr-LDH show the characteristic in-plane (110) peak of hexagonal Co-Cr-LDH at  $2\theta = \sim 60.2^\circ$  with broad sawtooth shape peak at  $\sim 32-45^\circ$ . The observation of these in-plane reflections clearly emphasizes the maintenance of in-plane Co-Cr-LDH monolayer structure and disordered turbostratic stacking structure of the CCV nanohybrids.

#### 4.4.3 FTIR analysis:



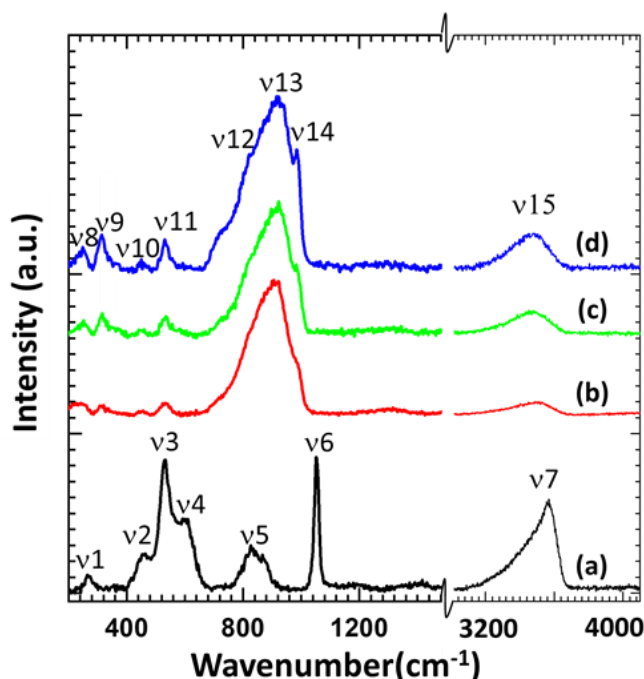
**Figure 4.4:** FTIR spectra of (a) Co-Cr-LDH, (b) CCV-1, (c) CCV-2 and (d) CCV-3 nanohybrids.

Figure 4.4 shows the FTIR spectra of CCV nanohybrids and the reference Co-Cr-LDH in the range of 400 to 4000  $\text{cm}^{-1}$ . The Co-Cr-LDH FTIR spectrum displays sharp absorption peaks at  $\nu_1$  (514  $\text{cm}^{-1}$ ),  $\nu_2$  (770  $\text{cm}^{-1}$ ),  $\nu_3$  (1380  $\text{cm}^{-1}$ ),  $\nu_4$  (1600  $\text{cm}^{-1}$ ), and  $\nu_5$  (3465  $\text{cm}^{-1}$ ). The peaks  $\nu_1$  (514  $\text{cm}^{-1}$ ) and  $\nu_2$  (770  $\text{cm}^{-1}$ ) are ascribed to the metal-oxygen (M-O) and metal-oxygen-hydrogen (M-O-H) bending vibrations in the brucite-like Co-Cr-LDH phase, respectively. [32, 34] The sharp absorption peak at  $\nu_3$  (1380  $\text{cm}^{-1}$ ) is ascribed to the anti-symmetric stretching mode of intrasheet nitrate anions. [35, 36] The broad absorption peak at  $\nu_5$  (3546  $\text{cm}^{-1}$ ) and sharp peak  $\nu_4$  (1610  $\text{cm}^{-1}$ ) are attributed to the stretching vibration of the H-bound O-H groups in Co-Cr-LDH and bending vibrational modes of the water molecule, respectively. [32] On the other hand, the CCV nanohybrids demonstrated

## Synthesis, characterization and electrochemical performance of Co-Cr-LDH-POV and AHSC device

complex IR spectra, covering absorption peaks of Co-Cr-LDH with POV-related absorption peaks. The intense absorption peak at  $\nu_8$  ( $812\text{ cm}^{-1}$ ) with an associated shoulder at  $\nu_7$  ( $674\text{ cm}^{-1}$ ) are assigned to the symmetric and anti-symmetric stretching modes of vanadium-oxygen chains in intercalated POV anions, respectively. [37, 38] The sharp absorption peak at  $\nu_9$  ( $940\text{ cm}^{-1}$ ) is attributed to the  $V=O$  symmetric stretching mode. [39-41] The absorption peak related to the anti-symmetric stretching mode of intrasheet nitrate or carbonate anions showing very mild signature at  $\nu_{10}$  ( $1380\text{ cm}^{-1}$ ), underscoring slight contamination of CCV nanohybrids with adsorbed carbonate or nitrate anions during exfoliation-restacking. [23] The broad absorption band at  $\nu_{13}$  ( $3546\text{ cm}^{-1}$ ) and sharp band  $\nu_{11}$  ( $1610\text{ cm}^{-1}$ ) are attributed to the stretching vibration of the H-bound O-H groups in Co-Cr-LDH and bending vibration of intergallery  $H_2O$ , respectively. [32] Obtained IR features confirm the maintenance of Co-Cr-LDH monolayers and intercalation of POV anions into the interlayer spaces of the Co-Cr-LDH.

### 4.4.4 Raman analysis:



**Figure 4.5:** Micro-Raman spectra of (a) Co-Cr-LDH, (b) CCV-1, (c) CCV-2 and (d) CCV-3 nanohybrids.

The type of intercalated POV anions, microscopic structural properties, and their chemical bonding characteristic upon the self-assembly are examined using Micro-Raman spectroscopy. As seen from figure 4.5, the Micro-Raman spectrum of Co-Cr-

## Synthesis, characterization and electrochemical performance of Co-Cr-LDH-POV and AHSC device

---

LDH displays  $\nu_1$  to  $\nu_7$  typical Raman peaks, which assigned to the characteristic Raman shift from the Co-Cr-LDH, intercalated nitrate anions and water molecules. The peaks at  $\nu_1$  ( $265\text{ cm}^{-1}$ ),  $\nu_2$  ( $455\text{ cm}^{-1}$ ),  $\nu_3$  ( $530\text{ cm}^{-1}$ ),  $\nu_4$  ( $600\text{ cm}^{-1}$ ),  $\nu_5$  ( $840\text{ cm}^{-1}$ ), and  $\nu_6$  ( $1055\text{ cm}^{-1}$ ) are assigned to the lattice (metal-oxygen) translational vibrations ( $E_g$  mode), O-Co-O bending ( $A_{1g}$  mode), Co-O stretching ( $A_{2u}$  mode), Co-O rotational ( $E_g$  mode), symmetric/anti-symmetric Cr-OH stretching and symmetric stretching of  $\text{NO}_3$  modes, respectively. [32-47] The broad signature peak around  $\nu_7$  ( $3575\text{ cm}^{-1}$ ) is assigned to the internal stretching of hydroxyl groups and intersheet  $\text{H}_2\text{O}$  molecules. Similarly, the CCV nanohybrids showed characteristic Raman peaks at  $\nu_8$  ( $250\text{ cm}^{-1}$ ),  $\nu_{10}$  ( $450\text{ cm}^{-1}$ ),  $\nu_{11}$  ( $532\text{ cm}^{-1}$ ), and  $\nu_{12}$  ( $827\text{ cm}^{-1}$ ), which are attributed to the Co-Cr-LDH lattice vibrational modes. [42-49]

Additionally, CCV nanohybrids show an intense peak at  $\nu_{13}$  ( $922\text{ cm}^{-1}$ ) and a signature peak at  $\nu_9$  ( $311\text{ cm}^{-1}$ ). The high-intensity broad peak  $\nu_{13}$  is formed due to the superposition of  $\nu_{12}$  ( $830\text{ cm}^{-1}$ ),  $\nu_{13}$  ( $922\text{ cm}^{-1}$ ), and  $\nu_{14}$  ( $984\text{ cm}^{-1}$ ) peaks. The peaks  $\nu_{12}$ ,  $\nu_{13}$  and  $\nu_{14}$  are assigned to the symmetric Cr-OH stretching, the symmetric tetrameric vanadate stretching (cyclic-metavanadate  $[\text{V}_4\text{O}_{12}]^{4-}$  anions) and symmetric decavanadate  $[\text{V}_{10}\text{O}_{28}]^{6-}$  anions stretching vibrations, respectively. [34-36, 50] During the exfoliation-restacking route, the POV solution being pH shocked from 5 to  $\sim 7$  that causes  $[\text{V}_{10}\text{O}_{28}]^{6-}$  anions decomposition to dimeric pyrovanadates  $[\text{V}_2\text{O}_7]^{4-}$  and cyclic-metavanadate  $[\text{V}_4\text{O}_{12}]^{4-}$  anions. [35, 51] The present spectroscopic analysis confirms the intercalative stabilization of dimeric pyrovanadates  $[\text{V}_2\text{O}_7]^{4-}$  and cyclic-metavanadate  $[\text{V}_4\text{O}_{12}]^{4-}$  anions at Co-Cr-LDH interlayer space. The broad peak around  $\nu_{15}$  ( $3470\text{ cm}^{-1}$ ) is flattened and red-shifted as compared to peak around  $\nu_7$  ( $3575\text{ cm}^{-1}$ ), which is ascribed to the intercalation of more free water molecules due to increased gallery space of Co-Cr-LDH upon hybridization. [29, 50] These characteristic Raman features corresponding to lattice vibrational modes of Co-Cr-LDH clearly emphasize the intactness of the pristine in-plane structure of Co-Cr-LDH monolayer Ns after hybridization.

4.4.5 FESEM analysis:

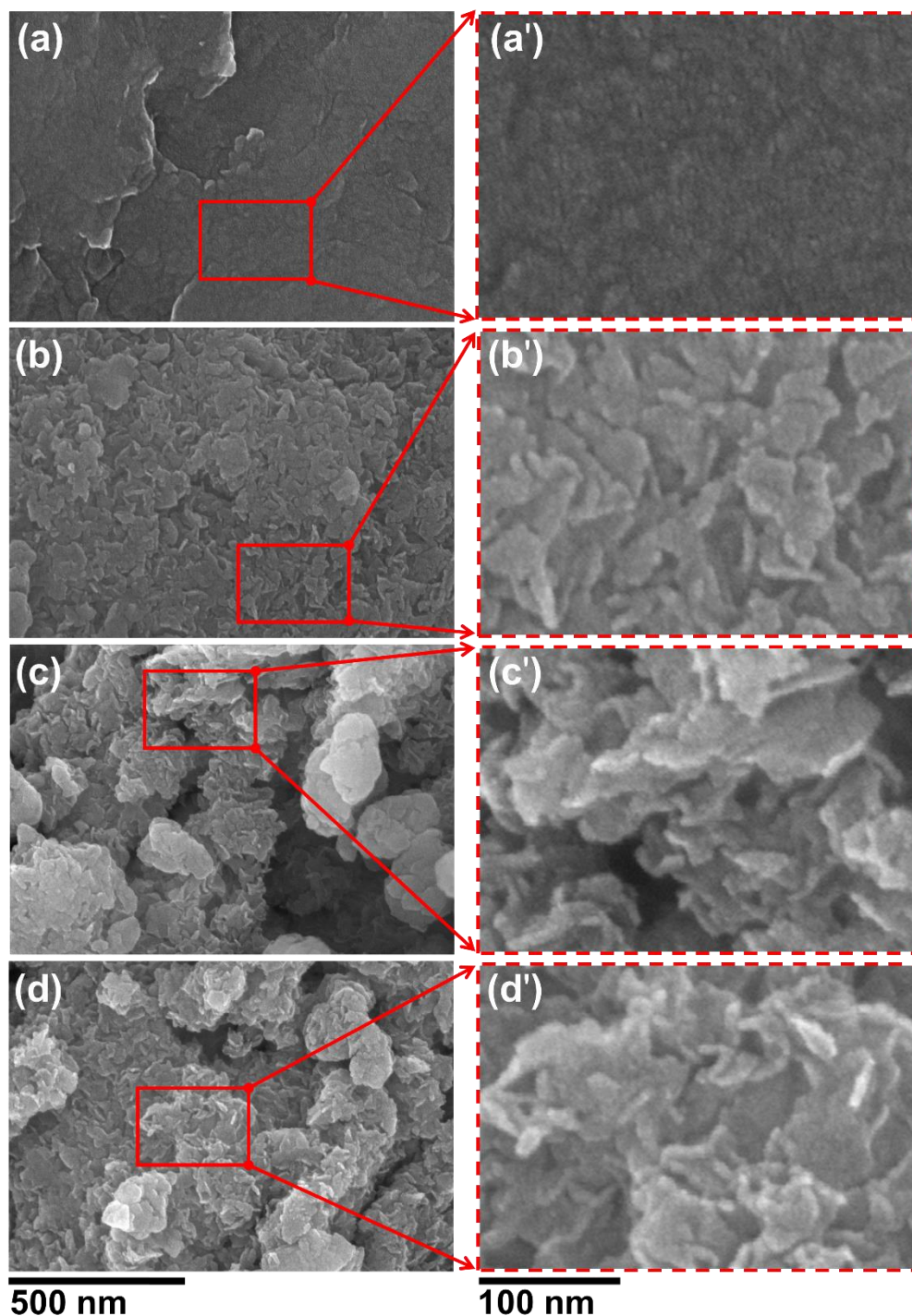


**Figure 4.6:** FESEM images of (a, a') Co-Cr-LDH, (b, b') CCV-1, (c, c') CCV-2 and (d, d') CCV-3 nanohybrids at various magnifications ((b-d) 100k and (b'-d') 300k).

The crystal shapes, sizes, and morphologies of the CCV nanohybrids and reference Co-Cr-LDH samples are examined with FESEM. The Co-Cr-LDH shows a non-porous flat surface morphology which is commonly observed in the co-precipitated LDH materials (figure 4.6 (a, a')). Alternatively, in figure 4.6 (b-b', c-c' and d-d'), the CCV nanohybrids typically display porous morphology composed of

## Synthesis, characterization and electrochemical performance of Co-Cr-LDH-POV and AHSC device

randomly aggregated sheet-like crystallites. Consequently, a large number of mesopores are formed due to the randomly aggregated sheet-like crystallites. A close topographical inspection of micrographs at high magnification reveals the thickness of the CCV nanohybrid sheet-like crystallites is between  $\sim 7$  to 15 nm and the lateral size is between  $\sim 40$  to 180 nm. The stacking structure obtained due to the edge-to-face interaction of restacked LDH Ns offers mesoporous spaces of  $\sim 10$  to 80 nm with irregular polygon shapes. The estimated thickness (7 to 15 nm) of the CCV nanohybrid sheet-like crystallites demonstrates the stacking of 6 to 14 layers of 2D Co-Cr-LDH monolayers and POV anions. Similar mesoporous morphologies are commonly observed for the self-assembled nanohybrids of 2D Ns and various nanostructures. [23-26]

### 4.4.6 EDS analysis:

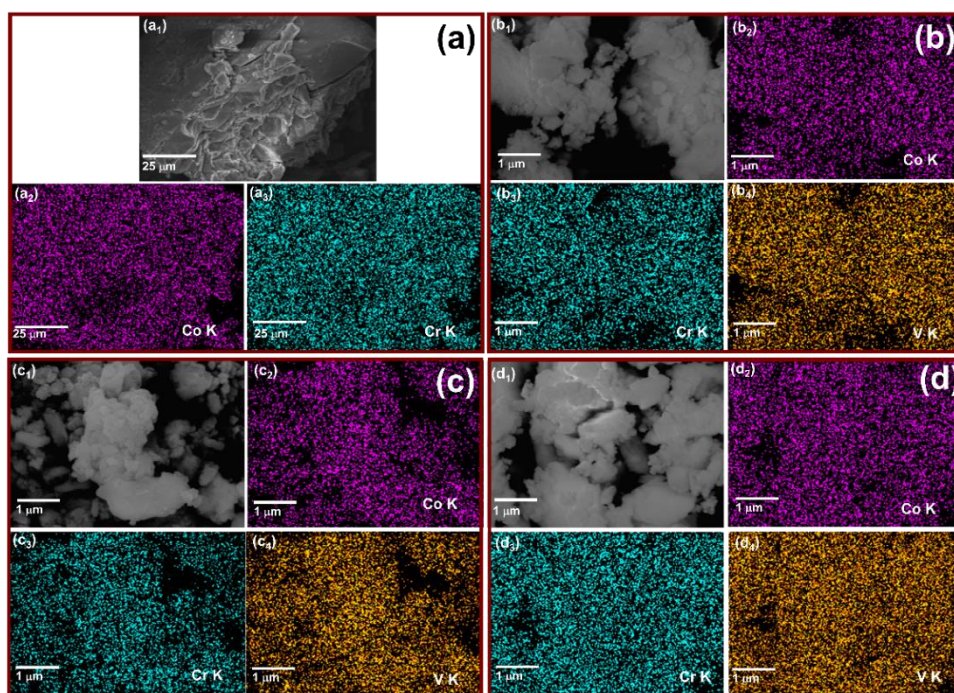


**Figure 4.7:** EDS-elemental mappings of (a) Co-Cr-LDH, (b) CCV-1, (c) CCV-2, and (d) CCV-3, subscript 1, 2, 3 and 4 represent FESEM images, Co, Cr, and V elements, respectively.

The spatial distributions of constituent elements and chemical composition of CCV nanohybrids and Co-Cr-LDH at the nanometer scale are examined with EDS and elemental mapping analysis. As shown in figure 4.7, all the constituent elements (Co, Cr and V) are uniformly distributed across the entire elemental mapping area, demonstrating the homogeneous hybridization of Co-Cr-(OH)<sub>2</sub> monolayers and POV anions without spatial phase separation (figure 4.7 and 4.8).

## Synthesis, characterization and electrochemical performance of Co-Cr-LDH-POV and AHSC device

The chemical compositions of reference Co-Cr-LDH and Co-Cr-LDH-POV nano hybrids are estimated as  $\text{Co}_{0.65}\text{Cr}_{0.35}(\text{OH})_2 \cdot 0.35(\text{NO})_3 \cdot y\text{H}_2\text{O}$ ,  $\text{Co}_{0.67}\text{Cr}_{0.33}(\text{OH})_2 \cdot 0.13(\text{V}_4\text{O}_{12}) \cdot y\text{H}_2\text{O}$ ,  $\text{Co}_{0.68}\text{Cr}_{0.32}(\text{OH})_2 \cdot 0.14(\text{V}_4\text{O}_{12}) \cdot y\text{H}_2\text{O}$ , and  $\text{Co}_{0.65}\text{Cr}_{0.35}(\text{OH})_2 \cdot 0.33(\text{V}_2\text{O}_7) \cdot y\text{H}_2\text{O}$  for Co-Cr-LDH, CCV-1, CCV-2, and CCV-3 nano hybrids, respectively.

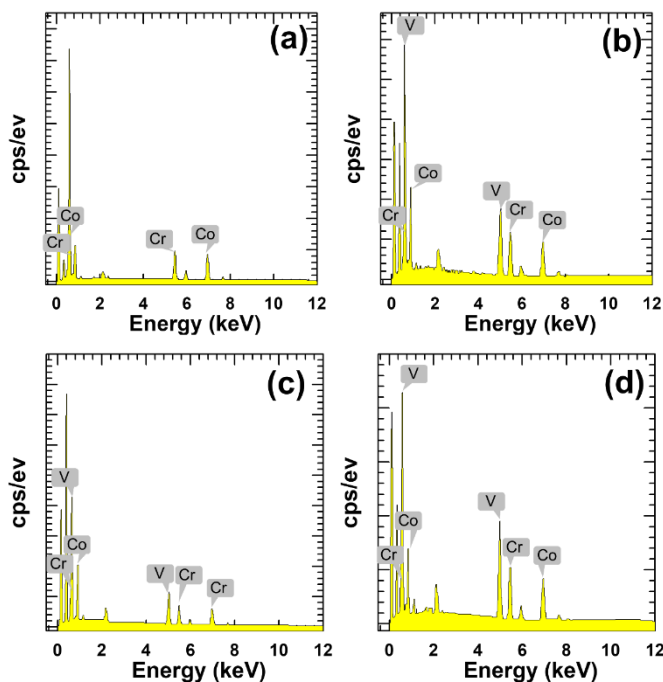


**Figure 4.8:** EDS spectra of (a) Co-Cr-LDH, (b) CCV-1, (c) CCV-2, and (d) CCV-3.  
**4.4.7 XPS analysis:**

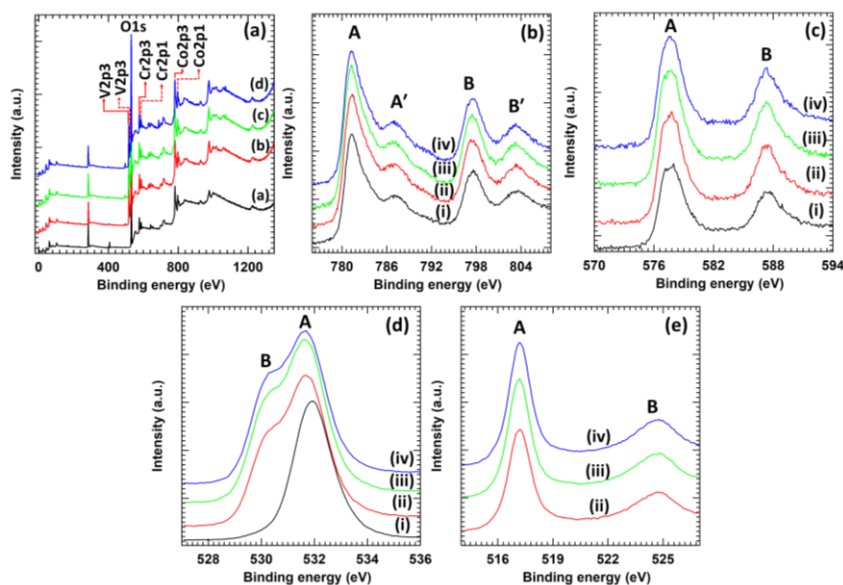


**Figure 4.9:** (a) Survey, (b) Co 2p, (c) Cr 2p, (d) O 1s and (e) V 2p XPS spectra of Co-Cr-LDH and CCV nano hybrids. Core levels, (i) Co-Cr-LDH, (ii) CCV-1, (iii) CCV-2 and (iv) CCV-3 nano hybrids.

## Synthesis, characterization and electrochemical performance of Co-Cr-LDH-POV and AHSC device

---

The surface chemical composition, diverse oxidation states of stabilized POV anions, and their influence on the chemical bonding nature of the pristine Co-Cr-LDH structure are studied using XPS measurements. The XPS survey spectra demonstrate that all the samples under investigation (figure 4.9 (a)) commonly show spectral features of the element Co, Cr, and O with additional features of V in nanohybrids. As plotted in figure 4.9 (b), the reference Co-Cr-LDH and CCV nanohybrids commonly exhibit two spectral features A (781.2 eV) and B (797.4 eV) with satellite peaks at A' (786.8 eV) and B' (803.2 eV). These spectral features are attributed to the spin-orbit splitting into Co 2p<sub>3/2</sub> and Co 2p<sub>1/2</sub>, respectively. [42, 34] The binding energy difference (16.2 eV) of peaks A and B can be regarded as an indicator for Co<sup>+2</sup> in Co-Cr-LDH. As shown in figure 4.9 (c), the high-resolution Cr 2p spectrum shows A (577.6 eV) and B (587.3 eV) peaks, that arised due to spin orbit splitting of Cr 2p<sub>3/2</sub> and Cr 2p<sub>1/2</sub> components. [52-53] The binding energy of broad peak A is associated with the Cr<sup>3+</sup> hydroxide state and Cr<sup>3+</sup> attached with intergallery ligands like OH<sup>-</sup> and H<sub>2</sub>O. [54-55] The O 1s XPS spectra of reference Co-Cr-LDH and Co-Cr-LDH-POV nanohybrids are represented in figure 4.9 (d). Interestingly, O 1s spectrum of Co-Cr-LDH demonstrates the broad peak A (531.9 eV), indicating the presence of oxygen from metal hydroxide, surface hydroxyl group and bound water. Alternatively, O 1s spectra of CCV nanohybrids display the broad peak A (531.7 eV) and a shoulder peak B (530.1 eV). [41, 56] The shoulder peak B is absent in reference Co-Cr-LDH which is aroused from the V-O in POV anions. As demonstrated in figure 4.9 (e), high-resolution V 2p XPS spectra are discernible only for CCV nanohybrids. As shown in figure 4.9 (e), the high-resolution V 2p spectrum shows A (517.1 eV) and B (524.7 eV) peaks, that arised due to spin orbit splitting of V 2p<sub>3/2</sub> and V 2p<sub>1/2</sub> components, respectively. [21, 31, 57, 58] These spectral features are attributed to the pentavalent vanadium from POV anions. The obtained XPS features vividly designate the intercalation of POV anions in interlayer space of Co-Cr-LDH.

4.4.8 TEM analysis:

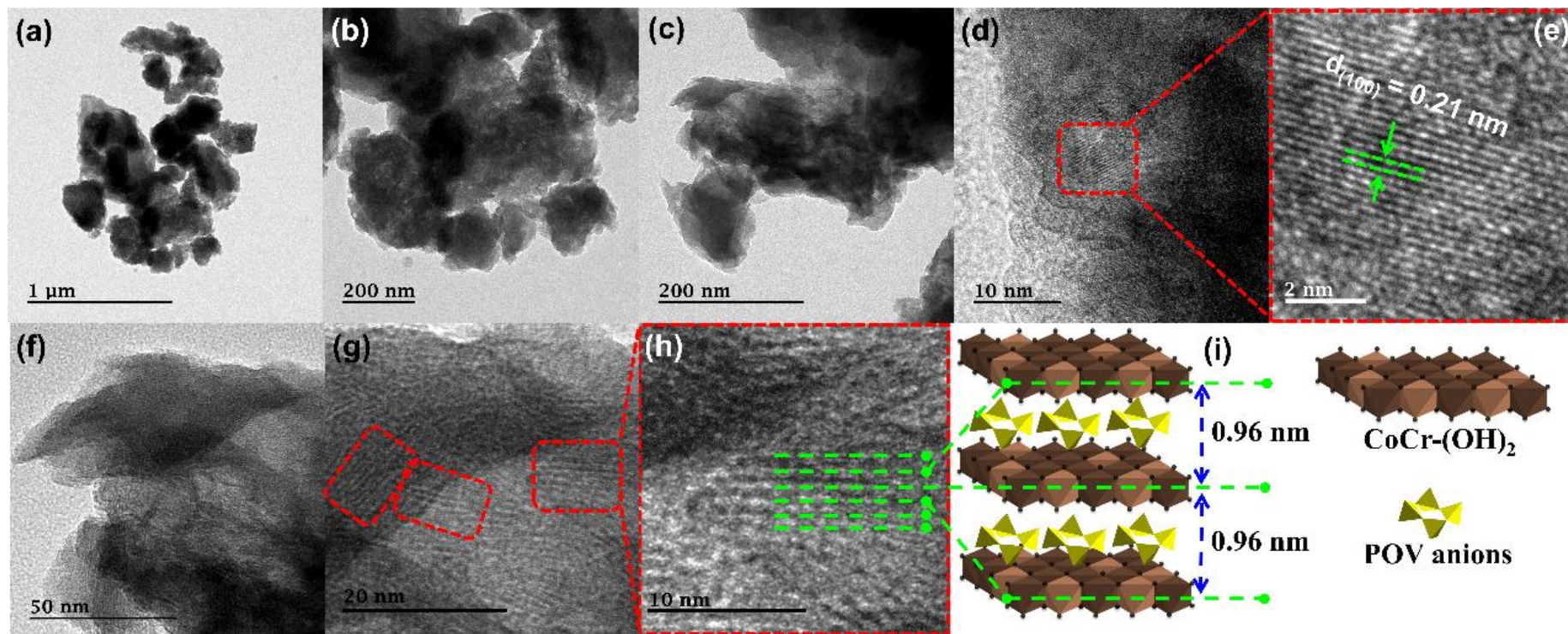


**Figure 4.10:** (a, b, c) Top view of TEM, (d, e) Top view of HRTEM and (f, g, h) Cross-sectional HRTEM images of CCV-2 nanohybrid at high magnifications with (i) its schematic representation.

The layer-by-layer-ordered stacking and shape of the as-prepared CCV nanohybrids at the nanometer scale are examined using TEM. As presented in figure 4.10 (a, b, c), the top-view TEM images of the CCV-2 nanohybrid vividly display randomly aggregated Co-Cr-LDH-POV sheet-like crystallites creating mesoporous stacking structure. As illustrated in figure 4.10 (d, e), the top-view HRTEM images of the nanohybrid clearly demonstrate a series of equally-spaced fringes separated by an interline distance of 0.21 nm. This interplanar distance is well-matched with the host Co-Cr-(OH)<sub>2</sub> hexagonal lattice (JCPDS card, No. 38-0487). Moreover, the cross-sectional HRTEM images in figure 4.10 (f, g, h) of the CCV-2 nanohybrid shows equally-spaced parallel-aligned dark lines corresponding to the Co-Cr-(OH)<sub>2</sub> monolayers. At a high resolution, zones of equally spaced parallel-aligned dark lines highlighted by the dotted lines (figure 4.10 (h)) are discernible; careful observation of these zones reveals alignment of 4 to 10 equally-spaced parallel dark lines with a total thickness of 4 to 9 nm. As judged from the Scherrer calculations, Co-Cr-LDH-POV nanohybrid crystallite thickness corresponds to ~10 POV-pillared Co-Cr-(OH)<sub>2</sub> layers. The observed zone thickness of 4-9 nm agrees with the Co-Cr-LDH-POV nanohybrid crystallite thickness. As illustrated in figure 4.10 (h, i), the distance between two consecutive dark lines is 0.96 nm, which agrees with the *c*-axis lattice parameter of CCV-2 nanohybrid estimated from XRD analysis. This observation demonstrates the intercalative stabilization of POV anions into Co-Cr-LDH with the formation of layer-by-layer stacking of Co-Cr-(OH)<sub>2</sub> and POV anions. The present HRTEM images of the CCV nanohybrids are corresponding to the nanohybrids prepared by the exfoliation-reassembling route. [21-26]

**4.4.9 N<sub>2</sub> adsorption-desorption (BET) analysis:**

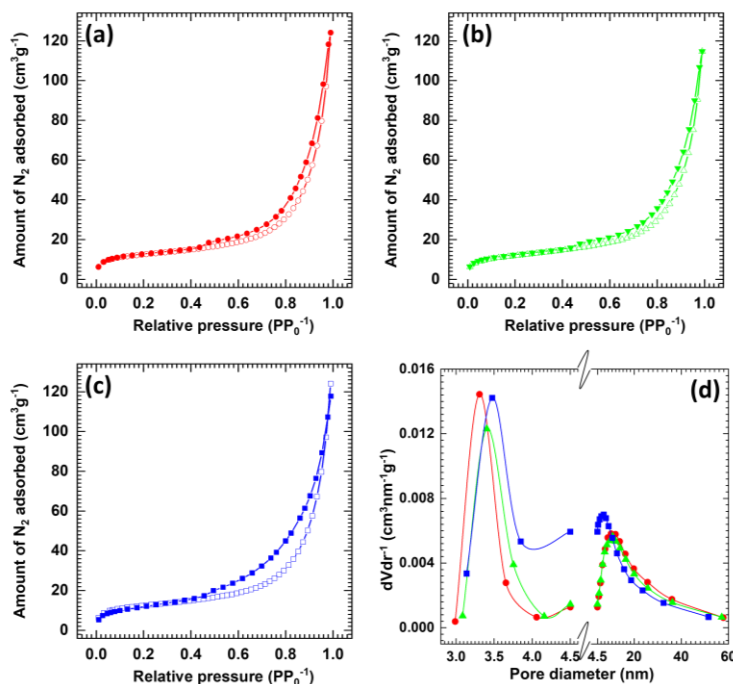


**Figure 4.11:** N<sub>2</sub> adsorption-desorption isotherms for (a) CCV-1, (b) CCV-2, and (c) CCV-3 nanohybrids. (d) Pore size distribution curves for (red) CCV-1, (green) CCV-2 and (blue) CCV-3. In (a, b, c), the open symbols represent the adsorption and closed symbols represent desorption data.

The effect of POV hybridization on the surface area and pore structure of the CCV nanohybrids is probed with N<sub>2</sub> adsorption-desorption isotherm analysis. From figure 4.11 (a, b, c), the CCV nanohybrids show significant N<sub>2</sub> adsorption at  $pp_0^{-1} < 0.4$  and distinct hysteresis at  $pp_0^{-1} > 0.45$  characteristic of the mesoporous materials. [57] According to the IUPAC classification, the observed isotherm shape and hysteresis behavior can be classified as H3-type hysteresis loops and BDDT type-IV isotherm shapes. The presence of H3-type hysteresis and type-IV isotherm is a typical characteristic of the aggregates of plate-like particles with slit shape mesopores. [57-58]

In contrast to Co-Cr-LDH (5 m<sup>2</sup> g<sup>-1</sup>) (**Chapter-3, figure 3.8 (a)**), upon the hybridization with POV anions, all of the CCV nanohybrids exhibit high surface areas of 47, 43 and 42 m<sup>2</sup> g<sup>-1</sup> for CCV-1, CCV-2 and CCV-3 nanohybrids, respectively. The present results highlight the crucial role of POV intercalation for surface area expansion of LDH via the exfoliation-restacking route. According to BJH method, the distribution of pore size is calculated and shown in figure 4.11 (d). Mesoporous character of the CCV nanohybrids is indicated by high distribution of pores with an average diameter of ~3-4 nm. Also, CCV nanohybrids show

broad pore distribution with an average diameter  $\sim$ 5-20 nm, emphasizing the formation of micropores due to random stacking of sheet-like CCV crystallites. The observed pore size distribution and surface area analysis revealed the crucial importance of the exfoliation-reassembling route for tuning the pore structure of the resulting CCV nanohybrids.

#### **4.5 Conclusions:**

A mesoporous layer-by-layer self-assembled CCV nanohybrids are prepared by self-assembly between the Co-Cr-LDH monolayer Ns and POV anions. Facile alteration of Co-Cr-LDH Ns and POV mixing proportions is an efficient way for tuning the type and amount of intercalated POV species with high flexibility in chemical composition. The obtained nanohybrids are characterized by XRD, FESEM, FTIR, Raman, EDS, XPS, TEM and N<sub>2</sub> adsorption-desorption analysis techniques to study crystal structure, chemical bonding, surface textural as well as compositional properties. The CCV nanohybrids show the layer-by-layer ordered structure, enlarged gallery height, mesoporous morphology (created by randomly aggregated sheet-like crystallites), and expanded surface area.

#### 4.6 Electrochemical performance of Co-Cr-LDH-POV:

#### 4.7 Result and discussion:

##### 4.7.1 Cyclic voltammetry (CV) study:

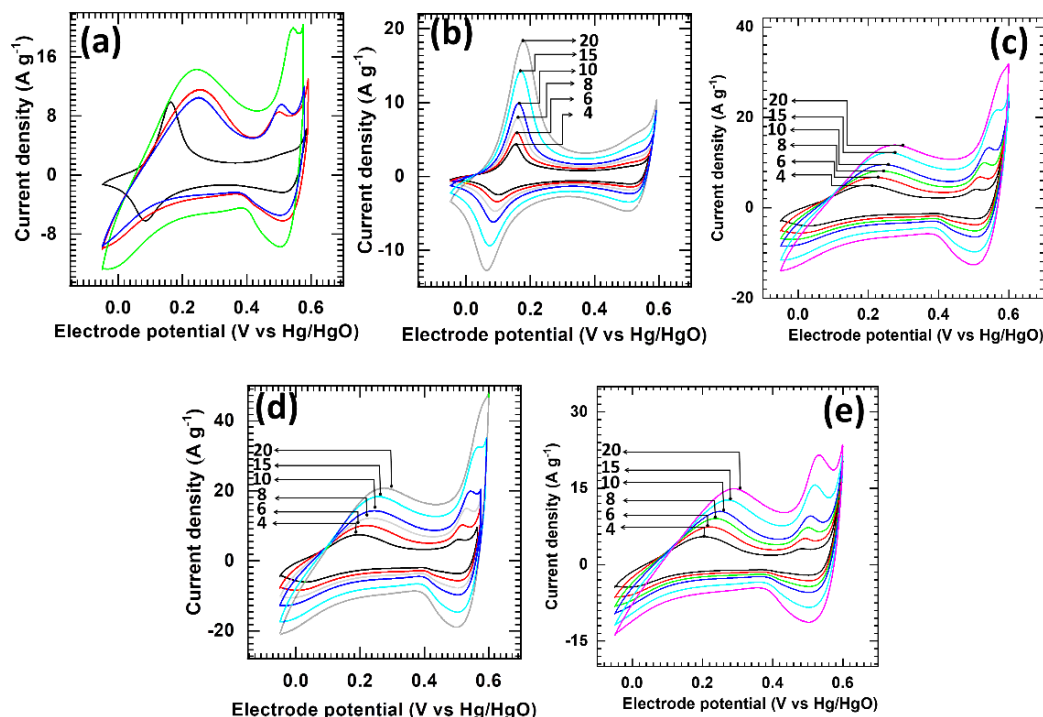


**Figure 4.12:** (a) CV plot of Co-Cr-LDH and CCV nanohybrids at a sweep rate of  $10 \text{ mV s}^{-1}$ . CV plot of the (b) Co-Cr-LDH and (c) CCV-1, (d) CCV-2 and (e) CCV-3 nanohybrid at various scan rates (scan rate:  $4 - 20 \text{ mV s}^{-1}$ ).

The electrochemical performance of reference Co-Cr-LDH and CCV nanohybrids are studied using a three-electrode electrochemical half-cell. In a half-cell, the Co-Cr-LDH or CCV nanohybrid served as working electrode, a platinum mesh served as counter electrode and Hg/HgO is utilized reference electrode. **(Chapter – 3, section 3.5)**. Figure 4.12 (a) presents the CV plot of Co-Cr-LDH and CCV nanohybrids electrodes at  $10 \text{ mV s}^{-1}$  in a  $2 \text{ M KOH}$  electrolyte. All the tested electrodes showed redox peak pairs, suggesting the electrochemical charge storage involving both diffusion-controlled and capacitive types of charge storage. The redox peaks are discernible at  $0.015 \text{ V}$  for the reference Co-Cr-LDH that are assigned to the quasi reversible oxidation-reduction reactions between  $\text{Co(OH)}_2$  and  $\text{CoOOH}$  transformation, according to the oxidation-reduction reaction **(equation 3.3, Chapter – 3)**: [31]

Moreover, noticeable redox peaks are observed at  $\sim 0.5$  to  $0.55 \text{ V}$  due to the reversible redox reaction of  $\text{Co}^{3+}$  to  $\text{Co}^{4+}$ . [59] Also, it is noted that CV shape changed according to increasing scan rate, as well as anodic and cathodic peak potentials

shifted towards the more anodic and cathodic potential direction. Interestingly, the hybridization with POV anions causes broadening of cathodic and anodic peaks, illustrating the improved accessibility of electrode materials for the percolation of electrolyte ions. POV intercalative hybridization significantly increases the area enclosed by the CV plot reference to pristine Co-Cr-LDH, underscoring the significance of the POV intercalation for the enhanced charge storage. Careful observation of CV shows the difference in the integral area of the CV curves with POV content; CCV-2 nano hybrid discern the largest area that highlights the important role of optimum POV content (Co-Cr-LDH/POV molar ratio =0.5) for the improvement of charge storing ability. Also, excess POV intercalation in CCV-3 nano hybrid (Co-Cr-LDH/POV molar ratio =0.2) causes a detrimental effect on its charge storing ability as it is visible from the decreased area under CV. As presented in figure 4.12 (b-e), the redox peak current and area under CV curves increases with scan rates. The shifting of the cathodic peak with scan rate towards more positive potential, indicating both charge storage mechanism of Co-Cr-LDH and CCV nano hybrids.

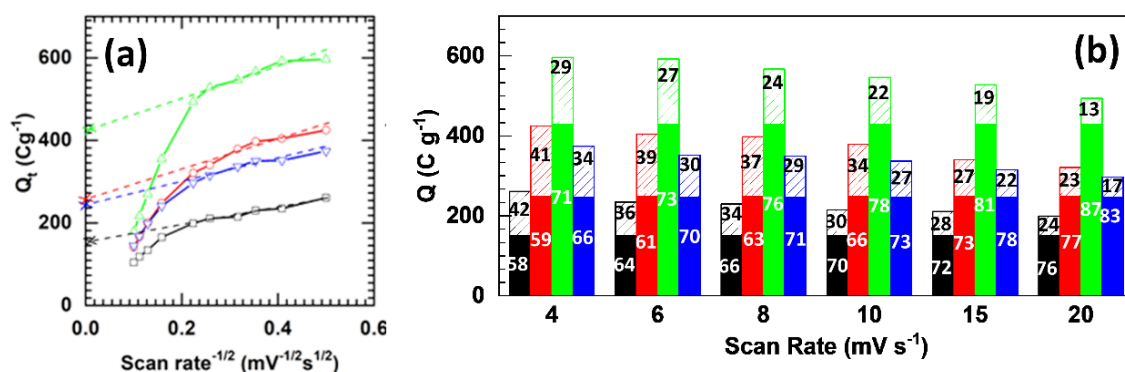


**Figure 4.13:** (a) Plot of total charge ( $Q_t$ ) vs the reciprocal of the square root of the scan rate ( $v^{-1/2}$ ). (b) The fraction of the capacitive (solid) and diffusion-controlled (pattern) contributions of Co-Cr-LDH (black), CCV-1 (red), CCV-2 (green) and CCV-3 (blue) nano hybrids. (Values in bar assigned for the respective percentage contributions)

As all of the present electrodes show typical CV curves involving both charge storage mechanisms such as diffusion-controlled and capacitive type and the contribution of each can be determined by electrochemical kinetics study via **equation 3.4, Chapter – 3**. The surface capacitive charge ( $Q_s$ ) can be resolved by  $Q_t$  vs  $(v)^{-1/2}$  (figure 4.13 (a)) plot and deducing  $v$  to infinity by assuming semi-infinite linear diffusion, within a reasonable range of sweep rates. The high scan rates above 20 mV s<sup>-1</sup> are ignored in the fitting to avoid the polarization effect. [60] Figure 4.13 (b) shows the fractions of capacitive and diffusion-controlled contributions Co-Cr-LDH and CCV

nanohybrids represented by solid-filled and pattern-filled columns, respectively. The tested electrodes display that the capacitive charge ( $Q_s$ ) distribution leads at high scan rates, where diffusion-controlled ( $Q_d$ ) charge is noticeable at a low scan rate. Interestingly, the CCV nanohybrids show capacitive contributions of 59, 71, and 66% at scan rate of  $4 \text{ mV s}^{-1}$  for CCV-1, CCV-2 and CCV-3 nanohybrids, respectively, that are higher than the capacitive contribution of Co-Cr-LDH (58%) at same scan rate. On the other hand, at higher sweep rate of  $20 \text{ mV s}^{-1}$ , the CCV nanohybrids exhibit capacitive contributions of 77, 87 and 83% for CCV-1, CCV-2, and CCV-3 nanohybrids, respectively as compared to capacitive contribution of Co-Cr-LDH (76%) at the same scan rate. Especially CCV-2 nanohybrid demonstrated 2.28-fold increased charge storage as compared to Co-Cr-LDH at  $4 \text{ mV s}^{-1}$ . The capacitive-dominant contribution for CCV nanohybrids compared to Co-Cr-LDH is attributable to the faster charge transfer kinetics via expanded surface area and accessible LDH gallery height upon the intercalative hybridization with POV anions.

#### 4.7.2 Galvanostatic charge-discharge (GCD) study:

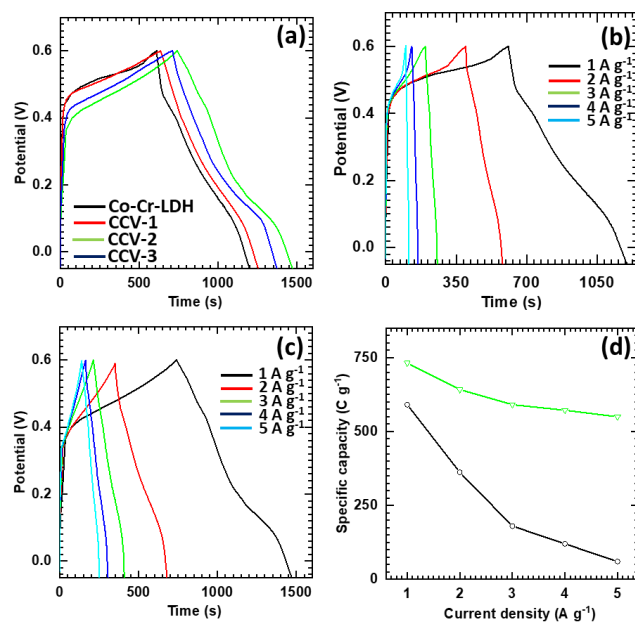


**Figure 4.14:** (a) GCD plot of the Co-Cr-LDH and CCV nanohybrids at  $1 \text{ A g}^{-1}$ . CD curves of the (b) Co-Cr-LDH and (c) CCV-2 nanohybrid at different current densities (current densities:  $1 - 5 \text{ A g}^{-1}$ ). (d) Variations of  $C_{sp}$  of Co-Cr-LDH and CCV-2 nanohybrids electrodes with current density.

The GCD cycling measurements further confirmed the beneficial role of POV intercalative hybridization on the electrode performance of LDH. Figure 4.14 (a) presents GCD curves of the CCV nanohybrids and reference Co-Cr-LDH, measured at a

current density of  $1 \text{ A g}^{-1}$ . The CCV nanohybrid electrodes exhibit characteristic nonlinear GCD curves with some curvature due to reversible Faradaic reactions, as observed for the reference Co-Cr-LDH. Similar to CV behavior, CCV electrodes show higher discharge time than Co-Cr-LDH electrode, highlighting improved charge storing ability upon intercalative hybridization. In contrast to Csp of Co-Cr-LDH ( $591 \text{ C g}^{-1}$ ), upon the hybridization with POV anions, all of the CCV nanohybrids exhibit enhanced Csp of 620, 732, and  $662 \text{ C g}^{-1}$  for CCV-1, CCV-2 and CCV-3 samples, respectively (**Chapter - 3, equation 3.1**). To probe the faster charge transfer kinetics upon the POV intercalation, GCD performances of Co-Cr-LDH and CCV-2 nanohybrids are tested at various current densities from 1 to  $5 \text{ A g}^{-1}$ , as displayed in figure 4.14 (b, c). All the CCV nanohybrids display and maintain higher (Csp) at a current density of  $5 \text{ A g}^{-1}$  compared to pristine Co-Cr-LDH, highlighting the better rate capabilities of CCV nanohybrids. The enhanced (Csp) of CCV nanohybrids are attributed to the enlarged interlayer gallery height of Co-Cr-LDH via intercalation of bulky POV anions. Such an expanded interlayer gallery height allows an easy percolation of electrolyte ions at the interior of Co-Cr-LDH during the GCD course. Compared to mono-charged  $\text{NO}_3^-$  anions in reference Co-Cr-LDH, the tetra-charged  $\text{V}_4\text{O}_{12}^{4-}$  POV in CCV nanohybrids offer a high charge to size ratio that enables free gallery height between the intercalated anions. Such expanded free gallery height accelerates ion diffusion and allows easy percolation of electrolyte ions leading to remarkable improvement in Csp values.

Among the CCV nanohybrids, CCV-2 nanohybrid showed the (Csp) of  $732 \text{ C g}^{-1}$ , which can be ascribed to the more freely accessible gallery height compared to other CCV nanohybrids (figure 4.14 (d)) due to optimum POV anions intercalation. On the other hand, CCV-3 nanohybrid with surplus POV anions showed a detrimental influence on (Csp) due to the blocking of pores by the excess POV anions at the edges. Moreover, along with expanded gallery height of Co-Cr-LDH, the surface area expansion due to the stacking structure of the restacked LDH Ns offers mesoporous spaces of 10 to 80 nm. This high surface area mesoporous structure provides a synergistic effect for the ease percolation of electrolytes ions, thus enhancing the (Csp) of CCV nanohybrids. These results emphasize the advantages of electrostatically induced self-assembly between the Co-Cr-LDH monolayer Ns and POV anions to enhance electrochemical activity.

#### 4.7.3 Electrochemical impedance spectroscopy (EIS) study:

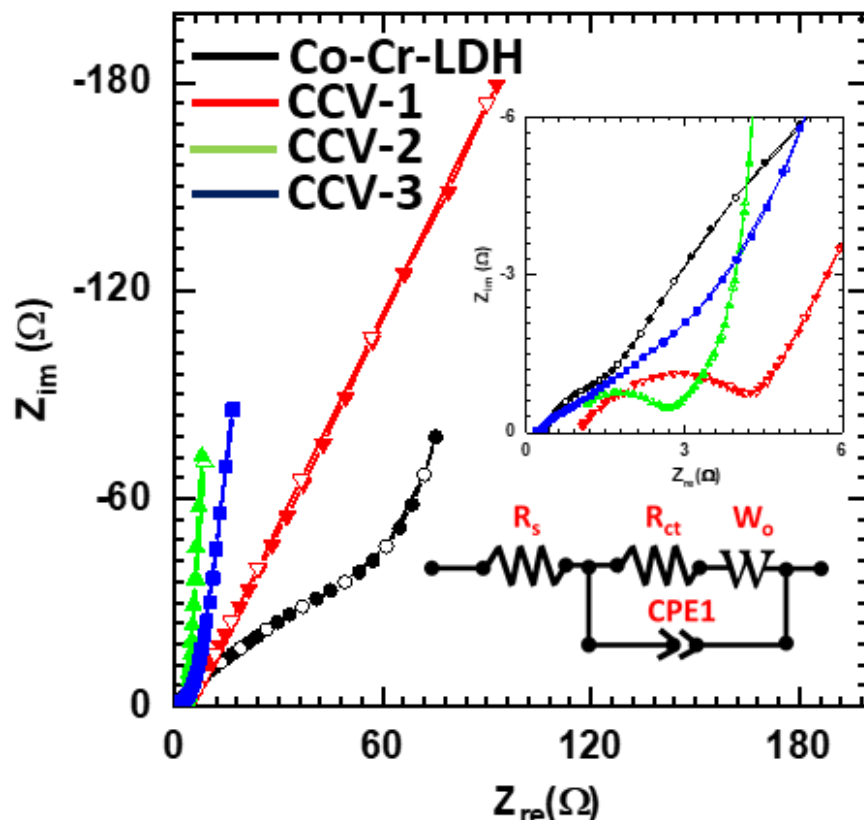


**Figure 4.15:** Nyquist plot of Co-Cr-LDH and CCV nanohybrids with the best fitted equivalent circuit, inset (high frequency region EIS spectrum).

The EIS analysis and corresponding Nyquist plots are presented in figure 4.15. As prepared CCV nanohybrids and reference Co-Cr-LDH electrodes collectively show a straight line at low-frequency and a semicircle at high-frequency regions. The starting point of the Nyquist plot represents series resistance ( $R_s$ ) and diameter of extrapolated semicircle represents charge transfer resistance ( $R_{ct}$ ). The POV intercalative hybridization of Co-Cr-LDH causes a significant reduction in the radius of semicircle in the Nyquist plot, which clearly indicates rapid and easy charge transfer kinetics upon the POV intercalation. Judging from the similar surface areas of the CCV nanohybrids, the sizes of semicircles are directly correlated with the electrical conductivity of the CCV nanohybrid electrodes. From the curve simulation and fitting analysis, all the CCV nanohybrids exhibit remarkably minimum  $R_s$  and  $R_{ct}$  values as compared to reference Co-Cr-LDH. The obtained  $R_s$  and  $R_{ct}$  values are 0.25  $\Omega$  and 2.85  $\Omega$  for CCV-1, 0.25  $\Omega$  and 2.84  $\Omega$  for CCV-2, 0.25  $\Omega$  and 3.9  $\Omega$  for CCV-3, and 0.25  $\Omega$  and 95  $\Omega$  for reference Co-Cr-LDH electrodes. Additionally, all the CCV nanohybrids

display steep slopes in low frequency region, indicating the lower electrolyte ion diffusion resistance (Warburg impedance). Consequently, the significantly improved CCV nanohybrids electrode performance is attributed to the expedited ion diffusion due to optimization of pore structure via POV intercalative hybridization. The present supercapacitive activity of CCV nanohybrids clearly highlights effectiveness of POV intercalative hybridization of Co-Cr-LDH as a redox electrode in HAS devices.

#### **4.8 Fabrication and supercapacitive performance of aqueous hybrid supercapacitor (AHSC) device: CCV-2||rGO**

##### ***Fabrication of CCV-2||rGO AHSC device***

The full-cell AHSC device was assembled by employing CCV-2 nanohybrid as a cathode and rGO Ns as an anode with 2M KOH as an electrolyte. The full cell AHSC assembly based on CCV nanohybrids and rGO Ns electrodes is presented in figure 4.16.

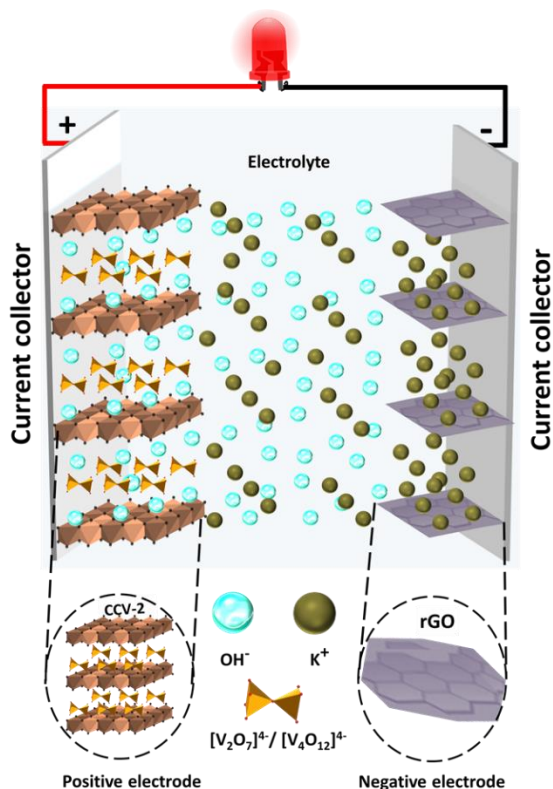


**Figure 4.16:** Schematic diagram of AHSC (Full cell) (CCV-2||rGO).

The beneficial EDLC-type electrochemical activity of rGO electrode in the negative potential window (0 to -1 V vs Hg/HgO) is tested using three-electrode system and obtained results are depicted in **Chapter-3, section-3.8**. As reflected

from three-electrode measurements, the CCV nanohybrid and rGO Ns electrode discern positive (-0.05 to 0.6 V vs Hg/HgO) and negative (0 to -1 V vs Hg/HgO) electrochemical active potential windows, respectively. Thus, a full-cell AHSC device is expected to operate in potential window of 0.00 to 1.65 V.

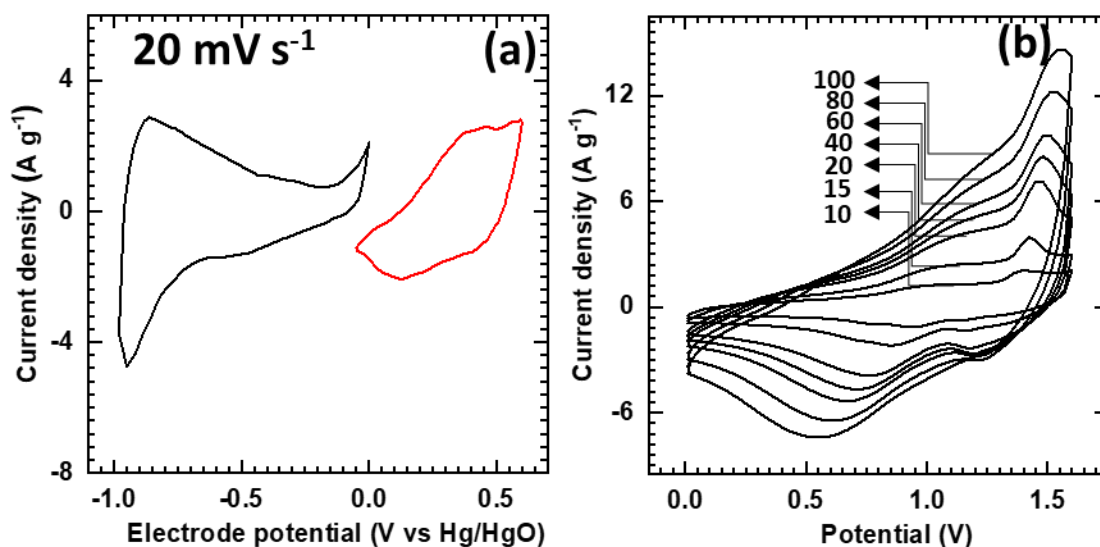
The important task for the fabrication of AHSC is to balance the masses of comprising electrodes before assembling the device; in which charges were balanced by adjusting the mass ratios of the positive and negative electrodes through equation 4.1.

$$\frac{m_+}{m_-} = \frac{C_- \cdot \Delta V_+}{C_+ \cdot \Delta V_-} \quad (4.1)$$

Where  $m_+$ ,  $C_+$ , and  $\Delta V_+$  are the mass, capacitance, and potential window for the positive electrode and  $m_-$ ,  $\Delta V_-$ , and  $C_-$  are the mass, capacitance, and potential window for the negative electrode. [22]

## 4.9 Result and discussion:

### 4.9.1 Cyclic voltammetry (CV) study:



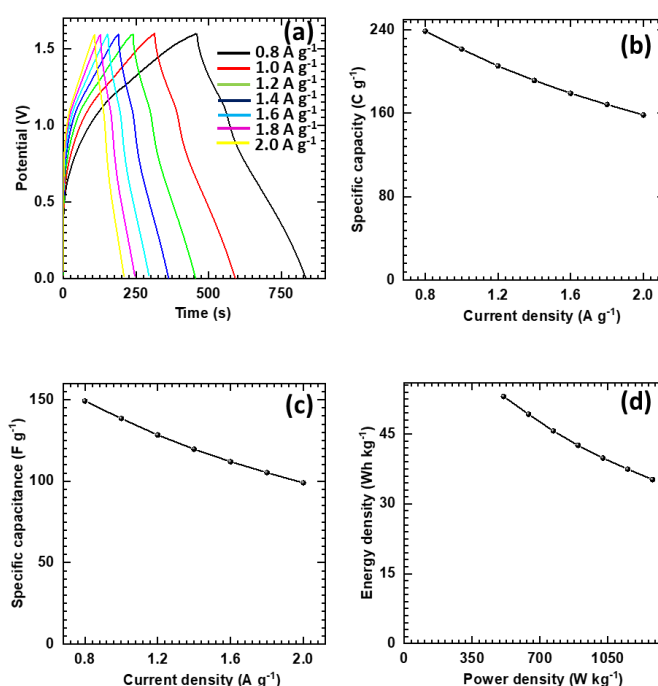
**Figure 4.17:** (a) Mass balance CV curves of rGO (black) and CCV-2 (red) at sweep rate  $20 \text{ mV s}^{-1}$ . (b) CV plot of the AHSC at different scanning rates (scan rates:  $10\text{-}100 \text{ mV}\cdot\text{s}^{-1}$ ) in voltage range from  $0\text{-}1.6 \text{ V}$ .

Figure 4.17 (a) depicts CV transients of CCV nanohybrids and rGO Ns electrodes at  $20 \text{ mV s}^{-1}$  scan rate in distinct potential windows. As CCV-2 and rGO electrodes possess various specific charge capacities, hence to maximize voltage window and  $C_{sp}$ , charge balance (**equation - 4.1**) is achieved via adjusting the

active electrode mass of both electrodes while assembling CCV-2||rGO AHSC device.

Judging from the charge balance calculations, the CCV-2 to rGO mass loading ratio is maintained at 1:3.9. Figure 4.17 (b) shows CV curves of the CCV-2||rGO AHSC device at various scan rates, which reveal pair of redox waves confirming both the capacitive and redox-type charge storage mechanisms. The CV curves replicate their shapes even at high scan rates of  $100 \text{ mV s}^{-1}$ , indicating fast redox reaction kinetics of the CCV-2 and rGO electrodes.

#### 4.9.2 Galvanostatic charge-discharge (GCD) study:



**Figure 4.18:** (a) GCD plot of the CCV-2||rGO at different current densities (current density: 0.8 (black), 1 (red), 1.2 (green), 1.4 (blue), 1.6 (cyan), 1.8 (magenta) and 2 (yellow)  $\text{A g}^{-1}$ ). (b) Variations of the  $C_{sp}$  of AHSC (Full cell) (CCV-2||rGO) with current density. (c) Variations of the  $C_s$  of AHSC (CCV-2||rGO) with current density. (d) Plot of ED against PD with their corresponding current densities.

The superior charge storing capabilities and fast delivery of the AHSC device is probed with GCD tests at various current densities, as shown in figure 4.18 (a). At all the charging-discharging current densities, the CCV-2||rGO AHSC device shows quasi-linear discharge plot with longer times of charge-discharge, demonstrating pseudocapacitive characteristics and high energy storing capacity. The  $C_{sp}$ s of CCV-2||rGO AHSC device assessed from the GCD curves based on the total mass of two electrodes are shown in figure 4.18 (b). Interestingly, CCV-

2||rGO AHSC device exhibits a  $C_{sp}$  of  $238.72 \text{ C g}^{-1}$  at  $0.8 \text{ A g}^{-1}$  and  $158.4 \text{ C g}^{-1}$  at  $2 \text{ A g}^{-1}$ , indicating excellent rate capability of CCV-2||rGO AHSC device (**equation 3.1, Chapter - 3**). As the shapes of GCD curves are approaching linear and pseudocapacitive nature, the electrochemical charge storage performance can be expressed in capacitive terminology. The calculated  $C_s$  values (**by using equation 3.2, Chapter - 3**) for various current densities are plotted as figure 4.18 (c). The SC performance of the recently reported Co-based LDH devices compared to the CCV-2||rGO AHSC device is shown in figure 4.19 and listed in Table 4.1. Based on the GCD curves, the ED and PD (figure 4.18 (d)) of CCV-2||rGO AHSC device for different current densities are calculated by using the following relations.

$$ED = \frac{C_s}{2} \frac{(\Delta V)^2}{3.6} \quad (4.2)$$

$$PD = ED \frac{3600}{\Delta t} \quad (4.3)$$

Where, ED is energy density (in  $\text{Wh kg}^{-1}$ ), PD is power density (in  $\text{W kg}^{-1}$ ).  $I$  is the applied current (in mA),  $\Delta t$  is the discharge time (in s),  $m$  is the mass of the active material (in mg) within the active area and  $\Delta V$  is the potential window (in V).

The CCV-2||rGO AHSC device delivers the ED of  $53.04 \text{ Wh kg}^{-1}$  with a PD of  $512 \text{ W kg}^{-1}$  at  $0.8 \text{ A g}^{-1}$ . Moreover, the CCV-2||rGO AHSC device continues to deliver the ED of  $35.2 \text{ Wh kg}^{-1}$  with an PD of  $1280 \text{ W kg}^{-1}$  at  $2 \text{ A g}^{-1}$ . Moreover, **Table 4.2** summarized the ED and PD of LDH based devices. Achieved values are excellent as compared to reported devices, like  $\text{Ni}_x\text{Co}_{1-x}\text{LDH-ZTO//AC}$  (ED:  $23.7 \text{ Wh kg}^{-1}$ ; PD:  $284.2 \text{ W kg}^{-1}$ ), [63]  $\text{KCu}_7\text{S}_4@\text{NiMn LDH//AG}$  (ED:  $15.9 \text{ Wh kg}^{-1}$ ; PD:  $9400 \text{ W kg}^{-1}$ ), [72]  $\text{ZIF-9@CoAl LDHs//activated carbon}$  (ED:  $32.1 \text{ Wh kg}^{-1}$ ; PD:  $1000 \text{ W kg}^{-1}$ ), [69]  $\text{NCLP@NiMn-LDH//AC}$  (ED:  $42.2 \text{ Wh kg}^{-1}$ ; PD:  $750 \text{ W kg}^{-1}$ ) [74],  $\text{NiO/Ni-Mn-LDH/AC ACS}$  (ED:  $27.8 \text{ Wh kg}^{-1}$ ; PD:  $401.3 \text{ W kg}^{-1}$ ), [75]  $\text{NiMn LDH@Co}_3\text{O}_4\text{//AG}$  (ED:  $26.49 \text{ Wh kg}^{-1}$ ; PD:  $350 \text{ W kg}^{-1}$ ), [76]  $\text{NiFe-LDH/MnO}_2\text{-16//AC}$  (ED:  $27.3 \text{ Wh kg}^{-1}$ ; PD:  $775.5 \text{ kW kg}^{-1}$ ) [77] and  $\text{H-OH-LDH//AC}$  (ED:  $44.8 \text{ Wh kg}^{-1}$ ; PD:  $850 \text{ kW kg}^{-1}$ ). [62] Present electrochemical activity of CCV-2||rGO

AHSC device shows the most state of the art aqueous symmetric, asymmetric and hybrid ES devices. [78-81]

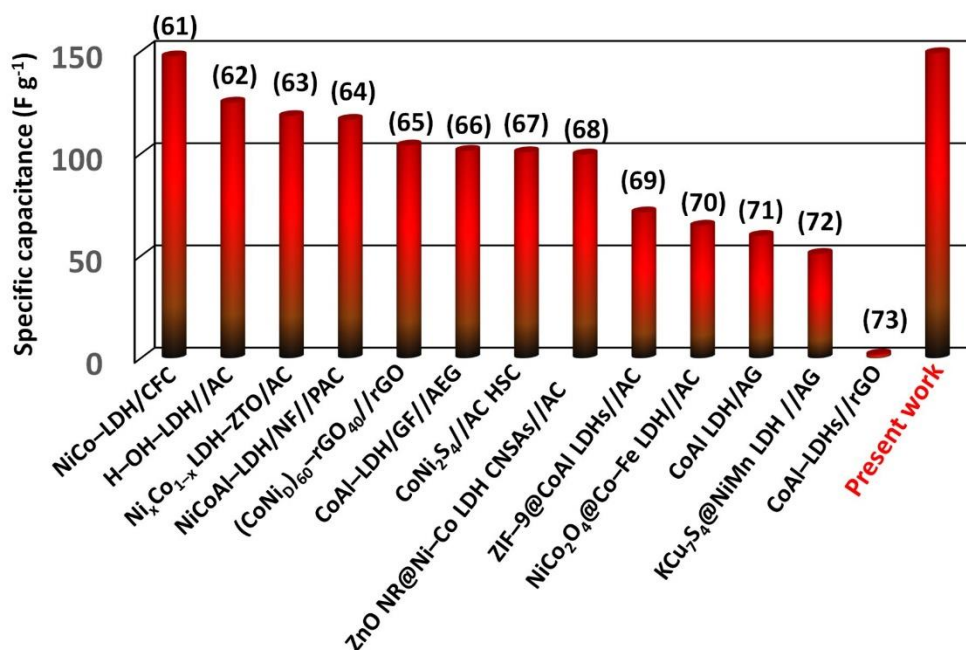


**Figure 4.19:** The literature survey of LDH-based AHSC devices (reference number are assigned in parenthesis).

## Synthesis, characterization and electrochemical performance of Co-Cr-LDH-POV and AHSC device

**Table 4.1:** Survey of supercapacitive performance of Co-based LDH devices

Sr. No.	Material	Method	Cs (F g <sup>-1</sup> ), Current density (A g <sup>-1</sup> )	ED (Wh kg <sup>-1</sup> )	Stability (%)	PD (W kg <sup>-1</sup> )	Cycles	Ref.
1	CoAl-LDHs//rGO	Hydrothermal	1.77 F cm <sup>-2</sup> , 2 mAcm <sup>-2</sup>	0.71 m Wh cm <sup>-2</sup>	92.9	17.05 mW cm <sup>-2</sup>	8000	73
2	KCu <sub>7</sub> S <sub>4</sub> @NiMn LDH //AG	Hydrothermal	51, 1	15.9	84.8	9.4 k	16000	72
3	CoAl LDH//AG	Hydrothermal	59.79, 1	16.27	87.57	3500	10000	71
4	NiCo <sub>2</sub> O <sub>4</sub> @Co-Fe LDH//AC	Hydrothermal	64.76, 1	28.94	76.9	950	5000	70
5	ZIF-9@CoAl LDHs//AC	Hydrothermal	71.3, 1	32.1	75	1000	5000	69
6	ZnO NR@Ni-CoLDH CNSAs//AC	Hydrothermal	99.6, 1	40.04	91.7	1118	5000	68
7	CoNi <sub>2</sub> S <sub>4</sub> //AC HSC	Hydrothermal	100.7, 1	35.8	132.3	800	50000	67
8	CoAl-LDH/GF//AEG	Hydrothermal	101.4, 0.5	28	~100	1420	5000	66
9	(CoNiD) <sub>60</sub> -rGO <sub>40</sub> //rGO	Co-precipitation	104, 2	52.8	95	2000	5000	65
10	NiCoAl-LDH/NF//PAC	Hydrothermal	116.56, 1	41.44	1.6	799.9	6000	64
11	Ni <sub>x</sub> Co <sub>1-x</sub> LDH-ZTO //AC	Electrochemical deposition	118.4 at 1.2 V. Working potential	23.7	92.7	284.2	5000	63
12	H-OH-LDH//AC	Hydrothermal	125, 1	44.8	92	0.85 k	2000	62
13	NiCo-LDH/CFC	Hydrothermal	147.6, 1	59.2	82	34 k	5000	61
<b>14</b>	<b>CCV-2  rGO AHSC</b>	<b>Self-assembly</b>	<b>149.2, 0.8</b>	<b>53.04</b>	<b>90</b>	<b>512</b>	<b>5000</b>	<b>Present work</b>

**Table 4.2:** Comparative ED and PD of LDH based devices.

<b>Sr. No.</b>	<b>Electrode material</b>	<b>ED (Wh kg<sup>-1</sup>)</b>	<b>PD (W kg<sup>-1</sup>)</b>	<b>Ref.</b>
1	Ni <sub>x</sub> Co <sub>1-x</sub> LDH-ZTO//AC	23.7	284.2	[73]
2	KCu <sub>7</sub> S <sub>4</sub> @NiMn LDH //AG	15.9	9400	[64]
3	ZIF-9@CoAl LDHs//AC	32.1	1000	[67]
4	NCLP@NiMn-LDH//AC	42.2	750	[74]
5	NiO/Ni-Mn-LDH/AC ACS	27.8	401.3	[75]
6	NiMn LDH@Co <sub>3</sub> O <sub>4</sub> //AG	26.49	350	[76]
7	NiFe-LDH/MnO <sub>2</sub> -16//AC	27.3	775.5	[77]
8	H-OH-LDH//AC	44.8	850	[74]
<b>9</b>	<b>CCV-2//rGO AHSC</b>	<b>53.04</b>	<b>512</b>	<b>Present work</b>

4.9.3 The capacitance retention, EIS, and demonstration of CCV-2||rGO AHSC device:

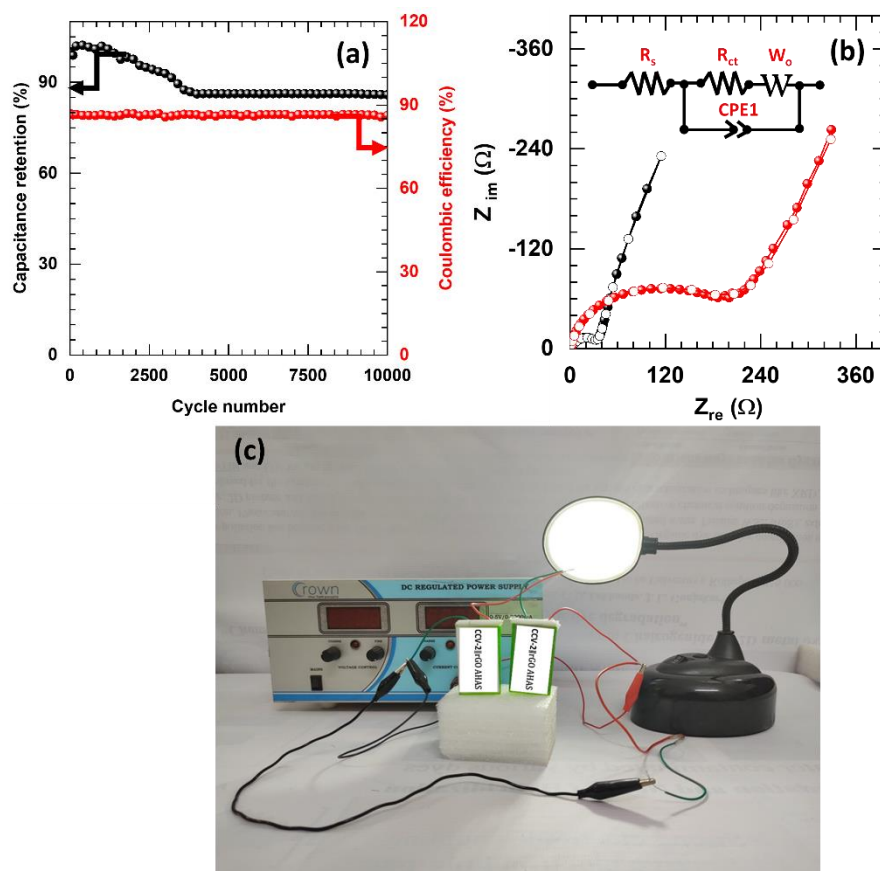


**Figure 4.20:** (a) The capacitance retention and columbic efficiency vs cycle numbers of CCV-2||rGO AHSC device. (b) The Nyquist plot of AHSC device before (black) and after (red) 10000 cycling performance with best fitted equivalent circuit. (c) Photograph of the developed CCV-2||rGO AHSC device.

The capacitance retention and Coulombic efficiency vs cycle number of CCV-2||rGO AHSC device subjected to 10000 GCD cycles are represented in figure 4.20 (a) (calculated by using the following relations).

$$CE = \frac{t_{discharge}}{t_{charge}} \quad (4.4)$$

Where CE is Coulombic efficiency,  $t_{charge}$  and  $t_{discharge}$  are the charging and discharging periods, respectively.

The CCV-2||rGO AHSC device demonstrated excellent electrochemical durability of up to 85% capacity retention and good Coulombic efficiency of about 86% after 10000 GCD cycles at a current density of  $6 \text{ A g}^{-1}$ , indicating its efficacy for the high-energy and power applications.

The excellent electrochemical performance of the CCV-2||rGO AHSC device is ascribable to the enlarged gallery height and mesoporous house-of-card morphology of the CCV-2 electrode. Further, the low resistance of the device is confirmed by the EIS analysis. As plotted in figure 4.20 (b), Nyquist plots for the CCV-2||rGO AHSC device before 10000 cycles show the  $R_s$  value of 1.39 and  $R_{ct}$  value of 34.2  $\Omega$ . However, after 10000 cycles CCV-2||rGO AHSC device show the  $R_s$  value of 2  $\Omega$  and  $R_{ct}$  value 205  $\Omega$ . The low  $R_s$  and  $R_{ct}$  values of CCV-2||rGO AHSC device reflects the crucial influence of POV intercalative hybridization in improving the charge transfer kinetics via superior conductivity and rapid ion diffusion during the electrochemical reactions. The outstanding rate capability and improved charge storage capacitance can be attributed to the rapid redox reactions, kinetic balance, and matching capacity of both the electrodes. The layer-by-layer stacking of Co-Cr-LDH and POV anions, mesoporous house-of-card morphology and the superior electrical conductivity of both electrodes are mainly responsible for such advantageous electrochemical properties. Eventually, real world application of the CCV-2||rGO AHSC device is shown by powering a light-emitting diode (LED) lamp as shown in figure 4.20 (c).

#### **4.10 Conclusions:**

In this chapter, a mesoporous layer-by-layer self-assembled CCV nanohybrids with promising electrode activity are prepared by self-assembly between the Co-Cr-LDH monolayer Ns and POV anions. Facile alteration of Co-Cr-LDH Ns and POV mixing proportions is an efficient way for tuning the type and amount of intercalated POV anions with high flexibility in chemical composition. The intimately coupled intercalative CCV nanohybrids showed much improved Csp ( $732 \text{ C g}^{-1}$ ) with high-rate capability than Co-Cr-LDH, highlighting the advantageous effect of POV intercalation via self-assembly on the electrode performance of Co-Cr-LDH. The remarkable electrochemical activity of CCV nanohybrids is credited to the expanded interlayer gallery space of Co-Cr-LDH upon restacking with the POV anions, superior electrical conductivity and high surface area house-of-card morphology that enable easy percolation of electrolyte ions and perform charge storing redox reaction with maximum utilization of interior electrode material. Considering the improved electrode functionality of POV intercalated Co-Cr-LDH, the present CCV nanohybrids are used to develop AHSC device, with CCV-2 nanohybrids as a positive and rGO as a negative electrode. The AHSC device delivered a maximum ED of  $53.04 \text{ Wh kg}^{-1}$  at a PD of  $512 \text{ W kg}^{-1}$  with high rate handling capability and exceptional capacitance retention of 85% over 10000 cycles. The present experimental findings demonstrate the effectiveness of the self-assembled hybridization between Co-Cr-LDH and POV anions for developing a new type of AHSC electrode with high ED and cycling life.

#### **4.11 References:**

1. P. Simon, Y. Gogosti, *Nat. Mater.*, 2020, 19, 1151–1163.
2. R. R. Salunkhe, J. Tang, Y. Kamachi, T. Nakato, J. H. Kim, Y. Yamauchi, *ACS Nano*, 2015, 9, 6288–6296.
3. J. Chimola, G. Yushin, Y. Gogosti, C. Portet, P. Simon, P. L. Teberna, *Science*, 2006, 313, 1760–1763.
4. B. E. Conway, Springer: US, Science Business Media, New York, 1999.
5. A. K. Thakur, M. S. Ahmed, G. Oh, H. Kang, Y. Jeong, R. Prabakaran, M. P. Vikram, S. W. Sharshir, J. Kim, J. Y. Hwang, *J. Mater. Chem. A*, 2021, 9, 2628–2661.
6. M. P. Down, S. J. Rowley-Neale, G. C. Smith, C. E. Banks, *ACS Appl. Energy Mater.*, 2018, 1, 707–714.
7. M. A. Bissett, S. D. Worrall, I. A. Kinloch, R. A. W. Dryfe, *Electrochim. Acta*, 2016, 201, 30–37.
8. R. Garg, A. Agarwal, M. Agarwal, *Mater. Res. Express*, 2020, 7, 022001.
9. S. M. Oh, S. J. Hwang, *J. Korean Ceram. Soc.*, 2020, 57, 119–134.
10. G. Pacchioni, *Nat. Rev. Mater.*, 2019, 4, 625.
11. S. Faraji, F. N. Ani, *J. Power Sources*, 2014, 263, 338–360.
12. M. Zhao, Q. Zhao, B. Li, H. Xue, H. Pang, C. Chen, *Nanoscale*, 2017, 9, 15206–15225.
13. L.-B. Jiang, X.-Z. Yuan, J. Liang, J. Zhang, H. Wang, G.-M. Zeng, *J. Power Sources*, 2016, 331, 408–425.
14. A. S. Patil, J. L. Gunjekar, C. D. Lokhande, U. M. Patil, S. V. Sadavar, N. S. Padalkar, R. B. Shinde, M. M. Wagh, J. S. Bagi, *Synth. Met.*, 2020, 264, 116371.
15. Q. Wang, D. O'Hare, *Chem. Rev.*, 2012, 112, 4124–4155.
16. M. V. Bukhtiyarova, *J. Solid State Chem.*, 2019, 269, 494–506.
17. M. Li, F. Liu, J. Cheng, J. Ying, X. B. Zhang, *J. Alloys Compd.*, 2015, 635, 225–232.
18. W. Xing, S. Qiao, X. Wu, X. Gao, J. Zhou, S. Zhuo, S. B. Hartono, D. H. Jurcakova, *J. Power Sources*, 2011, 196, 4123–4127.
19. S. Omwoma, W. Chen, R. Tsunashima, Y. F. Song, *Coord. Chem. Rev.*, 2014, 258–259, 58–71.
20. D. H. Park, S. J. Hwang, J. M. Oh, J. H. Yang, J. H. Choy, *Prog. Polym. Sci.*, 2013, 38, 1442–1486.
21. Y. Xiao, D. Su, X. Wang, S. Wu, L. Zhou, S. Fang, F. Li, *Sci. China Mater.*, 2018, 61, 263–272.
22. L. Wang, Z. H. Dong, Z. G. Wang, F. X. Zhang, J. Jin, *Adv. Funct. Mater.*, 2013, 23, 2758–2764.
23. J. L. Gunjekar, A. I. Inamdar, B. Hou, S. Cha, S. M. Pawar, A. A. Abu Talha, H. S. Chavan, J. Kim, S. Cho, S. Lee, Y. Jo, H. Kim, H. Im, *Nanoscale*, 2018, 10, 8953–8961.
24. J. L. Gunjekar, I. Y. Kim, J. M. Lee, Y. K. Jo, S. J. Hwang, *J. Phys. Chem. C*, 2014, 118, 3847–3863.
25. J. L. Gunjekar, T. W. Kim, I. Y. Kim, J. M. Lee, S. J. Hwang, *Sci. Rep.*, 2013, 3, 2080.
26. J. L. Gunjekar, I. Y. Kim, S. J. Hwang, *Eur. J. Inorg. Chem.*, 2015, 7, 2015, 1198–1202.
27. N. S. Padalkar, S. V. Sadavar, R. B. Shinde, A. S. Patil, U. M. Patil, D. S. Dhawale, H. M. Pathan, S. D. Sartale, V. G. Parale, A. Vinu, C. D. Lokhande, J. L. Gunjekar, *Adv. Mater. Interfaces*, 2021, 2101216.
28. R. Ma, Z. Liu, L. Li, N. Iyi, T. Sasaki, *J. Mater. Chem.*, 2006, 16, 3809–3813.

29. Z. Rezvani, F. A. Rad, F. Khodam, *Dalton Trans.*, 2015, 44, 988–996.
30. H. Asiabi, Y. Yamini, M. Shamsayei, *New J. Chem.*, 2018, 42, 9935–9944.
31. A. F. Al-Hossainy, A. Ibrahim, M. S. Zoromba, *J. Mater. Sci.:Mater. Electron.*, 2019, 30, 11627–11642.
32. S. K. Kiran, M. Padmini, H. T. Das, P. Elumalai, *J. Solid State Electrochem.*, 2017, 21, 927–938.
33. J. L. Gunjekar, B. Hou, A. I. Inamdar, S. M. Pawar, A. A. T. Ahmed, H. S. Chavan, J. Kim, S. Cho, S. Lee, Y. Jo, S.-J. Hwang, T. G. Kim, S. N. Cha, H. Kim, H. Im, *Small*, 2018, 14, 1703481–1703490.
34. R. A. Nyquist, C. Putzig, M. Leugers, Academic Press, Das Diego, CA, 1996.
35. M. Aureliano, C. A. Ohlin, M. O. Vieira, M. P. M. Marques, W. H. Casey, L. A. E. B. Carvalho, *Dalton Trans.*, 2016, 45, 7391–7399.
36. R. L. Frost, K. L. Erickson, M. L. Weier, O. Carmody, *Spectrochim. Acta. A Mol. Biomol. Spectrosc.*, 2005, 61, 829–834.
37. F. N. I. Sari, S. Abdillah, J.-M. Ting, *Chem. Eng. J.*, 2021, 416, 129165.
38. J. M. Vega, N. Granizo, D. de la Fuente, J. Simancas, M. Morcillo, *Prog. Org. Coat.*, 2011, 70, 213–219.
39. A. N. Salak, J. Tedim, A. I. Kuznetsova, J. L. Ribeiro, L. G. Vieira, M. L. Zheludkevich, M. G. S. Ferreira, *Chem. Phys.*, 2012, 397, 102–108.
40. J. L. Gunjekar, A. M. More, K. V. Gurav, C. D. Lokhande, *Appl. Surf. Sci.*, 2008, 254, 5844–5848.
41. C. Dong, X. Yuan, X. Wang, X. Liu, W. Dong, R. Wang, Y. Duan, F. Huang, *J. Mater. Chem. A*, 2016, 4, 11292–11298.
42. Yang, H. Liu, W. N. Martens, R. L. Frost, *J. Phys. Chem. C*, 2010, 114, 111–119.
43. F. N. I. Sari, K.-C. Lin, J.-M. Ting, *Appl. Surf. Sci.*, 2022, 576, 151805.
44. J. A. Koza, C. M. Hull, Y. C. Liu, J. A. Switzer, *Chem. Mater.*, 2013, 25, 1922–1926.
45. M. B. Nielsen, M. D. Allendorf, *J. Phys. Chem. A*, 2006, 110, 4093–4099.
46. Yang, W. N. Martens, R. L. Frost, *J. Raman Spectrosc.*, 2011, 42, 1142–1146.
47. A. S. O. Gomes, N. Yaghini, A. Martinelli, E. Ahlberg, *J. Raman Spectrosc.*, 2017, 48, 1256–1263.
48. R. L. Frost, M. L. Weier, J. T. Kloprogge, *J. Raman Spectrosc.*, 2003, 34, 760–768.
49. R. L. Frost, A. Soisnard, N. Voyer, S. Palmer, W. Martens, *J. Raman Spectrosc.*, 2009, 40, 645–649.
50. T. Tanaka, Y. Kameshima, S. Nishimoto, M. Miyake, *Anal. Methods*, 2012, 4, 3925–3927.
51. T. Kloprogge, D. Wharton, L. Hickey, R. L. Frost, *Am. Mineral.*, 2002, 87, 623–629.
52. M. C. Biesinger, C. Brown, J. R. Mycroft, R. D. Davidson, N. S. McIntyre, *Surf. Interface Anal.*, 2004, 36, 1550–1563.
53. J. Yang, A. G. Baker, H. Liu, W. N. Martens, R. L. Frost, *J. Mater. Sci.*, 2010, 45, 6574–6585.
54. S. Wu, X. Yang, J. Hu, H. Ma, Z. Lin, C. Hu, *Cryst. Eng. Comm.*, 2015, 17, 1625–1630.
55. G. Silversmit, D. Depla, H. Poelman, G. B. Marin, R. D. Gryse, *J. Electron Spectrosc.*, 2004, 135, 167–175.

56. W. Ma, W. J. Lee, J. M. Bae, K. S. Jeong, S. H. Oh, J. H. Kim, S. H. Kim, J. H. Seo, J. P. Ahn, H. Kim, M. H. Cho, *Nano Lett.*, 2015, 15, 7204–7210.
57. B. Condon, Elsevier, Amsterdam, Boston, 2006.
58. A. Gaber, M. A. A.-Rahim, A. Y. A.-Latief, M. N. A.-Salam, *Int. J. Electrochem. Sci.*, 2014, 9, 81-95.
59. I. G. Casella, M. Gatta, *J. Electroanal. Chem.*, 2002, 534, 31-38.
60. D. Perera, X. Ding, A. Bhargava, R. Hovden, A. Nelson, L. F. Kourkoutis, R. D. Robinson, *Chem. Mater.*, 2015, 27, 7861–7873.
61. T. Wang, S. Zhang, M. Lyu, L. Wang, J. Bell, H. Wang, *ACS Appl. Mater. Interfaces*, 2017, 9, 15510–15524.
62. X. Liu, A. Zhou, T. Pan, Y. Dou, M. Shao, J. Han, M. Wei, *J. Mater. Chem. A*, 2016, 4, 8421–8427.
63. X. Wang, A. Sumboja, M. Lin, J. Yan, P. S. Lee, *Nanoscale*, 2012, 4, 7266–7272.
64. P. Li, Y. Jiao, S. Yao, L. Wang, G. Chen, *New J. Chem.*, 2019, 43, 3139–3145.
65. P. Makkar, N. N. Ghosh, *ACS Omega*, 2020, 5, 10572–10580.
66. T. M. Masikhwa, M. J. Madito, D. Y. Momodu, J. K. Dangbegnon, O. Guellati, A. Harat, M. Guerioune, F. Barzegara, N. Manyala, *RSC Adv.*, 2016, 6, 46723–46732.
67. L. Yang, X. Lu, S. Wang, J. Wang, X. Guan, X. Guan, G. Wang, *Nanoscale*, 2020, 12, 1921–1938.
68. X. Liu, H. Liu, X. Sun, *Cryst. Eng. Comm.*, 2020, 22, 1593–1601.
69. G. Wang, Y. Li, Z. Jin, *New J. Chem.*, 2020, 44, 7528–7540.
70. W. Q. Chen, J. K. Wang, Y. Ma, M. Li, S. H. Guo, F. Liu, J. P. Cheng, *Appl. Surf. Sci.*, 2018, 451, 280–288.
71. C. Jing, X. Liu, H. Yao, P. Yan, G. Zhao, X. Bai, B. Dong, F. Dong, S. Li, Y. Zhang, *Cryst. Eng. Comm.*, 2019, 21, 4934–4942.
72. X. L. Guo, J. M. Zhang, W. N. Xu, C. G. Hu, L. Sun, Y. X. Zhang, *J. Mater. Chem. A*, 2017, 5, 20579–20587.
73. S. Li, P. Cheng, J. Luo, D. Zhou, W. Xu, J. Li, R. Li, D. Yuan, *Nano–Micro Lett.*, 2017, 9, 31.
74. H. Liang, J. Lin, H. Jia, S. Chen, J. Qi, J. Cao, T. Lin, W. Fei, J. Feng, *J. Mater. Chem. A*, 2018, 6, 15040–15046.
75. P.-F. Liu, J.-J. Zhou, G.-C. Li, M.-K. Wu, K. Tao, F.-Y. Yi, W.-N. Zhao, L. Han, *Dalton Trans.*, 2017, 46, 7388–7391.
76. H. Peng, C. Jing, J. Chen, D. Jiang, X. Liu, B. Dong, F. Dong, S. Lif, Y. Zhang, *Cryst. Eng. Comm.*, 2019, 21, 470–477.
77. W. Zheng, S. Sun, Y. Xu, R. Yu, H. Li, *J. Alloys Compd.*, 2018, 768, 240–248.
78. W. Zhang, C. Ma, J. Fang, J. Cheng, X. Zhang, S. Dong, L. Zhang, *RSC Adv.*, 2013, 3, 2483–2490.
79. T. X. Nguyen, Y.-C. Liao, C.-C. Lin, Y.-H. Su, J.-M. Ting, *Adv. Funct. Mater.*, 2021, 31, 2101632.
80. F. N. I. Sari, J.-M. Ting, *Electrochim. Acta*, 2019, 320, 134533.
81. F. N. I. Sari, J.-M. Ting, *Chem. Sus. Chem.*, 2018, 11, 897-906.



# CHAPTER-5

**SYNTHESIS,  
CHARACTERIZATION AND  
ELECTROCHEMICAL  
PERFORMANCE OF Co-Cr-LDH-  
POW AND AHSC DEVICE**

# CHAPTER-5

## Synthesis, Characterization and Electrochemical Performance of Co-Cr-LDH-POW and AHSC Device

Sr. No.	Title	Page No.
5.1	Introduction	133
5.2	Synthesis and characterization of Co-Cr-LDH-POW	133
5.3	Experimental details	133
	5.3.1 Chemicals	133
	5.3.2 Synthesis of Co-Cr-LDH-POW	133
5.4	Characterization of Co-Cr-LDH-POW	134
	5.4.1 XRD analysis	135
	5.4.2 FTIR analysis	136
	5.4.3 Raman analysis	137
	5.4.4 FESEM analysis	138
	5.4.5 EDS analysis	139
	5.4.6 TEM analysis	140
	5.4.7 XPS analysis	141
	5.4.8 N <sub>2</sub> adsorption-desorption (BET analysis)	143
5.5	Conclusions	145
5.6	Electrochemical performance of Co-Cr-LDH-POW	146
5.7	Results and discussion	146
	5.7.1 Cyclic voltammetry (CV) study	146
	5.7.2 Galvanostatic charge-discharge (GCD) Study	148
	5.7.3 Electrochemical Impedance (EIS) Study	149
5.8	Fabrication and electrochemical performance of aqueous hybrid supercapacitor (AHSC) device: CCW-2//rGO	150
5.9	Results and Discussion	151
	5.9.1 Cyclic voltammetry (CV) study	151
	5.9.2 Galvanostatic charge-discharge (GCD) study	152
	5.9.3 Electrochemical impedance (EIS) study	155
5.10	Conclusions	156
5.11	References	157

## **5.1 Introduction:**

The need and benefits of nanohybridization for improving the electrode performance of Co-Cr-LDH are described in the previous chapters (**Chapter 1, section 1.5, Chapter-2, section 2.3.3 and Chapter 3, section 3.1**). In this background, the POM anions derived from the controlled hydrolysis of early transition metals with exceptional redox properties, precise surface charge, and molecular size can be the most suitable guest species for the electrostatic self-assembly with Co-Cr-LDH Ns. To improve the electrode performance of Co-Cr-LDH, the polyoxotungstate (POW) anions with exceptional redox properties, precise surface charge, and molecular size are selected for the electrostatic self-assembly with positively charged Co-Cr-LDH Ns.

The present chapter deals with the exfoliation-reassembling route to achieve unusually high electrochemical activity by exploiting high surface area mesoporous nanohybrids of Co-Cr-LDH-POW (CCW) nanohybrids. Furthermore, the evolution of various physicochemical properties of Co-Cr-LDH upon the hybridization with POW anions are investigated together with the accompanying improvement in the electrode performance. Finally, the AHSC device is developed using CCW nanohybrid as positive and rGO as negative electrode.

## **5.2 Synthesis and characterization of Co-Cr-LDH-POW:**

### **5.3 Experimental details:**

#### **5.3.1 Chemicals:**

Co(NO<sub>3</sub>)<sub>2</sub>·6H<sub>2</sub>O, Cr(NO<sub>3</sub>)<sub>3</sub>·9H<sub>2</sub>O, NaOH, NaNO<sub>3</sub>, HNO<sub>3</sub>, sodium tungstate (Na<sub>2</sub>WO<sub>4</sub>·2H<sub>2</sub>O), graphite flakes, PVDF, NMP, PVA and KOH were purchased from Sigma-Aldrich. SS substrates (304 grade) were served as a current collector to prepare the Co-Cr-LDH and CCW nanohybrid electrodes.

#### **5.3.2 Synthesis of Co-Cr-LDH-POW:**

The pristine nitrate intercalated Co-Cr-LDH and exfoliated Co-Cr-LDH Ns were synthesized using the synthesis protocol described in **Chapter-3, section 3.2.3** and the results of physicochemical and electrochemical characterizations are compared with the CCW nanohybrids. [1] POW anion solution was obtained by pH-controlled hydrolysis of 0.1 M Na<sub>2</sub>WO<sub>4</sub>·2H<sub>2</sub>O. [2-3] The pH of the POW solution was adjusted by 0.1 M HNO<sub>3</sub>. The self-assembled CCW nanohybrids were synthesized by mixing Co-Cr-LDH Ns suspension and POW anion solution under constant

---

## Synthesis, characterization and electrochemical performance of Co-Cr-LDH-POW and AHSC device

stirring. The schematic presentation of the CCW nano hybrids synthesis process is shown in figure 5.1. The subsequent flocculation products of CCW nano hybrids were immediately collected by centrifugation, cleaned with formamide and absolute ethanol. Finally, to ensure solid CCW nano hybrid product freeze-drying process was adopted. All the processes were done with decarbonated water and under inert ( $N_2$ ) atmosphere to avoid contamination of Co-Cr-LDH and CCW nano hybrids from  $CO_3^{2-}$  anions. The various chemical compositions of CCW nano hybrid were attained by changing the mixing molar ratio of Co-Cr-LDH Ns and POW anions solution. The CCW nano hybrids prepared at Co-Cr-LDH/( $Na_2WO_4 \cdot 2H_2O$ ) molar ratios of 3.43, 1.72, and 1.14 are denoted as CCW-1, CCW-2, and CCW-3, respectively.

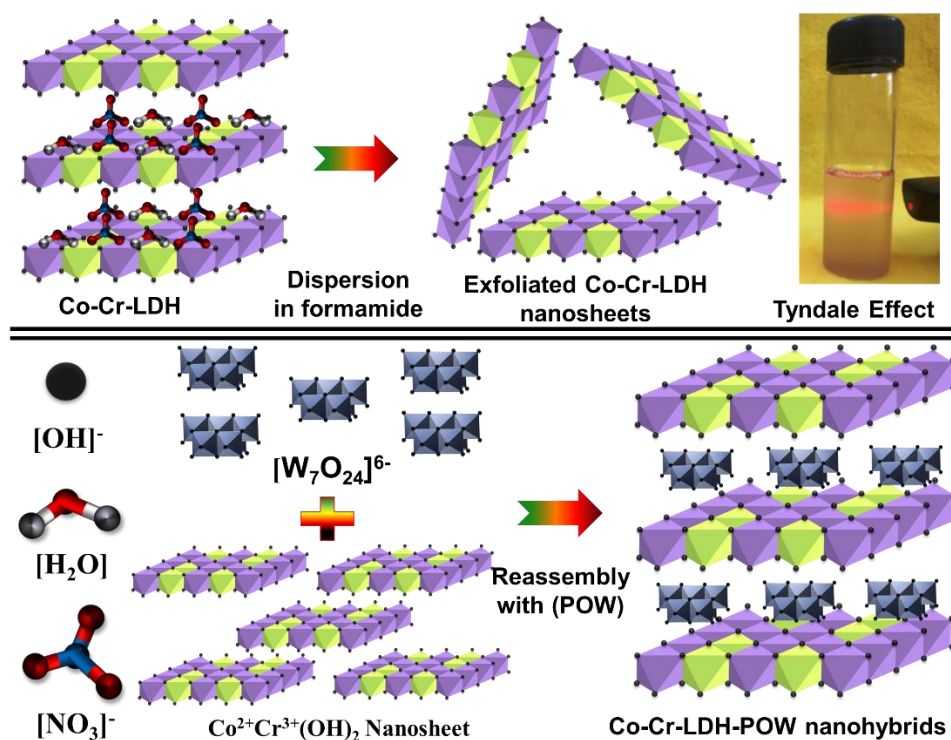


**Figure 5.1:** Schematic illustration for the formation of self-assembly between Co-Cr-LDH and POW anions by the exfoliation-restacking method.

### 5.4 Characterizations of Co-Cr-LDH-POW:

The pristine Co-Cr-LDH and the self-assembled CCW nano hybrids were characterized by various physicochemical characterization techniques as described in **Chapter-3, section 3.3**. The CCW electrode preparation and electrochemical performance evaluation were studied by a similar protocol as described in **Chapter-3, section 3.5**.

### 5.4.1 XRD analysis:

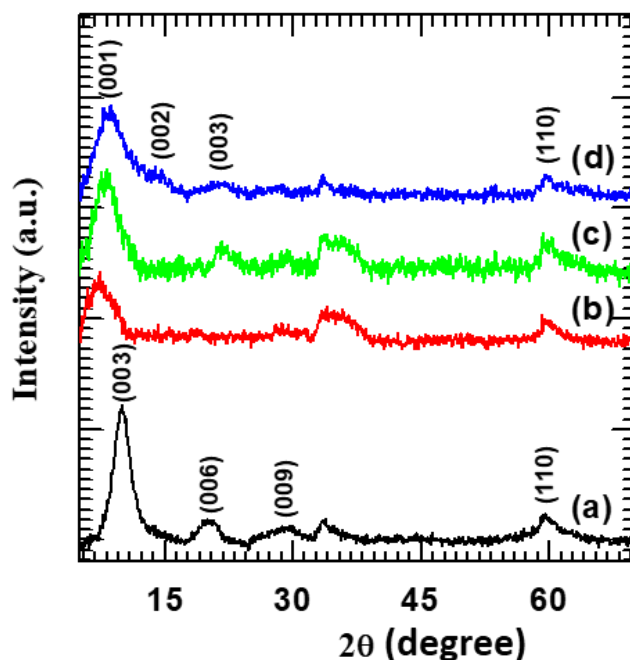


**Figure 5.2:** PXRD patterns of (a) Co-Cr-LDH and (b) CCW-1, (c) CCW-2 and (d) CCW-3 nanohybrids.

The PXRD patterns of Co-Cr-LDH and CCW nanohybrids are plotted in figure 5.2. The phase analysis of Co-Cr-LDH is described in **Chapter-3, section 3.3.1**. Analogous to Co-Cr-LDH, all CCW nanohybrids exhibit a well-resolved series of  $(00l)$  Bragg reflections which shows the development of layer-by-layer-stacked intercalated compounds. Interestingly, this  $(00l)$  series significantly shifted towards lower diffraction angles, indicating the expansion of basal spacing due to layer-by-layer stacking of Co-Cr-LDH Ns and POW anions. Such shifting can be observed in all CCW nanohybrids irrespective of their LDH/POW reactant ratio, indicating no distinct dependence of the basal spacing on the chemical composition. [4-6] This result demonstrates the high tolerance of the host LDH lattice for the variation of guest concentration and offers increased flexibility to tune the chemical composition of CCW nanohybrids. The in-plane  $(110)$  peak at  $2\theta = 60^\circ$  of hexagonal LDH phase and a broad hump at  $2\theta = 32-42^\circ$  are also discernible for CCW nanohybrids, revealing the maintenance of the in-plane structure of Co-Cr-LDH Ns with disordered stacking structure. [7] The lattice parameters of CCW nanohybrids are calculated by least-square fitting analysis. The estimated in-plane lattice parameters  $a(=b) = 0.31$  nm and  $c = 0.88$  nm are consistent with in-plane lattice parameters of pristine LDH, indicating maintenance of the in-plane LDH

## Synthesis, characterization and electrochemical performance of Co-Cr-LDH-POW and AHSC device

structure in hybrid samples. The expanded basal spacing of CCW nanohybrids are: CCW-1 (1.20 nm), CCW-2 (1.11 nm), and CCW-3 (1.06 nm). Thus, referring to the LDH Ns thickness of 0.48 nm, the corresponding gallery heights of CCW-1, CCW-2, and CCW-3 are 0.72, 0.63, and 0.58 nm, respectively. Present expanded gallery height of  $\sim 0.7$  nm corresponds to the stabilization of  $W_7O_{24}^{6-}$  anions with a c-axis perpendicular to the LDH layers. [8] The slight variation of gallery height with Co-Cr-LDH/POW molar ratio may be attributed to the diverse interactions between the POW anions and Co-Cr-LDH Ns. The average crystallite size of  $\sim 4-6$  nm along the c-axis is estimated using Scherrer calculations at the FWHM of the (001) reflections. Referring to the basal spacing of the CCW nanohybrids calculated from the XRD study (1.1 nm), the obtained crystallite thickness is equivalent to the  $\sim 4-6$  Co-Cr-LDH monolayers restacked with POW anions.

### 5.4.2 FTIR analysis:

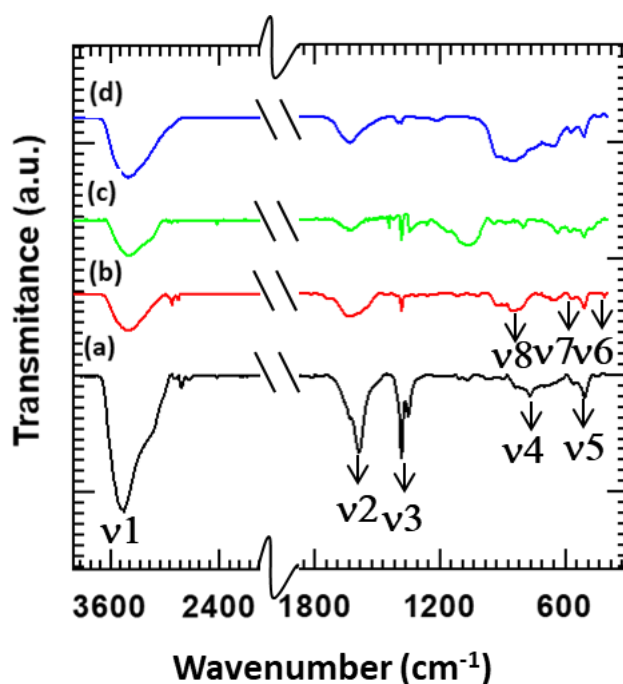


**Figure 5.3:** FTIR spectra of (a) Co-Cr-LDH, (b) CCW-1, (c) CCW-2 and (d) CCW-3 nanohybrids.

The chemical bonding nature of intercalated POW anions and their effect on Co-Cr-LDH are studied using FTIR spectroscopy. Figure 5.3 represents the FTIR spectra of Co-Cr-LDH and CCW nanohybrids. The FTIR analysis of Co-Cr-LDH is described in **Chapter-3, section 3.3.2**. Upon the hybridization with the POW anions, the resulting CCW nanohybrids show additional absorption peaks at  $v_6$  ( $440\text{ cm}^{-1}$ ),  $v_7$  ( $570\text{ cm}^{-1}$ ) and  $v_8$  ( $823\text{ cm}^{-1}$ ). The peak at  $v_6$  is associated with the

Co-O stretching. At the same time, peaks at  $\nu_7$  ( $570\text{ cm}^{-1}$ ) and  $\nu_8$  ( $823\text{ cm}^{-1}$ ) are related with the W-O bending and W-O-W stretching vibrations of  $\text{WO}_4^{2-}$  units in POW anions, respectively. [9-13] The presence of these IR features validates the presence of  $\text{WO}_4^{2-}$  units in POW anions and the intactness of Co-Cr-LDH Ns in CCW nanohybrids.

#### 5.4.3 Raman analysis:

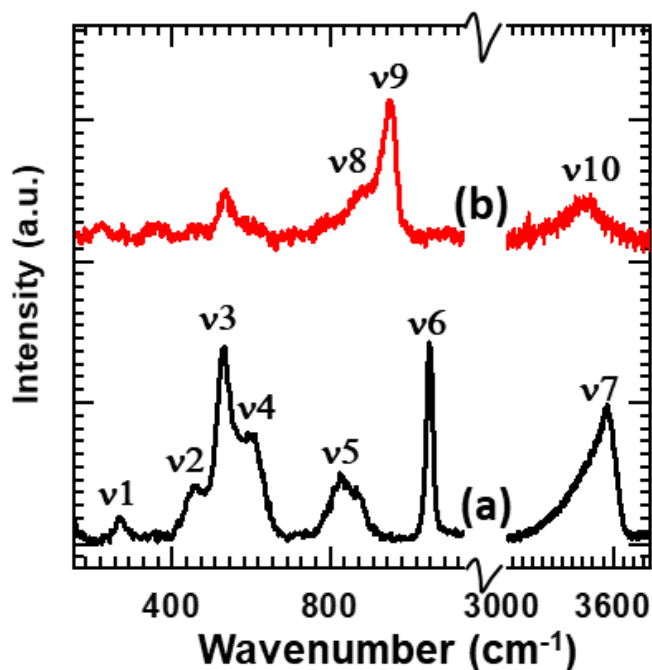


**Figure 5.4:** Micro-Raman spectra of (a) Co-Cr-LDH and (b) CCW-2 sample.

The microscopic structural properties of the CCW nanohybrids and pristine Co-Cr-LDH are further studied with Raman spectroscopy, as displayed in figure 5.4. The Raman analysis of Co-Cr-LDH is described in Chapter-3, section 3.3.3. CCW-2 nanohybrid and pristine Co-Cr-LDH commonly display Raman peaks  $\nu_1$  ( $265\text{ cm}^{-1}$ ),  $\nu_2$  ( $455\text{ cm}^{-1}$ ),  $\nu_3$  ( $530\text{ cm}^{-1}$ ), and  $\nu_4$  ( $600\text{ cm}^{-1}$ ), which are attributed to the  $E_g(T)$ ,  $O\text{CoO}$  ( $A_{1g}$ ) bending,  $\text{CoO}$  ( $A_{2u}$ ) symmetric stretching, and  $E_g(R)$  modes of host Co-Cr-LDH, respectively. [14-16] Additionally, CCW-2 nanohybrid display highly intense Raman peak at  $\nu_8$  ( $874\text{ cm}^{-1}$ ) and shoulder peak at  $\nu_9$  ( $950\text{ cm}^{-1}$ ), attributed to the symmetric W=O and anti-symmetric W=O vibrational modes of edge-sharing  $\text{WO}_4^{2-}$  units of POW anions, respectively. [17] The absence of characteristic peak ( $1055\text{ cm}^{-1}$ ) related to the nitrate anions in CCW nanohybrids indicates negligible nitrate contamination. The internal O-H stretching modes from the lattice OH and the intrasheet water molecules is displayed by the broad

signature peak around  $\nu_7$  ( $3575\text{ cm}^{-1}$ ). The  $\text{NO}_3^-$  intercalated Co-Cr-LDH phase with the incorporation of  $\text{H}_2\text{O}$  molecules is confirmed by the obtained Raman features. [18-21] The observed Raman features related to POW anions indicate the intercalative stabilization of  $\text{W}_7\text{O}_{24}^{6-}$  anions in Co-Cr-LDH.

#### 5.4.4 FESEM analysis:

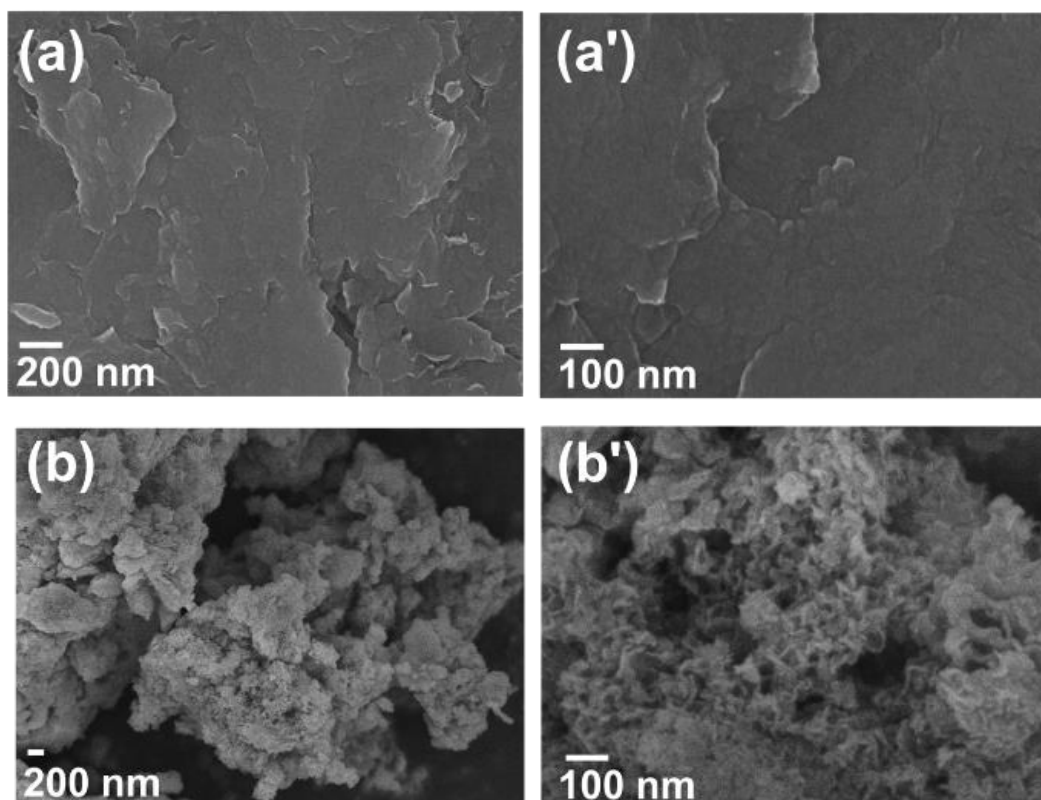


**Figure 5.5:** FESEM images of (a, a') Co-Cr-LDH and (b, b') CCW-2 nanohybrid at various magnifications (20000x and 100000x).

The surface morphological study of Co-Cr-LDH and CCW nanohybrids is investigated with FESEM analysis, as shown in figure 5.5. The surface microstructural analysis of Co-Cr-LDH is described in Chapter-3, section 3.3.4. As shown in figure 5.5, the self-assembled CCW-2 nanohybrid display highly porous nanoclusters made by randomly arranged Ns network making a petal-bunch appearance. This interconnected network forms slit-shaped pores deep inside the bulk of the material, leading to unusual porosity in the CCW nanohybrids. A close examination of restacked nanosheet crystallites at high magnification discloses thickness of  $\sim 8$  to 20 nm and lateral size between  $\sim 60$  to 110 nm. This type of surface feature is reported for the self-assembled Ns-based hybrids, which offer advantages of high percolation of electrolyte with low ion diffusion resistance

when used as an electrode in the electrochemical energy storage devices. [20, 22-24]

#### 5.4.5 EDS analysis:

The chemical composition and the distribution of constituent elements of Co-Cr-LDH and CCW nanohybrids are probed using the elemental mapping and EDS analyses (figure 5.6 and figure 5.7). The EDS-elemental mapping analysis of Co-Cr-LDH is described in Chapter-3, section 3.3.5. The chemical compositions of CCW nanohybrids are estimated as  $\text{Co}_{0.65}\text{Cr}_{0.35}(\text{OH})_2 \cdot 0.054(\text{W}_7\text{O}_{24}) \cdot y\text{H}_2\text{O}$ ,  $\text{Co}_{0.66}\text{Cr}_{0.34}(\text{OH})_2 \cdot 0.078(\text{W}_7\text{O}_{24}) \cdot y\text{H}_2\text{O}$ , and  $\text{Co}_{0.65}\text{Cr}_{0.35}(\text{OH})_2 \cdot 0.08(\text{W}_7\text{O}_{24}) \cdot y\text{H}_2\text{O}$  for CCW-1, CCW-2, and CCW-3 nanohybrids, respectively. All CCW nanohybrids display the uniform distribution of Co, Cr and W elements at the nanometer scale, indicating highly homogeneous intercalation of POW without any special phase separation. [4]

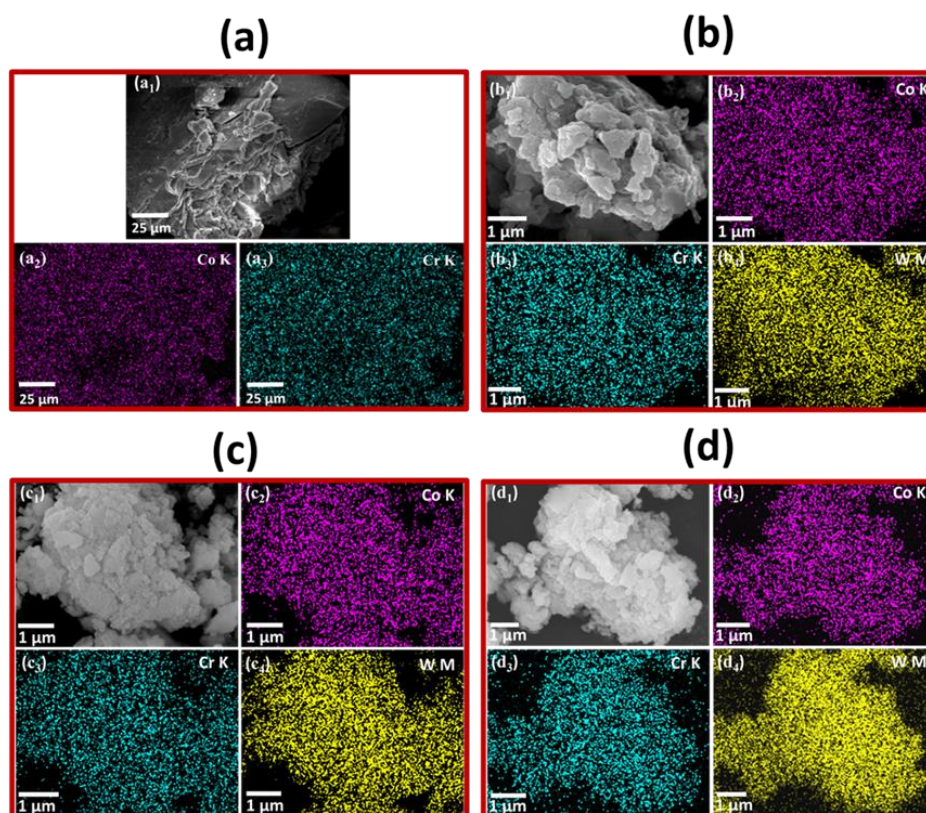


**Figure 5.6:** EDS-elemental maps of the (a) Co-Cr-LDH, (b) CCW-1, (c) CCW-2, and (d) CCW-3 nanohybrids.

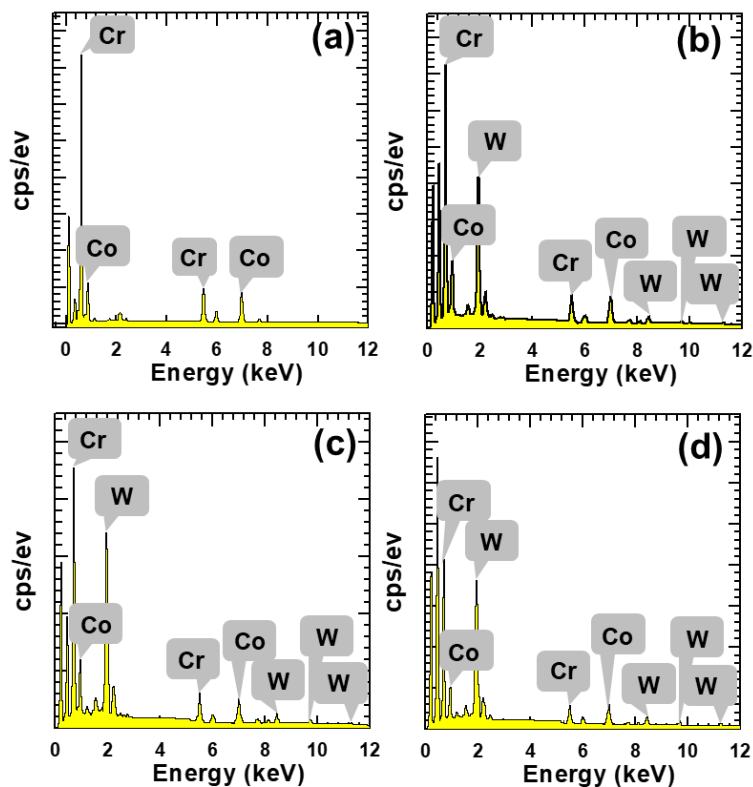


**Figure 5.7:** Energy dispersive X-ray spectroscopy (EDS) of (a) Co-Cr-LDH, (b) CCW-1, (c) CCW-2 and (d) CCW-3.

#### 5.4.6 TEM analysis:

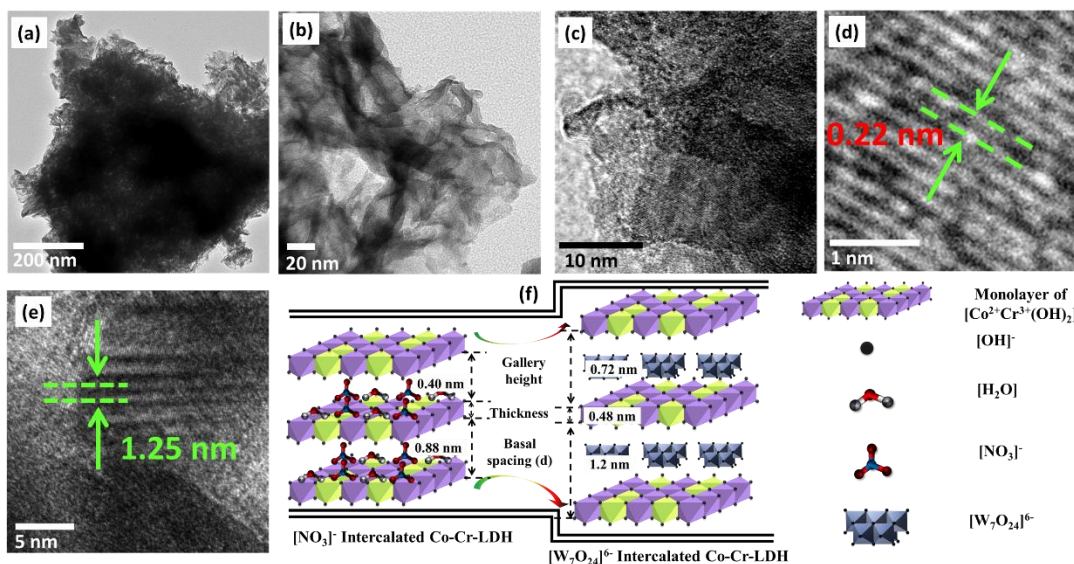


**Figure 5.8:** (a, b) Top-view TEM, (c, d) top-view HRTEM and (e) Cross-sectional HRTEM images of CCW-2 nanohybrid. (f) Structural model of Co-Cr-LDH and CCW nanohybrid.

The local crystal structure, shape and stacking order of CCW nanohybrids are examined by the HRTEM analysis. As shown in figure 5.8 (a, b), TEM images at low magnification show an interconnected Ns network composed of restacked CCW crystallites. The formation of a Ns network composed of edge-to-face

interaction leading the evolution of slit shape pores that can be visible at the edges of the nanohybrid sample. At high-resolution in figure 5.8 (d-e), two types of equally-spaced parallel-aligned lattice fringes can be clearly observable. One set of fringes equispaced by 0.22 nm corresponds to the in-plane Co-Cr-(OH)<sub>2</sub> Ns lattice. This set is extended over a wide range (>50 nm), confirming high in-plane crystallinity of restacked Co-Cr-(OH)<sub>2</sub> Ns. The other set observed in the cross-section is extended over a short range of 6-7 nm, with an interline distance of 1.25 nm. The observed interline distance in the cross-sectional view is well consistent with the c-axis parameter estimated from the XRD study. Obtained results validate the layer-by-layer stacking of Co-Cr-LDH Ns and POW anions with expanded basal spacing. Analogous structural and stacking features are reported for the nanohybrids prepared by the exfoliation-restacking route of Ns and nanoclusters. [4, 19]

#### 5.4.7 XPS analysis:

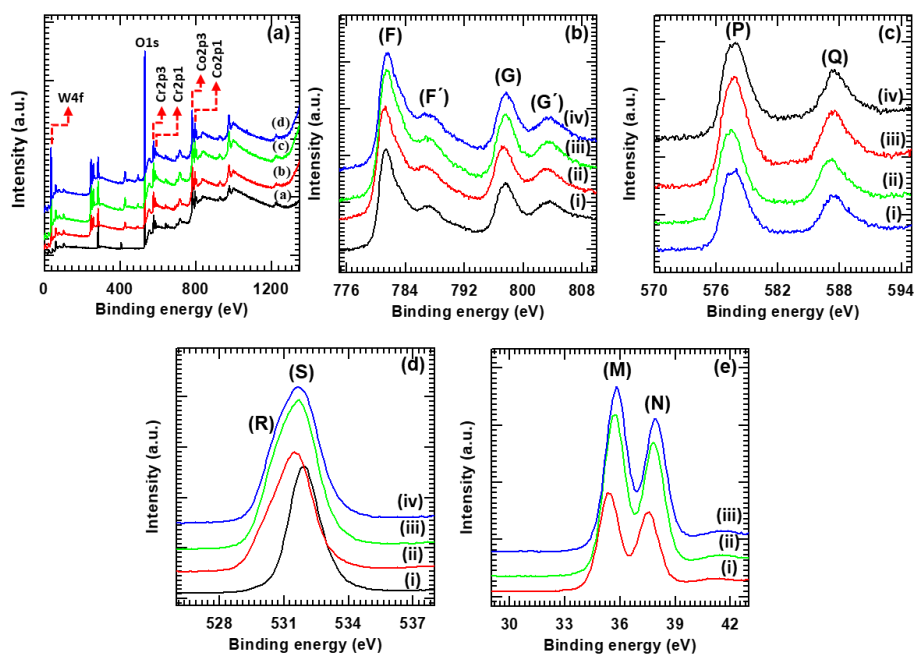


**Figure 5.9:** Chemical states of the pristine material and nanohybrids. XPS spectra of (a) survey (b) Co 2p, (c) Cr 2p, (d) O 1s core levels of the (i) Co-Cr-LDH, (ii) CCW-1, (iii) CCW-2, and (iv) CCW-3 and (e) W 4f core levels of the (i) CCW-1, (ii) CCW-2, and (iii) CCW-3

The surface chemical composition, diverse oxidation states of stabilized POW anions, and their influence on the chemical bonding nature of the pristine Co-Cr-LDH structure are studied using XPS measurements. The survey XPS spectra commonly display spectral features of the Co, Cr, and O elements for CCW

## Synthesis, characterization and electrochemical performance of Co-Cr-LDH-POW and AHSC device

---

nanohybrids and pristine Co-Cr-LDH, with additional elemental (W) features in nanohybrids (figure 5.9 (a)). The XPS analysis of Co-Cr-LDH is described in Chapter-3, section 3.3.6. The high-resolution Co 2p, Cr 2p, O 1s, and W 4f core-level XPS spectra of CCW nanohybrids and pristine Co-Cr-LDH are presented in figure 5.9 (b-e). As shown in figure 5.9 (b), all of the CCW nanohybrids and pristine Co-Cr-LDH commonly display intense peaks at F (781.46 eV) and G (797.53 eV) with their satellite peaks at F' (787.95 eV) and G' (803.26 eV) discernable to the spin-orbit splitting into Co 2p<sub>3/2</sub> and Co 2p<sub>1/2</sub>, respectively. [24-26] The binding energy difference (16.2 eV) of peaks P and Q can be regarded as an indicator for Co<sup>2+</sup> in Co-Cr-LDH. As shown in figure 5.9 (c), the high-resolution Cr 2p spectrum shows P (577.6 eV) and Q (587.3 eV) peaks, that arised due to spin orbit splitting of Cr 2p<sub>3/2</sub> and Cr 2p<sub>1/2</sub> components. The binding energy of broad peak P (577.52 eV) is associated with the trivalent chromium. [27] Figure 5.9 (d) shows the O 1s spectra of Co-Cr-LDH and CCW nanohybrids. The pristine Co-Cr-LDH shows a sharp peak at S (531.62 eV), corresponding to the characteristic signals of surface hydroxyl group, oxygen in M-O lattice, and bound water. [28] Conversely, CCW nanohybrids display complex XPS features at peak S (531.62 eV), which is formed by the superposition of peak R (530.33 eV) and S (531.62 eV). The peak R (530.33 eV) is visible only for CCW nanohybrids which can be attributed to the W-O bond of POW anions. [29] The high-resolution W 2p XPS spectra for CCW nanohybrids are shown in figure 5.9 (e). All of the CCW nanohybrids revealed two spectral features at M (35.78 eV) and N (37.97 eV) due to spin-orbit splitting of W 4f<sub>7/2</sub> at M (35.78 eV) and W 4f<sub>5/2</sub> at N (37.97 eV). These features correspond to the presence of W<sup>6+</sup> centers bonded to oxygen (W-O bond), typically observed in POW anions. [30-31] The obtained XPS features gives relevant sign about the presence of Co<sup>2+</sup>, Cr<sup>3+</sup>, and W<sup>6+</sup> states in CCW nanohybrids.

### 5.4.8 N<sub>2</sub> adsorption-desorption (BET analysis):

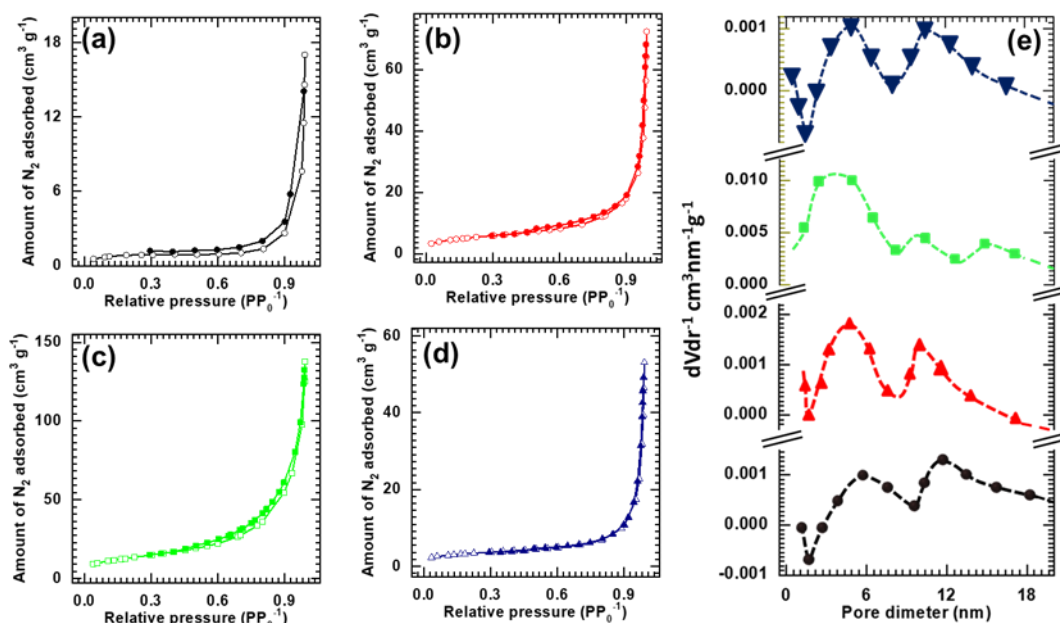


**Figure 5.10:** N<sub>2</sub> adsorption-desorption isotherms for (a) Co-Cr-LDH, (b) CCW-1, (c) CCW-2, (d) CCW-3 and (e) Pore size distribution curves for (black) Co-Cr-LDH, (red) CCW-1, (green) CCW-2 and (blue) CCW-3. In (a, b, c), the open symbols represent the adsorption and closed symbols represent desorption data.

The effect of POW hybridization on the surface area and pore structure of the CCW nanohybrids is probed with N<sub>2</sub> adsorption-desorption isotherm analysis as shown in figure 5.10 (a-d). The N<sub>2</sub> adsorption-desorption analysis of Co-Cr-LDH is described in **Chapter-3, section 3.3.7**. From figure 5.10 (a, b, c, d), the CCW nanohybrids show significant N<sub>2</sub> adsorption at  $pp_0^{-1} < 0.4$  and distinct hysteresis at  $pp_0^{-1} > 0.45$  characteristic of the mesoporous materials. [7, 33] According to the IUPAC classification, the observed isotherm shape and hysteresis behavior can be classified as H3-type hysteresis loops and BDDT type-IV isotherm shapes. The presence of H3-type hysteresis and type-IV isotherm is a typical characteristic of a possibly macroporous material with high adsorption energy and interconnected slit-shaped pores. This combination also indicates the presence of open, slit-shaped capillaries [34-35] The Co-Cr-LDH, CCW-1, CCW-2 and CCW-3 nanohybrid demonstrate surface areas of 5, 17.92, 45.77 and 11.41 m<sup>2</sup> g<sup>-1</sup>, respectively. Obtained result demonstrates the efficacy of POW-assisted intercalative hybridization by the self-assembly process for enhancing the surface area of the LDH.

The distribution of pore size is estimated by BJH method for the desorption branch, as shown in figure 5.10 (e). As a result, along with mesoporous character, the

## **Synthesis, characterization and electrochemical performance of Co-Cr-LDH- POW and AHSC device**

---

Co-Cr-LDH, CCW-1, CCW-2 and CCW-3 nanohybrids exhibit an average pore diameters of ~ 31.23, 23.77, 17.16, and 28.07 nm, respectively. These results indicate that the porosity in CCW nanohybrids originates from the porous petal-bunch surface morphology. Obtained results clearly showed the crucial importance of the self-assembly process for improving the pore structure of the resulting intercalative CCW nanohybrid. [7]

### **5.5 Conclusions:**

In present study, a mesoporous layer-by-layer ordered self-assembled nanohybrids of 2D Co-Cr-LDH intercalated with 0D POW anions (CCW nanohybrids) were synthesized by an exfoliation-reassembling method. The CCW nanohybrids were characterized by XRD, FESEM, FTIR, Raman, EDS, XPS, and N<sub>2</sub> adsorption-desorption (BET) analysis to study crystal structure, chemical bonding, and surface textural as well as compositional properties. The CCW nanohybrids displayed layer-by-layer stacking of Co-Cr-LDH Ns and POW anions with high surface area morphology. The exfoliation-restacking approach of hybridization provided control over the chemical composition and porous structure of resulting CCW nanohybrids. The rational growth of the intercalated CCW nanohybrids resulted into the development of an interconnected Ns morphology with a highly porous structure whose porosity was controlled by adjusting the ratio of Co-Cr-LDH and POW.

## 5.6 Electrochemical performance of Co-Cr-LDH-POW:

### 5.7 Result and discussion:

#### 5.7.1 Cyclic voltammetry (CV) study:

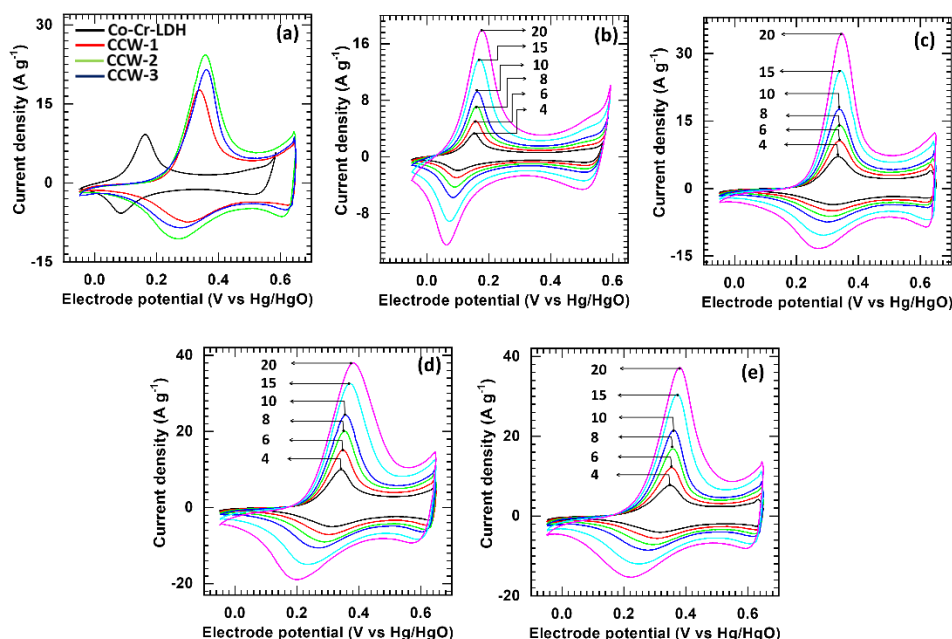


**Figure 5.11:** (a) The CV plot of Co-Cr-LDH and CCW nanohybrids at a sweep rate of  $10 \text{ mV s}^{-1}$ . CV plot of the (b) Co-Cr-LDH, (c) CCW-1, (d) CCW-2 and (e) CCW-3 nanohybrids at various scan rates ( $4\text{--}20 \text{ mV s}^{-1}$ ).

The effects of POW intercalation on the electrochemical activity of host Co-Cr-LDH are examined using CV, GCD, and EIS techniques. The three-electrode electrochemical set-up is described in **Chapter 3, section 3.5**. The CCW nanohybrid electrode was used as a working electrode in three-electrode electrochemical set-up. Herein, the electrochemical results of the Co-Cr-LDH in Chapter-3 are compared with the CCW nanohybrids. Figure 5.11 (a) represents the CV plot of Co-Cr-LDH and CCW electrodes at  $10 \text{ mV s}^{-1}$ . All CCW nanohybrid electrodes display distinct redox peaks corresponding to oxidation-reduction reactions between  $\text{Co}(\text{OH})_2$  and  $\text{CoOOH}$ . [33-36] The supercapacitive activity of these electrodes principally originated from pseudocapacitive nature based on reversible oxidation-reduction mechanism according to redox reaction described by **Chapter-3, equation 3.3**.

The CV curves of CCW nanohybrids show the markedly larger integral area under CV curves and higher current responses, indicating superior electrochemical activity than pristine Co-Cr-LDH electrode. Furthermore, the integral area under CV

## Synthesis, characterization and electrochemical performance of Co-Cr-LDH-POW and AHSC device

curves varies with intercalated POW content. Among the CCW electrodes, CCW-2 nano hybrid discerns the largest integral area, highlighting its higher electrochemical activity due to optimum intercalation of POW anions. Moreover, this nano hybrid exhibits a higher surface area and smaller pore diameter, leading to higher electrochemical activity via easy percolation of electrolytic ions at the electrode-electrolyte interface. CV profiles of all CCW nano hybrids and Co-Cr-LDH at different sweep rates ( $4\text{-}20\text{ mV s}^{-1}$ ) are displayed in figure 5.11(b-e). Present CCW nano hybrids and reference Co-Cr-LDH display increased area under CV curve and the shifting of cathodic peaks toward more positive potentials with scan rates. The present results indicate a hybrid charge storage mechanism such as pseudocapacitive and diffusion-controlled (battery-type) charge storage components. As the current responses in CV curves are arisen by the surface-capacitive ( $Q_s$ ) and diffusion-controlled ( $Q_d$ ) charges, the component of each can be resolved via electrochemical kinetics study by considering the **equation 3.4 in Chapter - 3**.

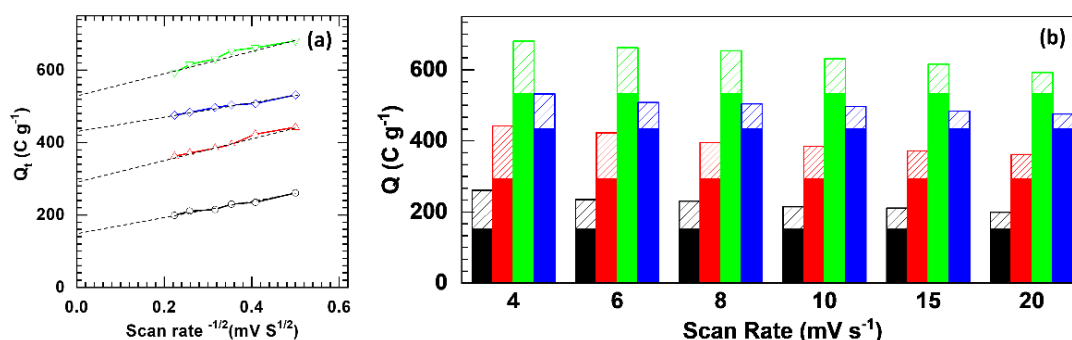


**Figure 5.12:** (a) Plot of total charge ( $Q_t$ ) vs the reciprocal of the square root of the scan rate ( $v^{-1/2}$ ). (b) The fraction of the capacitive (solid) and diffusion-controlled (pattern) contributions of Co-Cr-LDH (black), CCW-1 (red), CCW-2 (green) and CCW-3 (blue) nano hybrids.

The surface capacitive charge ( $Q_s$ ) can be resolved by  $Q_t$  vs  $(v)^{-1/2}$  as shown in figure 5.12 (a). The analysis ignores the high scan rates above  $20\text{ mV s}^{-1}$  to avoid polarization effects. [35] All the electrodes demonstrate prominent  $Q_s$  contributions at higher scan rates, whereas  $Q_d$  contributions are prominent at low scan rates. At low sweep rate of  $4\text{ mV s}^{-1}$ , the  $Q_s$  contributions of 66 % (CCW-1), 78 % (CCW-2), and 81 % (CCW-3) are evidenced for CCW nano hybrids as compared to pristine Co-Cr-LDH (58 %) at the same scan rate. Whereas, at a higher scan rate of  $20\text{ mV s}^{-1}$ , CCW nano hybrid electrodes exhibited markedly higher  $Q_s$

## Synthesis, characterization and electrochemical performance of Co-Cr-LDH-POW and AHSC device

contributions of 80, 89, and 91 % for CCW-1, CCW-2, and CCW-3 nanohybrids, respectively (figure 5.12 (b)). The capacitive dominant charge contributions observed for CCW nanohybrids can be attributed to the accelerated charge transfer kinetics due to the high surface area and expanded LDH gallery height of CCW nanohybrids.

### 5.7.2 Galvanostatic charge discharge (GCD) study:

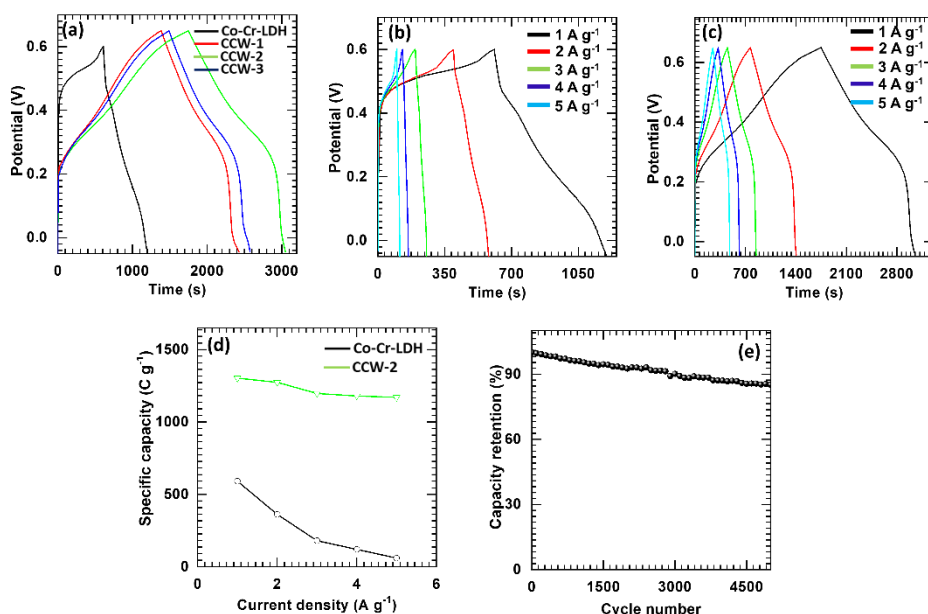


**Figure 5.13:** (a) GCD plot of Co-Cr-LDH and CCW nanohybrids at a constant current density  $1 \text{ A g}^{-1}$ . GCD plot of (b) Co-Cr-LDH and (c) CCW-2 nanohybrid at various current densities (current density:  $1\text{-}5 \text{ A g}^{-1}$ ). (d) The calculated  $C_{sp}$  of pristine Co-Cr-LDH and CCW nanohybrids at various current densities (current density:  $1\text{-}5 \text{ A g}^{-1}$ ). (e) Capacity retention of the CCW-2 electrode at current density of  $10 \text{ A g}^{-1}$ .

GCD measurements are further used to evaluate the electrochemical performance of CCW nanohybrids and Co-Cr-LDH electrodes. Figure 5.13 (a) shows that, all the tested electrodes typically exhibit characteristic quasi-linear charge-discharge behavior indicating pseudocapacitive charge storage due to reversible Faradaic reactions. Furthermore, all the CCW nanohybrids display prolonged charging-discharging periods compared to Co-Cr-LDH underscoring nanohybrids' enhanced charge storage ability. The  $C_{sp}$  values obtained from GCD analysis are  $591, 1045, 1303$  and  $1088 \text{ C g}^{-1}$  for Co-Cr-LDH, CCW-1, CCW-2 and CCW-3 electrodes, respectively (**Chapter - 3, equation 3.1**). All the CCW nanohybrid electrodes demonstrate considerably higher  $C_{sp}$ s than the pristine Co-Cr-LDH. They are highlighting the advantages of POW intercalation for improving the electrochemical activity of pristine Co-Cr-LDH. The highest  $C_{sp}$  of the CCW-2

electrode with an intermediate Co-Cr-LDH/POW precursor ratio is due to the best-optimized POW content amongst the present CCW nanohybrid electrodes. These findings elucidate the significant role of intercalated POW anions in improving the electrochemical activity of Co-Cr-LDH electrodes. In addition, a petal-bunch morphology of CCW nanohybrids offer mesopores of  $\sim 30$  to  $95$  nm that lead to the easy diffusion of electrolyte ions and contribute more redox reactions.

The GCD curves of CCW-2 nanohybrid and pristine Co-Cr-LDH at various current densities ( $1$  to  $5$  A  $g^{-1}$ ) are measured to assess the fast rate capability of CCW-2 nanohybrid (figure 5.13 (b, c)). The Csp's of pristine Co-Cr-LDH and CCW-2 nanohybrid are shown in figure 5.13 (d). Interestingly, as reference to Co-Cr-LDH, CCW-2 retain exceptional Csp's at higher current density ( $5$  A  $g^{-1}$ ), indicating a superior rate capability of CCW-2 nanohybrid. Such a superior rate capability upon the POW intercalation can be ascribed to the accelerated diffusion of electrolyte ions via mesopores formed by the interconnected Ns morphology and expanded interlayer gallery height ( $\sim 0.18$  to  $\sim 0.32$  nm) of nanohybrids. Moreover, the CCW-2 nanohybrid electrode exhibits capacity retention of  $85.43\%$  after the stability test, indicating its long-term stability (figure 5.13 (e)).

### 5.7.3 Electrochemical impedance spectroscopy (EIS) study:

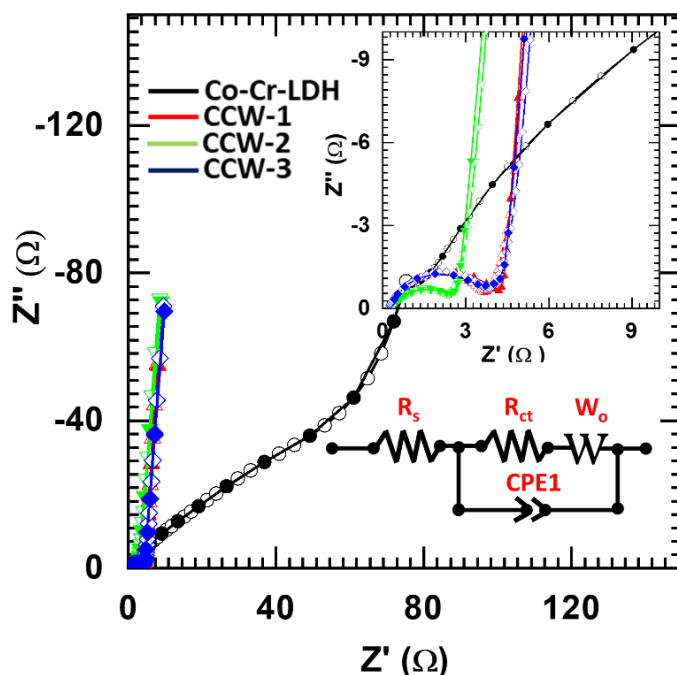


**Figure 5.14:** Nyquist plot of Co-Cr-LDH and CCW nanohybrids with the best fitted equivalent circuit, inset (high frequency region EIS spectrum).

## **Synthesis, characterization and electrochemical performance of Co-Cr-LDH-POW and AHSC device**

---

Furthermore, properties like  $R_s$ ,  $R_{ct}$  and Warburg impedance are estimated using EIS measurements. As shown in figure 5.14, Nyquist plots for Co-Cr-LDH and CCW nanohybrid electrodes typically exhibit partially overlapping semicircles and straight lines in the high-frequency and low-frequency regions, respectively. The x-axis intercept and diameter of the extrapolated semicircle are linked to the  $R_s$  and  $R_{ct}$ , respectively. [36] The observed stiff slope due to electrolyte ion diffusion of Co-Cr-LDH and CCW nanohybrid electrodes confirms its lower resistance (Warburg impedance). As compared to Co-Cr-LDH, CCW nanohybrids exhibited smaller diameters of extrapolated semicircles, indicating accelerated charge transfer kinetics and improved electrical conductivity after POW intercalation. The  $R_s$  and  $R_{ct}$  values of Co-Cr-LDH and CCW nanohybrid electrodes are estimated using simulation and fitting analysis. The estimated  $R_s$  and  $R_{ct}$  values are 0.25  $\Omega$  and 95  $\Omega$  for Co-Cr-LDH, 0.28  $\Omega$  and 4.1  $\Omega$  for CCW-1, 0.3  $\Omega$  and 2.4  $\Omega$  for CCW-2, and 0.25  $\Omega$  and 3.01  $\Omega$  for CCW-3 electrodes. Amongst the CCW nanohybrids, CCW-2 nanohybrid display the smallest semicircle signifying the optimum POW content for enhancing the electrochemical activity of nanohybrids. Moreover, the Nyquist plots of CCW nanohybrids in low-frequency regions display steeper slopes of the straight lines than pristine Co-Cr-LDH. This indicates a minimum resistance (Warburg impedance) to the diffusion of electrolyte ions and prominent capacitive behavior of nanohybrids. Thus, the significantly improved electrode performance of the CCW nanohybrids is not only attributed to the expanded surface area and gallery height but also to the enhanced electrical conductivity and electrolyte ion diffusion. Considering the exceptional performance of CCW nanohybrids, the best-optimized CCW-2 electrode is further employed to fabricate full-cell AHSC.

### **5.8 Fabrication and electrochemical performance of aqueous hybrid supercapacitor (AHSC) device: CCW-2//rGO**

#### ***Fabrication of CCW-2//rGO AHSC***

The AHSC is fabricated using CCW-2 nanohybrid as a positive (cathode) electrode and rGO Ns as a negative (anode) electrode, with an aqueous 2M KOH electrolyte.

The hydrothermally prepared rGO is selected as a negative (anode) electrode due to its excellent EDLC-type charge storage and electrochemical stability. [37] The electrochemical activity of rGO Ns electrode is studied using a

three-electrode system in a 2 M KOH electrolyte. As rGO Ns electrode is well studied for its charge storage mechanism like EDLC-type, its electrochemical activity in negative potential window (0 to -1 V vs Hg/HgO) is tested using the three-electrode system in 2 M KOH electrolyte. The obtained results of CV, GCD and EIS are displayed in **Chapter-3, section – 3.8.** [38]

## 5.9 Results and discussion:

### 5.9.1 Cyclic voltammetry (CV) study:

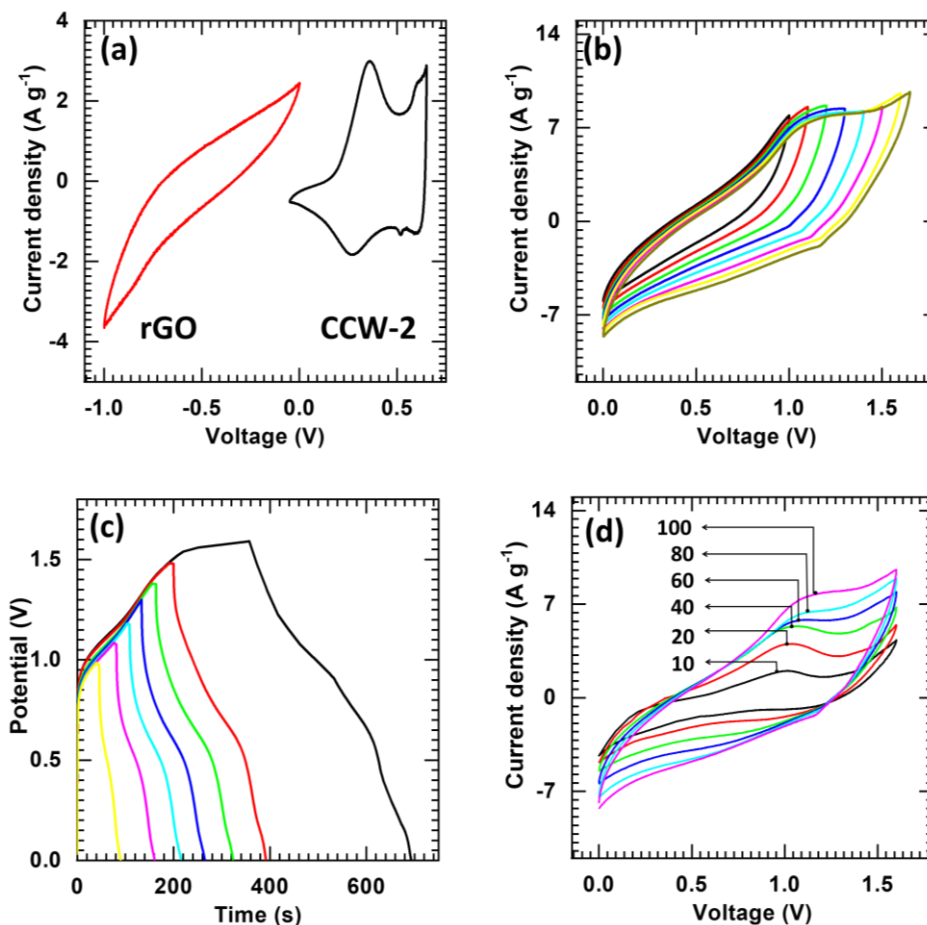


**Figure 5.15:** Electrochemical characteristics of CCW-2//rGO AHSC. (a) Mass balance CV plot of rGO (black) and CCW-2 (red) at sweep rate of 20 mV s<sup>-1</sup>. (b) CV plot of the AHSC at various potential windows from 0.0 to +1.0 and 0.0 to +1.65 V at a sweep rate of 100 mV s<sup>-1</sup>. (c) GCD plots of AHSC at different operating potential windows from 0-1 to 0-1.6 V. (d) CV curves of the AHSC at different scanning rates (scan rates: 10-100 mV s<sup>-1</sup>) collected in voltage range from 0 to 1.6 V.

The half-cell electrochemical analysis of CCW-2 and rGO electrodes indicates different C<sub>sp</sub>s associated with them. Therefore, to achieve optimum potential window and high C<sub>sp</sub> of AHSC, the charge balance between the CCW-2 and rGO electrodes is achieved by adjusting their mass ratio using **Chapter-4, equation 4.1.** According to the charge balance calculations, the CCW-2/rGO mass

## Synthesis, characterization and electrochemical performance of Co-Cr-LDH-POW and AHSC device

ratio is calculated as 0.39. Judging from the operating potential windows of CCW-2 (-0.05 to + 0.65 V vs Hg/HgO) and rGO (-1 to 0 V vs Hg/HgO) electrodes, the AHSC is projected to operate up to a potential window of 0 to 1.65 V (figure 5.15 (a)). The actual operating potential window for AHSC is determined by measuring CV curves at various potential windows ranging from 0-1.0 to 0-1.65 V at a scan rate of 100 mV s<sup>-1</sup> (figure 5.15 (b)). As a result, the AHSC displays stable operation up to +1.6 V without any significant electrolyte polarization, indicating that the optimal and safe operating potential window can be extended to 0 to +1.6 V. Moreover, the operating potential window for AHSC is additionally confirmed by the GCD measurements for different potential windows ranging from 0-1 to 0-1.6 V at current density of 0.8 A g<sup>-1</sup> (figure 5.15 (c)).

Figure 5.15 (d) displays the CV curves of the AHSC at various scan rates from 10 to 100 mV s<sup>-1</sup>. AHSC exhibits a pair of mild redox peaks for every tested scan rate, suggesting pseudocapacitive-type charge storage mechanisms. [39-41] Furthermore, the CV curves maintained analogous shape at high scan rates, insinuating superior redox reaction kinetics and an outstanding rate capability of the fabricated device.

### 5.9.2 Galvanostatic charge discharge (GCD) study:

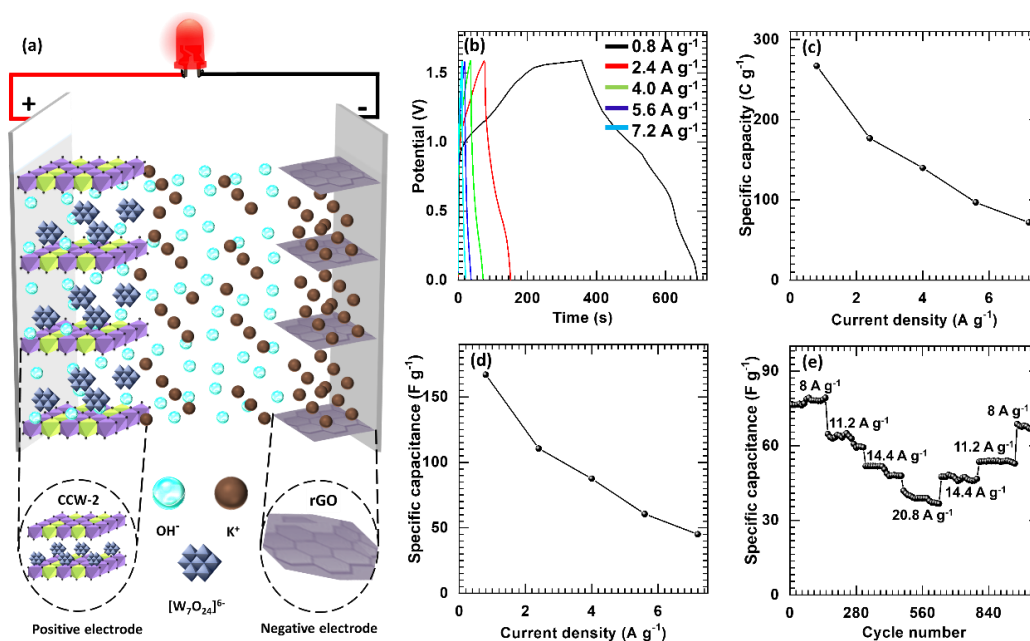


**Figure 5.16:** The charge–discharge characteristic of CCW-2//rGO AHSC device. (a) Schematic of AHSC device. (b) GCD curves of the AHSC device at various current densities (0.8 to 7.2 A g<sup>-1</sup>). (c) The plot of the variation of C<sub>sp</sub> with current density

(0.8 to 7.2 A g<sup>-1</sup>). (d) The plot of the variation of Cs with current density (0.8 to 7.2 A g<sup>-1</sup>). (e) The rate capability of the AHSC device.

The schematic representation of the AHSC is elucidated in figure 5.16 (a) and denoted by CCW-2//KOH//rGO. Figure 5.16 (b) shows the GCD profiles of AHSC at different current densities (0.8 to 7.2 A g<sup>-1</sup>). AHSC displays quasi-linear GCD curves at all current densities with prolonged charge-discharge times, suggesting excellent charge storing capability with the pseudocapacitive nature of the device. As plotted in figure 5.16 (c), the AHSC exhibits a Csp (**Chapter – 3, equation 3.1**) of 267.2 C g<sup>-1</sup> at 0.8 A g<sup>-1</sup> and 72 C g<sup>-1</sup> at 7.2 A g<sup>-1</sup>. The maintenance of high Csp at fast charging-discharging rates ensures superior rate capability of the device. As the AHSC displays quasi-triangular GCD curves with pseudocapacitive nature, the device's charge storage ability can also be expressed in terms of capacitive terminology. Thus, the Cs, ED, PD, and Coulombic efficiency are calculated from GCD analysis (**Chapter – 4, equation 4.2, equation 4.3 and equation 4.4**). As depicted in figure 5.16 (d), the AHSC delivered maximum Cs of 167 F g<sup>-1</sup> at 0.8 A g<sup>-1</sup> and 45 F g<sup>-1</sup> at 7.2 A g<sup>-1</sup>.

The rate characteristic of the present AHSC is examined for various current densities iterations (8 to 20.8 A g<sup>-1</sup>). As shown in figure 5.16 (e), the AHSC displays excellent rate capability with 88.47 % capacitance recovery, which indicates its capability to operate at distinct current densities without any significant operational performance degradation.

***ED and PD, capacitance retention, and columbic efficiency of AHSC device***

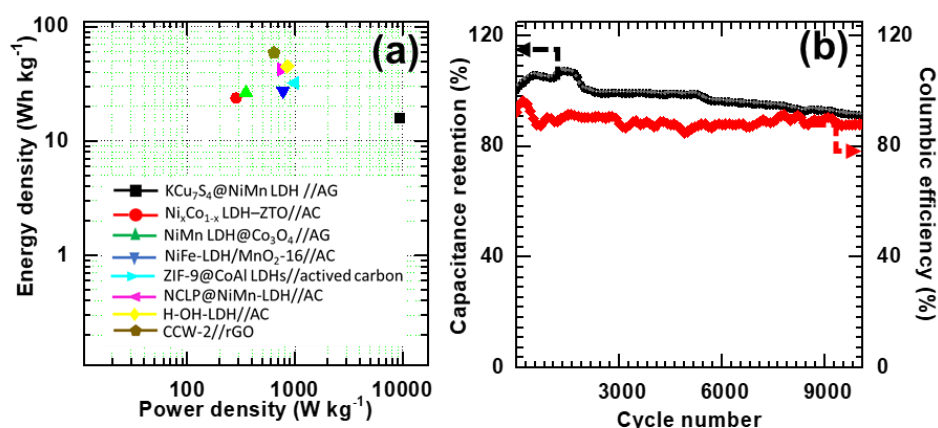


**Figure 5.17:** (a) Ragone plot of CCW-2//rGO AHSC correlated with recently reported electrochemical energy storage devices in the literature. (Ref. no. 42-48). (b) Capacitance retention with columbic efficiency of CCW-2//rGO AHSC.

## Synthesis, characterization and electrochemical performance of Co-Cr-LDH- POW and AHSC device

Furthermore, the AHSC delivers the maximum ED of 59.37 Wh kg<sup>-1</sup> with PD of 640 W kg<sup>-1</sup> at 0.8 A g<sup>-1</sup> and continues to deliver the ED of 16 Wh kg<sup>-1</sup> with PD of 5760 W kg<sup>-1</sup> at a current density of 7.2 A g<sup>-1</sup>. Present ED and PD of AHSC are presented on Ragone plot (Figure 5.17(a)) as compared to recently reported LDH based AHSC in the literature (Cell configuration, ED and PD are given in **Table 5.1**). The values of ED and PD obtained for AHSC are superior to the recently reported LDH based AHSC.

The electrochemical cycling stability of AHSC is examined by performing 10000 successive GCD cycles to ensure its long-term durability in real-time application. As plotted in (Figure 5.17 (b)), the AHSC demonstrates exceptional cyclic stability and exhibits capacity retention of 91 % over 10,000 successive GCD cycles. The capacitance of AHSC is increased for the initial 1500 cycles and decreased by 9 % for further cycles. The initial increment of capacitance can be attributed to the electrode's initial activation process. Moreover, AHSC displayed good Coulombic efficiency (Figure 5.17 (b)) of 88 % over 10,000 GCD cycles, which is exceptionally beneficial for long-term stability and high-power applications.

**Table 5.1:** ED and PD of the LDH based electrode materials

Sr. No.	Electrode material	ED (Wh kg <sup>-1</sup> )	PD (W kg <sup>-1</sup> )	Ref.
1	KCu <sub>7</sub> S <sub>4</sub> @NiMn LDH //AG	15.9	9400	42
2	Ni <sub>x</sub> Co <sub>1-x</sub> LDH-ZTO//AC	23.7	284.2	43
3	NiMn LDH@Co <sub>3</sub> O <sub>4</sub> //AG	26.49	350	44
4	NiFe-LDH/MnO <sub>2</sub> -16//AC	27.3	775.5	45
5	ZIF-9@CoAl LDHs//actived carbon	32.1	1000	46
6	NCLP@NiMn-LDH//AC	42.2	750	47
7	H-OH-LDH//AC	44.8	850	48
<b>8</b>	<b>CCW-2//rGO AHSC</b>	<b>59.02</b>	<b>640</b>	<b>Present work</b>

### 5.9.3 Electrochemical impedance spectroscopy (EIS) study:

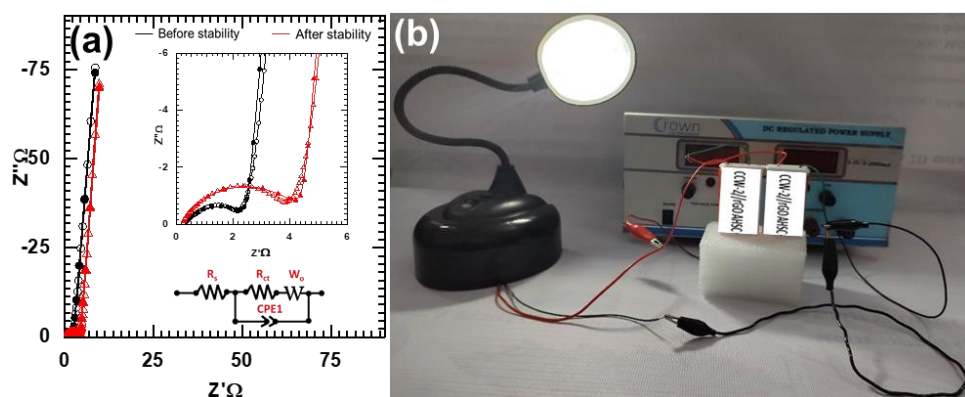


**Figure 5.18:** (a) The Nyquist plots of fabricated AHSC before and after 10000 cycling performance. (b) Demonstration of the developed CCW-2//rGO AHSC.

The Nyquist plots of AHSC before and after cycling stability are plotted in figure 5.18 (a). Before stability, the AHSC displays low  $R_s$  and  $R_{ct}$  values of  $0.2 \Omega$  and  $2.14 \Omega$ , respectively. Low  $R_s$  and  $R_{ct}$  indicate fast ionic transport and good electrical conductivity of constituting electrodes. Whereas, after stability, the AHSC maintains low  $R_s$  and  $R_{ct}$  values of  $0.2 \Omega$  and  $4.2 \Omega$ , respectively. Maintenance of low  $R_s$  and  $R_{ct}$  values by AHSC device suggests a minor alteration in electrical properties of AHSC. Moreover, in the low-frequency region, AHSC displays steeper slopes of the straight lines, signifying a minimum resistance (Warburg impedance) for electrolyte ions diffusion between constituent electrodes. Present results elucidate the beneficial influence of POW intercalation for improvement in charge transport properties, superior conductivity and accelerated electrolyte ions diffusion during electrochemical reactions. The remarkable electrochemical activity of AHSC is not only attributed to the favorable physicochemical properties of CCW nanohybrids electrode but also to the high electrical conductivity, 2D morphology, and high surface area of rGO. The real-life efficacy of the AHSC device is tested by powering an LED lamp using two serially connected AHSC. The intense initial glow of the LED lamp can validate the high power of AHSC, as shown from photograph in figure 5.18 (b).

### **5.10 Conclusions:**

A mesoporous layer-by-layer ordered nanohybrids of 2-D Co-Cr-LDH Ns intercalated with bulky POW anions are synthesized by the lattice engineering exfoliation-restacking route. The CCW nanohybrids enable interconnected Ns morphology, highly porous stacking structure, flexible chemical composition, and exceptional electrochemical activity. Controlled intercalation of POW significantly improves the electrochemical activity of pristine Co-Cr-LDH. The intimately coupled CCW nanohybrid with optimum POW content (CCW-2) demonstrated the highest Csp of 1303 C g<sup>-1</sup> with a capacity retention of 85.43 % over 5000 cycles. The significant improvement of the electrochemical energy storage capability of CCW nanohybrids is not only due to the development of a highly porous petal-bunch Ns network morphology but also to the enlarged freely available gallery space for ion diffusion and superior electrical conductivity. Furthermore, AHSC device is fabricated by employing the best optimized CCW-2 nanohybrid as a positive and rGO as negative electrodes. As a result, the AHSC displays the high Cs of 167 F g<sup>-1</sup>, ED of 59.37 Wh kg<sup>-1</sup> and PD of 640 W kg<sup>-1</sup> at 0.8 A g<sup>-1</sup>. Furthermore, the AHSC device demonstrate exceptional cycling stability over 10000 GCD cycles, with 91 % capacitance retention. The experimental outcomes obtained in the above study demonstrate that the LDH-POW nanohybrids can be effectively employed to develop the next-generation energy storage applications with efficient ED and better power output.

### **5.11 References:**

1. W. Reichle, *Solid State Ion.*, 1986, 22, 135-141.
2. C. F. Baes, R. E. Mesmer, Wiley-Interscience publication, Wiley, 1976, 489 pages.
3. E. Gardner, T. J. Pinnavaia, *Appl. Catal. A: Gen.*, 1998, 167, 65-74.
4. J. L. Gunjakar, T. W. Kim, H. N. Kim, I. Y. Kim, S. -J. Hwang, *J. Am. Chem. Soc.*, 2011, 133, 14998-15007.
5. J. Wang, L. Huang, Y. Gao, R. Yang, Z. Zhang, Z. Guo, Q. Wang, *Chem. Commun.*, 2014, 50, 10130-10132.
6. A. F. A. -Hossainy, A. Ibrahim, M. S. Zoromba, *J. Mater. Sci.: Mater. Electron.*, 2019, 30, 11627-11642.
7. J. L. Gunjakar, B. Hou, A. I. Inamdar, S. M. Pawar, A. T. A. Ahmed, H. S. Chavan, J. Kim, S. Cho, S. Lee, Y. Jo, S. -J. Hwang, T. G. Kim, S. N. Cha, H. Kim, H. Im, *Small*, 2018, 14, 1703481.
8. M. D. Arco, D. Carriazo, S. Gutierrez, C. Martin, V. Rives, *Inorg. Chem.*, 2004, 43, 375-384.
9. Z. Rezvani, F. A. Rad, F. Khodam, *Dalton Trans.*, 2015, 44, 988-996.
10. Q. Wu, A. Olafsen, O. B. Vistad, J. Roots, P. Norby, *J. Mater. Chem.*, 2005, 15, 4695-4700.
11. O. O. Balayeva, A. A. Azizov, M. B. Muradov, R. M. Alosmanov, G. M. Eyvazova, S. J. Mammadyarova, *Heliyon*, 2019, 5, e02725-e02731.
12. M. M. J. Sadiq, A. S. Nesaraj, *J. Nanostruct Chem.*, 2015, 5, 45-54.
13. T. Tian, J. Jiang, L. Ai, *Electrochim. Acta*, 2017, 224, 551-560.
14. J. A. Koza, C. M. Hull, Y. C. Liu, J. A. Switzer, *Chem. Mater.*, 2013, 25, 1922-1926.
15. J. Yang, W. N. Martens, R. L. Frost, *J. Raman Spectrosc.*, 2011, 42, 1142-1146.
16. A. S. O. Gomes, N. Yaghini, A. Martinelli, E. Ahlberg, *J. Raman Spectrosc.*, 2017, 48, 1256-1263.
17. C. Dong, X. Yuan, X. Wang, X. Liu, W. Dong, R. Wang, Y. Duan, F. Huang, *J. Mater. Chem. A*, 2016, 4, 11292-11298.
18. J. L. Gunjakar, T. W. Kim, I. Y. Kim, J. M. Lee, S. J. Hwang, *Sci. Rep.*, 2013, 3, 2080.
19. B. Kolesov, *Am. Mineral.*, 2006, 91, 1355-1362.
20. J. L. Gunjakar, A. I. Inamdar, B. Hou, S. Cha, S. M. Pawar, A. A. Abu Talha, H. S. Chavan, J. Kim, S. Cho, S. Lee, Y. Jo, H. Kim, H. Im, *Nanoscale*, 2018, 10, 8953-8961.
21. D. -G. Jeung, H. -J. Kim, J. -M. Oh, *Nanomaterials*, 2019, 9, 1262.
22. M. M. Islam, S. H. Aboutalebi, D. Cardillo, H. K. Liu, K. Konstantinov, S. X. Dou, *ACS Cent. Sci.*, 2015, 4, 206-216.
23. P. Moorthy, K. K. Sarigamala, N. Lakshminarasimhan, M. Sathish, *Electrochim. Acta*, 2017, 236, 359-370.
24. J. Long, Z. Yang, J. Huang, X. Zeng, *J. Power Sources*, 2017, 359, 111-118.
25. J. Yang, H. Liu, W. N. Martens, R. L. Frost, *J. Phys. Chem. C*, 2010, 114, 111-119.
26. R. A. Nyquist, R. O. Kagel, Academic Press Inc., New York, 1971, p. 3.
27. J. Yang, A. G. Baker, H. Liu, W. N. Martens, R. L. Frost, *J. Mater. Sci.*, 2010, 45, 6574-6585.
28. S. Wang, B. Gao, Y. Li, A. R. Zimmerman, X. Caod, *RSC Adv.*, 2016, 6, 17792.

## Synthesis, characterization and electrochemical performance of Co-Cr-LDH- POW and AHSC device

---

29. M. Vasilopoulou, A. Soultati, D. G. Georgiadou, T. Stergiopoulos, L. C. Palilis, S. Kennou, N. A. Stathopoulos, D. Davazoglou, P. Argitis, *J. Mater. Chem. A*, 2014, 2, 1738-1749.
30. H. A. -Kandari, F. A. -Kharafi, N. A. -Awadi, O. M. E. -Dusouqui, A. Katrib, *J. Electron Spectrosc. Relat. Phenom.*, 2006, 151, 128-134.
31. K. Liu, Y. Xu, Z. Yao, H. N. Miras, Y. -F. Song, *Chem. Cat. Chem.*, 2016, 8, 929-937.
32. J. F. Moulder, W. F. Stickle, P. E. Kennetlf, D. Bomben, Eden prairie, Minnesota 55344, United States of America, 1992.
33. J. B. Condon, 1<sup>st</sup> ed., Elsevier, Amsterdam, Boston 2006, p. 274.
34. S. J. Gregg, K. S. W. Sing, Academic press, London, New York, 1967, XI+ 371 seiten, 184 Abbildungen preis: 95 s.
35. S. J. Gregg, K. S. W. Sing, Adsorption, surface area, & porosity, 2<sup>nd</sup> ed, Academic press, London, New York, 1982, p. 303.
36. A. M. Patil, N. Kitiphatpiboon, X. An, X. Hao, S. Li, X. Hao, A. Abudula, G. Guan, *ACS Appl. Mater. Interfaces*, 2020, 12, 52749-52762.
37. C. Zhang, M. P. Kremer, A. S. -Ascaso, S. -H. Park, N. McEvoy, B. Anasori, Y. Gogotsi, V. Nicolosi, *Adv. Funct. Mater.*, 2018, 28, 1705506.
38. N. R. Chodankar, S. Selvaraj, S. -H. Ji, Y. Kwon, D. -H. Kim, *Small*, 2018, 15, 1803716.
39. S. D. Perera, X. Ding, A. Bhargava, R. Hovden, A. Nelson, L. F. Kourkoutis, R. D. Robinson, *Chem. Mater.*, 2015, 27, 7861-7873.
40. S. J. Marje, V. V. Patil, V. G. Parale, H. -H. Park, P. A. Shinde, J. L. Gunjekar, C. D. Lokhande, U. M. Patil, *Chem. Eng. J.*, 2022, 429, 132184.
41. H. Xie, S. Tang, J. Zhu, S. Vongehra X. Meng, *J. Mater. Chem. A*, 2015, 3, 18505-18513.
42. X. L. Guo, J. M. Zhang, W. N. Xu, C. G. Hu, L. Sun, Y. X. Zhang, *J. Mater. Chem. A*, 2017, 5, 20579-20587.
43. X. Wang, A. Sumboja, M. Lin, J. Yan, P. S. Lee, *Nanoscale*, 2012, 4, 7266-7272.
44. H. Peng, C. Jing, J. Chen, D. Jiang, X. Liu, B. Dong, F. Dong, S. Lif, Y. Zhang, *Cryst. Eng. Comm.*, 2019, 21, 470-477.
45. W. Zheng, S. Sun, Y. Xu, R. Yu, H. Li, *J. Alloys Compd.*, 2018, 768, 240-248.
46. G. Wang, Y. Li, Z. Jin, *New J. Chem.*, 2020, 44, 7528-7540.
47. H. Liang, J. Lin, H. Jia, S. Chen, J. Qi, J. Cao, T. Lin, W. Fei, J. Feng, *J. Mater. Chem. A*, 2018, 6, 15040-15046.
48. X. Liu, A. Zhou, T. Pan, Y. Dou, M. Shao, J. Han, M. Wei, *J. Mater. Chem. A*, 2016, 4, 8421-8427.

# CHAPTER-6

**SYNTHESIS,  
CHARACTERIZATION AND  
ELECTROCHEMICAL  
PERFORMANCE OF Co-Cr-LDH-  
GO AND AHSC DEVICE**

# CHAPTER-6

## Synthesis, Characterization and Electrochemical Performance of Co-Cr-LDH-GO and AHSC Device

Sr. No.	Title	Page No.
6.1	Introduction	159
6.2	Synthesis and characterization of Co-Cr-LDH-GO	160
6.3	Experimental details	160
	6.3.1 Chemicals	160
	6.3.2 Synthesis of Co-Cr-LDH-GO	160
6.4	Characterization of Co-Cr-LDH-GO	161
	6.4.1 XRD analysis	162
	6.4.2 FTIR analysis	163
	6.4.3 Raman analysis	164
	6.4.4 XPS analysis	165
	6.4.5 FESEM analysis	167
	6.4.6 TEM analysis	168
	6.4.7 N <sub>2</sub> adsorption-desorption (BET analysis)	169
6.5	Conclusions	171
6.6	Electrochemical performance of Co-Cr-LDH-GO	172
6.7	Results and discussion	172
	6.7.1 Cyclic voltammetry (CV) study	172
	6.7.2 Galvanostatic charge-discharge (GCD) study	174
	6.7.3 Electrochemical impedance spectroscopy (EIS) study	177
6.8	Fabrication and electrochemical performance of aqueous hybrid supercapacitor device (AHSC): CCG-2//rGO	178
6.9	Results and discussion	180
	6.9.1 Cyclic voltammetry (CV) study	180
	6.9.2 Galvanostatic charge-discharge (GCD) study	181
	6.9.3 Electrochemical impedance (EIS) study	183
6.10	Conclusions	185
6.11	References	186

## **6.1 Introduction:**

With reference to the nanohybridization advantages described in **Chapter 1, section 1.5, Chapter-2, section 2.3.3 and Chapter 3, section 3.1** to enhance the electrode performance of Co-Cr-LDH, the Co-Cr-LDH hybridized with POV, and POW anions are explored in Chapters 4 and 5, respectively. These strategies improved the electrode performance of Co-Cr-LDH by expanding the surface area and gallery space of Co-Cr-LDH via hybridization with POV and POW anions.

Exfoliated GO Ns; 2D hexagonal monolayers of oxidized graphite lattice, is regarded as a one of the best candidates as a hybridization matrix with various nanomaterials due to its unique physicochemical properties (negative surface charge, high surface area, high processability, high electrical conductivity and ultra-thin 2D morphology). [1, 2] Furthermore, considering that exfoliated Ns of Co-Cr-LDH and GO possess opposite surface charges, their self-assembly leads to Co-Cr-LDH-GO nanohybrids (CCG nanohybrids) with improved electrical conductivity and electrochemical activity of hybridized species. Also, such CCG nanohybrids can enable expansion of the surface area and highly porous structure by random aggregation of Ns. Similar self-assembled ZnCr-LDH-GO nanohybrid are reported as a highly active photocatalyst. [3] Moreover, NiCo-LDH-GO, NiAl-LDH-GO and CoAl-LDH-GO nanohybrids are reported as high-performance energy storage electrodes and electrocatalysts. [4-7]

The present chapter deals with the synthesise of CCG self-assembled nanohybrids by exfoliation-restacking of positively charged 2D Co-Cr-LDH Ns and negatively charged GO Ns. The effect of chemical composition on the electrochemical performance of the CCG nanohybrids is investigated together with corresponding variations in physicochemical properties. Finally, the AHSC is developed using the CCG nanohybrids as positive and rGO as negative electrodes.

## **6.2 Synthesis and characterization of Co-Cr-LDH-GO:**

### **6.3 Experimental details:**

#### **6.3.1 Chemicals:**

Co(NO<sub>3</sub>)<sub>2</sub>·6H<sub>2</sub>O, Cr(NO<sub>3</sub>)<sub>3</sub>·9H<sub>2</sub>O, NaOH, NaNO<sub>3</sub>, Graphite flakes, NMP, PVDF, PVA and KOH were purchased from Sigma-Aldrich. SS substrates (304 grade) were served as a current collector to prepare the Co-Cr-LDH and CCG HSC electrodes.

#### **6.3.2 Synthesis of Co-Cr-LDH-GO:**

The nitrate intercalated Co-Cr-LDH and exfoliated Co-Cr-LDH Ns were synthesized using the synthesis protocol described in Chapter-3, section 3.2.3, and the results of physicochemical and electrochemical characterizations are compared with the CCG nanohybrids. [8] The self-assembled CCG nanohybrids were synthesized by rate-controlled simultaneous addition of the aqueous GO solution and the colloidal suspension of exfoliated Co-Cr-LDH Ns at room temperature (figure 6.1). The colloidal suspensions of exfoliated Co-Cr-LDH Ns and GO solutions were added together that results into spontaneous flocculation of the exfoliated Co-Cr-LDH monolayers with the GO anions which demonstrates the development of the self-assembled CCG nanohybrids. The subsequent flocculation products of CCG nanohybrids were immediately collected by centrifugation, cleaned with formamide and absolute ethanol. Finally, to ensure solid CCG nanohybrid product freeze-drying process was adopted. All the processes were done with decarbonated water and under inert (N<sub>2</sub>) atmosphere to avoid contamination of Co-Cr-LDH and CCG nanohybrids from CO<sub>3</sub><sup>2-</sup> anions.

The ability of the exfoliation-restacking process to control the chemical composition of CCG nanohybrids was investigated by preparing the nanohybrid materials with three representatives GO weight percent ratios of 1.5, 3 and 4.5 and the obtained CCG nanohybrids were denoted as CCG-1, CCG-2 and CCG-3, respectively.

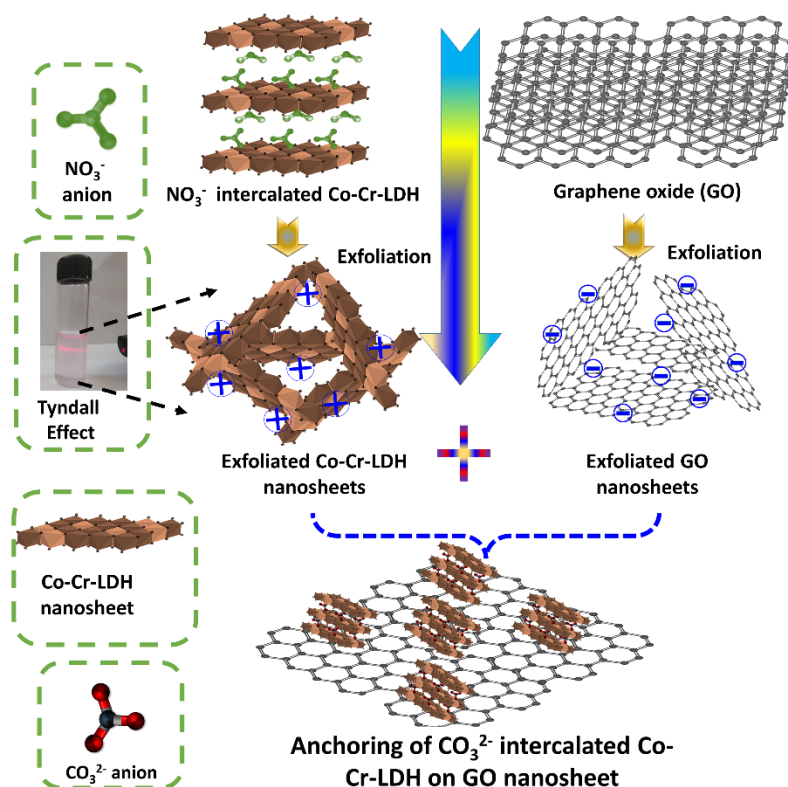


**Figure 6.1:** Schematic illustration for the formation of anchor assembly between Co-Cr-LDH and GO Ns via the exfoliation-restacking process.

#### 6.4 Characterizations of Co-Cr-LDH-GO:

The pristine Co-Cr-LDH and the self-assembled CCG nanohybrids were characterized by various physicochemical characterization techniques as described in **Chapter-3, section 3.3**. In addition, the CCG electrode preparation and electrochemical performance evaluation were examined by a similar protocol as described in **Chapter-3, section 3.5**.

#### 6.4.1 XRD analysis:

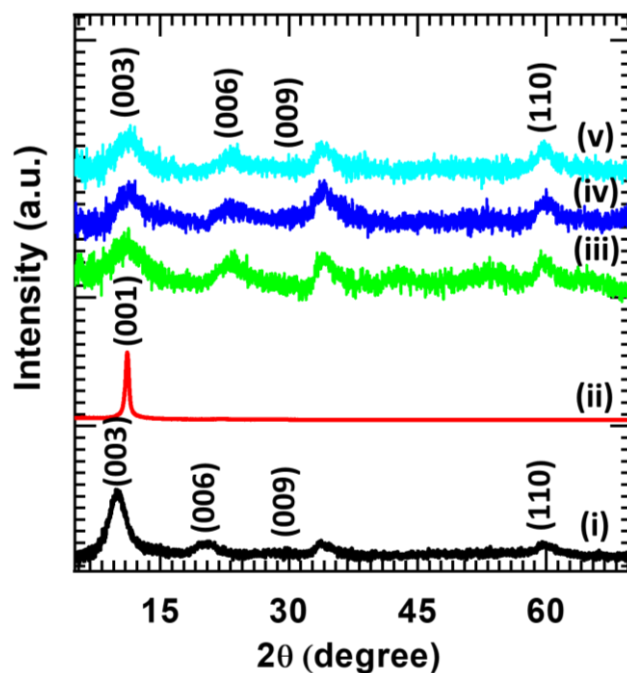


**Figure 6.2:** PXRD patterns of (i) Co-Cr-LDH, (ii) GO, (iii) CCG-1, (iv) CCG-2 and (v) CCG-3 nanohybrids.

Figure 6.2 represents the PXRD patterns of pristine Co-Cr-LDH, GO and CCG nanohybrids. The crystal phase investigation of Co-Cr-LDH and GO is described in **Chapter-3, section 3.3.1 and Chapter-3, section 3.3.8, respectively**. Similar to Co-Cr-LDH, all CCG nanohybrids exhibit a well-resolved series of  $(00l)$  Bragg reflections which shows the development of layer-by-layer-stacked intercalated compounds with the slight shifting of the first-order  $(001)$  peak towards higher diffraction angle ( $2^\circ$ ), indicating the reduction of the  $c$ -axis parameter. Moreover, CCG nanohybrids commonly display lattice parameters of  $a = b = 0.3$  nm and  $c = 0.78$  nm. With the reference of Co-Cr-LDH, CCG nanohybrids display reduced  $c$ -axis parameters, indicating the intercalation of divalent carbonate anions into the restacked LDH lattice. The  $(110)$  peak of the LDH phase is noticeably observable at higher  $2\theta = \sim 60^\circ$  for all nanohybrids, clearly indicating the maintainance of the LDH Ns over hybridization with GO Ns. Additionally, all nanohybrids show a broad diffraction peak at  $2\theta = 30\text{--}40^\circ$  attributed to turbostratic stacking structure of reassembled LDH Ns. Interestingly, in the XRD patterns, there are no graphene related peaks are observed which clearly indicate the excellent dispersion of GO Ns without any special phase separation.

#### 6.4.2 FTIR analysis:

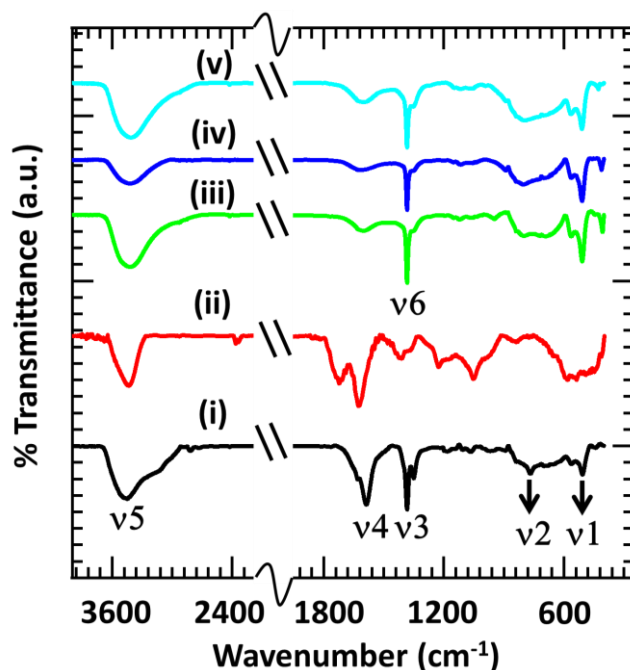


**Figure 6.3:** FTIR spectra of (i) Co-Cr-LDH, (ii) GO, (iii) CCG-1, (iv) CCG-2 and (v) CCG-3 nanohybrids.

The chemical bonding of all nanohybrids is studied by FTIR spectroscopy. The FTIR analysis of Co-Cr-LDH is described in **Chapter-3, section 3.3.2**. As seen from figure 6.3, the pristine Co-Cr-LDH and CCG nanohybrids commonly display the absorption peaks at v1 (505  $\text{cm}^{-1}$ ), v2 (770  $\text{cm}^{-1}$ ), v4 (1610  $\text{cm}^{-1}$ ) and v5 (3448  $\text{cm}^{-1}$ ), which are ascribed to the metal-oxygen (M-O), metal-oxygen-hydrogen (M-O-H) bending, bending vibrations of the water molecule and stretching vibrations of the H-bound O-H groups. [9] The Co-Cr-LDH shows a intense absorption peak at v3 (1383  $\text{cm}^{-1}$ ), ascribed to the anti-symmetric stretching mode of intercalated nitrate anions. [10-11] The GO displays strong IR bands (900-1800  $\text{cm}^{-1}$ ) which correspond to the carbon-oxygen bonds. On the other hand, CCG nanohybrids display the absorption peak of v6 (1385  $\text{cm}^{-1}$ ), which is attributed to the anti-symmetric stretching of intercalated carbonate anions (entrapped during the self-assembling process). [12-14] Obtained IR features confirm the maintainance of Co-Cr-LDH monolayers and intercalation of carbonate anions into the gallery space of Co-Cr-LDH during exfoliation-restacking process.

### 6.4.3 Raman analysis:

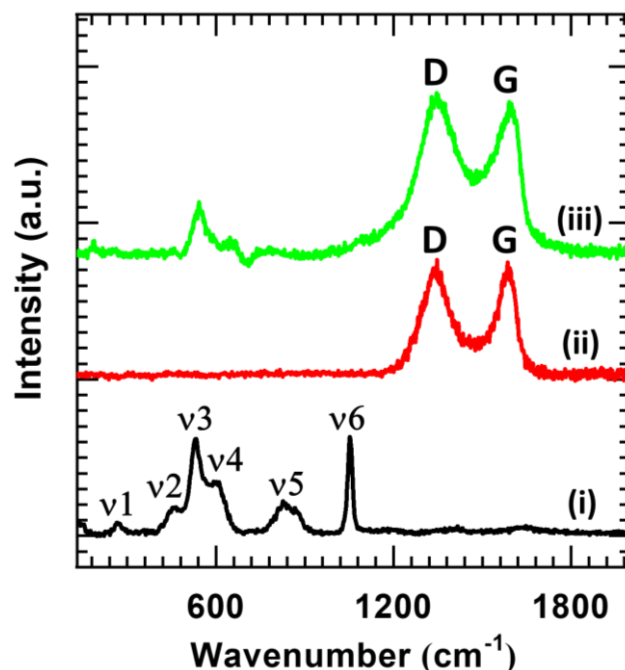


**Figure 6.4:** Micro-Raman spectra of (i) Co-Cr-LDH, (ii) GO and (iii) CCG-2 nanohybrid.

The chemical bonding character of the Co-Cr-LDH and CCG nanohybrids are further analyzed with micro-Raman spectroscopy, as plotted in figure 6.4. The micro-Raman analysis of Co-Cr-LDH is described in **Chapter-3, section 3.3.3**. Interestingly, the CCG-2 nanohybrid displays characteristic peaks related to LDH lattice and GO Ns confirming incorporation of GO Ns in CCG nanohybrids. The peaks at  $\nu_3$  ( $530\text{ cm}^{-1}$ ) and  $\nu_4$  ( $600\text{ cm}^{-1}$ ) in CCG nanohybrids are attributed to the characteristic CoO ( $A_{2u}$ ) symmetric stretching and  $E_g(R)$  modes of Co-Cr-LDH, respectively. Moreover, the peaks at  $\sim 1343$  and  $\sim 1585\text{ cm}^{-1}$  in CCG nanohybrids are attributed to the characteristic D and G bands of GO Ns. [15-16] The CCG-2 nanohybrid shows a slightly high D/G intensity ratio of 1.094 than reference GO ( $D/G = \sim 0.98$ ), indicating the increased crystal disorder due to the reduction process of the GO Ns during the hybridization process. [3]

#### 6.4.4 XPS analysis:

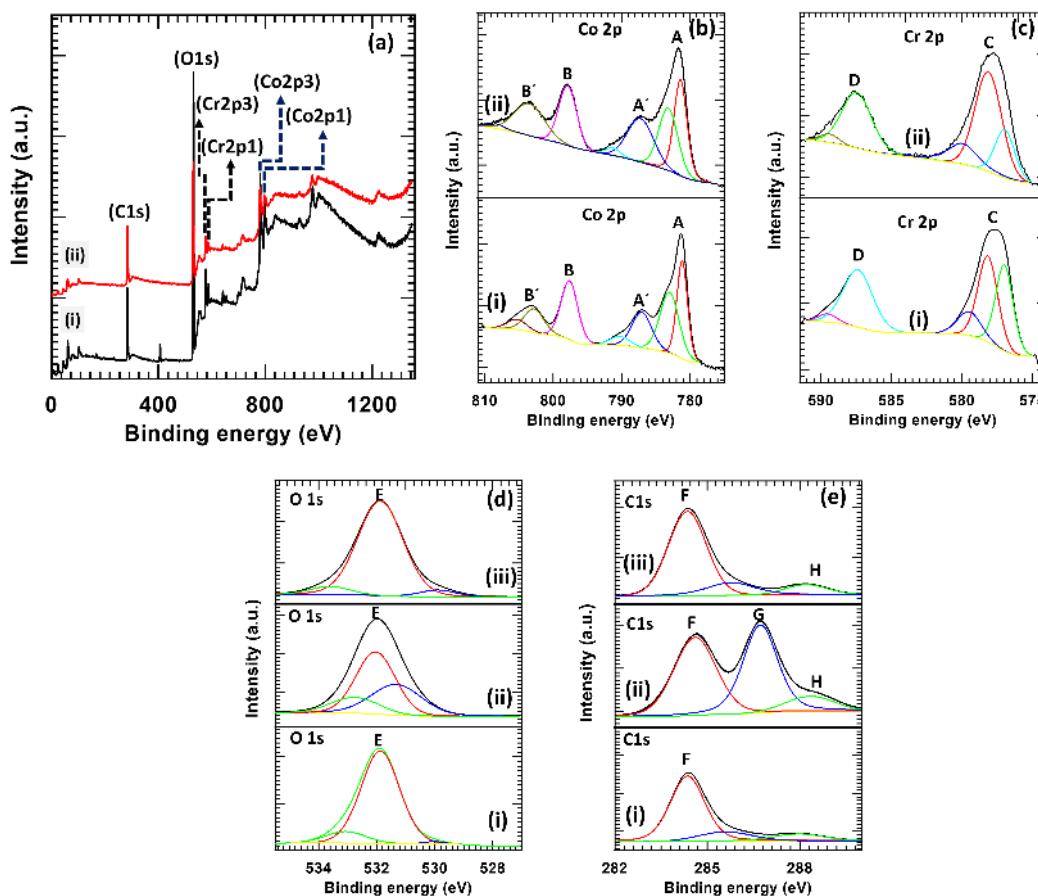


**Figure 6.5:** (a) Survey XPS spectra of (i) Co-Cr-LDH and (ii) CCG-2 nanohybrid, (b) Co2p and (c) Cr2p XPS spectra of (i) Co-Cr-LDH and (ii) CCG-2 nanohybrid, (d) O1s and (e) C1s XPS spectra of (i) Co-Cr-LDH, (ii) GO and (iii) CCG-2 nanohybrid.

Surface chemical composition, nature of oxygen species present and oxidation states of Co-Cr-LDH and CCG nanohybrids are investigated by XPS. The XPS of Co-Cr-LDH is described in **Chapter-3, section 3.3.6** The XPS survey spectra for all samples (figure 6.5 (a)) commonly show spectral features at BE of the element Co, Cr, O and C, indicating the presence of these elements in the samples. As shown in figure 6.5 (b), high-resolution Co 2p XPS spectra of Co-Cr-LDH and CCG-2 nanohybrid display spectral features at BE A (781.39 eV) and B (797.53 eV) with observable satellite features at BE A' (787.04 eV) and B' (803.37 eV) due to the split spin-orbit components Co 2p<sub>3/2</sub> and Co 2p<sub>1/2</sub>, respectively. [17] The BE difference of 16.24 eV between Co 2p<sub>3/2</sub> and Co 2p<sub>1/2</sub> components suggests presence of Co<sup>2+</sup> in the Co-Cr-LDH and Co-Cr-LDH-GO nanohybrids. As shown in figure 6.5 (c), Cr 2p XPS spectra reveal two broad spectral features at BE C (577.5

eV) and D (797.5 eV) associated with the split spin-orbit components Cr 2p<sub>3/2</sub> and Cr 2p<sub>1/2</sub>, respectively. [14, 18] These BE positions indicate trivalent chromium hydroxide and Cr<sup>3+</sup> co-ordinated with interlayer hydroxyl (OH<sup>-</sup>) and -water (H<sub>2</sub>O) moieties. Figure 6.5 (d) represents O 1s core-level spectra of Co-Cr-LDH, GO and CCG-2 nanohybrid. The pristine Co-Cr-LDH exhibits broad XPS feature at E (531.9 eV) that corresponds to oxygen from lattice (BE 529.9 eV), hydroxyl group (BE 531.86 eV) and bound water (BE 533.08 eV). [19] The reference GO exhibits characteristic XPS features corresponding to the O=C bonds in carbonyl C=O and carboxyl O=C-OH groups (531.0 eV), O-C bonds in hydroxyl C-OH and epoxy C-O-C moieties (532.07 eV) and O-H bonds in adsorbed water (533.2 eV). [20] The CCG-2 nanohybrid displays a broad peak at 531.9 eV that corresponds to the major contribution of oxygen from Co-Cr-LDH lattice (BE 529.9 eV), hydroxyl group (BE 531.86 eV) and bound water (BE 533.08 eV). [21] The high-resolution C 1s XPS spectra of CCG-2 nanohybrid, GO and pristine Co-Cr-LDH are presented in figure 6.5 (e). The reference GO exhibits complex XPS features at BE of 284.4 eV (C-C, non-oxygenated ring), 285.33 eV (C-O, hydroxyl C-OH and epoxy C-O-C moieties), and 286.8 eV (C=O, carbonyl), which are characteristic of functional groups attached to the GO Ns. [22-24] Notably, the CCG-2 nanohybrid displays an intense XPS feature at 284.36 eV and a mild signature at 285.8 eV, which corresponds to the C-C (non-oxygenated ring) and C-O (hydroxyl C-OH and epoxy C-O-C moieties), respectively. The CCG-2 nanohybrid displays a characteristic XPS feature at 288.25 eV ascribed to the intercalated carbonate anions. Of the prime importance, the XPS features related to the C-O (hydroxyl C-OH and epoxy C-O-C moieties) and C=O (carbonyl) functional groups are highly suppressed in nanohybrids indicating the reduction of GO Ns during hybridization. [25-26]

#### 6.4.5 FESEM analysis:

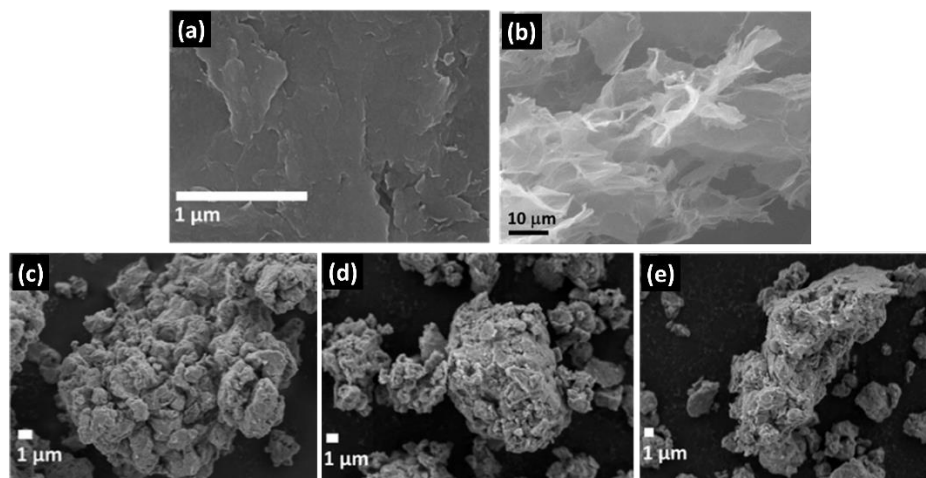


**Figure 6.6:** FESEM images of (a) Co-Cr-LDH, (b) rGO, (c) CCG-1, (d) CCG-2, and (e) CCG-3 nanohybrids at (b) 1500x, (c) 5500x, (d) 4500x, and (e) 3700x magnifications.

The crystal shapes, sizes, and morphologies of the Co-Cr-LDH, GO and CCG nanohybrids (figure 6.6) are probed using FESEM. The surface microstructural analysis of Co-Cr-LDH (figure 6.6 (a)) is described in **Chapter-3, section 3.3.4**. In contrast to Co-Cr-LDH and GO, the CCG nanohybrids in figure 6.6 (c-e) commonly display porous clusters composed of a wad of aggregated Co-Cr-LDH and GO Ns. The size of aggregated Co-Cr-LDH and GO Ns wad is between  $\sim 5$  to  $9 \mu\text{m}$  which is observed from the FESEM analysis. Considering lateral dimensions ( $\sim 5$  to  $10 \mu\text{m}$ , figure 6.6 (b)) and homogeneous dispersion of GO Ns, the GO Ns can cover the bulk of the present CCG nanohybrid wad. Thus, enabling high conducting channels in CCG nanohybrids. Such porous morphology is commonly observed for GO-based nanohybrids and is beneficial for electrochemical energy storage applications. [27-29]

#### 6.4.6 TEM analysis:

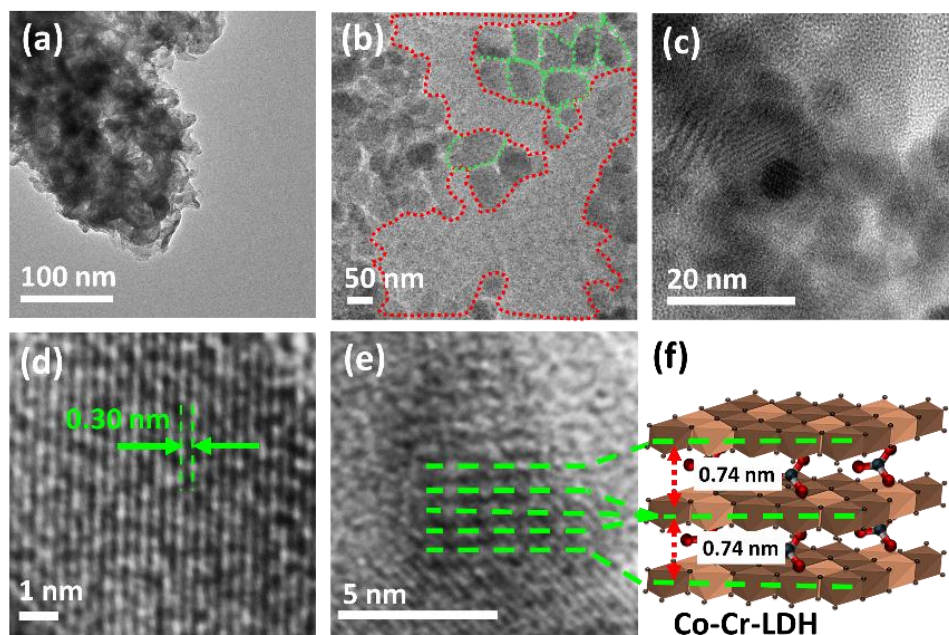


**Figure 6.7:** (a, b) Plane-view TEM, (c, d) top-view HRTEM and (e) Cross-sectional HRTEM images of CCG-2 nanohybrid. (f) Structural model of restacked Co-Cr-LDH.

The crystal structure, crystal shape, stacking structure of CCG nanohybrids are further confirmed by HRTEM analysis. As shown in figure 6.7 (a), the TEM image of CCG-2 nanohybrid demonstrates an aggregated cluster of restacked LDH and GO Ns making a wad-like appearance. As illustrated in figure 6.7 (b), the HRTEM image focused at the edges of CCG-2 nanohybrid displays two types of domains that co-existed with varying contrast. One type appeared darker with a lateral domain size of  $\sim 100$  nm (highlighted with green dotted lines), corresponding to the Co-Cr-LDH. The other extended over a large area and a lighter appearance corresponds to the GO Ns (highlighted with red dotted lines). The present results confirm the anchoring effect of restacked Co-Cr-LDH on the GO Ns platform. There are two kinds of parallel aligned lattice fringes having different fringe distances are observed in high resolution HRTEM images (figure 6.7 (c-e)) of CCG nanohybrid. One type with a smaller fringe distance of 0.3 nm (figure 6.7 (d)) is well-matched with the in-plane interatomic distance of the hexagonal host Co-Cr-LDH (JCPDS card, No. 38-0487). The other with a large fringe distance of  $\sim 0.74$  nm (figure 6.7 (e)) is well agree with c-axis lattice parameters of restacked Co-

Cr-LDH calculated from the XRD study. The schematic structural model of restacked Co-Cr-LDH intercalated with  $\text{CO}_3^{2-}$  anions is presented in figure 6.7 (f).

Thus, present HRTEM results indicate the anchoring of restacked Co-Cr-LDH on GO Ns at the nanometer length scale. Further, these anchored Co-Cr-LDH-GO Ns aggregated to form clusters of CCG nanohybrid, making a wad-like appearance.

#### 6.4.7 $\text{N}_2$ adsorption-desorption (BET analysis):

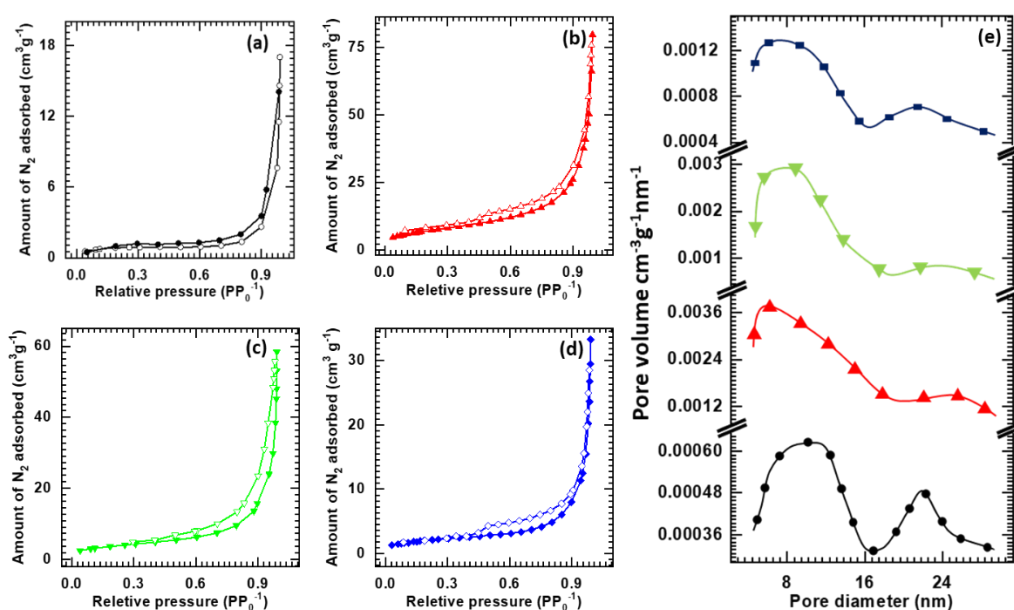


**Figure 6.8:**  $\text{N}_2$  adsorption-desorption isotherms for (a) Co-Cr-LDH, (b) CCG-1, (c) CCG-2, (d) CCG-3 and (e) Pore size distribution curves for (Black) Co-Cr-LDH, (Red) CCG-1, (Green) CCG-2 and (Blue) CCG-3; In (a), (b), (c) and (d), the open symbols represent the adsorption and closed symbols represent desorption data.

The effect of GO hybridization on the surface area and pore structure of the CCC nanohybrids is probed with  $\text{N}_2$  adsorption-desorption isotherm analysis as shown in figure 6.8 (a-d). The  $\text{N}_2$  adsorption-desorption analysis of Co-Cr-LDH is described in **Chapter-3, section 3.3.7**. However,  $\text{N}_2$  adsorption-desorption isotherms for CCG nanohybrids are significantly affected by the chemical composition. From figure 6.8 (a, b, c, d), the CCG nanohybrids show significant  $\text{N}_2$  adsorption at  $\text{pp}_0^{-1} < 0.4$  and distinct hysteresis at  $\text{pp}_0^{-1} > 0.45$  characteristic of porous nature of nanohybrids which is originated from the self-assembled stacking structure. [30] All of the CCG nanohybrids display BDDT type-III isotherm and noticeable H3-type hysteresis. The CCG-1 nanohybrid (1.5 wt % of GO) displays a surface area of  $13.01 \text{ m}^2 \text{ g}^{-1}$  that increases to 25

$\text{m}^2 \text{g}^{-1}$  for the CCG-2 nanohybrid (3 wt % of GO) and furthermore decrease to  $7.3 \text{ m}^2 \text{g}^{-1}$  for CCG-3 (4.5 wt % of GO). The observed low surface area in CCG-1 and CCG-3 nanohybrids can be attributed to the high LDH content in CCG-1 and pore-blocking effect by large amount of GO in CCG-3 nanohybrids. The present results indicate the crucial role of chemical composition for the optimization of pore structure of CCG nanohybrids.

The BJH method is used for calculations of pore size distribution of Co-Cr-LDH and CCG nanohybrids. As plotted in the figure 6.8 (e), CCG nanohybrids shows a comparatively narrow size pore distributions with an average diameter of Co-Cr-LDH ( $\sim 31.23 \text{ nm}$ ), CCG-1 ( $\sim 26.64 \text{ nm}$ ), CCG-2 ( $\sim 18.64 \text{ nm}$ ) and CCG-3 ( $\sim 26.31 \text{ nm}$ ), indicating the development of mesoporous materials. The development of stacking structure and wad like morphology of CCG nanohybrids is the result of creation of mesopores due to smaller basal spacings of of nanohybrids as compared to their pore diameters.

### **6.5 Conclusions:**

In conclusion, mesoporous self-assembly of CCG nanohybrids is prepared by the exfoliation-reassembling of positively charged 2D Co-Cr-LDH Ns and negatively charged GO Ns. The CCG nanohybrids are characterized by XRD, FESEM, FTIR, Raman, XPS, and N<sub>2</sub> adsorption-desorption (BET) techniques to study crystal structural, chemical bonding, surface textural as well as compositional properties. As a result, the CCG nanohybrids display wad-like porous morphology and highly porous ordered structures whose porosity is finely tuned by varying chemical composition. In addition, the CCG nanohybrids show the anchoring of restacked Co-Cr-LDH on GO Ns at the nanometer length scale. Further, these anchored Co-Cr-LDH-GO Ns aggregated to form clusters of CCG nanohybrid, making a wad-like appearance.

## 6.6 Electrochemical performance of Co-Cr-LDH-GO:

### 6.7 Result and discussion:

#### 6.7.1 Cyclic voltammetry (CV) study:

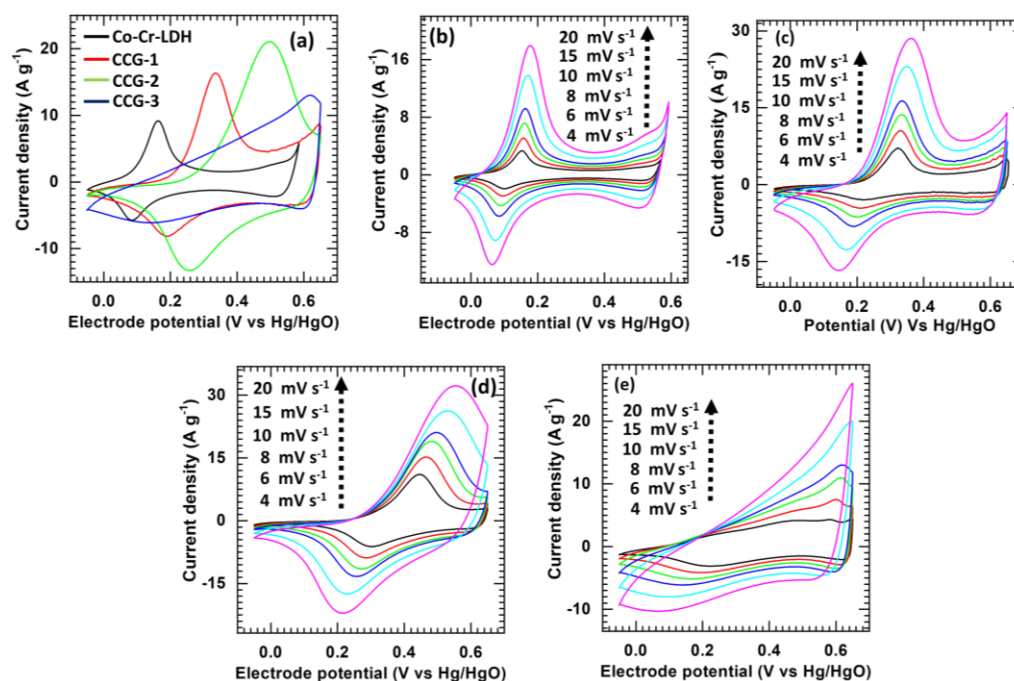


**Figure 6.9:** (a) CV plot of Co-Cr-LDH and CCG nanohybrids at a sweep rate of  $10 \text{ mV s}^{-1}$ , CV plot of the (b) Co-Cr-LDH and (c) CCG-1, (d) CCG-2 and (e) CCG-3 nanohybrids at various scan rates ( $4\text{--}20 \text{ mV s}^{-1}$ ).

The effect of the GO-NS matrix on the electrochemical activity of CCG nanohybrids are tested using the CV, GCD and EIS analysis techniques. The electrochemical characteristics are studied with a half-cell described in **Chapter – 3, section 3.5**. The Co-Cr-LDH or CCG nanohybrids, platinum mesh and Hg/HgO are utilized as working, counter and reference electrodes, respectively.

Figure 6.9 (a) represents CV plot of Co-Cr-LDH and CCG nanohybrids at constant sweep rate of  $10 \text{ mV s}^{-1}$ . All CCG nanohybrids and Co-Cr-LDH show pairs of well-defined oxidation-reduction peaks with non-rectangular CV curves indicating current responses arise due to both charge storage mechanisms such as EDLC-type and battery type (diffusion controlled). The hybridization between Co-Cr-LDH and GO-NS matrix leading an unusual increase current responses and broadening of redox peaks with notable shifts in redox peak positions towards more positive potentials. Moreover, hybridization also leads significant increase of area under CV curves, indicating enhanced charge storage ability of CCG

nano hybrids. The supercapacitive performance of CCG nano hybrid electrodes arises due to redox reaction mechanism (**Chapter – 3, equation 3.3**):

Generally, the potential difference ( $\Delta E_{c,a}$ ) between the cathodic and anodic peaks indicates the reversibility of the electrochemical redox reactions. The smaller ( $\Delta E_{c,a}$ ) indicates the higher reversibility of electrodes. [31] The calculated ( $\Delta E_{c,a}$ ) values of the Co-Cr-LDH, CCG-1, CCG-2 and CCG-3 electrodes were 44, 144, 242 and 467 mV, respectively. Among the CCG nano hybrids, CCG-2 nano hybrid displays the highest area under CV curve, highlighting its excellent supercapacitive activity. Figure 6.9 (b-e) show CV plot of Co-Cr-LDH, CCG-1, CCG-2 and CCG-3 electrodes at different sweep rates ranging from 4 to 20  $\text{mV s}^{-1}$ , respectively. The current responses for all tested electrodes increase with the scan rates along with the shifting of cathodic peaks near to more positive potential, indicating hybrid electrochemical activity comprising both charge storage mechanism such as pseudocapacitive and diffusion-controlled (battery-type) of Co-Cr-LDH and CCG nano hybrids. Hence by using the electrochemical kinetics analysis, the  $Q_s$  and  $Q_d$  components can be resolved by using the relation (**Chapter – 3, equation 3.4**).

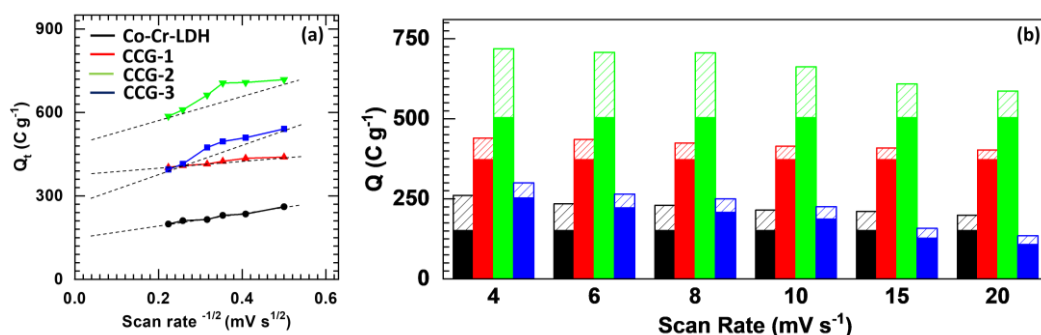


**Figure 6.10:** (a) Plot of total charge ( $Q_t$ ) vs the reciprocal of the square root of the scan rate ( $v^{-1/2}$ ). (b) The fraction of the capacitive (solid) and diffusion-controlled (pattern) contributions of Co-Cr-LDH (black), CCG-1 (red), CCG-2 (green) and CCG-3 (blue) nano hybrids.

The surface capacitive charge ( $Q_s$ ) can be resolved by  $Q_t$  vs ( $v$ ) $^{-1/2}$  as shown in figure 6.10 (a) and deducing  $v$  to infinity by assuming semi-infinite linear diffusion, within a reasonable range of sweep rates. The analysis ignores the high scan rates above 20  $\text{mV s}^{-1}$  to avoid polarization effects.[32] Figure 6.10 (b) shows the fractions of capacitive and diffusion-controlled contributions Co-Cr-LDH and CCG nano hybrids represented by solid-filled and pattern-filled columns, respectively. All tested electrodes show significant capacitive fraction at a high scan rate, whereas diffusion-

controlled fractions are prominent at a low scan rate. At a high scan rate, the CCG nano hybrids show 84.72 %, 70.12 %, and 53 % of  $Q_s$  for CCG-1, CCG-2, and CCG-3 nano hybrids, respectively as compared to the Co-Cr-LDH (58 %). These results signify escalated capacitive-dominant reactions upon GO hybridization. The observed capacitive-dominant reactions for nano hybrids are attributable to the faster charge transfer kinetics via accessible redox-active sites due to the random stacking structure of LDH and GO Ns, and high conductivity due to the hybridization with GO Ns matrix. [33]

### 6.7.2 Galvanostatic charge discharge (GCD) study:

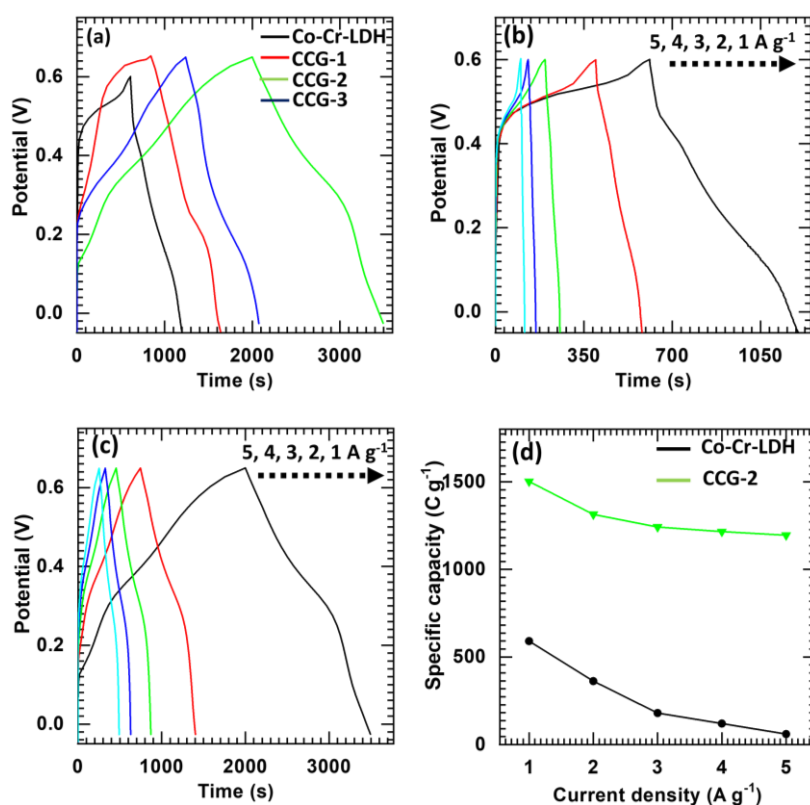


**Figure 6.11:** GCD curves of the (a) Co-Cr-LDH and CCG nano hybrids at constant current density of  $1 \text{ A g}^{-1}$ , (b) Co-Cr-LDH and (c) CCG-2 nano hybrid at different current densities ( $1\text{-}5 \text{ A g}^{-1}$ ), (d) Variations of the  $C_{sp}$  of Co-Cr-LDH and CCG-2 nano hybrid electrodes with current density ( $1\text{-}5 \text{ A g}^{-1}$ ).

The beneficial role of GO as a hybridization matrix and its effects on the electrochemical activity and charge transport rate kinetics of LDH are additionally examined by GCD and EIS analysis. Figure 6.11 (a) illustrates that Co-Cr-LDH and CCG nano hybrid electrodes show typical nonlinear charge-discharge behaviors, suggesting the reversible Faradaic reactions significantly contributed to the  $C_{sp}$  of the Co-Cr-LDH and CCG electrodes. The charge-discharge curves of Co-Cr-LDH and CCG-2 nano hybrid at current density  $1\text{-}5 \text{ A g}^{-1}$  are shown in figure 6.11 (b, c),

respectively. The  $C_{sp}$  values calculated (**Chapter – 3, equation 3.1**) for the Co-Cr-LDH and CCG-2 samples are 591 and 1502 C g<sup>-1</sup> at 1 A g<sup>-1</sup>, respectively, as shown in figure 6.11 (d). The CCG electrodes demonstrate considerably enhanced  $C_{sp}$ s than the pristine Co-Cr-LDH, highlighting the advantages of the self-assembly and synergistic effect of both Co-Cr-LDH and GO Ns matrix for enhancement of supercapacitive performance. [34] The achieved enhancement of the electrochemical activity over hybridization with GO matrix is responsible to high charge transport kinetics due to plenty of accessible redox-active sites and high conductivity of GO in the CCG nanohybrids.

Figure 6.11 (d) shows variation of  $C_{sp}$  with current density for CCG nanohybrid and Co-Cr-LDH electrodes. The observed reduction in the  $C_{sp}$  with current density is attributed to diffusion effect of solvated electrolyte ions in CCG electrodes, where active electrochemical sites cannot lead the oxidation-reduction reaction completely at high current densities. Improved diffusion of the solvated electrolyte ions is achieved due to anchor assembly of Co-Cr-LDH and GO Ns. At high current density, all the CCG nanohybrids maintain higher  $C_{sp}$ s than pristine Co-Cr-LDH which represents fast charging-discharging capability (high rate characteristic) of CCG nanohybrids. The high rate characteristic of CCG nanohybrids can be credited to the unique random stacking structure of CCG nanohybrids that facilitate fast charge transport through nanohybrid electrodes.

Moreover, the chemical composition of CCG nanohybrids has a significant effect on their charge storing ability. The CCG-2 nanohybrids with optimum GO matrix display a maximum  $C_{sp}$  of 1502 C g<sup>-1</sup> than CCG-1 (795 C g<sup>-1</sup>) and CCG-3 (841 C g<sup>-1</sup>). The low performance of CCG-1 may be attributed to the small GO percentage that is insufficient to provide conducting channels for rapid charge transport. On the other hand, the decreased performance of CCG-3 nanohybrid can be ascribed to excess GO incorporation, which reduces the active LDH content in CCG-3 nanohybrid. Thus CCG-2 nanohybrid can be regarded as the best-optimized nanohybrid composition among the prepared nanohybrids. The electrochemical performances of the previously reported Co-based LDHs are summarized in Table 6.1.

**Table 6.1:** Comparative SC performances of Co-based LDH.

Sr. No.	Material/Nanohybrid	Method	Cs (F g <sup>-1</sup> )	ED (Wh kg <sup>-1</sup> )	PD (Wh kg <sup>-1</sup> )	Stability (%)	cycles	Ref.
1	NCH11/G/NF	CVD	1410 at 2 A g <sup>-1</sup>	33.75	750	94.2	2500	35
2	Ni-Al-LDH-nanosheet array/graphene composite	LBL deposition	1329 at 3.57 A g <sup>-1</sup>	-	-	91	500	36
3	Co-Co-LDH/graphene	Reflux	1205	49.5	7000	60.3	-	37
4	Ni-Fe-LDH/GHA	Hydrothermal	1196 at 1 A g <sup>-1</sup>	17.6	650	80	2000	38
5	Ni-Al/G-50	Hydrothermal	1147 at 5mVs <sup>-1</sup>	-	-	83.3	2000	39
6	Co-Al-LDH-NS/GO	In situ growth	1031 at 1 A g <sup>-1</sup>	7.7	4.8	-	-	40
7	Graphene/Ni-Al-LDH	Hydrothermal	915	27.6	500	95	1500	41
8	Co-Al-LDH/GHAs	Hydrothermal	640 at 1 A g <sup>-1</sup>	-	-	97	10000	42
9	Ni-Al-LDH/rGO//AC	Hydrothermal	629.8 A 1 g <sup>-1</sup>	58.6	359	80.63	5000	43
10	Fe-Ni <sub>3</sub> -C (Graphene)	Calcination	607 at 10 mVs <sup>-1</sup>	16.9	10483.5	99	1000	44
11	Ni/Mn-LDH@graphene//AC	Hydrothermal	420 at 1 A g <sup>-1</sup>	34.83	1.01kW kg <sup>-1</sup>	94.9	1000	45
12	Graphene/NiAl-LDH	Hydrothermal	213.57 at 1A g <sup>-1</sup>	-	-	100	1000	46
13	NiCoMnLDH//AC	Solution method	206 at 5 A g <sup>-1</sup>	92.8	0.46 kWkg <sup>-1</sup>	-	-	47
14	Ni-Mn-LDH-NF@VG	Hydrothermal	160 at 2 mVs <sup>-1</sup>	56.8	260	87	10000	48
15	NiCoAl-LDH/3D RGO	Hydrothermal	141.6 at 0.4 A g <sup>-1</sup>	57.1	339.46	93.6	4500	49
16	GAL//GAL AFSC	Hydrothermal	127.2 at 1 A g <sup>-1</sup>	35. mWh cm <sup>-3</sup>	1.01 W cm <sup>-3</sup>	83.2	10000	50
17	Co-Al-LDH/GF//AEG	Hydrothermal	101.4 at 0.5 A g <sup>-1</sup>	28	1420	~100	5000	51
18	rGO/CoAl-LDH//rGO	Co-precipitation	99.5 at 1 A g <sup>-1</sup>	22.6	0.09 kW kg <sup>-1</sup>	94	5000	52
19	Ni-Mn-LDH/rGO-4//rGO	Solvothermal	82.5 at 0.5 A g <sup>-1</sup>	29.3	400	90.5	5000	53
20	Co-LDH/G2	Hydrolysis	76.4 F cm <sup>-3</sup>	-	-	90.4	10000	54
21	CCG-2	Co-precipitation	1502 C g <sup>-1</sup> at 1 A g <sup>-1</sup>	-	-	-	-	Present work
	CCG-2/KOH/rGO (AHSC)		181 at 0.8 A g <sup>-1</sup>	56.66	600	95	10000	

### 6.7.3 Electrochemical impedance spectroscopy (EIS) study:

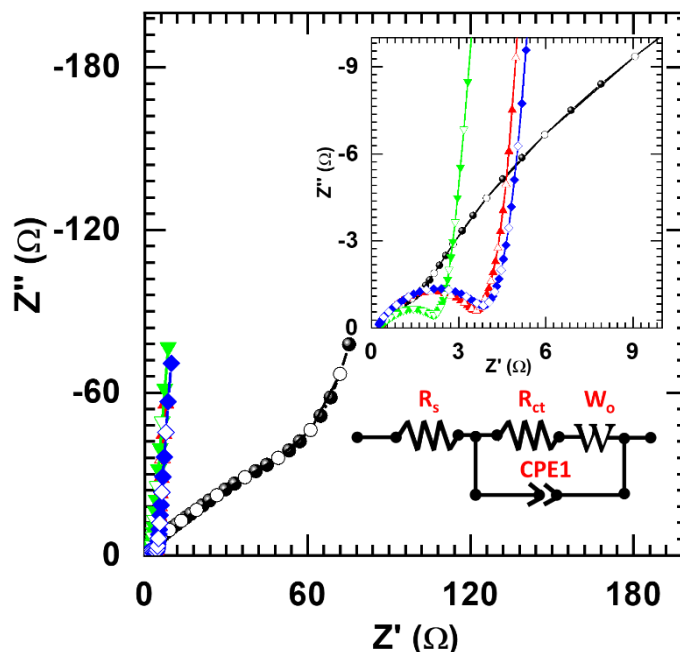


**Figure 6.12:** Nyquist plots of Co-Cr-LDH and CCG nanohybrids. Co-Cr-LDH (black), CCG-1 (red), CCG-2 (green) and CCG-3 (blue) nanohybrids.

The EIS analysis and corresponding Nyquist plots are presented in figure 6.12. As prepared CCG nanohybrids and reference Co-Cr-LDH electrodes collectively show a straight line at low-frequency and a semicircle at high-frequency regions. The starting point of the Nyquist plot represents series resistance ( $R_s$ ) and diameter of extrapolated semicircle represents charge transfer resistance ( $R_{ct}$ ). The CCG electrodes exhibit low  $R_{ct}$  and  $R_e$  values than Co-Cr-LDH electrode, indicating improved charge transfer and electrical conductivity. The electrode with the optimized GO content (CCG-2) has the smallest semicircle compared with the other electrodes. The  $R_e$  and  $R_{ct}$  values assessed from the curve simulation fitting analysis are displayed in Table 6.2.

**Table 6.2:** The  $R_s$  and  $R_{ct}$  values of Co-Cr-LDH and CCG nanohybrids.

Sr. No.	Nanohybrid	( $R_s$ )	( $R_{ct}$ )
1	Co-Cr-LDH	0.25 $\Omega$	95 $\Omega$
2	CCG-1	0.29 $\Omega$	2.95 $\Omega$
3	CCG-2	0.29 $\Omega$	2.12 $\Omega$
4	CCG-3	0.25 $\Omega$	4.01 $\Omega$

Additionally, all the CCG nanohybrids display steep slopes in low frequency region, indicating the lower electrolyte ion diffusion resistance (Warburg impedance). Compared with the pristine Co-Cr-LDH electrode, the CCG nanohybrids display steeper straight lines in the low-frequency region, indicating minimum resistance for the diffusion of the electrolyte ions through the electrode. Hence, the supercapacitive activity improvement in the CCG electrodes is also attributed to the improved electrical conductivity and low diffusion resistance of the electrolyte ions in nanohybrids [73]. Furthermore, the optimized CCG electrode was used to fabricate HSC.

## 6.8 Fabrication and electrochemical performance of aqueous hybrid supercapacitor device (AHSC): CCG-2//rGO

### *Fabrication of CCG-2//rGO AHSC*

The viability of CCG-2 electrode is tested by making AHSC with CCG-2 nanohybrid as a positive and 2D rGO Ns as negative electrodes. The 2 M KOH is served as electrolyte (**Chapter-3, section - 3.5**). The fabricated AHSC cell is denoted by the CCG-2/KOH/rGO AHSC. The schematic representation of the aqueous CCG-2/KOH/rGO AHSC is displayed in figure 6.13.

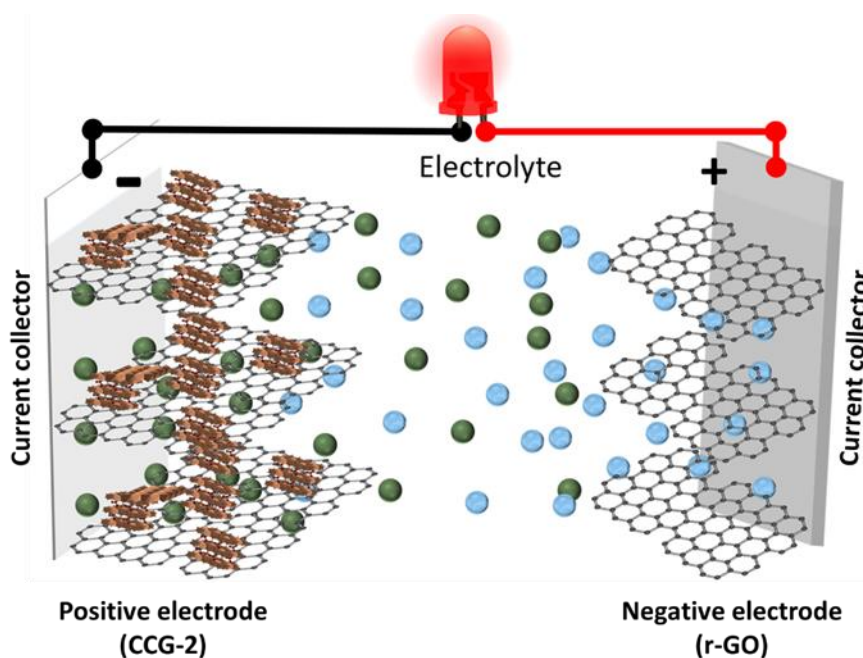


**Figure 6.13:** Schematic representation of CCG-2/KOH/rGO AHSC.

Considering outstanding electrochemical stability and EDLC-type charge storage mechanism rGO is selected as a negative electrode in HSC. [55, 56] In this work, rGO Ns are prepared with hydrothermal reduction of GO Ns. The electrochemical activity of the hydrothermally prepared rGO electrode is studied in a negative potential window using the three-electrode system in 2 M KOH electrolyte with CV, GCD, and EIS techniques. The electrochemical activity of the rGO electrode is described in **Chapter-3, section - 3.8**.

Prior to fabricating CCG-2/KOH/rGO AHSC, the charge delivery by the positive and negative electrodes is balanced by adjusting their respective masses. Based on the charge balancing calculations (**Chapter-4, equation - 4.1**), the mass ratio of the positive to the negative electrode is adjusted to 0.39. After fabricating the AHSC, its electrochemical performance was tested with various electrochemical techniques such as CV, GCD and EIS analysis. The  $C_{sp}$ , ED, PD and Coulombic efficiency for the AHSC are calculated according to the **Chapter - 3, equation 3.2, and Chapter-4, equations 4.2, 4.3, and 4.4**, respectively.

## 6.9 Results and discussion:

### 6.9.1 Cyclic voltammetry (CV) study:

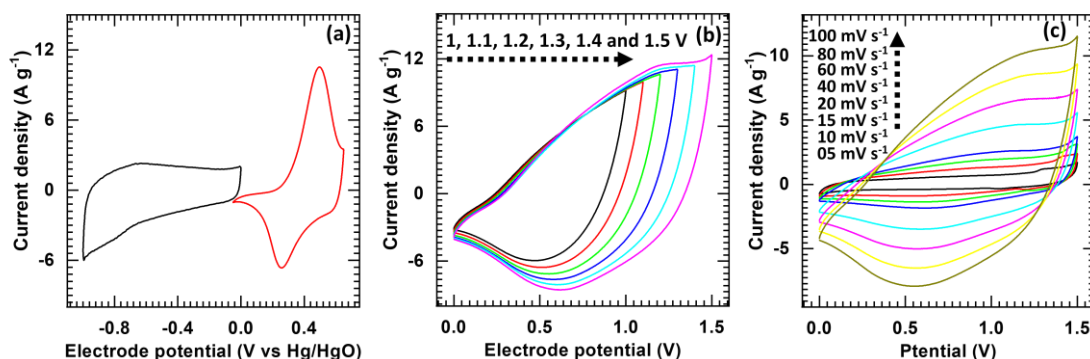


**Figure 6.14:** (a) Mass balance CV curves of rGO (black) and CCG-2 (red) electrodes at sweep rate of  $10 \text{ mV s}^{-1}$ , (b) CV plot ( $100 \text{ mV s}^{-1}$ ) of AHSC at various potential windows (from 0-1 V to 0-1.5 V), (c) CV curves of the AHSC at different scanning rates ( $5\text{-}100 \text{ mV s}^{-1}$ ).

The CV curves of mass balanced CCG-2 and rGO Ns electrodes at sweep rate of  $10 \text{ mV s}^{-1}$  in their respective operating potential windows are displayed in figure 6.14 (a). As reflected from the half-cell measurements, the working potential window for the CCG nanohybrid is  $-0.05$  to  $+0.65 \text{ V vs Hg/HgO}$ , and that of the rGO electrode is  $0$  to  $-1 \text{ V vs Hg/HgO}$ . Thus, fabricated AHSC can operate within the working potential window of  $0$  to  $+1.7 \text{ V}$ . The optimum working potential window is the most important factor to attain the maximum ED of AHSC. Thus, the CV tests for AHSC are performed within the various potential limits ( $0\text{-}1 \text{ V}$  to  $0\text{-}1.5 \text{ V}$ ) at a sweep rate of  $100 \text{ mV s}^{-1}$  to achieve maximum working potential window of the device (figure 6.14 (b)).

The AHSC displays stable current responses up to a potential  $+1.5 \text{ V}$  without any polarization current, suggesting the practical working potential window of  $0\text{-}1.5 \text{ V}$  to get the maximum ED. Figure 6.14 (c) represents the CV curves of AHSC at different sweep rates ( $5$  to  $100 \text{ mV s}^{-1}$ ). The AHSC replicate typical pseudo-rectangular CV shapes even at high scan rates of  $100 \text{ mV s}^{-1}$ , suggesting pseudocapacitive behavior with fast redox reaction kinetics of CCG nanohybrid and rGO electrodes.

### 6.9.2 Galvanostatic charge discharge (GCD) study:

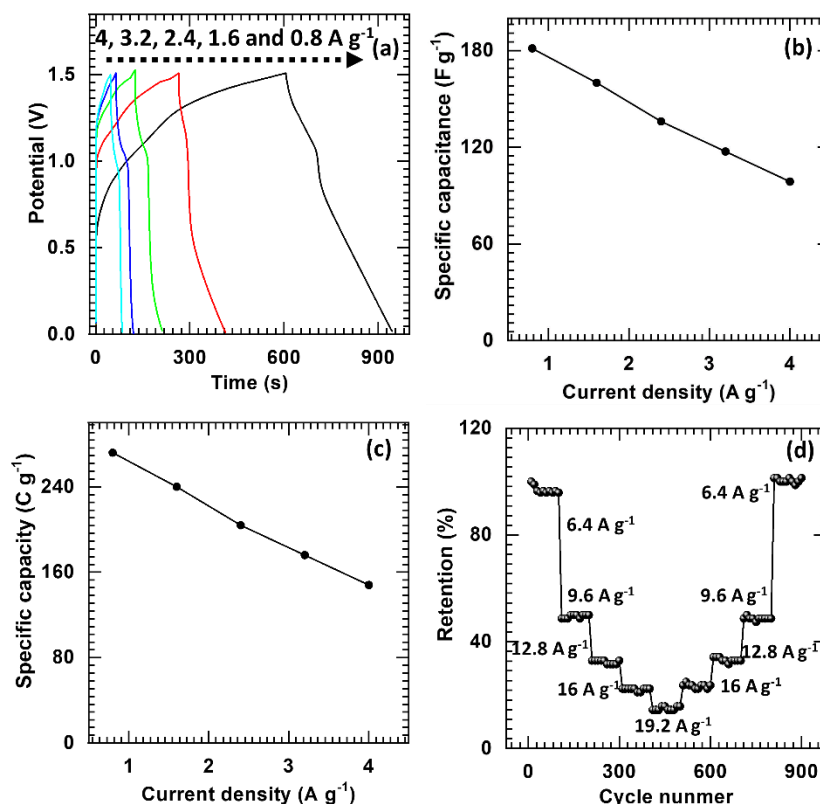


**Figure 6.15:** (a) GCD curves of the AHSC at various current densities (0.8-4.0 A g<sup>-1</sup>), (b) The plot of variation of C<sub>s</sub> with current densities (0.8-4 A g<sup>-1</sup>) for AHSC, (c) The C<sub>sps</sub> of AHSC at various current densities (0.8-4 A g<sup>-1</sup>), (g) The capacitance retention vs cycle number at various current densities (6.4 to 19.2 A g<sup>-1</sup>).

Further the electrochemical performance of AHSC is evaluated by GCD measurements at different current densities (0.8 to 4 A g<sup>-1</sup>), as shown in figure 6.15 (a). The AHSC exhibits pseudo-triangular charge-discharge plot with more extended charge-discharge periods, demonstrating pseudocapacitive characteristics and high energy storage capacity. As AHSC displays pseudo-triangular charge-discharge curves, the electrochemical charge storage performance can express in terms of C<sub>s</sub>. The AHSC delivered C<sub>ss</sub> of 181, 160, 136, 117.33, and 98.66 F g<sup>-1</sup> at current densities of 0.8, 1.6, 2.4, 3.2 and 4.0 A g<sup>-1</sup>, respectively (figure 6.15 (b)). The C<sub>sps</sub> of AHSC for various current densities are calculated from the GCD curves and plotted in figure 6.15 (c). The AHSC displays a maximum C<sub>sp</sub> of 234 C g<sup>-1</sup> at the current density of 2 A g<sup>-1</sup>. The AHSC maintains the high C<sub>sp</sub> of 148 C g<sup>-1</sup> even high current density (4.0 A g<sup>-1</sup>), highlighting its excellent rate capability.

The rate characteristic of the AHSC is probed by applying various charging-discharging current densities (6.4 to 19.2 A g<sup>-1</sup>) and corresponding capacitance variation for 100 GCD cycles is plotted for each current density (figure 6.15 (d)). Interestingly, AHSC recovers 90 % of its original capacitance at an initial applied current density indicating its exceptional rate capability. Present results indicate excellent rate characteristic of AHSC that enables its operation at high current densities without any substantial performance degradation.

**ED vs PD and capacitance retention of CCG-2//rGO AHSC**

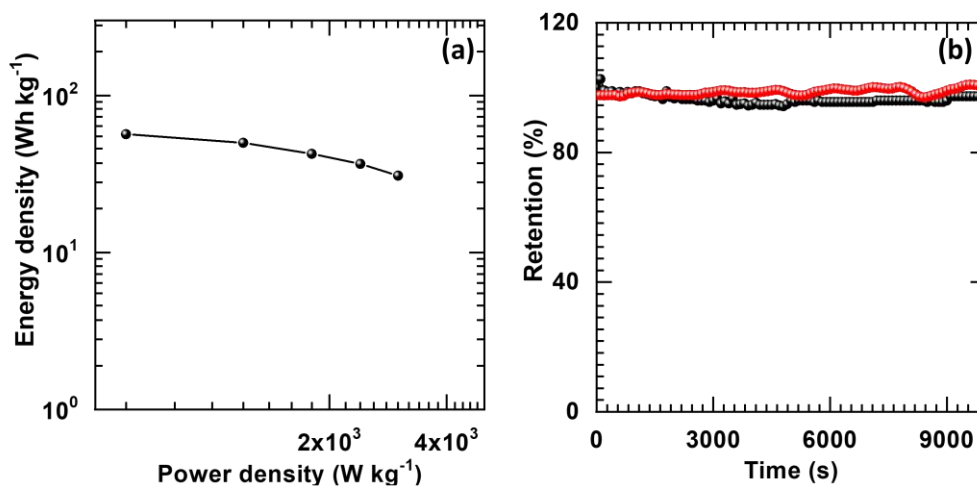


**Figure 6.16:** (a) Ragone plot for the AHSC at various current densities, (b) Capacitance retention and Coulombic efficiencies of the fabricated AHSC device over 10000 cycles.

Furthermore, ED and PD of AHSC are assessed from the GCD curves and plotted in figure 6.16 (a). The AHSC device delivers the maximum ED of 56.66 Wh kg<sup>-1</sup> and PD of 600 W kg<sup>-1</sup> at 0.8 A g<sup>-1</sup> and continues to deliver the ED of 30.83 Wh kg<sup>-1</sup> and PD of 3000 W kg<sup>-1</sup> at 4.0 A g<sup>-1</sup>. Present electrochemical performance of AHSC is superior to the most state of the art aqueous symmetric, asymmetric, and hybrid energy storage devices based on LDH (summarized in Table 6.3).

**Table 6.3:** Comparative SC performances (ED and PD) of Co-based LDH devices.

Sr. No.	Material/Nanohybrid	ED (Wh kg <sup>-1</sup> )	PD (W kg <sup>-1</sup> )	Ref.
1	GAL//GAL AFSC	35.75 mWh cm <sup>-3</sup>	1.01 W cm <sup>-3</sup>	50
2	Co-Al-LDH-NS/GO	7.7	4.8	40
3	Ni-Fe-LDH/GHA	17.6	650	38
4	Ni-Mn-LDH/PC-1	18.60	225.03	57
5	rGO@NiMn-LDH@NF	22.5	700	58
6	rGO/CoAl-LDH//rGO	22.6	0.09 kW kg <sup>-1</sup>	52
7	Co-Al-LDH/GF//AEG	28	1420	51
8	Ni-Mn-LDH/rGO-4//rGO	29.3	400	53
9	NCH11/G/NF	33.75	750	35
10	Ni/Mn-LDH@graphene//AC	34.83	1.01 kW kg <sup>-1</sup>	45
11	Co-Co-LDH/graphene	49.5	7000	37
12	CCG-2//rGO (AHSC)	56.66	600	Present work

### 6.9.3 Electrochemical impedance spectroscopy (EIS) study:

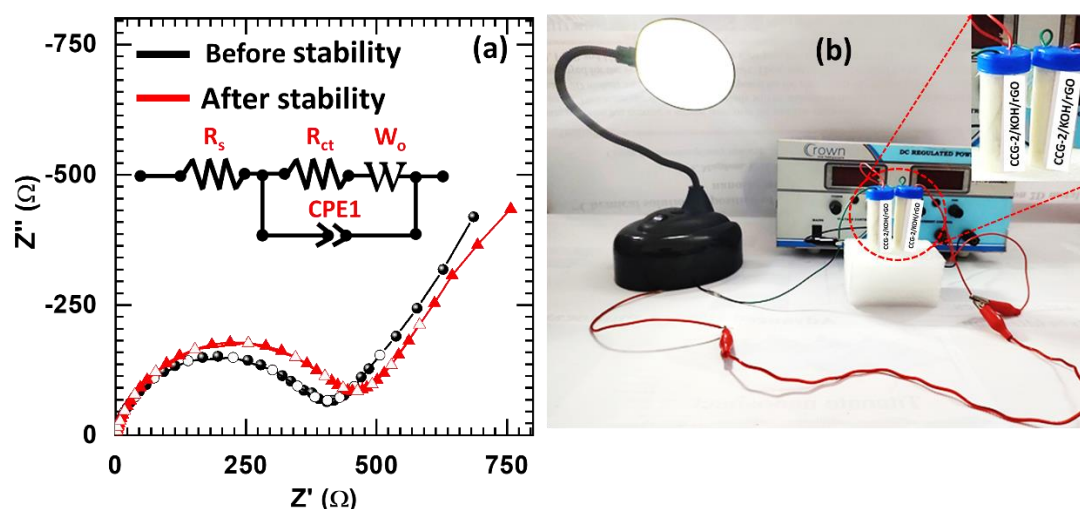


**Figure 6.17:** (a) The Nyquist plots for AHSC device (black) before and (red) after 10000 GCD cycles, (b) Demonstration of the developed AHSC device with a glowing white LED lamp.

The outstanding electrochemical performance of AHSC is ascribed to the high surface area random stacking structure and provision of conducting channels by GO matrix in Co-Cr-LDH-GO nanohybrids which is further confirmed by the EIS analysis. Figure 6.17 (a) shows the Nyquist plots of AHSC device before and after 10000 stability cycles. The AHSC exhibits low  $R_s$  (0.73  $\Omega$ ) and  $R_{ct}$  (414  $\Omega$ ) before

the stability test that slightly changes to  $R_s$  of  $0.78 \Omega$  and  $R_{ct}$  of  $451 \Omega$  after stability test. The low  $R_s$  and  $R_{ct}$  values represent exemplary capacitive behavior and excellent conductivity of both CCG-2 and rGO electrodes in AHSC. The real-life usefulness of the AHSC was tested by glowing a LED lamp, as shown in figure 6.17 (b). The intense glow of the LED lamp highlights its functionality for high-energy and power applications.

### 6.10 Conclusions:

In this work, mesoporous self-assembly of CCG nanohybrids is prepared by the exfoliation-reassembling of positively charged 2D Co-Cr-LDH Ns and negatively charged GO Ns. The present CCG nanohybrids enable wad-like porous morphology, high conductivity and many redox-active charge storage sites. Moreover, the CCG nanohybrids displayed highly porous structures whose porosity is finely tuned by varying the chemical composition. The best optimized CCG-2 nanohybrid demonstrates enhanced electrode performance with the maximum  $C_{sp}$  of  $1502 \text{ C g}^{-1}$  at  $1 \text{ A g}^{-1}$  than pristine Co-Cr-LDH ( $591 \text{ C g}^{-1}$  at  $1 \text{ A g}^{-1}$ ). The increased electrode performance of CCG nanohybrids is attributed to the high surface area wad-like morphology due to random stacking of LDH and GO Ns; high electrical conductivity due to GO matrix; ample redox-active electrochemical sites; and fast charge-transporting channels of CCG nanohybrids. Furthermore, AHSC device is developed using the best optimized CCG-2 nanohybrid as a positive electrode and rGO as a negative electrode. As a result, the AHSC delivered high  $C_s$  of  $181 \text{ F g}^{-1}$  with ED of  $56.66 \text{ Wh kg}^{-1}$  and PD of  $600 \text{ W kg}^{-1}$ . AHSC device display good capacitance retention of 95 % after 10000 GCD cycles. The present study vividly establishes the usefulness of conducting GO as an efficient hybridization matrix to improve the electrode performance of LDH. The present hybridization approach can readily extend to develop various nanohybrids based on diverse 2D LDH and GO Ns.

### 6.11 References:

1. C. Yingna, P. Yingchun, D. Qidong, A. Kumar, Z. Guoxin, C. Zheng, S. Xiaoming, *ACS Appl. Energy Mater.*, 2018, 1, 5685-5693.
2. B. Singh, A. Indra, *Mater. Today Chem.*, 2020, 16, 100404.
3. J. L. Gunjekar, I. Y. Kim, J. M. Lee, N.-S. Lee, S.-J. Hwang, *Energy Environ. Sci.*, 2013, 6, 1008-1017.
4. P. Yin, G. Wu, X. Wang, S. Liu, F. Zhou, L. Dai, X. Wang, B. Yang, Z.-Q. Yu, *Nano Res.*, 2021, 14, 4783-4788.
5. J. Xu, S. Gai, F. He, N. Niu, P. Gao, Y. Chen, P. Yang, *J. Mater. Chem. A.*, 2014, 2, 1022-1031.
6. L. Wang, D. Wang, X. Y. Dong, Z. J. Zhang, X. F. Pei, X. J. Chen, B. Chen, J. Jin, *Chem. Commun.*, 2011, 47, 3556-3558.
7. R. Zhang, H. An, Z. Li, M. Shao, J. Han, M. Wei, *Chem. Eng. J.*, 2016, 289, 85-92.
8. A. F. Al-Hossainy, A. Ibrahim, M. S. Zoromba, *J. Mater. Sci.: Mater. Electron.*, 2019, 30, 11627-11642.
9. J. Yang, C. Yu, C. Hu, M. Wang, S. Li, H. Huang, K. Bustillo, X. Han, C. Zhao, W. Guo, Z. Zeng, H. Zheng, J. Qiu, *Adv. Funct. Mater.*, 2018, 28, 1803272.
10. S. J. Marje, V. V. Patil, V. G. Parale, H. -H. Park, P. A. Shinde, J. L. Gunjekar, C. D. Lokhande, U. M. Patil, *Chem. Eng. J.*, 2022, 429, 132184.
11. Q. Wu, A. Olafsen, Ø. B. Vistad, J. Roots, P. Norby, *J. Mater. Chem.*, 2005, 15, 4695-4700.
12. I. Y. Kim, J. M. Lee, T. W. Kim, H. N. Kim, H.-I. Kim, W. Choi, S.-J. Hwang, *Small*, 2012, 8, 1038-1048.
13. R. A. Nyquist, R. O. Kagel, Academic press, Inc., New York, 1<sup>st</sup> ed<sup>n</sup>, 1971.
14. J. L. Gunjekar, B. Hou, A. I. Inamdar, S. M. Pawar, A. T. A. Ahmed, H. S. Chavan, J. Kim, S. Cho, S. Lee, Y. Jo, S.-J. Hwang, T. G. Kim, S. N. Cha, H. Kim, H. Im, *Small*, 2018, 14, 1703481.
15. D. Graf, F. Molitor, K. Ensslin, C. Stampfer, A. Jungen, C. Hierold, L. Wirtz, *Nano Lett.*, 2007, 7, 238-242.
16. T.-H. Gu, J. L. Gunjekar, I. Y. Kim, S. B. Patil, J. M. Lee, X. Jin, N.-S. Lee, S.-J. Hwang, *Small*, 2015, 11, 3921-3931.
17. X. Bai, Q. Liu, J. Liu, Z. Gao, H. Zhang, R. Chen, Z. Li, R. Li, P. Liu, J. Wang, *Chem. Eng. J.*, 2017, 328, 873-883.
18. C. Dong, X. Yuan, X. Wang, X. Liu, W. Dong, R. Wang, Y. Duan, F. Huang, *J. Mater. Chem. A.*, 2016, 4, 11292-11298.
19. Y. H. Kim, X. Jin, S.-J. Hwang, *J. Mater. Chem. A*, 2019, 7, 10971-10979.
20. M. Pedrosa, E. S. D. Silva, L. M. P.-Martínez, G. Drazic, P. Falaras, J. L. Faria, J. L. Figueiredo, A. M. T. Silva, *J. Colloid Interface Sci.*, 2020, 567, 243-255.
21. S. Wang, B. Gao, Y. Li, A. R. Zimmerman, X. Caod, *RSC Adv.*, 2016, 6, 17792.
22. B. Sivaranjini, R. Mangaiyarkarasi, V. Ganesh, S. Umadevi, *Sci Rep.*, 2018, 8, 8891.
23. S. Park, K.-S. Lee, G. Bozoklu, W. Cai, S. T. Nguyen, R. S. Ruoff, *ACS Nano.*, 2008, 2, 572-578.

24. H.-J. Shin, K. K. Kim, A. Benayad, S.-M. Yoon, H. K. Park, I.-S. Jung, M. H. Jin, H.-K. Jeong, J. M. Kim, J.-Y. Choi, Y. H. Lee, *Adv. Funct. Mater.*, 2009, 19, 1987–1992.
25. X. Li, J. Zhou, W. Xing, F. Subhan, Y. Zhang, P. Bai, B. Xu, S. Zhuo, Q. Xue, Z. Yana, *Electrochim. Acta.*, 2016, 190, 923–931.
26. W.-S. Tseng, C.-Y. Tseng, C.-T. Kuo, *Nanoscale Res. Lett.*, 2009, 4, 234–239.
27. X. Jin, M. Park, S.-J. Shin, Y. Jo, M. G. Kim, H. Kim, Y.-M. Kang, S.-J. Hwang, *Small*, 2019, 16, 1903265.
28. A. S. Patil, J. L. Gunjekar, C. D. Lokhande, U. M. Patil, S. V. Sadavar, N. S. Padalkar, R. B. Shinde, M. M. Wagh, J. S. Bagi, *Synth. Met.*, 2020, 264, 116371.
29. L. Zhang, K. N. Hui, K. S. Hui, H. Lee, *Electrochim. Acta.*, 2015, 186 522–529.
30. J. B. Condon, 1<sup>st</sup> ed., Elsevier, Amsterdam, Boston 2006, p. 274.
31. A. Mardegan, R. Kamath, S. Sharma, P. Scopece, P. Ugo, M. Madou, *J. Electrochem. Soc.*, 2013, 160, B132–B137.
32. E. I. R.-Medgaarden, I. E. Wachs, *J. Phys. Chem. C*, 2007, 111, 15089–15099.
33. Y. K. Jo, W. Tamakloe, X. Jin, J. Lim, S. B. Patil, Y.-M. Kang, S.-J. Hwang, *Appl. Catal. B.*, 2019, 254, 523–530.
34. K. K. Sarigamala, S. Shukla, A. Struck, S. Saxena, *Microsyst Nanoeng.*, 2019, 5, 65.
35. A. Tribalis, G. D. Panagiotou, G. Tsilomelekis, A. G. Kalampounias, K. Bourikas, C. Kordulis, S. Boghosian, A. Lycourghiotis, *J. Mater. Chem. A*, 2015, 3, 12530-12538.
36. J. Xu, S. Gai, F. He, N. Niu, P. Gao, Y. Chen, P. Yang, *J. Mater. Chem. A*, 2014, 2, 1022-1031.
37. X. Bai, J. Liu, Q. Liu, R. Chen, X. Jing, B. Li, J. Wang, *Chem. Eur. J.* 2017, 23, 14839-14847.
38. X. Gao, H. Lv, Z. Li, Q. Xu, H. Liu, Y. Wang, Y. Xia, *RSC Adv.*, 2016, 6, 107278-107285.
39. Y. Kim, S. Kim, *Bull. Korean chem. Soc.*, 2015, 36, 665-671.
40. L. Wang, D. Wang, X. Y. Dong, Z. J. Zhang, X. F. Pei, X. J. Chen, B. Chen, J. Jin, *Chem. Commun.*, 2011, 47, 3556-3558.
41. Y. Wimalasiri, R. Fan, X. S. Zhao, L. Zou, *Electrochim. Acta*, 2014, 134, 127-135.
42. A. Zhang, C. Wang, Q. Xu, H. Liu, Y. Wang, Y. Xia, *RSC Adv.*, 2015, 5, 26017-26026.
43. Q. Du, L. Su, L. Hou, G. Sun, M. Feng, X. Yin, Z. Ma, G. Shao, W. Gao, *J. Alloys Compd.*, 2018, 740, 1051-1059.
44. G. Abellán, E. Coronado, C. M.-Gastaldo, A. Ribera, T. F. Otero, *Part. Part. Syst. Charact.*, 2013, 30, 853-863.
45. W. Lia, Y. Lib, Q. Meng, Y. Xu, B. Yang, T. Li, *Mater. Res. Bull.*, 2020, 129, 110889-110897.
46. Z. Wang, X. Zhang, J. Wang, L. Zou, Z. Liu, Z. Hao, *J. Colloid Interface Sci.*, 2013, 396, 251-257.
47. M. Li, J. P. Cheng, F. Liu, X. B. Zhang, *Chem. Phys. Lett.*, 2015, 640, 5-10.
48. W. Guo, C. Yu, S. Li, J. Yang, Z. Liu, C. Zhao, H. Huang, M. Zhang, X. Han, Y. Niu, J. Qiu, *Small*, 2017, 13, 1701288.
49. X. Bai, Q. Liu, J. Liu, Z. Gao, H. Zhang, R. Chen, Z. Li, R. Li, P. Liu, J. Wang, *Chem. Eng. J.*, 2017, 328, 873-883.

50. L. Li, K. S. Hui, K. N. Hui, T. Zhang, J. Fu, Y.-R. Cho, *Chem. Eng. J.*, 2018, 348, 338-349.
51. T. M. Masikhwa, M. J. Madito, D. Y. Momodu, J. K. Dangbegnon, O. Guellati, A. Harat, M. Guerioune, F. Barzegar, N. Manyala, *RSC Adv.*, 2016, 6, 46723-46732.
52. R. Zhang, H. An, Z. Li, M. Shao, J. Han, M. Wei, *Chem. Eng. J.*, 2016, 289, 85-92.
53. L. Huang, B. Liu, H. Hou, L. Wu, X. Zhu, J. Hu, J. Yang, *J. Alloys Compd.*, 2018, 730, 71-80.
54. X. Chu, T. Deng, W. Zhang, D. Wang, X. Liu, C. Zhang, T. Qin, L. Zhang, B. Zhang, C. Chen, W. Zheng, *J. Energy Chem.*, 2017, 27, 507-512.
55. A. Tribalis, G. D. Panagiotou, G. Tsilomelekis, A. G. Kalampounias, K. Bourikas, C. Kordulis, S. Boghosian, A. Lycourghiotis, *J. Phys. Chem. C.*, 2014, 118, 11319-11332.
56. A. E. Rashed, A. A. E.-Moneim, *Mater. Today Chem.*, 2017, 3, 24-31.
57. L. Sun, Y. Zhang, Y. Zhang, H. Si, W. Qin, Y. Zhang, *Chem. Commun.*, 2018, 54, 10172-10175.
58. M. Yu, R. Liu, J. Liu, S. Li, Y. Ma, *Small*, 2017, 13, 1702616.



# **CHAPTER-7**

## **SUMMARY AND CONCLUSIONS**

**Summary and conclusions:**

At present worldwide conditions of energy crises, efficient energy conversion and storage systems are most needed. Also, efficient energy storage systems played a crucial role in effectively utilizing renewable energy sources. Due to their advantages described in the first two chapters, batteries and SCs are attracting intense research attention as energy storage systems. Furthermore, SCs gain much attention from researchers due to their unique characteristics like high ED, PD, long cycle durability, fast recharge ability, and safe operation. However, symmetric SC cells based on the EDLC-type electrodes can deliver high PD and long cycle durability but limited ED. On the other hand, asymmetric SC cells based on pseudocapacitance-type electrodes can deliver enhanced ED and PD but suffers from limited cycle durability and low ED than batteries. Thus HSC cells are proposed that comprise one EDLC-type and other battery-type electrodes. Thus, HSC can deliver a high power, short charging/discharging periods, ED comparable to the batteries, and long cycle life. However, HSC performance is decided by the efficient working of comprising components like electrode material, electrolyte, and current collector. Therefore, efficient electrochemical activity comprising electrodes is key to achieving high PD, ED, and long cycle life of HSC.

The rGO, an allotrope of carbon, demonstrated excellent EDLC-type HSC electrode performance, thus regarded as the best choice for EDLC-type HSC electrode. On the other hand, lots of research efforts are put forward on battery-type HSC electrode materials (metal oxides, hydroxides, LDHs, metal chalcogenides) to enhance their ED and cycle life. Recently, Co-Cr-LDH, a typical material from the class of LDH, received high attention as an SC electrode material due to its unique layered structure, tunable chemical composition, ion-exchange capability, and redox-active chemical composition. Moreover, the redox-active metal ions are stabilized in the octahedral sites of an LDH lattice which leads to sheet-like morphology of Co-Cr-LDH. Its hydrated gallery space between the hydroxide layers affords the accumulation of a large amount of charge via EDLC-type and the Faradaic (redox) process. However, such gallery space is blocked by the guest anions with a greater charge-to-size ratio. Thus, Co-Cr-LDH material

posses low electrode activity owing to limited accessibility regarding its intergallery space and functionality.

In this regard, present research is focused on improving electrode performance of Co-Cr-LDH by hybridizing it with various nanostructures to enable high surface area, accessible gallery space, and improved conductivity. Typically present research work relies on exfoliation of Co-Cr-LDH (positively charged Ns) and hybridized it with POV anions, POW anions and GO Ns. Conventional chemical co-precipitation followed by exfoliation in the formamide method was used for the synthesis of Co-Cr-LDH Ns. The POV and POW were synthesized by the hydrolysis method at constant pH. GO and rGO were synthesized using modified Hummers and hydrothermal methods, respectively. Furthermore, the Co-Cr-LDH-based nanohybrids were prepared by self-assembly between the positively charged Co-Cr-LDH Ns and POV, POW anions, and GO Ns. The Co-Cr-LDH Ns nanohybrids with POV anions, POW anions, and GO Ns were denoted as CCV, CCW, and CCG, respectively.

The Co-Cr-LDH-based nanohybrids were characterized using Zeta potential, PXRD, FTIR, Micro-Raman spectroscopy, FESEM with EDS, HRTEM /SAED, XPS and BET techniques. Subsequently, electrochemical properties of Co-Cr-LDH-based nanohybrid electrodes were studied by CV, GCD and EIS techniques. Finally, the best-performance CCV, CCW, and CCG nanohybrids were used as positive electrodes to fabricate HSC device. The hydrothermally prepared rGO was used as an EDLC-type negative electrode in HSCs. Consequently, the three types of HSCs are fabricated with cell configuration CCV-2||rGO, CCW-2//rGO and CCG-2//rGO. The present thesis work is distributed into seven chapters.

**Chapter 1** deals with a general introduction that provides general information about the need for energy storage devices, current achievements, basic terminology, and classification of the energy storage systems with a literature survey of various electrode materials for SC. The basic requirements of SC electrode materials are defined and discussed in detail. Moreover, it contains a comprehensive description of LDHs for SC electrodes. Furthermore, the literature survey on Co-based LDH, LDH-based hybrids and 2D INs-based hybrids for SC

electrodes are summarized. Finally, at the end of chapter 1, the orientation and purpose of the dissertation is described.

**Chapter 2** includes the theoretical background of LDH, synthesis methods of LDH, synthesis method of 2D Ns with their exfoliation techniques, and various Ns-based nanostructures. Moreover, this chapter also describes various characterization techniques and instruments with theoretical backgrounds such as Zeta potential, PXRD, FTIR, Micro-Raman spectroscopy, FESEM with EDS, HRTEM, XPS and BET. Finally, the theoretical backgrounds of CV, GCD and EIS electrochemical techniques are explained briefly.

**Chapter 3** deals with the synthesis, characterization and electrochemical performance evaluation of pristine Co-Cr-LDH, GO and rGO. The pristine Co-Cr-LDH, GO and rGO are characterized and analyzed by the XRD, FTIR, Raman, FESEM, EDS, HRTEM, XPS, and N<sub>2</sub> adsorption-desorption (BET) techniques. Pristine Co-Cr-LDH demonstrated nitrate intercalated layered hexagonal structure with nonporous compact surface morphology. The hydrothermally prepared rGO demonstrated characteristic features that confirmed high surface area rGO NSs sponge with high conductivity.

This chapter also deals with electrochemical performance evaluation of Co-Cr-LDH and rGO by CV, GCD, and EIS techniques. The Co-Cr-LDH electrode showed a hybrids-type charge storage mechanism that involves EDLC and battery-type contributions. The electrochemical measurements of the Co-Cr-LDH electrode showed a  $C_{sp}$  of 591 C g<sup>-1</sup> at 1 A g<sup>-1</sup>. In addition, the Co-Cr-LDH exhibited low values of  $R_s$  (0.36 Ω) and  $R_{ct}$  (95 Ω). Also, the rGO electrode shows  $C_s$  of 149 F g<sup>-1</sup> at 0.8 A g<sup>-1</sup> current density. From the analysis of physicochemical characterizations and electrochemical performance evaluation, it is concluded that Co-Cr-LDH and rGO are suitable as redox-type and EDLC-type electrode materials in HSC. However, the compact layered structure, nonporous surface morphology, and low electrical conductivity limit the electrode performance of Co-Cr-LDH.

**Chapter 4** describes the synthesis, characterization, and electrochemical performance evaluation of CCV nanohybrids. The zeta potential measurements displayed effective exfoliation of Co-Cr-LDH and the formation of positively charged monolayered Co-Cr-LDH Ns. This chapter describes the successful synthesis of CCV nanohybrids by self-assembly of Co-Cr-LDH NSs and POV anions. The XRD, FTIR, Micro-Raman, FESEM, EDS, HRTEM, BET, and XPS are used to probe the physicochemical properties of CCV nanohybrids, and results are compared with pristine Co-Cr-LDH. The CCV nanohybrids demonstrated layer-by-layer stacking of Co-Cr-LDH and POV anions, expanded gallery space, mesoporous house-of-card surface morphology, and expanded surface area. Moreover, this chapter deals with the electrochemical performance evaluation of CCV nanohybrids. The best optimized CCV nanohybrid (CCV-2) electrode demonstrated a highly improved Csp of 732 C g<sup>-1</sup> at 1 A g<sup>-1</sup>.

Chapter-4 also deals with the fabrication of AHSC comprising CCV-2 nanohybrid as positive and rGO as negative electrode (CCV-2//rGO AHSC). The CCV-2//rGO AHSC demonstrated high Cs of 149.2 F g<sup>-1</sup> at 0.8 A g<sup>-1</sup>, ED of 53.04 Wh kg<sup>-1</sup>, and PD of 512 W kg<sup>-1</sup> with capacity retention of 85% after 10000 GCD cycles. The highly improved electrode performance of CCV nanohybrids is ascribed to enlarged gallery space, mesoporous house-of-cards type morphology, and expanded surface area of CCV nanohybrids.

**Chapter 5** describes the synthesis, characterization, and electrochemical performance evaluation of CCW nanohybrids. This chapter describes the efficacious preparation of CCW nanohybrids using electrostatically-driven self-assembly of positively charged Co-Cr-LDH NSs and POW anions. The physicochemical properties of CCV nanohybrids are probed with XRD, FTIR, Micro-Raman, FESEM, EDS, HRTEM, BET, and XPS techniques, and the obtained results are compared with pristine Co-Cr-LDH. The analysis of physicochemical characterizations indicated the formation of the layered structure, highly porous surface morphology, high surface area, and expanded gallery space of CCW nanohybrids. The electrochemical performance evaluation of CCW nanohybrids is described in this chapter. The CCW nanohybrids with optimum POW content (CCW-2) displayed enhanced Csp of 1303 C g<sup>-1</sup> at 1 A g<sup>-1</sup> with capacity retention of

---

85.43 % after 5000 GCD cycles. Furthermore, CCW-2 nanohybrid and rGO are further used as positive and negative electrode materials, respectively, to fabricate AHSC (CCW-2//rGO AHSC). The CCW-2//rGO AHSC exhibited Cs of 166 F g<sup>-1</sup> at 0.8 A g<sup>-1</sup>, ED of 59.02 Wh kg<sup>-1</sup>, PD of 640 W kg<sup>-1</sup> with excellent capacitance retention of 91.06 % after 10000 cycles. The real-life usefulness of the CCW-2//rGO AHSC is tested by a powering white LED lamp.

**Chapter 6** describes the synthesis, characterization, and electrochemical performance evaluation of CCG nanohybrids. This chapter describes the effective preparation of CCG nanohybrids using electrostatically-driven self-assembly of Co-Cr-LDH Ns and GO Ns. The physicochemical properties of CCG nanohybrids were probed with XRD, FTIR, Micro-Raman, FESEM, HRTEM, BET, and XPS techniques, and the obtained results are compared with pristine Co-Cr-LDH. As a result, the CCG nanohybrids displayed wad-like porous morphology and highly porous ordered structures whose porosity is finely tuned by varying chemical composition. In addition, the CCG nanohybrids showed the anchoring of restacked Co-Cr-LDH on GO Ns at the nanometer length scale. Further, these anchored Co-Cr-LDH-GO Ns aggregated to form clusters of CCG nanohybrid, making a wad-like appearance.

Moreover, chapter 6 demonstrates the electrochemical performance evaluation of the CCG nanohybrid electrodes. Finely tuned CCG nanohybrid (CCG-2) exhibited improved Csp of 736 C g<sup>-1</sup> at 1 A g<sup>-1</sup>. In addition, the AHSC device was fabricated using CCG-2 as positive and rGO as negative electrodes. The AHSC cell is denoted by notation CCG-2//rGO AHSC. The CCG-2//rGO AHSC device carried a Cs of 170 F g<sup>-1</sup> at 0.8 A g<sup>-1</sup>, ED of 60.44 W h kg<sup>-1</sup>, PD of 640 W kg<sup>-1</sup> with excellent capacitance retention of 95% after 10000 GCD cycles. Finally, the real-world application of CCG-2//rGO AHSC is tested by glowing a white light LED lamp.

**Chapter 7** deals with the summary and conclusions made on results and analysis. From the materials synthesis point of view, it is concluded that the exfoliation-restacking process is highly beneficial to synthesize high surface area mesoporous layer-by-layer nanohybrids of CCV, CCW, and CCG. Also, the

exfoliation-restacking process improves the electrode performance of CCV, CCW, and CCG nanohybrid electrodes.

Furthermore, the electrochemical performance evaluation indicated redox-type charge storage in CCV, CCW, and CCG nanohybrid electrodes with improved electrochemical activity. Therefore, it is concluded that CCV, CCW, and CCG nanohybrids are potential redox-type electrode materials to fabricate AHSC devices. Based on the electrochemical performance of CCV, CCW, and CCG nanohybrids, CCV-2//rGO, CCW-2//rGO and CCG-2//rGO AHSC devices were fabricated. The electrochemical performance of all AHSC are summarized in table 7.1.

Table 7.1 clearly highlights that all the CCV-2//rGO, CCW-2//rGO, and CCG-2//rGO AHSC underscores the advantages of nanohybridization for the improved electrode performance in HSC. Furthermore, from table 7.1, it is also reflected that among tested devices, CCG-2//rGO AHSC demonstrated maximum electrochemical performance with a  $C_s$  of  $170 \text{ F g}^{-1}$ , ED of  $60.44 \text{ Wh kg}^{-1}$ , PD of  $640 \text{ W kg}^{-1}$  and excellent capacitance retention of 95 % after 10000 GCD cycles. The observed electrochemical performances concluded that the CCG nanohybrids are more beneficial redox-type electrodes in HSC fabrication. This fact underscores that GO NSs are the best choice for hybridization with Co-Cr-LDH to enhance electrode performance.

**Table 7.1:** Comparative electrochemical performance of CCV-2//rGO, CCW-2//rGO and CCG-2//rGO AHSC.

Sr. No.	AHSC	Csp ( $\text{C g}^{-1}$ )	Cs ( $\text{F g}^{-1}$ )	ED ( $\text{Wh kg}^{-1}$ )	PD ( $\text{W kg}^{-1}$ )	Capacitance Retention (%)	Cycles
1	CCV-2//rGO	238.72	149.2	53.04 at $0.8 \text{ A g}^{-1}$	512	85	10000
2	CCW-2//rGO	265	166	59.02 at $0.8 \text{ A g}^{-1}$	640	91.06	10000
3	<b>CCG-2//rGO</b>	<b>272</b>	<b>170</b>	<b>60.44 at <math>0.8 \text{ A g}^{-1}</math></b>	<b>640</b>	<b>95</b>	<b>10000</b>



# **CHAPTER-8**

## **80-Recommendation**

# CHAPTER-8

## 80-Recommendation

<b>Sr. No.</b>	<b>Title</b>	<b>Page No.</b>
8.1	Recommendations	195
8.2	Conclusions of the research work	196
8.3	Summary	198
8.4	Future findings	199

### 8.1 Recommendations:

Co-Cr-LDH, a typical material from the LDHs class, is one of the potential redox-type electrode material for the AHSC. Nevertheless, its electrode performance is restricted by the low surface area, compact anion intercalated layered structure and high electrical resistivity. In this regard, present research is focused on improving electrode performance of Co-Cr-LDH by hybridizing it with various nanostructures to enable high surface area, accessible gallery space, and improved conductivity. The exfoliation-restacking approach of exfoliated LDH Ns with oppositely charged guest species attracted intense research attention due to its advantages in obtaining high electronic coupling, mesoporous morphology, flexibility in choosing the hybridized species, and well control over the chemical composition of the hybrids. On these backdrops, the present research is designed on exfoliation of Co-Cr-LDH (positively charged Ns) and hybridized it with POV anions, POW anions and GO Ns. The Co-Cr-LDH Ns nanohybrids with POV anions, POW anions, and GO Ns were denoted as CCV, CCW, and CCG, respectively. Numerous recommendations are made on the findings and conclusion of the synthesis, characterization, and electrochemical performance of Co-Cr-LDH-based nanohybrids. The CCV and CCW nanohybrids demonstrated expanded surface area, highly mesoporous surface morphology, and expanded gallery space. All these unique features of CCV and CCW nanohybrids are highly beneficial for the application in HSC electrodes. Thus, the exfoliation-restacking method is recommended to synthesize LDH-based nanohybrids to achieve high surface area, mesoporous morphology, tunable gallery space and flexible chemical composition.

Similarly, the CCG nanohybrids displayed wad-like porous morphology and highly porous ordered structure whose porosity is finely tuned by varying chemical composition. Also, the CCG nanohybrids showed the anchoring of restacked Co-Cr-LDH on GO Ns at the nanometer length scale.

All the Co-Cr-LDH-based nanohybrid electrodes displayed enhanced electrode performance with a redox-type charge storage mechanism. Thus, the HSC devices were fabricated by using either CCV or CCW or CCG nanohybrids as redox-type electrodes and rGO as an EDLC-type electrode in KOH electrolyte. The three types of HSCs were fabricated with cell configurations CCV-2||rGO, CCW-2//rGO and CCG-2//rGO. All of the AHSC devices performed outstandingly. Among the

tested AHSC devices, the CCG-2//rGO AHSC demonstrated the highest electrode performance with Cs of 170 F g<sup>-1</sup>, ED of 60.44 Wh kg<sup>-1</sup>, and PD of 640 W kg<sup>-1</sup>. Therefore GO Ns are recommended as the best hybridizing species to improve electrode performance of Co-Cr-LDH.

Therefore, the exfoliation-restacking method is recommended to obtain mesoporous layer-by-layer Co-Cr-LDH-based nanohybrids and fine-tuning of AHSC electrode performance. In addition, an exfoliation-restacking route is also recommended to achieve 2D-2D nanohybrids of Co-Cr-LDH wrapped by GO Ns for HSC electrodes.

## 8.2 Conclusions of the research work:

The conclusions from the present research work are listed as follows:

1. Conclusion made from the first two chapters (literature survey): As low Cs and limited cycle life limit AHSC performance, exploring high-performance pseudocapacitive-type or redox-type electrode materials is essential. Though Co-Cr-LDH exhibited a redox-type electrochemical behavior, its electrode performance is restricted by the compact anion intercalated layered structure, low surface area morphology, and high electrical resistivity. Thus, efforts are escalated to improve the electrode performance of LDH-based materials by hybridization with other guest species at the nanoscale.
2. Nitrate anions intercalated Co-Cr-LDH with exfoliation capability is successfully synthesized by the co-precipitation method. The high surface area conducting rGO was successfully synthesized via hydrothermal reduction of GO. Co-Cr-LDH demonstrated redox-type charge storage behavior in KOH electrolyte with Csp of 591 C g<sup>-1</sup> at 1 A g<sup>-1</sup>. The rGO demonstrated EDLC-type charge storage behavior in KOH electrolyte with Cs of 149 F g<sup>-1</sup> at 0.8 A g<sup>-1</sup> and high electrochemical stability.
3. Mesoporous CCV nanohybrids are successfully prepared by the electrostatically driven exfoliation-restacking of Co-Cr-LDH Ns and POV anions. The CCV nanohybrids displayed unique characteristics of expanded gallery space, high surface area, mesoporous morphology, tunable pore structure and flexible chemical composition. As compared to pristine Co-Cr-LDH (591 C g<sup>-1</sup>), the optimized CCV (CCV-2) nanohybrid exhibited enhanced Csp of 732 C g<sup>-1</sup> at 1 A g<sup>-1</sup> and redox-type charge storage mechanism. These results clearly indicate the applicability of CCV nanohybrids as a redox-type electrode in AHSC. The AHSC

fabricated with CCV nanohybrid as a positive electrode and rGO as a negative electrode (CCV-2||rGO HSC device) performed exceptionally with Cs of 149.2 F g<sup>-1</sup> at 0.8 A g<sup>-1</sup>, ED of 53.04 Wh kg<sup>-1</sup> at a PD of 512 W kg<sup>-1</sup> and capacitance retention of 85 % after 10,000 charge-discharge cycles. The obtained electrochemical performance of CCV-2||rGO AHSC highlights its applications in various portable/flexible electronic devices and high-power engineering tools.

4. Mesoporous CCW nanohybrids were successfully prepared by the electrostatically driven self-assembly of 2D Co-Cr-LDH Ns and POW anions. The physicochemical properties of CCW nanohybrids indicating the formation of POW intercalated CCW structure, high surface area mesoporous house-of-card-type morphology, tunable pore structure, and flexible chemical composition. As compared to pristine Co-Cr-LDH (591 C g<sup>-1</sup>), the optimized CCW (CCW-2) nanohybrid exhibited enhanced Csp of 1303 C g<sup>-1</sup> at a 1 A g<sup>-1</sup> and redox-type charge storage mechanism. These results clearly indicate the applicability of CCW nanohybrids as a redox-type electrode in AHSC. The AHSC fabricated with CCW nanohybrid as a positive electrode and rGO as a negative electrode (CCW-2||rGO HSC device) performed exceptionally with Cs of 166 F g<sup>-1</sup> at 0.8 A g<sup>-1</sup>, ED of 59.02 Wh kg<sup>-1</sup> at a PD of 640 W kg<sup>-1</sup> and capacitance retention of 91.06 % after 10,000 cycles. The obtained device performance of CCW-2//rGO AHSC highlights its application in various high-power engineering tools.

5. Mesoporous CCG nanohybrids were effectively synthesized via self-assembly of cationic Co-Cr-LDH Ns with anionic GO Ns. The CCG nanohybrids displayed wad-like porous morphology and highly porous ordered structure whose porosity is finely tuned by varying chemical composition. In addition, the CCG nanohybrids showed the anchoring of restacked Co-Cr-LDH on GO Ns at the nanometer length scale. Further, these anchored Co-Cr-LDH-GO Ns are aggregated to form clusters of CCG nanohybrid, making a wad-like appearance. As compared to pristine Co-Cr-LDH (591 C g<sup>-1</sup>), the optimized CCG (CCV-2) nanohybrid exhibited enhanced Csp of 1502 C g<sup>-1</sup> at a 1 A g<sup>-1</sup> and redox-type charge storage mechanism. These results clearly indicate the applicability of CCG nanohybrids as a redox-type electrode in AHSC. The AHSC fabricated with CCG nanohybrid as a positive electrode and rGO as a negative electrode (CCG-2||rGO HSC device) performed exceptionally with Cs of 170 F g<sup>-1</sup> at 0.8 A g<sup>-1</sup>, ED of 60.44 Wh kg<sup>-1</sup> at a PD of 640 W kg<sup>-1</sup> and capacitance

retention of 95 % after 10,000 cycles. Obtained electrochemical performance of CCG-2//rGO AHSC highlights its applications in various high-power electronic devices and high- engineering tools.

The high-performance AHSCs are made by Co-Cr-LDH-based redox-type and rGO-based EDLC-type electrodes in KOH electrolytes. All of these AHSCs performed outstandingly, signifying importance of the exfoliation-restacking strategy to develop high performance LDH-based HSC electrodes. Therefore, it is concluded that CCV, CCW and CCG nanohybrids are beneficial as a redox-type electrode in HSC. The comparison between the CCV-2//rGO, CCW-2//rGO and CCG-2//rGO AHSC devices indicated, that CCG-2//rGO AHSC device performed exceptionally with highest electrochemical performance. Thus in conclusion GO Ns are regarded as a best choice for the hybridization with Co-Cr-LDH to improve its electrode performance useful for the AHSC.

### 8.3 Summary:

1. The nitrate intercalated Co-Cr-LDH was prepared using the co-precipitation method. The GO and rGO Ns were prepared using modified Hummers and hydrothermal reduction methods, respectively.
2. The Co-Cr-LDH demonstrated redox-type electrode behavior in 2 M KOH with Csp of 591 C g<sup>-1</sup> at 1 A g<sup>-1</sup>.
3. The hydrothermally prepared rGO displayed excellent EDLC-type electrode activity in 2 M KOH electrolyte with Cs of 149 F g<sup>-1</sup> at 0.8 A g<sup>-1</sup>.
5. The CCV, CCW, and CCG nanohybrids were successfully synthesized by the exfoliation-restacking method.
6. All the CCV, CCW, and CCG nanohybrids exhibited redox-type electrochemical activity. The best-optimized CCV-2, CCW-2 and CCG-2 nanohybrids displayed the enhanced Csp of 732, 1303 and 1502 C g<sup>-1</sup> at 1 A g<sup>-1</sup>, respectively.
7. The AHSC device fabricated using CCV-2 as a positive electrode and rGO as a negative electrode showed Cs of 149.2 F g<sup>-1</sup> at a 0.8 A g<sup>-1</sup>, ED of 53.04 Wh kg<sup>-1</sup> at a PD of 512 W kg<sup>-1</sup> and capacitance retention of 85 % after 10,000 GCD cycles.
8. The AHSC device fabricated using CCW-2 as a positive electrode and rGO as a negative electrode delivered a Cs of 166 F g<sup>-1</sup> at a 0.8 A g<sup>-1</sup>, ED of 59.02 Wh kg<sup>-1</sup> at a PD of 640 W kg<sup>-1</sup> and capacitance retention of 91.06 % after 10,000 GCD cycles.

9. The AHSC device fabricated using CCG-2 as a positive electrode and rGO as a negative electrode delivered a Cs of  $170 \text{ F g}^{-1}$  at  $0.8 \text{ A g}^{-1}$ , ED of  $60.44 \text{ Wh kg}^{-1}$  at a PD of  $640 \text{ W kg}^{-1}$  with capacitance retention of 95 % after 10000 GCD cycles.

#### **8.4 Future findings:**

In this research work, problems associated with the low electrode performance of Co-Cr-LDH are addressed successfully by making CCV, CCW and CCG nanohybrids. A novel way of exfoliation-restacking was used to synthesize CCV, CCW and CCG nanohybrids for enabling high surface area morphology, high conductivity, tunable pore structure and flexible chemical composition.

The present exfoliation-restacking strategy can be applicable for numerous other LDHs and various guest species to further enhance the electrode performance of LDH-based electrodes.

Though this research work established state-of-the-art achievements from CCV, CCW and CCG nanohybrids electrodes, some issues must be addressed in the future to further increase AHSC performance.

- ❖ To further enhance electrode performance of Co-Cr-LDH-based electrodes, transition metal doping in Co-Cr-LDH and its hybridization must need to study.
- ❖ The various nanostructure of carbons like carbon nanotube and fullerene can further tune the electrical properties of Co-Cr-LDH-based electrodes.
- ❖ The use of organic and redox electrolytes in HSC can increase ED of Co-Cr-LDH-based HSC.
- ❖ Negative electrode materials other than rGO can be employed to achieve higher PD and electrochemical stability.